# Measurement of Annealing Phenomena in High Purity Metals with Near-field High Energy X-ray Diffraction Microscopy

by

Hefferan, Christopher M.

Submitted in partial fulfillment of the
requirements for the degree of
Doctor of Philosophy
at
Carnegie Mellon University
Department of Physics
Pittsburgh, Pennsylvania

Advised by Professor Robert M. Suter

September 23, 2012

# Contents

**1 Introduction 1**

1.1 Microstructures and Energy . . . . . . . . . . . . . . . . . . . . . . . . . . 2
1.2 Annealing Phenomena . . . . . . . . . . . . . . . . . . . . . . . . . . . . . 4
  1.2.1 Recovery . . . . . . . . . . . . . . . . . . . . . . . . . . . . . . . 4
  1.2.2 Recrystallization . . . . . . . . . . . . . . . . . . . . . . . . . . . 5
  1.2.3 Grain Growth . . . . . . . . . . . . . . . . . . . . . . . . . . . . . 6
1.3 Synchrotron Based Microstructure Mapping Techniques . . . . . . . . . . . 9
  1.3.1 Differential-Aperture X-ray Microscopy . . . . . . . . . . . . . . . . 9
  1.3.2 Diffraction Contrast Tomography . . . . . . . . . . . . . . . . . . . 10
  1.3.3 High Energy X-Ray Diffraction Techniques . . . . . . . . . . . . . . 11
1.4 Orientations and Misorientations . . . . . . . . . . . . . . . . . . . . . . 12
  1.4.1 Orientation Space . . . . . . . . . . . . . . . . . . . . . . . . . . . 12
  1.4.2 Misorientation Space . . . . . . . . . . . . . . . . . . . . . . . . . 13
1.5 Outline . . . . . . . . . . . . . . . . . . . . . . . . . . . . . . . . . . . . 14

**2 X-Ray Diffraction 17**

2.1 Introduction . . . . . . . . . . . . . . . . . . . . . . . . . . . . . . . . . 17
2.2 X-ray Scattering . . . . . . . . . . . . . . . . . . . . . . . . . . . . . . . 18
2.3 Near-Field High Energy X-ray Diffraction Microscopy . . . . . . . . . . . . 21
  2.3.1 X-ray beam . . . . . . . . . . . . . . . . . . . . . . . . . . . . . . 21
  2.3.2 Mathematics of nfHEDM . . . . . . . . . . . . . . . . . . . . . . . . 22
  2.3.3 Beam Attenuator . . . . . . . . . . . . . . . . . . . . . . . . . . . 23
  2.3.4 Imaging System . . . . . . . . . . . . . . . . . . . . . . . . . . . . 24
  2.3.5 nfHEDM as a Rotating Sample Experiment . . . . . . . . . . . . . . 25
  2.3.6 Coordinate Systems, Rotations and Orientations . . . . . . . . . . . 27
  2.3.7 Sample Rotation . . . . . . . . . . . . . . . . . . . . . . . . . . . . 28
  2.3.8 Diffraction Geometry in nfHEDM . . . . . . . . . . . . . . . . . . . 29
2.4 Example Diffraction Calculation . . . . . . . . . . . . . . . . . . . . . . . 32

**3 Recovery in Polycrystalline Aluminum 39**

3.1 Motivation . . . . . . . . . . . . . . . . . . . . . . . . . . . . . . . . . . . 39
3.2 Aluminum . . . . . . . . . . . . . . . . . . . . . . . . . . . . . . . . . . . 39

3.3 Experiment . . . . . . . . . . 40
  3.3.1 Reconstruction . . . . . . . . . . 44
  3.3.2 Map Results . . . . . . . . . . 47
3.4 Recovery . . . . . . . . . . 51
  3.4.1 Interpretation of Recovery through Diffraction . . . . . . . . . . 51
  3.4.2 Kernel Averaged Misorientation . . . . . . . . . . 52
  3.4.3 Tracked Microstructural Analysis . . . . . . . . . . 53
  3.4.4 Global Microstructural Changes . . . . . . . . . . 56
  3.4.5 Recovery - Detector Space . . . . . . . . . . 69

**4 Critical Events** **77**
4.1 Tracking Statistics . . . . . . . . . . 77
4.2 Surface Nucleation . . . . . . . . . . 80
  4.2.1 Kernel Averaged Misorientation . . . . . . . . . . 80
  4.2.2 Intra-granular Misorientation . . . . . . . . . . 82
  4.2.3 Confidence . . . . . . . . . . 84
  4.2.4 Detector Space Analysis of Critical Events on Surface . . . . . . . . . . 86
  4.2.5 Misorientation Relationships of Critical Events on Surface . . . . . . . . . . 88
4.3 Bulk Critical Events . . . . . . . . . . 90
  4.3.1 Bulk Extinction . . . . . . . . . . 90
  4.3.2 Kernel Averaged and Intra-granular Misorientation . . . . . . . . . . 92
  4.3.3 Detector Space . . . . . . . . . . 94
  4.3.4 Neighborhood Misorientation . . . . . . . . . . 95
4.4 Bulk Recrystallization . . . . . . . . . . 96
  4.4.1 Reconstruction Maps . . . . . . . . . . 98
  4.4.2 Internal Misorientation Distributions . . . . . . . . . . 98
  4.4.3 Detector Space Evidence . . . . . . . . . . 99
  4.4.4 Neighborhood Misorientations . . . . . . . . . . 100
4.5 Discussion . . . . . . . . . . 107

**5 Grain Growth in Polycrystalline Nickel** **109**
5.1 Sample Preparation . . . . . . . . . . 110
5.2 nfHEDM Measurement . . . . . . . . . . 111
  5.2.1 Progress in Experimental Setup . . . . . . . . . . 111
  5.2.2 Experiment . . . . . . . . . . 114
5.3 Forward Modeling . . . . . . . . . . 117
5.4 Volumetric Data . . . . . . . . . . 123
5.5 Roadmap . . . . . . . . . . 125
5.6 Grain Growth Topology . . . . . . . . . . 126
  5.6.1 Orientation Spread . . . . . . . . . . 126
  5.6.2 Meshing Parameter Study - Rectilinear Grid Results . . . . . . . . . . 129
  5.6.3 Meshing Parameter Study - Tetrahedral Mesh Results . . . . . . . . . . 134

5.7 Coarsening in Nickel Microstructure . . . . . . . . . . . . . . . . . . . . . . 136
5.7.1 Grain Size Distribution . . . . . . . . . . . . . . . . . . . . . . . . . . 136
5.7.2 Microstructure Evolution with Annealing . . . . . . . . . . . . . . . 138

**6 Microstructure Evolution in Nickel 145**
6.1 Orientations and Misorientations in Nickel Microstructure . . . . . . . . 145
6.1.1 Orientation Distributions in Rodrigues-Frank Space . . . . . . . . 145
6.1.2 Misorientation Distribution . . . . . . . . . . . . . . . . . . . . . . . . 148
6.2 Grain Boundary Character Distribution . . . . . . . . . . . . . . . . . . . . 160
6.3 Calculation and Representation of the Grain Boundary Character Distribution . . . . . . . . . . . . . . . . . . . . . . . . . . . . . . . . . . . . . . . . . 162
6.3.1 Microstructure tesselation in GBCD space . . . . . . . . . . . . . 162
6.3.2 Boundary Resolution and Meshing . . . . . . . . . . . . . . . . . . . 163
6.4 Coherent Twin Distribution through Anneals . . . . . . . . . . . . . . . . . 175
6.5 Sharpening of the Σ3 distribution . . . . . . . . . . . . . . . . . . . . . . . . 178
6.5.1 Microstructure Correlation . . . . . . . . . . . . . . . . . . . . . . . . . 180
6.5.2 Description of Tracked Microstructure . . . . . . . . . . . . . . . . . 181
6.5.3 Misorientation Evolution . . . . . . . . . . . . . . . . . . . . . . . . . . 183
6.5.4 Coherent Twins and Interfacial Area . . . . . . . . . . . . . . . . . . 189
6.5.5 Coherent Twins and Boundary Normal Evolution . . . . . . . . . . 192
6.5.6 Comments on the Coherent Twin Sharpening . . . . . . . . . . . . 196
6.5.7 Comments on the Σ3 Distribution . . . . . . . . . . . . . . . . . . . . 197

**7 Conclusions and Future Work 201**
7.1 Summary . . . . . . . . . . . . . . . . . . . . . . . . . . . . . . . . . . . . . . 201
7.2 Suggestions for Future Work . . . . . . . . . . . . . . . . . . . . . . . . . . . 202
7.2.1 Nickel . . . . . . . . . . . . . . . . . . . . . . . . . . . . . . . . . . . . . 203
7.2.2 Aluminum . . . . . . . . . . . . . . . . . . . . . . . . . . . . . . . . . . . 204

# List of Tables

2.1 X-ray $e^{-1}$ lengths for experimental materials . . . . . . . . . . . . . . . . 22
2.2 Sample Grain Properties . . . . . . . . . . . . . . . . . . . . . . . . . . . 33
2.3 $\boldsymbol{G}_{hkl}$vectors and scattering angles . . . . . . . . . . . . . . . . . . . . . 35
2.4 Angle restrictions for nfHEDM . . . . . . . . . . . . . . . . . . . . . . . . 37

3.1 Distribution of Changes in Grain Averaged *KAM* and Grain Size . . . . 56

4.1 Number of Critical Events by Anneal State and Event Type for Aluminum 78
4.2 Distribution of Kernel Averaged Misorientation of Sample Surface Critical Events . . . . . . . . . . . . . . . . . . . . . . . . . . . . . . . . . . . 82
4.3 Distribution of Intra-granular Misorientation of Sample Surface Critical Events . . . . . . . . . . . . . . . . . . . . . . . . . . . . . . . . . . . 85
4.4 Confidence Statistics for Surface Grains that Disappear in Final Anneal State . . . . . . . . . . . . . . . . . . . . . . . . . . . . . . . . . . . . 86
4.5 Confidence Statistics for Surface Grains that Nucleated in First Anneal State . . . . . . . . . . . . . . . . . . . . . . . . . . . . . . . . . . . . 87
4.6 Misorientation Relationships for Critical Events in First Anneal State . . 90
4.7 Voxel Statistics for Bulk Recrystallization Event . . . . . . . . . . . . . . 98
4.8 Overlapping Peaks for Recrystallized Bulk Grain . . . . . . . . . . . . . . 100
4.9 Misorientation relations of grains in the neighborhood of the nucleated grain. . . . . . . . . . . . . . . . . . . . . . . . . . . . . . . . . . . . . 101

5.1 Annealing Schedule for Polycrystalline Nickel . . . . . . . . . . . . . . . . 115
5.2 Volume Collection of Polycrystalline Ni . . . . . . . . . . . . . . . . . . . 115
5.3 Ten Layer Statistics For Polycrystalline Ni . . . . . . . . . . . . . . . . . 127

6.1 Statistics for Tracked Boundaries in Nickel Microstructure . . . . . . . . 182
6.2 Statistics for $\Sigma 3$ boundaries with changed misorientations . . . . . . . . . 186

# List of Figures

1.1 Boundary energy vs. misorientation angle ($\theta_{mis}$) illustrating a linearly increasing energy with boundary misorientation until $\theta_{mis} \lesssim 15°$, then an approximately constant value. This energy-misorientation curve is adapted from the measurements in [1]. . . . . . . . . . . . . . . . . . . . . . 3

1.2 Boundary energy vs. misorientation angle ($\theta_{mis}$), except grain boundary character is considered by interpreting both misorientation and boundary normal's contribution to the energy of the interface. Each point in the graph represents a single boundary in this 5D space. The plot is based upon bicrystal molecular dynamics simulations in [2]. The simulation data show that the simple one-parameter characterization is insufficient to capture the boundary energy variation. For any misorientation angle, there are boundaries with a wide range of different excess energies. . . . . 4

2.1 Illustration of Bragg scattering from a (2D) periodic lattice. The crystal planes responsible for the scattering are indicated by solid red lines, with solid black dots denoting atoms. The incident ($\boldsymbol{k}_i$) and diffracted ($\boldsymbol{k}_f$) beams are shown in black. (a) shows scattering occuring from the ($hk$), (10) planes, while (b) is from the (41) planes. (b) contains two diffracted beams: black is scattering from the (41), while green is the (10) from (a). The scattering is specular, so $\theta$ between the beam and crystal plane is the same for the incident and exiting beams. $\boldsymbol{Q}$ is indicated in (b) with a cyan arrow. Lattice spacings, indicated by $d$, are different for the two sets of planes and therefore result in different scattering geometries. The additional path length travelled by the second incident beam is shown in green in (a). Constructive interference requires the length to be an integer multiple of the incident beam wavelength. . . . . . . . . . . . . . . . . . . 19

2.2 Simplified schematic of nfHEDM setup employed at the Advanced Photon Source. High energy, monochromatic x-rays (red) are microfocused into a planar sheet, a few microns in height. The beam interacts with a thin cross section of polycrystalline sample (green) and is attenuated by a beam stop. Grains with a crystal plane satisfying the Bragg condition (black) give rise to diffraction that can be imaged on downstream detectors. Peaks can be quantified by their Bragg angle $2\theta$ and detector-plane angle, $\eta$. . . 22

2.3 Sketch illustrating the geometry obtained by rotating the same about $\hat{\boldsymbol{z}}_{lab}$. The green cone is defines a surface which confines the $\boldsymbol{G}_{hkl}$vector and is centered about the $\hat{\boldsymbol{z}}_{lab}$. The cone shows the locus of all configurations for $\boldsymbol{G}_{hkl}$and displays the motion of a physical vector. The red cone illustrates the $\boldsymbol{Q}$ configurations that will produce scattering for a given Bragg angle, $2\theta$. The diffracted beams fall on the blue cone, which is along the $\hat{\boldsymbol{x}}_{lab}$direction, with an opening angle that is twice the Bragg angle. The axis of symmetry for $\boldsymbol{Q}$ and the blue ($\boldsymbol{k}_f$) cones are orthogonal. Bragg scattering occurs at the intersections of the green and red cones. . . . . . 30

2.4 All scattering generated by a grain of the orientation listed in Table 2.2. The scattering is shown when the grain is on the rotation axis and offset by the position $[-0.146, -0.091, 0]$ at $\omega = 0$. All peaks that are generated up to the $\{420\}$ reflection are shown, while a black box indicates the region that would be imaged in a nfHEDM experiment. Black dots indicate scattering that would not be seen due to violation of the angle restrictions itemized in Table 2.4. The points we are sensitive to are colored by their $\omega$ interval. Points in black that fall within our detector box are not observed due to their $\omega$ interval falling outside $[-90°, 90°]$. The projection of the rotation axis-direct beam intersection is marked with an ×. . . . . . . . . 38

3.1 Plots monitoring the motion of the CCD camera as the $LN_2$ evaporates during the course of the 11 layer measurement. (a) illustrates the drift of the horizontal pixel position of the direct beam on the camera, while (b) shows the vertical position. The position is determined by fitting the 'direct beam shadow' to a gaussian, which appears on every camera image and is composed of a weak intensity that maintains a nearly constant profile during the data collection. The fit is conducted in both dimensions and the center is tabulated and plotted in these charts. Vertical lines on both plots indicate the location of a new layer of microstructure, and breaks the graph into 11 sets associated with each 2D cross-section that was measured. Within these vertical lines, three camera distances were used for the measurement and their clustering is also evident. Stray centers, outside of the trend can be attributed to poor fits to the image of interest, due to continued camera motion after translation or weak intensities in the diffraction image. . . . . . . . . . . . . . . . . . . . . . 41

3.2 Calibration curve produced for an aluminum sample of approximately the same dimensions as the one used for the nfHEDM experiment. Horizontal axis is the input temperature, while the response variable is the temperature of the sample measured at the approximately the same location as the aluminum microstructure ($\sim$ 1 mm below the sample tip). . . . . . . 42

3.3 Scan of the aluminum sample tip, prior to one of the measurement volumes. The graph illustrates the sample tip position through the measurement of absorption on a diode, $\sim 2m$ downstream of the sample. Fitting this profile to an error function yields a half-width of $27.2\mu m$ for the transition. This profile showed repeatability after thermal expansion during the heating process and after collection of layers, indicating that we have good agreement between our layer measurements for this experiment. . . 43

3.4 The image processing routine for the aluminum data, illustrating each processing step. (a) illustrates a raw detector image that is associated with an integrated $\delta\omega = 1°$ rotation, from the initial state microstructure. The image was collected at the $L_1$ detector-to-rotation axis distance. (b) displays the statistical background image, composed of the the mean intensity for each pixel in the 100 images used in the single detector distance collection. (c) is the first reduction, subtracting (a) from (b). A 5×5 median filter eliminates 'hot pixels' that are not associated with diffraction and is shown in (d). The pixels that are retained and serve as input to the forward modeling simulation are shown in (e). To better illustrate the diffraction signal, the color scale saturates at 3000 counts for images (a) and (b), while (c)-(e) saturates at 500. . . . . . . . . . . 45

3.5 Two layers of reconstructed orientation maps from the aluminum microstructure. Rows show maps from the same layer of microstructure, while the two set of maps are separated vertically by 80 $\mu$m. The columns indicate sample state. The same granular structure can easily be seen both across states and across layers, with the changes within a layer being more subtle than the vertical translation. Orientations were represented as Rodrigues vectors in a single fundamental zone, then mapped to red-green-blue space. Only voxels exceeding 0.25 confidence ($C = 0.25$) are shown. . . . . . . . . . . . . . . . . . . . . . . . . . . . . . . . . . . . 48

3.6 Expanded color scale image of lower right grain found in Figure 3.5, colored dark green and indicated with a white ×, in the top left map. Instead of allowing the red-green-blue coloring scheme to cover all of fundamental zone of Rodrigues space, it only maps the portion that includes the voxels composing this grain. Therefore, orientation variations are more evident, as is the voxel-based reconstruction achieved with the forward modeling reconstruction. The evolution of these variations will be a point of emphasis in the material to follow. . . . . . . . . . . . . . . . . . . . . . . 49

3.7 Confidence maps corresponding to the orientation maps found in Figure 3.5. Black lines border all voxels where the neighboring voxel exceeds 2° in misorientation. Multiple lines fall over regions of white space, since the boundary map is created with a map containing voxels with confidences as low as 0.1, while these maps have 0.25 as the minimum. Superimposed on Figure 3.5, the black lines would outline the regions of visibly distinct colors. . . . . . . . . . . . . . . . . . . . . . . . . . . . . . . . . . 50

3.8 Histogram of confidence values for the 33 maps measured in three distinct sample states. Confidence bin widths are 0.025. Each layer is individually histogrammed and normalized. The errorbars on each data point are the variation in the bin across the 11 layers composing that state's measurement. 51

3.9 Kernel Averaged Misorientation ($KAM$) maps of the same three layers of microstructure shown in Figure 3.5. The gray scale saturates at $KAM = 0.1°$ (white) and $KAM = 0.5°$ (black) degrees. All three maps use the same gray scale and have red lines outlining boundaries exceeding 2°. . . 53

3.10 $KAM$ histograms for the three anneal states. Horizontal bin widths are 0.1°. Points are average values of histograms computed for each of the 11 layers and error bars are corresponding standard deviations. . . . . . . . 54

3.11 Grain size distribution for tracked grains. Plot has sorted grains by their volume in the initial state. The first and second anneal state corresponding to this grain have the same value on the ordinate axis. The vertical red line shows the demarcation between 'small' and 'large' grains in the microstructure, based upon size variations through anneals. . . . . . . . . 55

3.12 Tracked grains histogrammed by average $KAM$ through the three anneal states. . . . . . . . . . . . . . . . . . . . . . . . . . . . . . . . . . . 55

3.13 Changes in grain averaged $KAM$ in comparison to growth/shrinkage of the grain size through anneals. This is a differential change plot of what was shown in Figure 3.12. Table 3.1 shows the distribution of points by quadrant. Red dots illustrate changes from the initial to the first anneal, while green dots move are differences between the first and final anneal averages. . . . . . . . . . . . . . . . . . . . . . . . . . . . . . . . . . 56

3.14 Changes in grain averaged $KAM$ for tracked grains through anneals. Blue shows the distribution of $KAM$ after the first annealing, while red shows the results of the second anneal. The histogram is similar to 3.12, except now we show a one-to-one evolution. . . . . . . . . . . . . . . . . . . . . 57

3.15 Rodrigues-Frank representation of misorientation between layer and volume for grains in the three sample states. Colors correspond to layers. Plots on the right display the (0,0,0) corner of the misorientation fundamental zone on an exaggerated length scale. . . . . . . . . . . . . . . . 59

3.16 Rodrigues-Frank representation of misorientation between layer and volume for grains in the three sample states. Colors correspond to $\log_{10}$ of the number of voxels in a given 2D layer. Plots on the right display the (0,0,0) corner of the misorientation fundamental zone on an exaggerated length scale. . . . . . . . . . . . . . . . . . . . . . . . . . . . . . 60

3.17 Histograms of misorientation angle between volume averaged grain orientation and layer averaged grain orientation. Only grains that have cross-sections appearing in multiple layers are shown in this graph. Further, only grains containing at least 25 voxels are used in this histogramming. 61

3.18 Histogram of the distribution of *IGM* across the three sample states. The vertical axis is the fraction of voxels which are associated with grains and exceed 0.2 confidence in their orientation assignment. . . . . . . . . . . 61

3.19 Histogram of the distribution of *IGM* across the three sample states. The vertical axis is the fraction of voxels which are associated with grains and exceed 0.2 confidence in their orientation assignment. . . . . . . . . . . 62

3.20 Histogram of the distribution of the change in *IGM* across the three sample states. A total of 114 grains are tracked in this figure. Binning is done in 0.025° increments. . . . . . . . . . . . . . . . . . . . . . . . . . 63

3.21 *IGM* maps of the top ($z_1$) layer of microstructure. Each row denotes a different sample state, while the left column shows voxels colored by the full 3-parameter *IGM*, where the grain averaged orientation is determined by averaging all voxels within a 3D grain (defined by the 2° boundary). Coloring is done by misorientation from this averaged orientation. The right column shows voxels colored by the 1-parameter *IGM* rotation angle (in degrees) from the averaged orientation. White regions in both maps indicate voxels that exceed 2° in *IGM*. . . . . . . . . . . . . . . . . . . 64

3.22 *IGM* maps for single grain in microstructure in the three anneal states. Left column shows voxels colored by the full 3-parameter *IGM*, while the right column shows the *IGM* angle in degrees. The figures show that within a given state, colors (and therefore misorientations from average orientation) are consistent between layers and are spatially localized. Further, that the same colors show up between states indicates that there is a physicality to this substructure within the grain and suggests the existence of subgrains with the microstructure. . . . . . . . . . . . . . . . . 65

3.23 *IGM* plot like Figure 3.22, except for the focus grain of the following analysis. The plots are used to emphasize the layer-to-layer consistency in measurement as well as the repeatability of the underlying structure through anneal states. . . . . . . . . . . . . . . . . . . . . . . . . . . 67

3.24 Evolutionary description of the grain shown in Figure 3.23. The portion of the grain that is in the top layer ($z_1$) of microstructure is shown. The initial anneal state is shown in the top row, while the first and second anneals are rows 2 and 3, respectively. The left most column is an *IGM* map, showing the presence of sub-grains within the microstructure, which become more ordered after each anneal step. The second column is *IGM* parameterized by misorientation angle from the local, 3D lattice. The third column plots confidence, while the final column illustrates *KAM*. . 68

3.25 Histogram of peak widths for the three states of the aluminum sample. Peaks from all 11 layers in each of the three states are listed. Width of peaks are determined by counting the number of distinct $\delta\omega$ intervals for a given diffraction spot. A peak is present in a $\delta\omega$ interval if the reduction program retains a pixel that belongs to a peak. . . . . . . . . . . . . . . 71

3.26 Histograms illustrating the change in $\delta\omega$ peak widths for a subset of grain cross-sections which exhibited both minimal areal change during anneals and remained within the bulk of the wire. (a) displays all $\delta\omega$ width changes for peaks between sequential anneal states. A total of 1149 peaks are binned in this histogram, with 672 followed from the initial to 80C state and 477 in the next annealing sequence. (b) partitions the binning from (a) into the anneal progression from which it originated. (c) shows how peaks (which can be correlated among all three states) have evolved from the initial state. There are 409 of these tracked peaks, emanating from the 57 distinct cross-sections. . . . . . . . . . . . . . . . . . . . . . . 73

3.27 Histogram of $\delta\omega$ changes from the initial peak width, after the sample has been annealed once and twice. The plot is the same as Figure 3.26(c), except peaks are now classified by their origins in the microstructure. Cross-sections of grains which exhibited a decrease in average *KAM* are illustrated in cyan and magenta, while 2D sections that exhibited an increase in KAM during at least one of the anneals are shown in red and blue. The red and magenta bars correspond to changes in peak width after the first anneal. The cyan and blue bars are from changes between the final and initial states. . . . . . . . . . . . . . . . . . . . . . . . . 74

3.28 Three dimensional scattering picture illustrating the differences in peak geometry for a grain with orientation spread (left) and with a single orientation (right). The existence of tails in $\omega$ is clearly evident in the grain with orientation spread. Peaks have been colored by ID to make them visually distinct. The grain used to produce the diffraction is from the first layer of the initial state of the microstructure. $j$ and $k$ correspond to the horizontal and vertical camera pixel addresses. . . . . . . . . . . 74

3.29 Plot illustrating the differences in peak cross-section for a grain with orientation spread and the same grain with a single (grain-averaged) orientation assigned to the same set of voxels. The peaks are those shown in Figure 3.28. Areas have been determined by identifying individual peaks in detector space and collapsing them through $\omega$ space. This tabulation is done for both sources. The number of unique (x,y) pixels that remain are then counted and plotted on the axes. The majority of peaks have a larger area in the presence of orientation spread. . . . . . . . . . . . . . . . 75

4.1 Spatial location of critical events in the aluminum microstructure. Dots indicate the location of events that are the appearance of a new grain that was not present in the previous state, while × denote the disappearance of grains. Markers in red correspond to the event being seen in the final anneal state, while green is associated with the first anneal. The black outline gives a reference for the averaged edge of the sample for both the first and final anneal states. . . . . . . . . . . . . . . . . . . . . . . . . 79

4.2 *KAM* distribution for grains in the initial and final microstructure states. Horizontal axis shows the size of the grain in the given state as counted by the number of composing voxels (in 3D). Each point represents a grain in the interior microstructure that is described in the text. Each dot represents the average *KAM* of all voxels within the grain in the target state, while errorbars denote the standard deviation of these values. The colored points in the plot on the left indicate grains would eventually disappear from the measured microstructure, with red points indicating disappearing surface grains in the final state, blue points as those that disappear in the first anneal state and green points as grains that were in the bulk that vanished in the final anneal state. The red and blue convention indicating the final and first anneal state, respectively, are used in the the plot on the right to denote nucleation events and their distribution in the final state. . . . . . . . . . . . . . . . . . . . . . . . 81

4.3 Reconstructed microstructure maps for the fifth layer of the aluminum microstructure, with voxels colored by their *KAM*. Colored outlines indicate the location of critical events within the microstructure, with red lines forming the boundary of recrystallized grains and green lines circling the grains that are not present in the final state. . . . . . . . . . . . . . . 83

4.4 *IGM* distribution for grains in the initial and final microstructure states. Each point represents a grain in the interior microstructure , just like Figure 4.2, only now *IGM* is shown instead of *KAM*. Each dot represents the average *IGM* of all voxels within the grain in the target state, while errorbars denote the standard deviation of these values. The colored points in the plot on the left indicate grains that would eventually disappear from the measured microstructure, with red points indicating disappearing surface grains in the final state, blue points as those that disappear in the first anneal state and green points as grains that were in the bulk that vanished in the final anneal state. The red and blue convention indicating the final and first anneal state, respectively, are used in the the plot on the right to denote nucleation events and their distribution in the final state. . . . . . . . . . . . . . . . . . . . . . . . . . . . . . . . . . . . . 84

4.5 Spatial distribution of *IGM* with boundary lines enclosing the critical events. Top row has each voxel colored by its *IGM* angle (in degrees), while the bottom row shows the three component misorientation with a coloring scale that maps Rodrigues space to red-green-blue. Events outlined in green indicate grains that disappear in the final state, while those marked in yellow in the top row (and red in the bottom row), show nucleation events. This layer of microstructure is the same as shown for the *KAM* presentation in Figure 4.3. . . . . . . . . . . . . . . . . . . . . . 85

4.6 Detector space images of diffraction emanating from Grain *P* found in Table 4.5. Diffraction is shown in each state for the $(1\bar{3}1)$ reflection in the top row, and (024) reflection in the bottom row. The images have been subjected to background subtraction, but no median filtering or baseline subtraction, to retain the purest form of experimental data. The red outline illustrates where simulated scattering is placed on the detector from the nucleating grain. Evidently, there is some scattering from the nucleating grain in the initial state, but the lack of background separable peaks results in a lack of grain identification. . . . . . . . . . . . . . . . . 88

4.7 Orientation and confidence maps illustrating the bulk interior grain that vanishes in the final anneal state. We show the sixth layer of microstructure ($z_6$), which has the most voxels present for this grain in the first two measurement states. The disappearing grain is in the center of the image and has been colored dark brown. The bottom row illustrates confidences associated with the maps in the top row. It is obvious that the grain is of low confidence in the first two states, then replaced by high confidence voxels associated with neighboring grains. The pink grain that appears near the location of the disappearing grain, in the final state, has the same orientation as the grain towards the bottom right corner of the image and is connected in the layer above the one presented here. . . . . . . . . . . 91

4.8 3D perspective of spatial location of the vanishing grain in the microstructure, shown in Figure 4.7. Red dots indicating voxels that are from the initial state and green dots from the first anneal. Gaps are evident in the microstructure by having given vertical locations without any voxels, specifically the first anneal state. . . . . . . . . . . . . . . . . . . . . . . 92

4.9 Statistical distribution of simple voxel quantities for vanishing grain in bulk microstructure, shown in Figure 4.7. (a) histograms all voxels composing the grain in the initial and first anneal state in 2.5° bins. (b) and (c) show the distribution of confidences and number of voxels by layer, respectively. The errorbars in (b) are tabulated by taking the standard deviation of voxel confidences in the given layer. . . . . . . . . . . . . . . 93

4.10 Spatial distribution of the kernel averaged misorientation for the layer of microstructure presented in Figure 4.7. The maps are centered upon the grain that disappears, which clearly shows a disordered microstructure as evident by the dark voxels associated with large *KAM* values. The disorder is present in the first two states, but in the final state, the region is now part of an adjacent grain(s), with low *KAM* values. This suggests that the ordered microstructure is exhibiting grain growth in the vicinity of this weakly ordered grain and replacing it with a lower energy configuration. . . . . . . . . . . . . . . . . . . . . . . . . . . . . . . . 94

4.11 Distribution of the average *KAM* per voxel as a function of layer in the microstructure. Errorbars are the result of *KAM* variation for the voxels within the given layer. . . . . . . . . . . . . . . . . . . . . . . . . . . 94

4.12 Distribution of the average *IGM* per voxel as a function of layer in the microstructure. Errorbars are the result of *IGM* variation for the voxels within the given layer. The majority of voxels are populated in the sixth and seventh layer, which therefore dominates the grain averaged orientation. 95

4.13 3D spatial distribution of the *IGM* for the grain that vanishes from the bulk in the final anneal state. As can clearly be seen, the grain is neither connected over all layers as well as having different layers misoriented with respect to each other. Voxels in each state are misoriented from the average by as much as 3°. This is quite reasonable for a grain elongated by deformation. . . . . . . . . . . . . . . . . . . . . . . . . . . . . 95

4.14 Detector space scattering illustrating the vanishing signal emanating from the grain in the first two measurement states, but absent in the final anneal state. The diffraction is from a $(1\bar{1}3)$ peak and the red outline illustrates the diffraction pixels that are generated by the grain via the forward modeling simulation. This peak comes from the sixth layer of microstructure and the disappearance of the peak has been verified by looking at neighboring $\delta\omega$ intervals, as well as the adjacent layers (5 and 7) in the final state diffraction images. In the initial and first anneal state, the peak occupies four contiguous $\delta\omega$ intervals; the middle interval with the most substantial intensity is displayed here. . . . . . . . . . . . . . . 96

4.15 Illustration clarifying the discovery of the nucleating grain in the initial microstructure, after improvements to the reconstruction and data reduction algorithms. The same portion of microstructure is magnified in the orientation maps in the top row. With the old software, the reconstruction was unable to find any resolvable orientation that was consistent with the experimental diffraction. (Appears we have one voxel with the correct orientation in the original map with $C \sim 0.2$, indistinguishable from noise.) The improvement in confidences is dramatically illustrated, showing that the new algorithms not only discovered a grain with a weak diffraction signal, but also improved the confidences of all voxels in general. The data that has been presented for the aluminum measurement are based upon these newer fits using improved reconstruction algorithms and the new data reduction program. Interestingly, another grain is also identified in the new fit, colored in pink. . . . . . . . . . . . . . . . . . . . 97

4.16 Confidence and orientation maps from two layers of microstructure to illustrate the nucleation of a grain from a region of low confidence, associated with no strong scattering signal. The top two rows show the orientation and confidence map for the layer originally investigated and stated to be the location of the nucleation event. [3] The bottom two rows are from an adjacent layer, where the grain was found to be present in all three states, only with a weak confidence signal in the initial state. An outline of the grain boundary in each state is shown in black, while the confidence map for the initial state map where the grain is not present (row two, column one) has an outline of the first anneal state's grain boundary location. . . . . . . . . . . . . . . . . . . . . . . . . . . 102

4.17 *KAM* distribution of voxels for the two layers of microstructure shown in Figure 4.16. The color scale saturates at 0.5°. Outlines illustrate the location of the grain in the actual map, except for the first map, which has the same outline as the grain in the final state for that layer, simply to illustrate the region that is eventually engulfed by the nucleating grain. Both layers illustrate that the grain is highly ordered in the final state, as evidenced by its composition of low *KAM* voxels, while the initial state was composed of high *KAM* voxels in the region of nucleation. . . . . . . 103

4.18 *IGM* distribution for the recrystallizing grain in the bulk microstructure. Top row shows each voxel colored by the full three parameter misorientation from average, while the bottom row has voxels on a red-blue scale, colored by misorientation angle from average; the one dimensional parameterization of misorientation. Note the small rotation angle scale for the bottom row. This new grain is effectively composed of a single orientation, with noise about this singular value a result of the reconstruction resolution. . . . . . . . . . . . . . . . . . . . . . . . . . . . . . . . . . . . 104

4.19 Scattering from the nucleating grain through the three sample states for the layer where the grain was aways present. Each row shows a different reflection, with the top row being the (133) reflection and the bottom row ($1\bar{3}1$). The top row had the experimental signal extractable in all three scattering states, while the initial state for the bottom row had the intensity too weak to be seperable from background with the newest reduction routine. Red outlines indicate the pixels that are hit by the nucleating grain in the forward modeling simulation. . . . . . . . . . . . 105

4.20 Scattering from the layer where the nucleating grain is only present in the final two sample states. Each row consists of the raw detector images that have been background subtracted, but not subjected to a median filter. Peaks are isolated in $\delta\omega$ to this singular interval. Red lines indicate the simulated scattering signal that originates from the nucleating grain. Top row illustrates the (133) reflection, while the bottom row shows the ($\bar{2}04$). 106

5.1 Profiles of the tip of the nickel sample in the transmitted beam. Images are the result of translating the sample vertically by $1mm$, with (a) as the top projection and (b) the transition region into a full cylinder. The red circles indicate the reference position that was used for determining geometrical changes in the sample as well as marking the vertical displacement required to collect overlapping sample volumes. In the fourth anneal state, the sample began to exhibit a bow, which resulted in the distance between the two recorded circles to expand. Hypotheses concerning the origin of this bowing are discussed in the text. . . . . . . . . . . . . . . . 110

5.2 Example pattern of a raster scan used to determine pixel pitch of the nfHEDM camera. In this image, a $50\mu m$ beam is placed on the camera, which is translated to produce the pattern seen here. In the event of distortions, such as spatial variation in the imaged beam, adjustments can be made to the camera mount to approach a flat imaging plane. . . . 113

5.3 Comparison between the two beam attenuators used during the course of development of the dedicated nfHEDM setup at 1-ID-B. The nominally single crystal tungsten beam attenuator used for the nickel experiment is shown in (a), while (b) and (c) are from the aluminum experiment using the polycrystalline tantalum beam block. The images produced here are the statistical background images that have been discussed previously, which has each pixel assigned the median intensity over the $\delta\omega$'s used for that single detector distance. (a) and (b) are from the first detector distance ($L_1$), while (c) is from the final detector distance and is used to further illustrate what is beam block and what is scintillator artifacts. Peaks that change spatial location, but move consistently, are due to beam attenuator diffraction. The features that look the same at $L_1$ and $L_3$ are due to imperfections on the scintillator, which was also changed for the nickel experiment to a free standing single crystal. Specifically, the fine, curved line features are imperfections on the Ce scintillator. The cameras used for these measurements were also different, with different number of pixels, pixel sizes, and dynamic ranges. Lastly, the shadow at the base of the aluminum images is not the direct beam, but diffuse scattering off the surface of the tantalum beam attenuator. . . . . . . . . . . . . . . . . . 114

5.4 Orientation and confidence maps from a layer of the *Anneal4* state of the nickel microstructure. Triangles in the map have $2.8\mu m$ side widths. Axis dimensions are in millimeters. . . . . . . . . . . . . . . . . . . . . . . . . 119

5.5 Orientation and confidence maps using the new *LoG* reduction routine. The reconstructed layer is the same as that in Figure 5.4, with only the reduction having changed. Parameters have not been optimized using this new reduction. Confidences are slightly reduced as can be seen by using the same confidence scale as the earlier figure. (c) shows a point-to-point misorientation between the maps produced by the two different reductions. Here, the misorientation between voxels in the same location in each map is tabulated and colored by the misorientation angle. While boundary widths show differences between the fits, which is expected as edges of peaks are changed between the two diffraction image reductions, the appearance of several new grains is also evident. Specifically, many of these new grains have a twin misorientation with the neighboring grain(s). (d) illustrates this twin relationship by only displaying the voxels within 60° of the twin misorientation. . . . . . . . . . . . . . . . . . . . . . . . . 120

5.6 Confidence histograms for all states of the nickel microstructure. Voxels in each layer populate a 0.01° binning scheme. This is converted to a fraction of total voxels for the layer. This normalized histogram is then averaged over all layers composing a volume and produces the points seen in the histogram above. The error bars are standard deviations within the layer for the given bin. The repeatable distribution of confidences through the anneals shows that the quality of fit is repeatable. The initial state has a population below 0.3 because its fits permitted voxels with a confidence of 0.1 to be retained, while the final five states moved this lower bound to 0.3. These low confidence voxels occur on the perimeter of the sample and are not associated with poorly fit grains within the bulk. This is suggested by noting that the *.mic* files used for *Anneal0* had an average of $320k$ voxels per layer, while the later anneals average $269k$ voxels per layer. . . . . . . . . . . . . . . . . . . . . . . . . . . . . . . . . . . . 121

5.7 Single $\delta\omega$ interval diffraction image from the *Anneal4* microstructure. Black pixels illustrate experimental scattering that is not matched by the forward modeling, while red pixels indicate overlap between simulated and experimental diffraction. Green pixels show simulated peaks which do not hit experimental intensity. Fits were conducted to a maximum $|\boldsymbol{Q}| = 10\mathring{A}^{-1}$, which explains why the unfit peaks near the top of this image do not overlap the simulation. They fall beyond the simulated diffraction range. The large peak sizes are representative of the large grains that are present in the microstructure in this state. Fitting to higher order peaks ($|\boldsymbol{Q}| = 12\mathring{A}^{-1}$) would further improve positional and orientational resolution, but at a substantial computational cost. . . . . . 122

5.8 Mesh microstructures from the first four sample states. Anneal state increases from left to right, with the initial state obliquely cut to illustrate the interior microstructure. These meshes are based of a rectilinear grid with in-plane elements of $1.2\mu m$ side-widths. . . . . . . . . . . . . . . . . . 125

5.9 Intragranular misorientation distribution as interpreted on the voxel scale. Plot on left shows how the distribution of all voxels that are associated with grains (fitting our criteria) vary from state to state. The histogram shows the fraction of voxels in the given volume by partitioning by both anneal state and intergranular misorientation value. The number of voxels in each state is shown in Table 5.3. . . . . . . . . . . . . . . . . . . . . . . 127

5.10 Intragranular misorientation interpreted on the grain scale. The first plot is similar to the plot on the left in Figure 5.9, only now the averaging is done over grains. Specifically, an intragranular misorientation average and deviation is determined by averaging this quantity for all voxels that compose a grain. This is then averaged to produce the distribution seen. The right plot shows how voxels are distributed within each grain in each of the anneal states. The large, outlier points are explained in the text and are due to fundamental zone edge effects. . . . . . . . . . . . . . . 128

5.11 Confidences maps of a representative layer of microstructure from our measurement. The maps illustrate the spatial distribution of low confidence voxels, which is used populating the rectilinear grid. Only voxels with confidences less that 0.5 and 0.7 are shown in (a) and (b), respectively. (c) shows voxels that are in excess of 0.7. . . . . . . . . . . . . . . 130

5.12 Number of grains in rectilinear grid as a function of misorientation threshold in grain orientation averaging. Data is presented from tesselating each of the volumes differently to see how the distribution changes. Obviously, since the microstructures vary in number of layers collected, the number of grains will be variable between states. The same grid resolution was used for the study and was composed of voxels with an in-plane resolution of $0.923\mu m$ square, except for *Anneal0* that used $1.2\mu m$ square, which is the grid resolution used in the tracked microstructure analysis. . . . . . . 131

5.13 Boundary maps from the final state microstructure. In (a), black lines outline boundaries in excess of 15° in misorientation angle, while green lines fall between $[5°, 15°]$. A finer misorientation scale is used for (b), with black lines showing all boundaries greater than 0.25°, while green is in the $[0.1°, 0.25°]$ range. The pink-blue coloring of a grain near $[0.35, -0.35]$ mm is due to the grain's orientation falling on the edge of the fundamental zone in orientation space (as discussed in Section 5.6.1). Despite the dramatically differing colors, this is actually a single grain of minimal orientation variation, like the remaining ensemble. . . . . . . . . . . . . 132

5.14 Number of grains as a function of in-plane grid sizes. The vertical line indicates the $1.2\mu m$ resolution used for the grain boundary tracking measurement. Horizontal axis shows the (square) in-plane resolution of the grid. Convergence appears to be present for the fine resolution initial state points. . . . . . . . . . . . . . . . . . . . . . . . . . . . . . . . . . 133

5.15 Number of grains in smoothed mesh as function of (a) misorientation threshold in grain orientation averaging and (b) in-plane mesh resolution. Data is in comparison to Figures 5.12 and 5.12, which used the straight rectilinear grid for grain counting. (c) takes the ratio of grains in the tetrahedral mesh to those in the *.dx* file from which it originated. Variation in number of grains between meshes is due to changes in the volume of measured microstructure in each sample state. . . . . . . . . . . . . 135

5.16 Grain size distributions for *Anneal0* state, using the rectilinear grid with variable in-plane resolution (a-b) and misorientation threshold (c-d). Grain sizes (represented as both number of grid elements and grain volumes) are plotted on the logarithmic scale. The plots using grain volume as the dependent variable (a,b,d) are the result of multiplying each grid element by the constant building block volume of that grid. For the mesh resolution study (a-b), the grid elements are variable, while in (d), we have used elements with volumes of $5.76\mu m^3$ that correspond to the $1.2\mu m$ grid. (c) histograms by the grain size as number of voxels in a grain. Plots (a,c) illustrate fraction of grains in the microstructure with a given size, while (b,d) uses volume fraction of the measured microstructure as the bin value. 137
5.17 Grain size distribution's using the tetrahedral mesh with variable in-plane resolution (a-b) and misorientation partitioning (c-d). Plots display the same quantities as Figure 5.16, except we use the smoothed tetrahedral mesh instead of the rectilinear grid. . . . . . . . . . . . . . . . . . . . . . . . 138
5.18 Single grain extracted from the meshes in Figure 5.8. The anneal state increases from left to right, with the initial state on the left. The grain increased by 25% in volume from the initial to third anneal state and is one of the larger tracked grains with $\bar{R} = 109\mu m$ (see Section 5.7.2). . . . 139
5.19 Scaled grain size distribution across all anneals, using a grid elements of $1.2 \times 1.2 \times 4\mu m$. For each grain in the rectilinear grid representation (a) and tetrahedral mesh representation (b), a sphere equivalent radius is calculated for the grain's volume, $\bar{R}$, and scales the distribution. . . . . . 140
5.20 Scaled grain size distribution across all anneals. For each grain in the rectilinear grid representation (a) and tetrahedral mesh representation (b), a sphere equivalent radius is calculated for the grain's volume, $\bar{R}$, and scales the distribution. . . . . . . . . . . . . . . . . . . . . . . . . . 141
5.21 Grain volume distributions for 976 tracked grains through the first four sample states. The volume of grains is shown in (a), where volume is represented as number of $5.76\mu m^3$ that compose the grain. (b-c) show the changes in volumes of individual grains, plotted as incremental changes $\frac{dV}{V}$. Changes in grain size between consecutive states is shown in (b), while the evolution with respect to the initial grain size is shown in (c). The red line in (b-c) illustrates the 'no size change' position. . . . . . . . 142
5.22 Number of neighbor distributions for 976 tracked grains through the first four sample states. (a) illustrates the number of grain neighbors through each state, while (b-c) look at differential changes for each grain. (b) shows changes incremental, between consecutive anneal states. . . . . . . 143
5.23 Correlation between grain sizes and number of neighbors for the tracked grains. The coarsening process, leading to larger grain sizes, is easily seen by the black points (*Anneal3*) falling above the red points (*Anneal0*) in the plot. . . . . . . . . . . . . . . . . . . . . . . . . . . . . . . . . . 144

6.1 The orientation distribution of the initial nickel microstructure is shown in (a). (b) shows both the initial and third anneal state, with the third state represented with green points. Each point represents a single grain in the microstructure, extracted from the tetrahedral mesh. We can deduce that while the orientation distribution remains static as we anneal, we do have an anisotropic distribution of orientations in our microstructure, as evidenced by regions of orientation space that remain empty through the entire experiment. Specifically, orientations near the octahedral faces of the fundamental zone space remain absent. . . . . . . . . . . . . . . . . . . 146

6.2 Plots of the orientation distribution from the initial microstructure shown in Figure 6.1, only rotated (a) to illustrate the non-uniform distribution of grains in orientation space. (b) shows the $x-y$ plane projection of the fundamental zone and permits easy identification of the five regions with significant orientation density. This anisotropy in orientation influences the evolution of the microstructure as we anneal and is part of the dominant signal in this experiment. In technical terms, this distribution of orientations describes a $\{111\}$ and $\{100\}$ fiber texture. . . . . . . . . . . 147

6.3 Misorientation angle distribution for nickel microstructure through all sample states. Histogram is partitioned with 0.25° bins in misorientation angle and the distribution has been weighted by patch area or number of boundaries, then normalized. (a) illustrates the area weighted distribution for all states and all possible misorientation angles. (b) shows the distribution of boundaries by misorientation angle, with each boundary given a weight of unity. (c) shows the same results as (b), but changes the vertical scale to a maximum of 1% to display that the underlying distribution of misorientation angles is random. The Mackenzie curve for randomly oriented cubes is shown as a heavy black line. . . . . . . . . . . 149

6.4 Expanded view of the two peaks in Figure 6.3, binned with 0.01° resolution in misorientation angle. The peak distribution is shown only in the initial state, though the later anneal states illustrate the same behavior. The peak on the left indicates that $\sim 10\%$ of the interfacial area has a misorientation angle of $60 \pm 0.005°$. The peak is asymmetric due to the physical origins of the responsible misorientation and is clarified in the text. A symmetric peak about 38.95° is shown in (b) and accounts for $\sim 0.5\%$ of the interfacial area. . . . . . . . . . . . . . . . . . . . . . . . 150

6.5 Initial state misorientation distribution of the nickel microstructure, represented in the Rodrigues-Frank misorientation fundamental zone. Each dot corresponds to a different boundary within the microstructure, $\sim 19k$ in all. The plot shows the 3D distribution of the zone, with several clusters present, but not immediately apparent. Figure 6.6 shows integrated slices along the vertical axis to better illustrate such high density regions. 151

6.6 Collapsed sections of the misorientation distribution displayed in Figure 6.5. Each two dimensional plot is an projection of points falling with in a different cross-section of misorientation space, where integration is done over the z-axis. All of the fundamental zone is captured in these images and easily illustrates the clustering that is not readily apparent in the 3D representation shown earlier. Here, a 2D histogram with bin widths of 0.01 in $RF_x$ and $RF_y$ are populated by the number of boundaries falling in that $RF_z$ slice of misorientation space. The bins are colored by the number of boundaries in a given partition of misorientation space. The color scale uses the natural logarithm to illustrate the distribution of boundaries. Most of misorientation space is uniformly filled, which is colored in blue and corresponds to a population of only a few boundaries ($\sim 5$). Regions with a large number of boundaries ($\gtrsim 100$) are colored red, with the largest population occuring in the bottom right slice, with over 1000 boundaries in a single bin. Black circles indicate the location of special misorientation relationships related to the twin misorientation and can be described by $\Sigma 3^n$ in coincident site lattice theory. . . . . . . . 155

6.7 (a) Distribution of interfacial area in the initial microstructure obtained by classifying misorientations with the nearest coincident site lattice point. 98 distinct $\Sigma$ values are used for this classification, ranging from $\Sigma 3$ to $\Sigma 133$. For the population in a bin, the misorientation of the patch must be closer to that $\Sigma$ value than the remaining 97 configurations. No consideration of the misorientation angle from the associated $\Sigma$ is used in (a), while (b) invokes the Brandon criterion for misorientation, only counting those patches that fall within the Brandon angle of the associated $\Sigma$. The Brandon threshold angle, $\theta_{Brandon}$ is shown in (c). All boundaries that fall within the Brandon critierion for a given $\Sigma$ are colored in cyan, while pink illustrates the remaining boundaries. Since the Brandon angle scales as $\frac{1}{\sqrt{\Sigma}}$, the distribution expectedly satisfies the small $\Sigma$ configurations, but there are still a collection of large $\Sigma$ values that fall within the threshold angle. . . . . . . . . . . . . . . . . . . . . . . . . . . . . . . . . . . . 156

6.8 Area fraction of microstructure as associated by $\Sigma$ value. The red and green points indicate two different populations in the data. Red dots are based upon the subset of boundaries that are within 0.25° of a *CSL* misorientation. The green dots relax this distance-from-*CSL* restriction and looks at the area fraction of boundaries associated with a given *CSL* (regardless of misorientation from this *CSL* point). Simply, its a measure of the fraction of boundaries that are closer to the given *CSL* than any other *CSL* point in the utilized list. To clarify, the $\Sigma 3$ red dot has a value close to unity, indicating that of all the boundaries within 0.25° of a *CSL*, approximately all of them are of the $\Sigma 3$ misorientation. The green dot for $\Sigma 3$ is $\sim 0.2$. Therefore, 20% of the interfacial area in our polycrystal is closer to the $\Sigma 3$ misorientation than any other *CSL* in our list. The plot shows that the largest values in both distributions are associated with $\Sigma 3^n$ misorientation configurations. . . . . . . . . . . . . . . . . . . . . . . . 157

6.9 Integrated area distribution as a function of misorientation from *CSL* configuration. The horizontal axis shows the misorientation from the *CSL* configuration ($\theta_{CSL}$), while the vertical axis indicates the fractional area (of patches associated with this $\Sigma$) that have a $\theta < \theta_{CSL}$. . . . . . . 158

6.10 Results of fitting the rising edge portion of integrated area distribution of Figure 6.9 to Equation 6.2. The horizontal axes show the $\Sigma$ number, with only $\Sigma 3^n$ displayed, and for configurations with the same $\Sigma$, points are offset ($\Sigma 27, \Sigma 81$). (a) illustrates the center of the distribution, while (b) shows the width. The information is combined in (c) to illustrate the peak distribution. . . . . . . . . . . . . . . . . . . . . . . . . . . . . . 159

6.11 Molecular dynamics simulation results from [2], for nickel, illustrating the dependence of grain boundary energy on misorientation (a) and boundary plane (b). A total of 388 distinct points in *GBCD* space were investigated and their results reproduced here. The misorientation plot takes all $\Sigma$ values and shows the variation associated with changes in boundary plane orientation. The error bars are the standard deviations associated with different boundaries within the misorientation, while the blue (red) dots indicate the maximum (minimum) energy observed for a given configuration. Energy as a function of boundary plane is shown in (b). All points in *GBCD* space are sorted by increasing energy (horizontal axis in (b)) and a selection of specific boundary plane types are shown with colored dots. . . . . . . . . . . . . . . . . . . . . . . . . . . . . . . . . . . 161

6.12 Distribution of all interface boundaries in the crystal frame for the initial state microstructure. Here, each patch populates the standard stereographic triangle, which uses 1° bins in spherical normal. The distribution is normalized by the total interfacial area, with red regions indicating large population. . . . . . . . . . . . . . . . . . . . . . . . . . . . 163

6.13 *GBCD* plots for the initial state nickel microstructure. The procedure for producing such maps is detailed in the text. Here, the $\Sigma3$ and $\Sigma9$ are illustrated, with the $\Sigma3$ represented on a linear and logarithmic color scale, to illustrate both the sharpness of the $\{111\}$ peak and the distribution of normals in the tails. The $\Sigma9$ distribution is also illustrated (on a linear MRD scale) and displays the prevalance of tilt boundaries, perpendicular to the [110] misorientation axis. The colorbars indicate MRD values, except for the second $\Sigma3$ plot, which is shown on a $\ln(MRD)$ scale. . . . 164

6.14 $\Sigma3$ distribution illustrated with variable in-plane grid resolutions. The coherent twin peak exists for all grid resolutions, but the maximum and width are highly sensitive to the grid resolution. . . . . . . . . . . . . . . 165

6.15 $\Sigma3$ distribution illustrated by fraction of the interfacial area of the microstructure. The plot is analogous to Figure 6.9, except we eliminate the *CSL* association and determine every patch's distance from the $\Sigma3$, as judged by misorientation angle. The horizontal axis indicates the misorientation angle threshold (all boundaries less than this angle are counted), while the vertical axis indicates the fraction of the total interfacial area of the present state's microstructure. . . . . . . . . . . . . . . . . . . . . 166

6.16 Grain boundary normal distribution for patches with a misorientation angle within 0.75° of the $\Sigma3$. The plot is parameterized as $\cos\theta$ vs. $\phi$ and illustrates the peak for the $6\mu m$ resolution grid in (a) and the $0.6\mu m$ grid in (c). Fits to these area weighted histograms are shown in (b) and (d). The histogram is area weighted and normalized to unity. The color scale is the same for all four plots. . . . . . . . . . . . . . . . . . . . . . . . 168

6.17 Results from fitting the $\Sigma3$ boundary normal peak to the von Mises-Fisher distribution. (a) illustrates the maximum value of both the fit (black) and the raw 2D histogram. The fit underestimates the maximum found in the data set, shown in red. (b) displays the peak widths of the distribution, which is a FWHM estimation. Error bars are estimated from the 95% confidence intervals on the fit parameters. . . . . . . . . . . . . . . . . 169

6.18 Strength distribution parameter as determined with the orientation tensor analysis for the initial state microstructure of variable in-plane resolution. Only two unique eigenvalues were found for the distribution, indicating the peak is symmetric about the principal direction ([111]). The strength parameter quantifies how strongly peaked the distribution is. . . . . . . . 171

6.19 Results of fitting each dimension of the 2D area weighted histogram of boundary normals to a Lorentzian functional form. (a) is the normalized, area weighted boundary normal histogram for the initial state microstructure with an in-plane grid resolution of $1.5 \mu m$. The plots in (b) and (c) are the results of integrating across one histogram dimension and fitting the distribution (shown in red). (b) is the $\phi$ distribution, which is produced by integrating vertically in (a), while (c) is the result of integrating horizontally. . . . . . . . . . . . . . . . . . . . . . . . . . . . . . . . . 172

6.20 Results of fitting a Lorentzian function to the coherent twin peak of the $\Sigma 3$ distribution in the initial anneal state. The evolution of the $\cos\theta$ distribution((a),(c)), and the $\phi$ distribution ((b),(d)) are shown as a function of variable mesh resolution. The top row illustrates the amplitude of the normalized distribution, while the bottom row displays the peak's FWHM.173

6.21 Width of the coherent twin as defined by the $\theta_{cone}$ quantity from Equation 6.10. Error bars are described in the text. . . . . . . . . . . . . . . . . . 173

6.22 Grain boundary normal distribution for the $\Sigma 3$ misorientation partition of *GBCD* space. Color scale is the same for each plot and maximizes at an *MRD* value of 800. . . . . . . . . . . . . . . . . . . . . . . . . . 175

6.23 (a) and (b) show the results of fitting von Mises - Fisher function to the $\Sigma 3$ patch normal distribution peak for each of the six sample states, while (c) illustrates the result of using the orientation tensor to determine the strength paramter, defined in Equation 6.7. Results for both $1.2 \mu m$ and $0.92 \mu m$ in-plane resolution are presented. (a) shows the maximum of the coherent twin peak as determined from the raw 2D histogram, like that shown in Figure 6.16(a),(c) and from the von Mises-Fisher fit. (b) displays the FWHM of the peak, with errorbars determined from the 95% confidence interval around the $\kappa$ parameter of Equation 6.4. All three plots indicate a sharpening of the $\Sigma 3$ with each successive anneal. . 176

6.24 Analogous set of plots to Figure 6.20, only now anneal state, instead of in-plane mesh resolution is the dependent variable. Volumetric grid elements are $1.2 \times 1.2 \times 4 \mu m$ for all six sample states. (a) and (b) show how the peak amplitude changes with anneal for the $\cos\theta$ and $\phi$ distributions, respectively. (c) and (d) show peak width changes with anneal, with (c) as the $\cos\theta$ width and (d) the $\phi$ width. . . . . . . . . . . . . . . . . . . . 177

6.25 Annealing evolution of the $\theta_{cone}$, obtained by determining peak widths of $\cos\theta$ and $\phi$ using Lorentzian forms. This quantity gives an estimate of the breadth of the $\Sigma 3$ peak in boundary normal space as a single angle. . 178

6.26 Comparison illustrating the inverse relation between grain boundary energy (top row) and grain boundary population (bottom row) for the initial state microstructure. The inverse relation is apparent for Σ3 and Σ5, but not the Σ9, with a peak in population near the energy maxima. This is attributed to the close relationship between Σ9s and the coherent twins. Simply, the global energy minima of the coherent twin dominates the local energy maxima for the Σ9 misorientation. See the text for further details. The energy plots are based on molecular dynamics simulations for nickel [2] and are reproduced from [6]. Here, each point in *GBCD* space was subjected to interpolation so that the entire boundary normal space could be associated with an energy for a fixed misorientation type. The interpolation is based upon energy values for 388 distinct boundary configurations [2]. The bottom row illustrates the *GBCD* for the configurations shown in the top row. The color scales are different for each plot and selected to fully illustrate the grain boundary normal distribution for a given misorientation. The color scales are $\frac{J}{m^2}$ for the energy plots and MRDs for the population plots. The Σ3 population is colored via $\ln(MRD)$ to illustrate the coherent twin boundary minima. . . . . . . . . 179

6.27 *GBCD* map of the Σ3 misorientation using only the tracked microstructure, consisting of $5,294$ unique boundaries. The location of the coherent twin has been expanded to illustrate that sharpening is present. The color scale is in *MRD*s and is the same scale for each plot and only locations above 250 *MRD*s are illustrated. . . . . . . . . . . . . . . . . . . . . . . . 181

6.28 Grain-to-grain misorientation introduced through sample registration via macroscopic rotation. The distribution is binned by misorientation angle in 0.01° increments. . . . . . . . . . . . . . . . . . . . . . . . . . . 183

6.29 Misorientation-to-misorientation distribution of tracked boundaries within the microstructure, compared to the initial state. (a) bins the misorientation angle between the initial state and later anneal state misorientations. All boundaries in excess of 0.7° are placed in the last bin, which contains 66, 71 and 112 boundaries, for the three anneal states, respectively. (b) and (c) show the full three parameter misorientation in Rodrigues-Frank space. The zone is projected into the $RF_x - RF_y$ plane and contains all misorientation points ($RF_z \leq 0.027$). Each point in the distribution is colored by the second misorientation state, with comparisons always being performed with respect to the initial state. The majority of misorientations are at the origin of the fundamental zone, which is magnified in (c), but there does exist several outliers. . . . . . . . . . . . . . . . . . . . 184

6.30 Misorientation from the $\Sigma 3$ configuration for patch misorientations across the four tracked states. Figure is the tracked analog to Figure 6.9, except now we look at area fraction for the entire microstructure, not just within the *CSL* association. (a) illustrates the distribution integrated over interfacial area, while (b) is over number of boundaries. Vertical red line indicates a misorientation angle of 0.75°, while vertical blue line is at 4.28°. 185

6.31 Misorientation distribution in Rodrigues-Frank space of boundary-to-boundary misorientation with respect to the initial state. Each boundary has a misorientation in each state. Here, we compare this misorientation with that of its corresponding boundary in the initial state. The space is projected into the $x, y$ plane ($RF_z \leq 0.027$). The majority of points are at the origin of the fundamental zone, which is magnified in (b), but there exists a few boundaries that are far from this origin. . . . . . . . . . . . . . . . . . . . 186

6.32 Distribution of boundary normals for Grain 1 from Table 6.2. Boundary normals are represented in the crystal frame of the grain that has exhibited a 'rotation' towards the coherent twin misorientation. The collection of patches composing the boundary, as evolved through the four sample states are presented in a 1° binning. Colors indicate the sum of patch areas (for this one $\Sigma 3$ boundary) falling in the given boundary normal space bin. The color scale is in $\mu m^2$. . . . . . . . . . . . . . . . . . . . . . 187

6.33 Distribution of boundary normals for Grain 2 from Table 6.2. Boundary normals are represented in the crystal frame of the grain that has exhibited a 'rotation' towards the coherent twin misorientation. The collection of patches composing the boundary, as evolved through the four sample states are presented in a 1° binning. Colors indicate the sum of patch areas (for this one $\Sigma 3$ boundary) falling in the given boundary normal space bin. The color scale is in $\mu m^2$. . . . . . . . . . . . . . . . . . . . . . 188

6.34 Patch area weighted histograms in $(\cos\theta, \phi)$ space of boundary normals for patches with misorientation angle within 4.28° of $\Sigma 3$, encompassing $1,034$ boundaries. The distribution is normalized over area, with the same color scale illustrated for each histogram. . . . . . . . . . . . . . . . . . . 189

6.35 Distribution of tracked interfacial area through the four sample states. (a) and (c) histogram the individual triangular elements (or patches) that compose the boundary, while (b) and (d) histogram by boundary area. Hence, (a) and (c) show the size distribution of the building blocks of our mesh, while (b) and (d) illustrate how those building blocks are collected into boundaries. (a) illustrates the distribution of patches that compose the boundaries seen in (b). A few outlier patches of large area exist in (a), but have been supressed. (b) is displayed on a logarithmic scale in fraction, to illustrate that a few exceptionally large boundaries are present. The second row shows the distribution of the $\Sigma3$ boundaries in terms of interfacial area, analogous to (a) and (b). The difference is that the area fractions are with respect to the collection of $\Sigma3$ patches and boundaries. Binning is accompished with $5\mu m^2$ and $250\mu m^2$ increments for the patch and boundary distributions, respectively. . . . . . . . . . . 190

6.36 Histogram of the $\overline{(}\cos\alpha)$ quantity for tracked $\Sigma3$ boundaries. A $\overline{(}\cos\alpha) \sim 1$, indicates that the boundary normal is aligned with the $\{111\}$ direction. 192

6.37 Histograms illustrating the area distribution as classified by grain boundary normal coherence. Boundaries that are coherent fall within the FWHM of the *GBCD* peak in the initial state, which means boundary normals are within 15.8° of the $\{111\}$ direction. The binning is done with respect to fractional change in boundary area, where the plot in (a) uses the initial state boundary area as the reference, while (b) interprets incremental changes in area and uses the previous state as the reference. Distinction is not made for anneal state in (b). All incremental changes are binned. . 193

6.38 Patch area weighted histograms in $(\cos\theta, \phi)$ space of boundary normals for patches with misorientation angle within 4.28° of $\Sigma3$, encompassing $1,034$ boundaries. The boundary plane normal distribution has been held static, using the patch normals from the initial anneal state. Corresponding areas of the tracked patches for each anneal state were assigned to this boundary normal distribution. Normalization is performed over area, with the same color scale illustrated for each histogram, which is the same scale Figure 6.34. . . . . . . . . . . . . . . . . . . . . . . . . . . . . . . . . . . . . 194

6.39 Plots illustrating the coherent twin character of the boundary normal distribution as defined by $\overline{\cos\alpha}$, the area weighted boundary normal projection onto the coherent twin ({111}) axis. Each boundary is composed of two atomic planes, one for each composing grain, and here we compare their relative magnitudes. (a) illustrates the distribution with the different crystal frames on the two axes. The scatter plot shows a clustering towards both unity and $\cos\alpha_A = \cos\alpha_B$ as we anneal, suggestive of a higher coherent twin population. See text for details. (b) shows the top right corner of (a), to illustrate the movement towards $\cos\alpha_A = \cos\alpha_B$, with increasing anneal state. Specifically, the third anneal state shows a large number of boundaries with $\cos\alpha_A = \cos\alpha_B$, suggesting many coherent twin patches composing the boundary. (c) and (d) are histograms showing the difference in coherent twin character in the two crystal frames. (c) shows the population as a function of anneal state, while (d) shows incremental differences after each anneal. . . . . . . . . . . . . . . . . . . . . 195

6.40 Changes in $\overline{\cos\alpha}$ for a given boundary as a function of anneal state. (a) uses the initial state as a reference, while (b) shows the incremental changes. The distribution in (a) is peaked at positive $\overline{\cos\alpha} - \overline{\cos\alpha_0}$, indicating that boundaries become more coherent as we anneal. (b) displays incremental changes after each anneal and the distribution is centered around zero. . . . . . . . . . . . . . . . . . . . . . . . . . . . . . . 196

6.41 Fractional integrated area of the $\Sigma3$ boundaries as described by their coherent twin character ($\overline{\cos\alpha}$). For a given $\overline{\cos\alpha}$ on the horizontal, its integrated area is the fractional area of all boundaries, in that given state, that have $\overline{\cos\alpha_i} \leq \overline{\cos\alpha}$. The shift in curves from left to right indicates that more of the boundary area is aligned with the {111} direction than the previous anneals. . . . . . . . . . . . . . . . . . . . . . . . . . . 197

6.42 Plots illustrating the $(\cos\theta, \phi)$ distribution of the coherent twin. The interfacial area of the distribution has been held fixed with each tracked patch being assigned its initial state area. The boundary normals are maintained to their observed values in the given anneal state. This is the complement to Figure 6.38. The black points are the actual $\Sigma3$ anneal signal, while green is attributed to changes in area and red to changes in normal direction. . . . . . . . . . . . . . . . . . . . . . . . . . . . . 198

6.43 Summary of fits with a Lorentzian function to the decomposed $\Sigma3$ peak, where each anneal state was assigned either the boundary plane normal distribution or area distribution of the initial state. (a) and (b) show the peak amplitude with respect to $\cos\theta$ and $\phi$. (c) and (d) illustrate changes in the peak width, while (e) describes the cone angle that provides a width of the distribution on a sphere. . . . . . . . . . . . . . . . . . . . . . . 199

# Acknowledgments

A thesis is never a work produced by the efforts of a single person, but instead is the culmination of support from a large number of people, filling both personal and professional roles. I would like to thank my advisor, Bob Suter, for many years of patience and guidance in making this thesis a reality. We have stuck together through the peaks and valleys of this technique and seeing it finally blossom in recent years has been incredibly rewarding. It could not have happened without his direction, insight, and style, in the instruction of his students.

I would like to thank the members of my committee, all of which have been heavily involved in my professional career. Tony Rollett has been our closest CMU collaborator and his guidance in the development of the group cannot be overshadowed. By having us look at much of our data from the prospective of a materials scientist, he has helped us produce both good and cutting edge science. Steve Garoff was one of my first scientific mentors, dating back to my lowly undergraduate days at Carnegie Mellon. I want to thank Steve for always being accessible for all things science and non-science. Finally, the dedicated work of Ulrich Lienert has probably been the most instrumental part of making nfHEDM a reality. I am forever grateful for the late nights he would spend at the synchrotron, ensuring that the data in this thesis could be collected. I would like to thank the support staff at the Advanced Photon Source for their assistance during my numerous trips to Chicago, including Ali Mashayekhi, Roger Ranay, Sarvjit Shastri, Dean Haeffner, Jon Almer, Peter Kenesei, Joel Bernier, Kurt Goetze, and Brian Tiemann. The data shown could not have been produced without their help. I also would like to acknowledge the Kerry Piper for making many synchrotron trips a success.

I would like to thank my peers in the graduate program at CMU for making this a very enjoyable seven years. Having inane conversations with BV, Buck, Bepples, PS, Megan, Shiang Yong, RC, Elisa, JB, Booth, Raja, Sauerwine, Lilli, and others have kept me sane, though maybe driven them insane. I thank them for putting up with Crazy Heff. Further, I would like to thank the graduate students most directly involved with my career in nfHEDM. Dan Hennessy's help in my first beam run was key to putting me on the right path in this field. Jon Ledonne's assistance in all things sample preparation and microscopy will always be remembered. I would like to thank Reeju Pokharel for her assistance in collecting the nickel data set shown in this thesis. Frankie Li is mentioned several times in the text and without his dedicated work, I feel this thesis could not have happened. His help in developing most of the analysis software has been essential to our success. It is no coincidence that his entrance into the group also coincided with our dramatic ascent. These sentiments are echoed with Jon Lind. The three of us formed a great team that was delicately balanced and became a well oiled machine. It has been an absolute pleasure working with them.

Lastly, I would like to thank my family for their continued support during my graduate career. I would specifically like to single out my parents. They never really understood the science I was doing or why I was always traveling to Chicago, but they were always supportive in the decisions I made. For that, I will always be grateful.

# Abstract

The forward modeling method (FMM) for analysis of near-field High Energy X-ray Diffraction Microscopy (nfHEDM) has emerged as a powerful tool for materials characterization, with the ability to non-destructively measure microstructures deep within the bulk of materials. A synchrotron based technique, nfHEDM images X-ray diffraction from polycrystals with high resolution cameras. The diffraction signal is used to reconstruct the ensemble of grains in the form of 2D maps with high orientation and spatial resolution, and can be extended to volumetric measurements through sequential measurement. The hallmark of this technique is the ability to monitor the same ensemble of grains as they evolve in response to an external stimuli.

This thesis will investigate the response of microstructure to annealing. The three thermally activated phenomena of recovery, recrystallization, and grain growth will be observed with two high purity metal wire samples. The first measurement, performed on aluminum, demonstrates the replacement of a deformed microstructure with well ordered grains in the recovery and recrystallization processes. A grain growth measurement performed on a fully recrystallized nickel sample demonstrates sensitivity to the evolution of a population of low energy grain boundaries, common to many fcc metals.

# Chapter 1

# Introduction

## Motivation

The use of metals in constructing society's infrastructure has been ubiquitous for centuries. They have served as fundamental building blocks for the construction of shelters, vehicles for transportations, energy systems, mediums of communication, and other integral parts of society. Metals processing and manufacture served as one of the foundations for the Industrial Revolution, which had a profound global impact on the human condition. Simply the conversion of metals into useable media was responsible for the economic boom of industrial cities, like Sheffield, England and Pittsburgh, Pennsylvania. Its economic impacts resulted in the fortunes of many, such as J.P. Morgan and Andrew Carnegie; the founder and benefactor of the university where the research to follow was accomplished.

It is the use of metals, in pure and alloyed forms, for achieving a specific service function that has made them prevalent for industrial application. Silicon exhibits semiconductor properties and consequently is presently in the majority of the world's electronics [7]. Both terrestrial and aeronautical turbine engine blades are typically comprised of nickel-based superalloys because of their strength and long lifetimes to failure, while operating in extreme thermal and mechanical conditions [8]. Zircaloys are used as claddings for nuclear fuel pellets, primarily because of their resistance to corrosion, exceptional strength, and neutron permeability [9]. All these materials are used because they perform their specific function better (or more cost-effectively) than any other available material.

For millennia, it has been understood that applying work to metals can significantly impact their properties. In fact, we have denoted historical periods of history where specific materials were focal points, such as the Bronze and Iron Ages. During these epochs, it was first observed that heating or deforming a material could drastically change its macroscopic properties, such as strength. Still not fully understood was that all these metals were composed of atoms and that material performance was largely due to the way these atoms were assembled. It is these processing steps that influence the material's microscopic properties and consequently its macroscopic performance.

Atoms in metals assemble into regular arrays at ambient temperatures and pressures, because the process is energitically favorable. These regular arrays (called grains or crystals) can be variable in size, ranging from a few nanometers to many millimeters in extent. Further still, the grains can be randomly oriented in space and their relative spatial arrangement with reference to the local environment (termed microstructures) influences macroscopic properties.

It is investigation on the length scales of these heterogeneties that will be the purpose of this work. More specifically, we detail how the application of heat to a microstructure evolves its composite grain ensemble in terms of both arrangement and properties. This motivates the need for a microscope that can overcome the visible light opacity intrinsic to nearly all metals. Additionally, we require sensitivity to the properties of the metal that are responsible for material evolution on the microstructural scale. With these requirements, we introduce the concept of (near-field) high energy x-ray diffraction microscopy and its analysis with the forward modeling method. We will use this volumetric microstructure mapping technique to generate spatially resolved orientations of the same ensemble of grains (on the intra-granular level) and gain insight into the sample material's response to the external stimulus of heat, which is referred to as annealing.

## 1.1 Microstructures and Energy

In the solid phase, metals are composed of regularly spaced atoms arranged in a specific way as defined by its crystal structure. It is in this enviroment that the vast majority (bulk) of atoms reside in a polycrystalline microstructure. While in an ideal polycrystal, all atoms in the interior of grains have the same number of neighbors and consequently atomic bonds, this is not true of real materials. The processing of metals intentionally introduces defects in the form of dislocations into these grains, which make an imperfect crystal. Each of these defects strain the ideal lattice and therefore have an associated excess energy. This energy increases with increasing deformation.

The presence of defects introduces disturbances on very small length scales. On larger scales (microns), the periodic arrangements of atoms can be disrupted, defining a surface where the the orientation of the lattice differs from that of a neighboring region. The portion of space where one grain's lattice (either in orientation, chemical composition, or crystal structure) is abruptly changed into a neighboring configuration is defined as a *grain boundary*. On a much smaller scale, these boundaries are actually the result of the accumulation of many defects. The denser their clustering, the greater the mismatch between the adjacent grains. This mismatch between grains is termed *misorientation* and (geometrically) is described as a rotation required to bring the two lattices into coincidence. Since rotations can be represented as a finite revolution about a fixed axis, the differences betwen boundaries is typically quantified by their rotation angle, $\theta_{mis}$.

Like the defects present within the bulk, these grain boundaries also have an associated excess energy (typically represented as an energy per area of a particular boundary

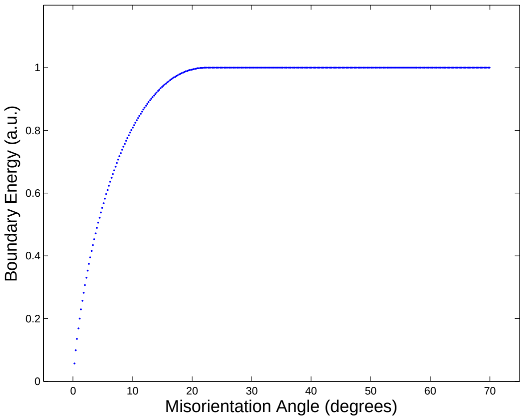

*Figure 1.1: Boundary energy vs. misorientation angle ($\theta_{mis}$) illustrating a linearly increasing energy with boundary misorientation until $\theta_{mis} \lesssim 15°$, then an approximately constant value. This energy-misorientation curve is adapted from the measurements in [1].*

type). These energies are much larger than any single defect and were originally associated with boundary misorientation, as shown in Figure 1.1 [1]. Evidently, boundary energy has a misorientation dependence, with low angle boundaries ($\lesssim$ 15°) having lower energy per area than the roughly constant high angle boundaries. While a good approximation for low angle boundaries when interpreted as a sequence of evenly spaced defects, the curve in Figure 1.1 only takes into account one (misorientation angle) of the five meso-scopic variables (3D misorientation, boundary plane) required to give a complete description of a grain boundary [10, 11, 12]. When interpreted in the entire five parameter boundary space, it is found that energy is actually highly anisotropic. These variations are illustrated in Figure 1.2, which is the result of a molecular dynamics simulation based on a large number of bicrystal pairs[2].

Lastly, polycrystals, as all materials, have external surfaces where interactions differ from deep inside the bulk. It is the interaction of these surfaces with the external environment that can cause adverse effects, such as rust in copper and steel. Just like grain boundaries, which define a solid-solid interface, these free surfaces on metals also increase the energy of the system and can be altered if in an energetically unfavorable state.

The common theme of this discussion is that free energy is associated with imperfections that exist in real materials, and their presence is due to both processing and handling. Therefore, it is exceptionally rare that a given piece of metal is in a global minimum of its energy space (presumably a single crystal in pure metals). Instead, real materials are in metastable states, where the introduction of energy can lead to the activation of mechanisms that move the polycrystal to a lower energy configuration. The new state is infrequently the global minimum of the entire energy landscape, but another local minimum, with lower free energy (Gibbs free energy) than the previous

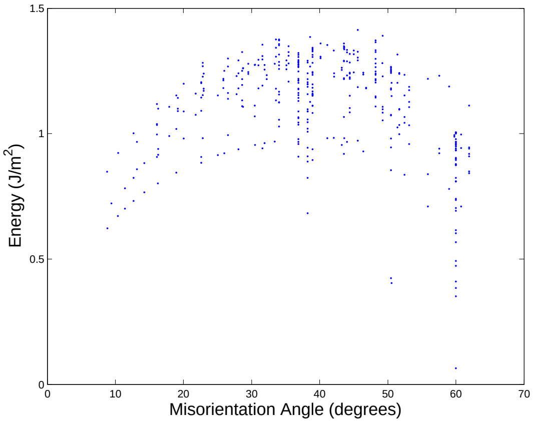

*Figure 1.2: Boundary energy vs. misorientation angle ($\theta_{mis}$), except grain boundary character is considered by interpreting both misorientation and boundary normal's contribution to the energy of the interface. Each point in the graph represents a single boundary in this 5D space. The plot is based upon bicrystal molecular dynamics simulations in [2]. The simulation data show that the simple one-parameter characterization is insufficient to capture the boundary energy variation. For any misorientation angle, there are boundaries with a wide range of different excess energies.*

state. While the energy required to move the system into these different systems can be achieved by numerous thermomechanical processes, it is thermal effects that we will be concerned with in this thesis.

## 1.2 Annealing Phenomena

In the language of metallurgy, the application of heat to a material that evokes a change in its physical properties is defined as annealing [13, 14]. It is widely understood that annealing phenomena can be classified into three categories, each of which can be concurrently present at a given instance. While different in their mechanism, each annealing stage is responsible for progressing a microstructure towards a lower energy configuration. These annealing phenomena are classified as *recovery*, *recrystallization*, and *grain growth*, and investigation of each with near-field High Energy X-ray Diffraction Microscopy will be the goal of this thesis. We will first qualitatively describe each of these phenomena and then provide evidence for their observation in two sets of experiments in the chapters to follow.

### 1.2.1 Recovery

In the bulk of (deformed) real materials there exists a distribution of crystal lattice imperfections called defects. The source of these imperfections can be numerous, including impurities, vacancies, and dislocations (topological mistakes in the lattice construction). These defects are typically heterogenous in spatial distribution. Their locations in the lattice are largely the result of different methods of processing, which can range from general methods to industrially specific recipes that produce a very unique microstructure by controlling several variables.

The introduction of dislocations, via processing, leaves the material in a deformed state, with higher energies due to lattice strain than in a perfect crystal. It is during recovery that the application of heat influences how these dislocations are re-distributed or eliminated so as to begin the process of moving the polycrystal to a less deformed state. In general terms, this involves altering the distribution of dislocations, within regions outlined by high angle grain boundaries. The change can be in terms of both number (density) and spatial distribution.

During thermally activated migrate, multiple dislocations can interact. This can result in annihilation, where the irregular geometries, associated with two interacting dislocations, cancel. The migration can also result in the accumulation of multiple dislocations in a localized region of microstructure. This has the net effect of forming a low angle grain boundary, which is a lower energy configuration than if the dislocations were interspersed (in isolation) throughout the grain. This segregation frequently encompasses regions of defect-free microstructure called subgrains. It is this process that can result in the development of orientation gradients within a grain, as each subgrain has a (small) misorientation with its surrounding [13, 15].

The rate of their production, material temperature, and mode of deformation all play differing roles in determining the distribution of defects. The type of material also influences deformation properties. One way to quantify this is with the stacking fault energy, which is an intrinsic property of materials and is correlated with dislocation mobility [13]. Materials of contrasting stacking fault energy have differing mechanisms for dislocation evolution. Generally, a material with a lower stacking fault energy will have lower dislocation mobility.

### 1.2.2 Recrystallization

Recovery provides one mechanism for returning a deformed microstructure into an undeformed state. Recrystallization can also evolve a microstructure to this end state. The main distinction between recovery and recrystallization is the mechanism for this transformation. Recovery is associated with changes on an intra-granular level achieved with the motion of defects and a redistribution of dislocations. These actions result in the formation of subgrains within pre-existing grains, outlined by high angle boundaries. Therefore, grain boundaries are static during this process. Conversely, recrystallization replaces deformed microstructure with new (undeformed) grains through nucleation and growth. This process involves the migration of high angle boundaries, which move under the driving force of the stored energy produced during deformation [15].

For recrystallization, the term ‘nucleation’ is actually a misnomer. The new grains which appear during the recrystallization stage are not assembled on an atom by atom basis as the phrase would suggest. If this were the case, and new grains were formed by thermal fluctuations in the bulk, they would never be observed. This is because the energy content of the deformed lattice and the interfacial energy of the new high angle grain boundary produces an energy barrier that can not be overcome by thermal activation, even at temperatures approaching the material's melting point, $T_m$ [16, 17, 18]. Therefore, if recrystallization would require *multiple* thermally activated nucleation events, its observation should be forbiddingly rare. But, recrystallization is readily observed in deformed microstructures at temperatures much lower than $T_m$.

Instead of 'nucleation', recrystallized grains have been accepted as being due to incubation cells already present in the deformed microstructure, associated with some grain at some earlier stage [16, 13]. Hence, in recrystallization, we are not observing the atomic assembly of a grain, but instead seeing a portion of microstructure behave in an exceptional manner. Such an observation can be thought of as a critical event. It has been suggested that the origins of these recrystallized grains are special subgrains within the microstructure, which can exhibit dramatic growth due to a favorable environment. Since recrystallization is a heterogenous process, the resulting initiation sites must have some property that makes them perferable. Having a high mobility with the neighboring deformed microstructure (possible through large misorientation) or having a distinct size advantage in comparison to other subgrains have been suggested as possible causes for recrystallization [16].

### 1.2.3 Grain Growth

In many ways, the process of recovery and recrystallization describe a two phase system, where a deformed microstructure is replaced with undeformed grains. At its completition, these first two processes will leave a microstructure containing only well ordered grains. It is at this point that the driving force for remaining microstructure evolution is the areal reduction of grain boundaries. Since each boundary is an abrupt change in lattice orientation, it results in a surface containing many broken atomic bonds (with atoms across the boundary). It is these broken bonds on the interface that result in the boundary having an associated free energy.

The reduction in area of grain boundaries is achieved by thermally activated migration, where atoms traverse a boundary and change their grain association. The rate at which boundaries migration through atomic jumps is given by the boundary velocity ($\nu$)

$$\nu = -M\gamma\kappa \tag{1.1}$$

where $\kappa$ is the local boundary curvature, $M$ is boundary mobility, and $\gamma$ is the interfacial energy. The negative sign is a result of the sign convention on the curvature variable and leads to grains growing towards their center of curvature. Boundary curvature is a geometrical description of an interface and has been extensively studied in grain growth models. In 2D, it's most famous result is the *n - 6 Rule*, which states that boundary migration results in an equilibrium grain shape (hexagon) [19, 20]. Interestingly, this theory was based on the approximation of a (2D) microstructure as soap bubbles in a froth, which evolve through diffusion [21]. The *n-6* term can be seen in the equation governing growth of 2D grains and results from integrating the mean curvature around a grain's perimeter

$$\frac{dA}{dt} = -\frac{M\gamma\pi}{3}(n-6) \tag{1.2}$$

$A$ and $n$ are the area and number of boundaries (edges) of the 2D grain, respectively. Equation 1.2 shows that grains with less than six sides will shrink, while those with more than six should grow. Correlating this to curvature, it is expected that small grains ($n < 6$) should have convex boundaries and the many sided large grains have concave boundaries. It is expected that hexagonal grains will have flat boundaries.

This two dimensional result was later extended to three dimensions by MacPherson and Srolovitz [22], where the volume change of grains was geometrically quantified with the introduction of the mean width of a grain. Conceptually interpreted as an average caliper width through an object, the mean width less total length of edges, was found to be the 3D counterpart to the $n-6$ quantity. While hexagons are the stable geometry in 2D, a 13.4 faced polyhedron has been predicted as the stable 3D geometry [23] through simulation.

The remaining two variables $(M, \gamma)$ in Equation 1.1 are commonly multiplied and reported as a 'reduced mobility' and unlike curvature, they have their values deeply correlated to the crystallographic properties of the boundary. In recent years, the grain boundary character distribution (*GBCD*) has proved a descriptive metric for grain boundary space [24, 25, 26, 27, 28]. This characterization describes the meso-scale properties of grain boundaries, which requires five variables: three to fully describe the misorientation between the grains forming the boundary and two variables to identify the atomic plane that produces the interface. *GBCD*s has been studied extensively and have demonstrated many properties, including an inverse relationship between grain boundary energy and grain boundary population in polycrystals [29, 30]. Boundary energy and mobility have been estimated for different materials through simulations [2] and experiment [31] using this representation of grain boundary space.

The anistropy with these reduced mobility variables was suggested earlier, where the energy landscape was shown in the context of misorientation angle (Figure 1.1) and the full five parameter *GBCD* space (Figure 1.2) were illustrated. Figure 1.1 experimentally captures the low energy - small misorientation relationship that is prevalent in most materials, for misorientation (angles) $\lesssim 10-15°$. The generation of such low angle boundaries as been interpreted as the assembly of a periodic spacing of dislocations and the energy of the boundary attributed to the lattice distortion involved with such a configuration [1]. This model fails when misorientation becomes appreciable with high angle grain boundaries, since boundary approximation through individual dislocations becomes prohibitively complicated. Evidence of this is shown in Figure 1.2, where the simulated bicrystal results illustrate high angle boundaries with a wide range of energy variations. The figure shows energy as a function of both misorientation angle (horizontal axis) and boundary plane (identical plot characters). For small misorientations, it appears that a convergence is present and approximation by the Read-Shockley curve of Figure 1.1 is appropriate.

For high angle boundaries in Figure 1.2 a wide range of energies are observed, including a boundary near zero energy for a 60° misorientation. This is termed the *coherent twin* and is a special high angle grain boundary that exhibits large geometrical symmetry [32, 33, 31, 34]. In grain boundary space, it is described as a 60° rotation about the grain's [111] direction in misorientation and has a boundary that is the {111} crystal plane. Boundaries exhibiting this misorientation structure, but not possessing the {111} boundary plane are known as incoherent twins. The figure labels these twin boundaries with red diamonds and the coherent twin with a black diamond. The legend refers to this as a $\Sigma 3$ boundary, which is nomenclature based on coincident site lattice theory.

The coincident site lattice *CSL* is a geometrical method of representing misorientation space by determining what fraction of lattice sites will overlap, when the misorientated lattices interpenetrate [32, 28, 35, 35, 36, 37]. The fraction is reported as a reciprocal, $\Sigma N$, where $N$ means that $\frac{1}{N}$ sites (in each lattice) share the same spatial position. *CSL* theory was originally proposed as a method of characterizing boundary properties, since highly symmetric boundaries (low $\Sigma$) might have special properties that are distinct from other high angle grain boundaries. This fact is true for some *CSL*s, including the very low energy of the coherent twin ($\Sigma 3$) [2, 38] and high mobility of some $\Sigma 7$ boundaries [39, 40]. While occasionally able to predict these special boundary properties, its description of boundary space is incomplete. It is only when incorporated with the boundary plane normal (via the *GBCD*) that correlations between boundary character and boundary properties become stronger.

We mention *CSL*s only because of their use as a compact description of boundary misorientation, which will be employed in this thesis. In tandem with *CSL*s is the use of the Brandon angle, $\theta_{Brandon}$, which is a type of misorientation away from a point in *CSL* space [41]. Since perfect mismatch, as described with a *CSL*, is infrequent in real materials, a threshold angle for association is necessary. Boundaries within $\theta_{Brandon}$ from a given *CSL* point were hypothesized to exhibit properties associated with that *CSL*. The relationship is given as $\theta_{Brandon} = \frac{15^\circ}{\sqrt{\Sigma}}$.

While energy displays a large dependence on boundary character, grain boundary mobility does as well. Bicrystal simulations have been performed that display the same anisotropy in *GBCD* space for boundary mobility as boundary energy [42].

## 1.3 Synchrotron Based Microstructure Mapping Techniques

The measurement of changes in a microstructure in response to annealing has been performed for over a century, but only recently have the tools become available to directly observe the process. Initially, the three annealing phenomena were measured indirectly, through the monitoring of response variables in the microstructure. For instance, in a high purity material, coarsening of the microstructure leads to increased electrical conductivity, so passing a current through a specimen and measuring its resistance can indirectly describe properties associated with the underlying microstructure [43]. These same ideas were used in calorimetry measurements and hardness tests, both deduce microstructural properties based on the response to a known stimulus [14].

While these techniques can qualitatively (and sometimes quantitatively) describe a microstructure, they paint a broad statistical picture of the responsible microstructure. It was only with the advent of orientation imaging techniques, such as electron backscatter diffraction microscopy (*EBSD*) [44, 45, 46, 47, 48] that investigation of annealing phenomena could be quantified on length scales where the variables known to influence microstructure evolution could be identified (grain orientations, interface shapes, location of impurities). Further still, with the development of automated serial sectioning methods achieved with focused ion beams, large volumetric measurements of microstructure can now be performed on relatively short (days) time scales [31, 49, 50].

The benefits of automated microstructure mapping with electron microscopy has greatly influenced the field of materials science by providing a picture of a microstructure on the granular level. But through its operation as a surface technique, it must inherently destroy the measured sample to produce three dimensional pictures of the microstructure. While this practice works for statistical comparison among different samples, it does not afford the ability to perform one-to-one measurements of the microstructural response to some external stimuli. It is because of this difficulty that microstructure mapping through synchtrotron based techniques have emerged as essential tools for materials characterization, and specifically High Energy X-ray Diffraction Microscopy (*HEDM*). We will briefly summarize some diffraction based measurement techniques, including *HEDM*, that are readily available at different third generation light sources, worldwide.

### 1.3.1 Differential-Aperture X-ray Microscopy

Differential-Aperture X-ray Microscopy (*DAXM*) is a mapping technique that takes advantage of high brilliance and highly focused synchrotron x-ray beams to determine the spatial distribution of microstructure properties of fine grained ensemble ($\lesssim 10\mu m$ grains). Specifically, *DAXM* can provide high resolution information about the orientation distribution among and within grains, while also determining deformation state, including the elastic strain within sub-regions of the polycrystal. [51]

*DAXM* is based upon diffraction of polychromatic x-rays in the $8 - 20keV$ range, which are focused into a $\sim 0.5\mu m$ diameter beam. These x-rays interact with a polycrystalline sample and the diffraction emanating from the interaction is imaged on an x-ray sensitive area detector. This camera sits tens of millimeters away from the sample surface. By using a polychromatic beam instead of single energy photons, each grain in the polycrystal should have some collection of crystal planes that generate diffraction in this beam-sample-camera configuration. While the diffracting grains can be confined to two dimensions via their intersection with the focused beam, the third dimension (or depth from the surface), is determined by scanning the sample with a platinum wire. This wire is incrementally stepped over the surface of the sample and in each configuration, a diffraction image is collected. The wire serves to resolve x-ray scattering vectors by absorbing the diffraction signal. Knowledge of when a peak is not present in conjunction with the wire position, can be used to deduce spatial information about the sample's microstructure.

By fully characterizing the state of a polycrystalline sample with high spatial (submicron), orientation ($\sim 0.01°$), and strain state ($10^{-4}$) resolution, *DAXM* is a powerful microscope. It has demonstrated the capability of monitoring a microstructure's response to annealing [52]. Limiting the measurements widespread use is the relatively small lengths scales which the technique can capture. While well suited for measurement of small volumes of microstructures ($\sim 10 \times 10 \times 10\mu m$), the technique is infeasible for collecting bulk microstructural information from large samples on the order of millimeters. Further, the determination of the microstructure through the use of a small beam and scanning probe makes the collection of microstructure information time consuming. It is for these reasons that *in-situ* measurements are difficult (yet not prohibited) with *DAXM*.

### 1.3.2 Diffraction Contrast Tomography

Diffraction contrast tomography or *DCT* is a technique that combines the elements of x-ray absorption tomography and x-ray diffraction to produce volumetric orientation maps of polycrystalline materials [53, 54]. The concept is based upon a rotating sample technique, where a box beam (macroscopic height and width) of monochromatic, high energy photons continuously illuminates the same volume of microstructure. When the sample is rotated into such a configuration that an embedded grain satisfies the diffraction (or Bragg) condition, intensity will be removed from the incident beam, which leaves an deficit of measureable photons in the radiograph. Effectively, a hole appears in the transmitted beam profile. The displaced intensity has been diffracted in a certain direction, as determined by the grain orientation and along the resultant scattering vector. Imaging both the tomography signal (radiograph) and diffraction signal (intensity outside the radiograph) permits the determination of the orientation of the grains in the measured microstructure.

*DCT* is an effective tool for the measurement of polycrystalline microstructures with minimal orientation spread. It has demonstrated the ability of monitoring grain coarsening in a polycrystalline aluminum sample [54] and the growth of a stress corrosion crack in austenitic stainless steel [55] . Determination of grain boundary shapes is difficult. Most reconstructions required space-filling procedures ($\sim 59\%$ filled in a coarse grained structure [55]), and therefore determination of grain boundaries can be unreliable. Additionally, there are challenges with spatially resolved orientation variations within grains. There has been some development with dealing with orientation spreads [56], but this is still a work in progress. With rapid acquistion times, $DCT$ is well suited for real time, *in-situ* experiments.

### 1.3.3 High Energy X-Ray Diffraction Techniques

The final technique can be classified as the use of monochromatic high energy x-ray photons ($\geq 50keV$) for the interrogation of individual grains via diffraction. It is a robust technique in its ability to monitor the evolution of the same ensemble of grains as the microstructure is subject to thermomechanical stimulation. X-ray microscopes to perform these measurements have been developed in parallel at different synchrotron facilities. 3D X-Ray Diffraction Microscopy (*3DXRD*) is the technique associated with diffraction measurements performed at the European Synchrotron Radiation Facility ($ESRF$) in close collaboration with Henning Poulsen and collaborators from the Risoe National Laboratory of Denmark [57, 58]. High Energy X-Ray Diffraction Microscopy ($HEDM$) refers to the set of measurements performed at the 1-ID beamline of the Advanced Photon Source ($APS$) at Argonne National Laboratory [59, 60]. One of the variants of HEDM, near-field High Energy X-Ray Diffraction Microscopy, was developed in conjunction with the Carnegie Mellon University group lead by Robert Suter [61, 62, 63, 64, 65, 66, 67], and will be the method of analysis for this thesis.

Both *HEDM* and *3DXRD* are unique in their ability to resolve spatial information about the strain state, grain geometries, and orientations of bulk polycrystals. Unlike *DAXM* and *DCT*, both *HEDM* and *3DXRD* have the ability to vary their collection protocols to determine different physical properties of individual grains. At the fundamental level, both high energy diffraction techniques operate as rotating sample measurements, where illuminated grains are brought in and out of the diffraction condition. The geometry of the resulting diffracted peaks can be resolved on x-ray sensitive area detectors. When this diffraction is collected far from the sample (on the order of meters), the setup is operating in the far field. The cameras used for far field measurement are typically composed of $\sim 200\mu m$ pixels and used to measure strain states of grains through the monitoring of shifts in diffraction peaks due to distortions of the unit cell [60, 68, 69, 70].

While capable of providing strain states of individual grains, far field measurements are insensitive to the spatial location of these grains. It is near field measurements that can supply such information through high resolution imaging of diffraction beams. In this collection routine, high resolution ($\sim 1\mu m$) cameras image diffraction only a few millimeters from (millimeter sized) samples. The resulting diffraction covers multiple pixels on the camera, which provides sensitivity to the diffracted beam geometry (cross-section). By collecting these images at multiple sample-to-camera distances, full scattering vectors (direction) can be resolved. Using both diffraction beam shape and direction, the location and orientations of grains can be determined.

Analysis of this high energy diffraction data can be accomplished with 'back projection', where crystallographically consistent peaks in detector space are extrapolated back to the sample [71, 57]. Such processes can typically yield the center-of-mass locations of grains in the ensemble and a grain averaged orientation [58]. Observations in the realm of annealing phenomena and deformation have been performed with this method [72]. Alternatively, 'forward modeling' reconstructions finely grid sample space and assign orientations to each element based on maximum overlap between theoretical and observed scattering. While computationally intensive, this technique can capture orientation variations on the intra-granular level [3, 73, 74]. By operating in sample space and checking for consistency in detector space, the technique is also capable of overcoming difficulties in peak extraction. This is non-negligible since peak overlap is possible in fine grained (many diffraction peaks) or textured (spatial clustering of diffraction peaks) samples.

For completeness, 'high angular resolution 3DXRD' is a final variant of high energy x-ray diffraction, which could be described as very far-field HEDM. Here, a detector is placed $\sim 4m$ from the sample and composed of pixels finer than far field ($\sim 80\mu m$). The imaging regime can produce very high resolution images of individual diffraction peaks emanating from a single grain within a polycrystal. Such high resolution imaging of a very small portion of reciprocal space is intended to compliment either near or far field measurements. Peaks of interest can be identified in near/far field and then rotated onto the very far field camera. Measurements have demonstrated the ability to monitor dislocation cell evolution during the tensile deformation of copper [75].

## 1.4 Orientations and Misorientations

### 1.4.1 Orientation Space

A significant portion of this thesis is based upon analysis in both orientation and misorientation space. While representations of rotations have yet to be formally presented (see Chapter 2, we will note their existence and provide a description of these two spaces of importance in microstructure characterization. We note that these rotations relate the crystal's reference frame (based upon atomic positions in the lattice) with respect to the sample coordinate system.

While at liberty to choose different formalisms for describing an orientation (rotation matrix, Euler angles, axis-angle pairs, quaternions), the representation is not unique if certain symmetries are present. For face-centered cubic materials, like nickel and aluminum, an underlying cubic symmetry is present. This means that there are 24 different, yet equivalent, ways to represent the same orientation, $g$. These 24 different orientations are all related through the application of a symmetry operator, $O_i$, which is a set of 24 operators. When operated on an orientation, $O_i g$, the resulting orientation is equivalent to $g$.

Because of confusion that can arise is having multiple representations of the same quantity, it is convenient to represent all orientations in some consistent manner. An orientation space that contains only one copy of every possible orientation is called a fundamental zone of orientation. Consequently, there are 24 unique fundamental zones of orientation for cubic symmetry systems. For our discussion of fundamental zones, orientations are calculated in Rodrigues-Frank space [76],

$$\boldsymbol{\rho} = \tan\frac{\omega}{2}\boldsymbol{v} \tag{1.3}$$

which is an axis-angle representation of orientation, $\boldsymbol{v}$ defining a unit vector that is the direction of the rotation axis and $\omega$ is the rotation angle. The fundamental zone of orientations in Rodrigues-Frank space is useful because it is a compact space. It is because of this feature and its easy visual representation that we illustrate orientations in this space. The specific fundamental zone that we choose is the compact zone which surrounds the origin in Rodrigues-Frank space. Therefore, the representation with minimum $\omega$, in Equation 1.3, will be the orientation that is in the fundamental zone. Figure 6.1 illustrates the geometry of this space. Plots of the Rodrigues-Frank orientation fundamental zone can be used to identify unique distributions of orientations within a microstructure. Specifically, clusterings of orientations in a compact region of orientation space suggests the presence of texture in the microstructure.

### 1.4.2 Misorientation Space

While orientations describe how a grain is configured with respect to some fixed coordinate system, it is how this orientation compares to the neighboring microstructure that is typically of interest. This motivates misorientation, which is the rotation required to bring one orientation into coincidence with another. Hence, misorientations are just a special kind of rotation. Mathematically, $g_B = \Delta g_{AB} g_A$, where $\Delta g_{AB}$ is the misorientation required to bring $g_A$ into coincidence with $g_B$. Since each orientation for an object with cubic symmetry has 24 equivalent representations, that means there are $24 \times 24 \times 2$ equivalent ways to represent misorientation, where the 2 is due to the choice of reference frame for rotation (i.e. grain A to grain B or grain B to grain A). Effectively, $\Delta g_{AB}$ can be written as

$$\delta g_{AB} = O_i g_B (O_j g_A)^{-1} \tag{1.4}$$

where $O_i$ and $O_j$ are symmetry operators mentioned in our discussion of orientations.

Misorientations are usually presented in either a one or three parameter representation. For one parameter descriptions, misorientation angle ($\theta_{mis}$) is used to quantify the misorientation. This is the smallest rotation angle required to rotate one crystal frame into another. For cubic materials, 62.8° is the largest rotation angle needed to bring two orientations into coincidence [77]. Representing misorientation ($\Delta g$) as a rotation matrix, $\theta_{mis}$ is found to be

$$\theta_{mis} = min\{\arccos(\frac{tr(O_i\Delta g) - 1}{2})\} \tag{1.5}$$

The three parameter representation incorporates misorientation axis in addition to angle. Like orientations, a misorientation fundamental zone exists for describing unique misorientations and because of its mathematical niceties, the Rodrigues-Frank representation of misorientation space [78] will be used in the presentation to follow. For cubic symmetry, the shape of the zone is pyramidal and shown in Figure 6.5. Also like orientation space, the distance from the origin for a point in the misorientation fundamental zone indicates the magnitude of the rotation angle.

We emphasize that both orientation and misorientation fundamental zones, when represented in Rodrigues-Frank space, are compact. Consequently, polygons define a bounding box for the space. In the calculations to follow, presentations involving these two types of fundamental zones will always perform a component check that the representative point falls within this bounding box.

## 1.5 Outline

The content to follow is based on measurements using near-field High Energy X-ray Diffraction Microscopy at the 1-ID beamline of the Advanced Photon Source synchrotron and reconstructed using the aforementioned forward modeling analysis method. In Chapter 2, we provide an overview of the physics of the rotating sample technique and provide an explanation of how orientations are responsible for the location of peaks that are measured. This will be followed by measurements of two separate samples, each of which demonstrate the efficacy of nfHEDM and forward modeling to monitor the annealing of polycrystalline microstructures and both of which yield several interesting and unique observations of thermal responses. Both measurements are dynamics based, meaning that the same microstructure is tracked after multiple anneals and certain properties of the orientation and spatial distribution of grains can be quantified.

The first, *in-situ* annealing measurement was performed on a high purity aluminum wire. The volumetric sample reconstruction will demonstrate an ability to monitor both the recovery (Chapter 3) and recrystallization (Chapter 4) processes. A deformed microstructure was present in the initial sample state, which must be present for observation of the two annealing phenomena as outlined above. It is the sensitivity to intra-granular orientation variations, with respect to anneal state, that displays the process of recovery. The observation of new grains, in later states, suggests the onset of recrystallization.

The second sample was composed of a finer grained polycrystalline nickel microstructure and is described in Chapters 5 and 6. To complement the aluminum experiment, the sample was brought to a fully recrystallized state for the initial measurement. Therefore, the subsequent *ex-situ* anneals resulted in grain growth as the response to heat treatment and not the transformation of a deformed state. Measurements resulted in the collection of six sample volumes, with each volume comprised of thousands of grains. We will present statistics concerning the tracking of the same ensemble of grains. Unlike aluminum, nickel has a low stacking fault energy, which results in an abundance of annealing twins in the microstructure. The previously described coherent twin will be investigated and changes in its distribution in *GBCD* space will be quantified.

While both measurements produce sufficent microstructure maps to explore evolving properties within a microstructure, they were measured in very different experimental settings. During the course of this thesis, the near-field setup at the 1-ID beamline matured from a loose ensemble of measurement equipment to a highly characterized, dedicated setup. Consequently, while the experimental time allotments for the nickel and aluminum microstructure are comparable, the nickel measurements consists of twice as many sample states as the aluminum. Further, each of these nickel volumes contains approximately 86 2D maps. This is more than double the *total* number of maps collected in the aluminum experiment (33). The advancements of our experimental microscope should not be understated. Additionally, the reconstruction software has constantly evolved and the maps presented are (unless otherwise noted) the result of the current analysis package. We will conclude this work in Chapter 7 with suggestions for further work on these two data sets.

# Chapter 2

# X-Ray Diffraction

## 2.1 Introduction

The purpose of this chapter is to introduce the mathematics associated with the forward modeling method, most specifically how an orientation within a (poly)crystalline sample produces a collection of Bragg peaks on the set of detectors in our synchrotron setup. While the principles of this experiment have been discussed in previous publications and theses [61, 66, 67], we will attempt to present the content as a gateway to understanding the underlying physics and geometry which make near-field HEDM possible. The steps involved in going from raw diffraction images to fully reconstructed orientation maps are computationally intensive, but at its most fundamental level the process is built upon basic scattering physics and careful book-keeping of several coordinate systems that exhibit relative motions. The sections that follow will detail these two aspects of spatially resolved orientation reconstruction and provide a worked example of forward modelling.

X-rays have been used for a century in numerous capacities to serve the scientific community and in each instance, the x-ray photons provide information about different aspects of the nature of material. When x-ray photons are incident on a piece of material they can either be absorbed or scattered. The absorption of photons is the underlying science behind such techniques as x-ray absorption spectroscopies (XAS) and can be used to determine the elemental composition of a specimen, while x-ray tomography can be used to generate 3D pictures of multi-phase material, where the spatial distribution of electron density is used to identify different materials. Alternatively, x-rays that are scattered can also be used to determine some properties of the matter with which they interacted. X-rays have wavelengths on the order of a few Angstroms and are therefore a useful tool for probing quantities on that length scale, such as the periodic arrangement of atoms in a crystalline material. When an (x-ray) photon scatters from an electron, the outgoing beam can have the same energy as the incident beam (elastic scattering) or with a lower energy, having transferred energy to the electron (in-elastic scattering). This later phenomena is the basis of the Compton effect, which is the main interaction in radiation therapy. The elastic scattering of photons can be broken down into two classes, kinematic and dynamic. nfHEDM is built upon kinematic diffraction, which assumes that the photon-electron interaction is a singular event and that the scattered photon is not responsible for secondary scattering events. Most concisely summarized, the near-field HEDM technique images kinematic scattering from polycrystalline material. Through the cataloging of peak geometries and their locations in space, the forward modeling analysis method can then resolve the microstructure (both grain shapes and orientations) responsible for the measured peak distribution.

## 2.2 X-ray Scattering

Before discussing how grain information is gathered from diffraction images, we outline the basic scattering geometry involved with Bragg diffraction. We use the simplistic picture of the x-ray - crystal interaction that is seen in most introductory physics texts. This is displayed in Figure 2.1. In this picture, monochromatic x-rays are specularly reflected off a set of crystal planes composed of a spatially periodic array of atoms. The incident x-rays are described by the wave vector, $\boldsymbol{k}_i$. $\boldsymbol{k}_i$ points in the direction of propogation and its magnitude is $\frac{2\pi}{\lambda}$. When viewed as a propogating electro-magnetic disturbance, it has mutually orthogonal electric and magnetic fields that are both perpendicular to $\boldsymbol{k}_i$. Upon interaction with the electron's within the lattice, the electric field of the x-ray beam imparts a force on the electrons which generates an oscillation with the same frequency as the incident wave. Each electron is the source of a spherical electro-magnetic waves, which can either constructively or destructively interfere with each other. Constructive interference requires that the difference in propogation length is an integer multiple of the wavelength. When constructive interfence of waves from many lattice sites is present the diffracted beam with $\boldsymbol{k}_f$ results. Noting that the wavelength, $\lambda$, of the scattered photon remains the same through this elastic scattering process, we see that diffraction requires

$$2d_{hkl}\sin\theta = n\lambda \tag{2.1}$$

where $\theta$ is the angle made between the plane of atoms and the incident beam, and $d_{hkl}$ is the spacing between these parallel planes. Equation 2.1 is known as Bragg's Law. The subscript $hkl$ refers to the Miller indices of the diffracting plane, which is a method of identifying a configuration of parallel planes within a crystal. The geometry of such a scattering event is shown in Figure 2.1(a), where a periodic arrangement of atoms is diffracting an incident beam, $\boldsymbol{k}_i$. In Figure 2.1(b), the same periodic arrangement of atoms is displayed, but red lines within the lattice illustrate a different set of crystal planes responsible for scattering. Both pictures show the same incident beam, but for the scattering beam to exhibit constructive interference, the differences in path length must statisfy Equation 2.1, which would require a different wavelength.

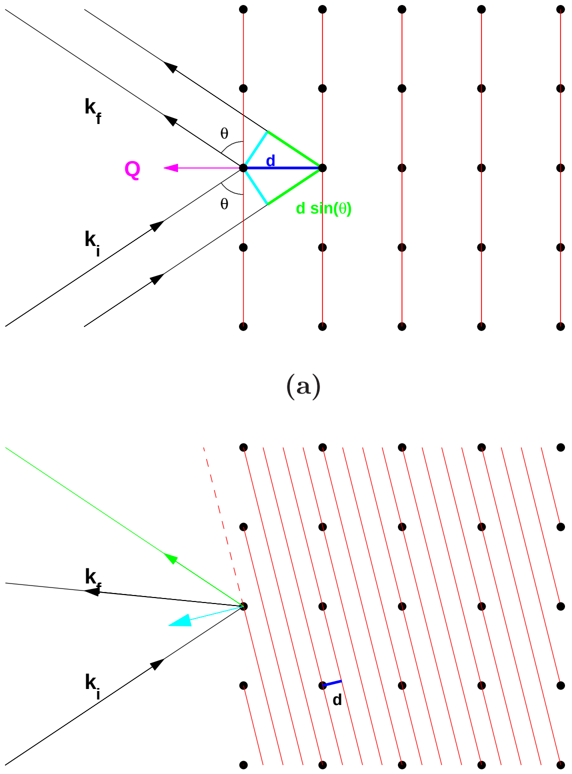

**(a)**

**(b)**

*Figure 2.1: Illustration of Bragg scattering from a (2D) periodic lattice. The crystal planes responsible for the scattering are indicated by solid red lines, with solid black dots denoting atoms. The incident ($\boldsymbol{k}_i$) and diffracted ($\boldsymbol{k}_f$) beams are shown in black. (a) shows scattering occuring from the ($hk$), (10) planes, while (b) is from the (41) planes. (b) contains two diffracted beams: black is scattering from the (41), while green is the (10) from (a). The scattering is specular, so $\theta$ between the beam and crystal plane is the same for the incident and exiting beams. $\boldsymbol{Q}$ is indicated in (b) with a cyan arrow. Lattice spacings, indicated by $d$, are different for the two sets of planes and therefore result in different scattering geometries. The additional path length travelled by the second incident beam is shown in green in (a). Constructive interference requires the length to be an integer multiple of the incident beam wavelength.*

The geometry of Figure 2.1 shows that we can resolve a difference vector between the incident and scattered beams, by acknowledging that the scattering is elastic and therefore the magnitude of the two vectors are equivalent. Admitting specular reflection, we also know that the angle between these two vectors is $2\theta$. We define this difference vector (known as the momentum transfer vector) as $\boldsymbol{Q}$, and can immediately see that

$$\boldsymbol{k}_i + \boldsymbol{Q} = \boldsymbol{k}_f \tag{2.2}$$

Intepreting both Equation 2.2 and Figure 2.1, it is easily seen that the $\boldsymbol{k}_i$, $\boldsymbol{Q}$, and $\boldsymbol{k}_f$ are coplanar, and therefore $\boldsymbol{Q}$ must be normal to the diffracting crystal plane. Noting that $\boldsymbol{k}$ can be represented as $\frac{2\pi}{\lambda}\hat{\boldsymbol{r}}$, where $\hat{\boldsymbol{r}}$ is wave propogation direction, we can relate the scalar quantities of Equation 2.1 with the vector constraint of Equation 2.2. Squaring both sides of Equation 2.2 and realizing that the magnitude of the incident and scattered wave vectors are the same

$$\begin{aligned}
|\boldsymbol{k}_i|^2 + 2\boldsymbol{G}\cdot\boldsymbol{k}_i + |\boldsymbol{G}|^2 &= |\boldsymbol{k}_f|^2 \\
2\boldsymbol{G}\cdot\boldsymbol{k}_i &= -|\boldsymbol{G}|^2 \\
(\frac{4\pi}{\lambda})\hat{\boldsymbol{G}}\cdot\hat{\boldsymbol{k}_i} &= -|\boldsymbol{G}| \\
(\frac{4\pi}{\lambda})\sin\theta &= 2k\sin\theta \\
&= |\boldsymbol{G}|
\end{aligned}$$

where the last step uses the geometry of Figure 2.1. Substituting for $\sin(\theta)$ and $\lambda$ from Bragg's Law

$$\boldsymbol{Q} = \frac{2\pi}{d_{hkl}}\hat{\boldsymbol{n}} \tag{2.3}$$

where $\hat{\boldsymbol{n}}$ points normal to the atomic plane that is responsible for the scattering. The Bragg condition can also be written as $\boldsymbol{Q} = \boldsymbol{G_{hkl}}$ where $\boldsymbol{G_{hkl}}$ is a reciprocal lattice vector. A discussion of reciprocal lattice space is not presented here, but can be found in any introductory solid state physics text [79, 80]. Conceptually, reciprocal space is the Fourier transform of the periodic (real space) arrangement of atoms. Since each point in reciprocal space is associated with a different periodic arrangement of atomic planes; it is a powerful tool for diffraction measurements. Specifically, constructs like the Ewald sphere [80] take advantage of the properties of reciprocal space and can be used to geometrically solve for expected Bragg reflections, given the geometry of the incident beam. The work presented in this thesis is based on materials with a (face-centered) cubic crystal structure. For cubic materials

$$\boldsymbol{G}_{hkl} = \frac{2\pi}{a_0}(h\hat{\boldsymbol{x}} + k\hat{\boldsymbol{y}} + l\hat{\boldsymbol{z}}) \tag{2.4}$$

with $a_0$ being the lattice parameter for the unit cell of the cubic material and $(hkl)$ being the Miller indices of the reflecting plane. The coordinate system associated with $\hat{\boldsymbol{x}}$, $\hat{\boldsymbol{y}}$, $\hat{\boldsymbol{z}}$ in Equation 2.4 is the crystal's reference frame, where the $(hkl)$ representation of crystal planes is straightforward. Figure 2.1 establishes that diffraction will occur from a given plane when $\boldsymbol{G} = \boldsymbol{Q}$, known as the Laue condition. We can now motivate the nf-HEDM experiment and forward modeling method of spatial orientation determination.

## 2.3 Near-Field High Energy X-ray Diffraction Microscopy

We put the discussion of Bragg scattering in the context of the near-field High Energy X-ray Diffraction (nfHEDM) experiments conducted at the 1-ID beamline of the Advanced Photon Source synchrotron at Argonne National Laboratory. We use the term near-field to distinguish the method of High Energy X-ray Diffraction Microscopy (HEDM) used for this paper. In general, HEDM is a much broader field. In summary, it entails the use synchrotron produced high energy (or hard) x-rays to interrogate a sample and then deduce physical properties by analyzing the diffraction signals. The methods of collecting and interpreting these diffraction signals is where the various HEDM techniques deviate. Here, near-field is a process where the imaging of Bragg scattering is done very close to the sample, resulting in large solid angle coverage of the exiting, diffracted beams. Imaging is done with cameras of high resolution, composed of micron-sized pixels. The collected diffraction images are analyzed with the forward modeling method to produce orientation maps of high spatial resolution. An illustration of the important components of the nfHEDM experimental setup are shown in Figure 2.2. We will detail the relevant components in the proceeding sections.

### 2.3.1 X-ray beam

The beam characteristics are what makes nfHEDM reliant upon synchrotron radiation for the diffraction experiment. Specifically, the delivered beam is of high energy, as well as brilliant, monochromatic, and microfocused. These final three properties can not be produced in a laboratory setting equipped with a rotating anode setup.

For nfHEDM experiments, high energy means an operating energy $\geq 50keV$. We use $50keV$ and $64.351keV$ as the two operating energies for the aluminum and nickel experiments, respectively. Such high energies are necessary because their penetration depth ($\frac{1}{e}$ lengths) is very large for much of the periodic table. In fact, the majority of the photons pass through our samples without interaction. This is necessary for the efficacy of nfHEDM, since diffraction must be possible from all points within the sample. If significant attenuation is present, the probability of diffraction will be influenced by the grain's location within the sample, with grains closest to the incident beam-sample surface interface being more likely to diffract than those furthest downstream.

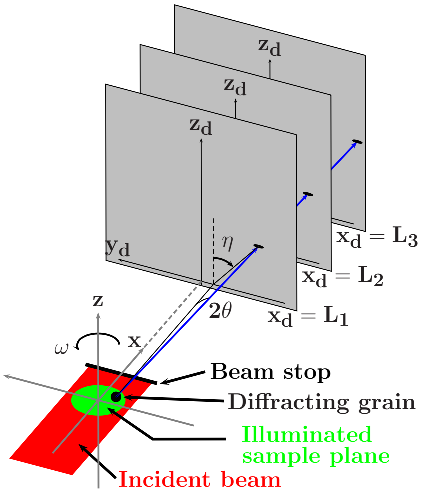

*Figure 2.2: Simplified schematic of nfHEDM setup employed at the Advanced Photon Source. High energy, monochromatic x-rays (red) are microfocused into a planar sheet, a few microns in height. The beam interacts with a thin cross section of polycrystalline sample (green) and is attenuated by a beam stop. Grains with a crystal plane satisfying the Bragg condition (black) give rise to diffraction that can be imaged on downstream detectors. Peaks can be quantified by their Bragg angle $2\theta$ and detector-plane angle, $\eta$.*

This is undesirable, so operating energies are chosen that are large enough that x-ray attentuation is not a limiting factor in the measurement. The target materials discussed in this thesis are gold, aluminum, and nickel. Table 2.1 shows their $\frac{1}{e}$ lengths at the energies used for their respective measurements.

*Table 2.1: X-ray $e^{-1}$ lengths for experimental materials*

| Material | Energy ($keV$) | $e^{-1}$ length (mm) |
|---|---|---|
| Au | 50.0 | 0.073 |
| Au | 64.351 | 0.140 |
| Al | 50.0 | 104.862 |
| Ni | 64.351 | 0.934 |

### 2.3.2 Mathematics of nfHEDM

High brilliance synchrotron beams allow the diffraction experiment to be achieved in reasonable timeframes. The data required to produce a single 2D map of microstructure is on the order of tens of minutes with a third generation synchrotron source. Using a rotating anode or a standard fixed target tube source to produce the same diffraction content is simply unachievable. The yield of photons will never be large enough to measure appreciable polycrystalline diffraction peaks above background.

The monochromicity of the beam allows for higher resolution in orientation space. In the context of Bragg's law (2.1), a bandwidth in wavelength (energy) permits the diffraction condition to be possible over a distribution of lattice spacings and diffraction angles. This can be seen from the differential form of (2.1)

$$\frac{\Delta E}{E} = \frac{\Delta \lambda}{\lambda} = \frac{\Delta d}{d} + \cot\theta \Delta\theta \tag{2.5}$$

Therefore, if we have a spread in energies, we expect a deviation in direction of the diffracted beam. We assume the lattice is perfect and therefore, $\Delta d = 0$. The energy bandwidth used for nfHEDM is $\frac{\Delta E}{E} \sim 10^{-3}$. With typical scattering angles of $\sim 5^\circ - 20^\circ$, we get an angular deviation that is of the same order as our energy dispersion. Hence, for near field measurements, the deviation in the diffracted beam will be less than the size of a pixel on the camera, when propogated over the sample-to-detector distance. For the measurements presented, this energy deviation will not appreciably influence the direction of diffracted beams, so we use the standard form of Bragg's Law (2.1). Alternatively, if we were doing an experiment where the lattice was under strain, the spacings between crystal planes would become variable ($\Delta d \neq 0$) and these differential relations will be non-negligible. Specifically, shifts in $2\theta$ will be the experimental response of straining.

Finally, the ability to focus the beam to micron width also affords greater spatial resolution. The nfHEDM technique has a beam that is effectively a sheet that is thin in the vertical dimension ($\sim 5\mu m$) and wide in the horizontal ($\sim 1mm$). This narrowness ensures that each point within the plane of the sample contains only a single orientation. Thus, there is no spatial ambiguities in the reconstruction of 2D maps. The horizontal dimension of the beam is set by tungsten slits and the width used is sample dependent. The extent is made wide enough that the entire sample cross section can be illuminated at all times. It will be later discussed that nfHEDM is a rotating sample technique, with the sample centered on the rotation axis. Therefore, the focused beam has to be wide enough that the sample is within the beam for all rotation geometries. Typically, samples are cylinders, so this is not a difficulty.

### 2.3.3 Beam Attenuator

The majority of photons pass through the sample without interaction, as was indicated by Table 2.1 and noting that our samples are smaller than the $e^{-1}$ length. Therefore, a high-Z attenuator is placed after the sample to prevent the transmitted beam from saturating the high resolution imaging system. The attenuator is shown as a black line in Figure 2.2.

During the lifetime of the setup, when the experiments to follow were conducted, two different mediums served as the attenuator. For the aluminum experiments, a polycrystalline tantalum beam stop served as the first generation design. This was replaced by an (approximately) single crystal, polished tungsten beam stop. The latter design not only reduced the number of undesirable stray Bragg peaks falling on the detector, but was also dimensioned to allow a small percentage of the beam to pass through the material and leave a constant profile on the diffraction images. The transmitted beam information is useful in characterizing changes in the detector's orientation, or position as well as providing a signal for x-ray tomography of the measured layer, which has been demostrated [81].

### 2.3.4 Imaging System

The near-field distinction to this HEDM variant originates from the distance between the rotation axis (approximate center of sample) and the imaging plane. While samples range from tens of microns to millimeter in diameter, the distance between the first imaging plane ($x = L_1$) and the rotation axis is $\sim 4 - 7mm$. This contrasts with the far field measurement, which has detectors several meters from the sample and are predominantly used for characterization of strain content within a sample.

The near field measurement affords high resolution spatial mapping of the polycrystal, by imaging numerous Bragg peaks from every grain (individual crystal) within the sample. The charge coupled device (CCD) camera covers a field of view on the order of a few millimeters and is composed of pixels that have an effective side length of a few microns. The small pixel lengths are achieved with microscope objective attached to the CCD camera. Currently, pixel size is the limiting resolution of the orientation map reconstructions. For the aluminum measurement, a 1024 × 1024 pixel camera with 4.11 $\mu m$ effective pixels was used. This camera employed a liquid nitrogen cooling system to minimize electronic noise. Alternatively, the nickel experiment, which was collected after the experimental setup at 1-ID B-hutch had matured, used a 2048 × 2048 camera with 1.47 $\mu m$ effective pixels and a Peltier cooling method.

Figure 2.2 shows three cameras, while the physical system used for these experiments uses only one, which was translated to successive distances for data collection at multiple $L$s. The use of multiple detector distances allows for the resolution of 3D scattering vectors. Peaks move radially outward on the camera as it moves downstream. The choice of $L$ is optimized by balancing the need for multiple diffraction peaks from each grain (upper $L$ limit), while noting that at small distances, peaks can begin to overlap to an extent where their individual shapes can not be separated. Though the reconstruction algorithm is rather insensitive to spot overlap, the reduction procedure that turns the *.tif* image files into lists of peaks and intensities can be hintered by massive overlap. Additionally, hope for intensity fitting of the diffraction data would be made difficult with multiple overlaps. Lastly, there is a spatial restriction in the experimental setup where camera supports and the beamblock inhibit how close the camera can get to the sample. Typically, $\Delta L \sim 2mm$, and the use of a third detector distance is done for calibration of the reconstruction and is utilized only sporadically.

The conversion of x-ray photons into camera-readable visible light is achieved with a scintillation screen. The scintillators for the presented work were of two materials. For the aluminum experiment, a Ce-doped YAG (Yttrium-Aluminum-Garnet) crystal with an active layer of $\sim 20\mu m$ was used, while a free standing LuAG (Lutetium-Aluminum-Garnet) was employed for the Ni experiment, with a thickness of $18\mu m$. For equal efficency in the production of visible light photons, a thinner scintillator is desired, since the longer the effective path through the material, the more likely "tails" can be produced in the imaged Bragg peaks. Specifically, these "tails" would have an asymmetry, depending on which surface of the scintillator is imaged. If it is the side closest to the sample, tails will appear "above the peak", meaning the on the portion of the peak that is furthest from the on-camera projection of the direct beam - rotation axis intersection. Conversely, imaging the surface closer to the camera would result in tails "below the peak".

### 2.3.5 nfHEDM as a Rotating Sample Experiment

As discussed earlier, nfHEDM is a rotating sample technique that images Bragg scattering emanating from a polycrystalline microstructure, with its experimental setup shown in Figure 2.2. We will motivate the necessity for a rotating sample collection routine. The components of the setup have already been outlined, but we will add that the coordinate system shown in the figure is the one we will use for our experimental description. It is not the convention of the APS, but will suffice. Specifically, for the right-handed coordinate system of 1-ID-B, $\hat{\boldsymbol{x}}$ is the direction of the incident beam and $\hat{\boldsymbol{z}}$ is the direction of the rotation axis.

Referencing Figure 2.1, it is evident that there is a geometrical constraint on Bragg scattering that enforces a specific relationship between $\boldsymbol{G}_{hkl}$ and $\boldsymbol{k}_i$. In our setup, $\boldsymbol{k}_i = |\boldsymbol{k}_i|\ \hat{\boldsymbol{x}}$, with $|\boldsymbol{k}_i|$ well defined due to the small energy bandwidth. Further, the location of the detectors used to image the diffraction peaks restrict the geometry of measurable $\boldsymbol{k}_f$. The experiment's geometry requires positive $\hat{\boldsymbol{x}}$ and $\hat{\boldsymbol{z}}$ components for $\boldsymbol{k}_f$. Hence, it is expected that not all grains will be suitably oriented such that any of their crystal planes produce Bragg scattering.

To alievate this problem and ensure a statistically significant number of imageable diffraction peaks are produced from each grain, a rotation is applied to the sample. This allows the $\boldsymbol{G}_{hkl}$s to reorient with respect to the fixed camera and incident beam setup. [1] From the geometry of Figure 2.2, the rotation is done about $\hat{\boldsymbol{z}}$, which results in $\boldsymbol{G}_{hkl}$ sweeping out a cone about that axis.

---

[1] For a given collection of crystal planes, two normals can be defined: $\boldsymbol{G}$ and -$\boldsymbol{G}$. Since the beam is placed at the base of our camera, we only see diffraction where the z component of $\boldsymbol{k}_f$is positive. This requires that for a given reciprocal lattice vector, $\boldsymbol{G}_z > 0$. If the direct beam was placed in the center of our camera, the $\boldsymbol{G}_z < 0$ peak would appear diametrically opposite this positive plane peak (although at a different $\omega$), on a line passing through the diffraction spot and the rotation axis-direct

A rotation will eventually bring a given $\boldsymbol{G}_{hkl}$ into the Bragg condition, but the rotation when this is satisfied is very specific, as is evidenced by (2.5) and our mimimal energy bandwidth and well defined lattice spacings. Thus, we only expect specific $\boldsymbol{G}_{hkl}$ orientations to generate diffraction. To ensure that we capture all possible scattering for a given $\boldsymbol{G}_{hkl}$ we image during intervals of rotation ($\delta\omega$), which amounts to sampling a continuum of $\boldsymbol{G}_{hkl}$ orientations. For the work presented, $\delta\omega = 1°$, and covers contiguous intervals ranging from 100° to 180°. The motion is accomplished with an air-bearing rotation stage, which has minimal coning angles and high angular reproducability.

It is imperative that this rotation axis is normal to the plane of the incident beam and the beam is wide enough to illuminate the entire sample. If the latter is not satisfied, a different set of grains will appear in the beam at different $\delta\omega$ intervals. Therefore, it is possible for a given $\boldsymbol{G}_{hkl}$ to never satisfy the Bragg condition. Further, since the reconstruction looks for a consistent set of peaks that map back to the same spatial location within the sample, having a beam that is narrower than the sample will limit the expected experimental signal and influence the generation of a microstructure map.

Lastly, spot shapes can be used to deduce the planar shapes of the grains responsible for the scattering. In Figure 2.2, the diffracting grain produces a peak for the displayed rotation, $\omega$, which falls within a rotation interval $\delta\omega$. The Bragg scattering is along $2\theta$, the Bragg angle between the incident and scattered wave vector. The shape of the peak, as seen on the detector, is a 2D projection of the in-plane grain shape along the $2\theta$ direction. In this geometry, grains that are circular would project as ellipses. By detecting numerous peaks from the same grain, but with different geometries attributed to the sample's rotation, one obtains a significant number of cross-section projections, leading to higher spatial resolution grains. Because the imaging of many peaks from the same grain means many different $\boldsymbol{G}_{hkl}$ vectors are resolved, we can highly constrain the orientation of the grain.

Thus far, we have qualitatively discussed the nfHEDM experiment and what requirements are necessary for Bragg diffraction and a peak to be imaged on our detector. These diffraction signals originate from different locations in the illuminated 2D plane of polycrystalline microstructure. Typically, cross-sections can have tens to hundreds of grains, where in addition to differences in lattice orientation relative to its neighbors, it can also possess a different phase, strain state or other physical trait that further distinguishes itself from the remaining ensemble. The main goal of nfHEDM, when analyzed with the forward modeling method, is to determine local lattice orientation for all points within the measured microstructure. This determination is entirely accomplished through the interpretation of the experimental diffraction images.

The sections that follow will outline the mathematics associated with the nfHEDM experiment. We will present the analysis from the ground up and introduce new concepts as warranted. We conclude with a worked example of forward projection, where we have *a priori* orientation and spatial information and determine what Bragg peaks it will generate. One can think of this as a single step in the forward modeling recon-

---

beam projection. Such peak geometry is readily seen in Figure 2.4.

struction, which searches thousands of orientations to find the best agreement between the theoretical and experimentally observed scattering.

### 2.3.6 Coordinate Systems, Rotations and Orientations

Figure 2.2 illustrates the coordinate system that we will adopt for the calculations that follow. It remains fixed during the duration of data collection. While this "laboratory" frame appears the most obvious, and all math can be done in this singular frame, it is convienent to introduce additional coordinates that make calculations of the relevant scattering quantities easier. These additional frames are useful, though we must return to the laboratory frame in the final calculation since that is the frame of physical measurement in nfHEDM. Summarily, the beam ($\boldsymbol{k}_i$) travels in $\hat{\boldsymbol{x}}$, while the x-ray sensitive detectors sit at $x = L_1, L_2, L_3$ and image in the $y - z$ plane. The sample is rotated by $\omega$ clockwise about $\hat{\boldsymbol{z}}$. We shall refer to vectors in this coordinate system as $\boldsymbol{v}_{lab}$ and unless explicitly stated, $\hat{\boldsymbol{x}}$, $\hat{\boldsymbol{y}}$, and $\hat{\boldsymbol{z}}$ will refer to this laboratory frame.

#### Crystal, Sample and Laboratory Frames

Our measured samples are polycrystalline, with grains of variable sizes. Each grain is composed of a periodic arrangement of atoms, whose uniformity is broken at grain boundaries, which marks the transition between lattices. A new frame, known as the sample frame, describes the location of grains within the sample. Since the measured microstructure is a 2D section of the 3D sample, it is convinent to assign a coordinate system where two axes can be used to define all points. Additionally, we assign the origin for these two, in-plane axes as the rotation axis. Therefore, the sample frame ($\boldsymbol{r}_{sam}$) is aligned with the laboratory frame when $\omega = 0$ , with $\hat{\boldsymbol{z}}_{sam} = \hat{\boldsymbol{z}}_{lab}$.

Each grain has a fixed configuration with respect to the sample frame. It is the relative configuration within this sample frame that is of interest in spatially-resolved orientation mapping. Since the materials presented in this thesis are of the face-centered cubic (fcc) crystal structure and are of a single phase, both the in-plane spacing of atoms as well as the type of atom at each lattice point is well defined. We assign a reference frame, $\boldsymbol{r}_{sam}$, known as the crystal frame, to this fcc lattice. The crystal frame is aligned with the sample frame in the reference orientation and other orientations are given by a rotation, $g$.

#### Orientations and Rotations

When we speak of the orientation of a grain, we are referring to how its crystal frame is oriented with respect to the sample frame. We can characterize this relative orientation with Euler angles, $(\phi_1, \Phi, \phi_2)$, which describe the geometry of a rigid body in 3D Euclidean space by defining rotation angles about three different axes. In this case, the first rotation is $\phi_1$ about $\hat{\boldsymbol{z}}$, followed by a $\Phi$ rotation about the new x direction ($\hat{\boldsymbol{x'}}$), and finally a $\phi_2$ rotation about the newest z direction ($\hat{\boldsymbol{z''}}$). Compactly, we could represent this as a sequence of rotation operators $R(\hat{\boldsymbol{z''}},\phi_2)\ R(\hat{\boldsymbol{x'}},\ \Phi)\ R(\hat{\boldsymbol{z}},\ \phi_1)$, where the first argument of each rotation matrix is the axis about which the rotation is performed and the second is the magnitude of the rotation. The $R$ matrices listed are rotation matrices that belong to the $SO(3)$, or rotation, group. While not extensively discussed here [82], we do note several properties of these matrices that represent a proper rotation in Euclidean space. When operated on a system of vectors, these rotations preserve both length and inner product. Additionally, these matrices are orthogonal, with columns of the matrix forming an orthonormal basis. Their determinant is unity and their inverse equals its transpose. The group is closed, so the product of any sequence of $SO(3)$ matrices is also an $SO(3)$ matrix. Hence, the sequence $R(\hat{\boldsymbol{z''}},\phi_2)\ R(\hat{\boldsymbol{x'}},\ \Phi)\ R(\hat{\boldsymbol{z}},\ \phi_1)$ is another matrix in $SO(3)$, but has been decomposed into three rotations because of the transparency of their interpretation. The sequence can be written as a coordinate transformation matrix

$$\boldsymbol{U} = \begin{pmatrix} \cos\phi_2\cos\phi_1 - \sin\phi_2\sin\phi_1\cos\Phi & \cos\phi_2\sin\phi_1 + \sin\phi_2\cos\phi_1\cos\Phi & \sin\phi_2\sin\Phi \\ -\sin\phi_2\cos\phi_1 - \cos\phi_2\sin\phi_1\cos\Phi & -\sin\phi_2\sin\phi_1 + \cos\phi_2\cos\phi_1\cos\Phi & \cos\phi_2\sin\Phi \\ \sin\Phi\sin\phi_1 & -\sin\Phi\cos\phi_1 & \cos\Phi \end{pmatrix} \tag{2.6}$$

$\boldsymbol{U}$ represents a passive rotation, which can be interpreted as a change of basis operator. Alternatively, the inverse (transpose) of Equation 2.6 is an active rotation, which performs physical displacement. In our representation, the active transformation can also be used to convert vectors (or orientations) in the sample frame into the crystal frame. This is useful in the discussion of grain boundary geometry and their composing crystal planes, which are identified in the sample frame. In describing an orientation, we use the sample frame, which describes our sample macroscopically. Hence, we perform a change of basis, where $\boldsymbol{U}$ maps from the crystal frame to the sample frame, or $\boldsymbol{r}_{sam} = \boldsymbol{U}\boldsymbol{r}_{cry}$.

The observed Bragg scattering in the nfHEDM experiment is done in the laboratory frame, but the Bragg condition is most easily solved with $\boldsymbol{G}_{hkl}$ vectors, which are physically meaningful in the crystal frame as seen by Equation 2.4. Therefore, the orientation matrix, $\boldsymbol{U}$, will be heavily utilized in connecting experimental peaks with their source of diffraction.

### 2.3.7 Sample Rotation

We have defined three coordinate systems (laboratory, sample, and crystal) and the transformation matrix, $\boldsymbol{U}$ that takes us from the crystal frame to the sample frame (and vice-versa). If nfHEDM were a static sample technique, the laboratory and sample frame could be made equivalent and their distinction would be unnecessary. Because data collection entails the rotation ($\varphi$) of the sample about $\hat{\boldsymbol{z}}_{lab}$, we must introduce another rotation matrix that gets us from the sample frame to the laboratory frame.

First we note that at all times, $\hat{\boldsymbol{z}}_{lab}$= $\hat{\boldsymbol{z}_{sam}}$. The rotation angle about this axis, $\omega$, is the angle with respect to the -$\hat{\boldsymbol{x}}_{lab}$ axis and increases with a clockwise rotation, and when $\varphi = 0$, the laboratory and sample frames are coincident. We can define this sample rotation as $R_\omega$ =$R(\hat{\boldsymbol{z}}_{lab}$,$\varphi)$, where

$$R_\varphi = \begin{pmatrix} \cos\varphi & -\sin\varphi & 0 \\ \sin\varphi & \cos\varphi & 0 \\ 0 & 0 & 1 \end{pmatrix} \tag{2.7}$$

To summarize, we have introduced the coordinate systems that define the nfHEDM experiment: the crystal frame, sample frame, and laboratory frame. The crystal frame takes advantage of the symmetric and repeated arrangement of atoms and is the reference frame in which we represent $\boldsymbol{G}_{hkl}$ as in (2.4). The sample frame is a coordinate system attached to the physical sample and is composed of many spatially compact regions where the lattice arrangement is uniform. To represent the orientation of these different lattices with respect to the common sample frame, we use the orientation matrix ($\boldsymbol{U}$). To produce imageable diffraction from every grain on our set of detectors, we rotate the sample about $\hat{\boldsymbol{z}}_{lab}$, in intervals of $\delta\omega$. When the Bragg condition is satisfied, a diffracted beam is generated in the laboratory frame, which is static through the course of the experiment.

### 2.3.8 Diffraction Geometry in nfHEDM

Now that we have defined the necessary reference frames for describing the nfHEDM experiment and their inter-relationships, we can begin the calculation that takes us from orientations within our polycrystalline sample to diffraction spots. Specifically, we solve for $\boldsymbol{k}_f$ geometries and rotation intervals where a peak is found. We begin with $\boldsymbol{G}_{hkl}$ as our starting point in the crystal frame, which can be written in the sample frame as $\boldsymbol{G}^{sam}_{hkl} = \boldsymbol{U}\boldsymbol{G}^{cry}_{hkl}$. With the application of the $R_\varphi$ rotation, this $\boldsymbol{G}^{sam}_{hkl}$ (which we will now unambiguously call $\boldsymbol{G}$) will sweep out a conical section, with an opening angle $\chi$. If $\boldsymbol{G}$ is placed on the rotation axis, it sweeps out a cone centered on $\hat{\boldsymbol{z}}_{lab}$. The integrated motion of $\boldsymbol{G}$ is shown in Figure 2.3. For simplicity, we assume the diffracting element is on the rotation axis $\hat{\boldsymbol{z}}_{lab}$. We set $\varphi = 0$ when $\boldsymbol{G}$'s $x - y$ plane projection points in the -$\hat{\boldsymbol{x}}_{lab}$ direction.

From our discussion of scattering geometry in Figure 2.1 and Equation 2.2, we know that $\boldsymbol{k}_i$ $\boldsymbol{k}_f$ and $\boldsymbol{Q}$ vectorially define a triangle. For this experiment, $\boldsymbol{k}_i$ is fixed and along the $\hat{\boldsymbol{x}}_{lab}$ direction. The outgoing diffracted beam $\boldsymbol{k}_f$ is imaged on our set of CCD cameras. This geometry entails $\boldsymbol{k}_z > 0$, while $\boldsymbol{k}_{x,y}$ must be arranged to intersect the detector plane. Therefore, for a given Bragg angle $2\theta$, our vector $\boldsymbol{Q}$ must have a fixed magnitude as defined by (2.1) and (2.3). Geometrically, this means $\boldsymbol{k}_f$ defines a cone

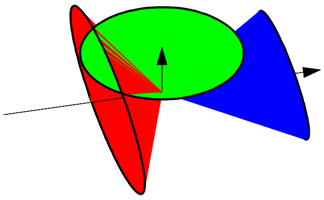

*Figure 2.3: Sketch illustrating the geometry obtained by rotating the same about $\hat{\boldsymbol{z}}_{lab}$. The green cone is defines a surface which confines the $\boldsymbol{G}_{hkl}$vector and is centered about the $\hat{\boldsymbol{z}}_{lab}$. The cone shows the locus of all configurations for $\boldsymbol{G}_{hkl}$and displays the motion of a physical vector. The red cone illustrates the $\boldsymbol{Q}$ configurations that will produce scattering for a given Bragg angle, $2\theta$. The diffracted beams fall on the blue cone, which is along the $\hat{\boldsymbol{x}}_{lab}$direction, with an opening angle that is twice the Bragg angle. The axis of symmetry for $\boldsymbol{Q}$ and the blue ($\boldsymbol{k}_f$) cones are orthogonal. Bragg scattering occurs at the intersections of the green and red cones.*

about $\hat{\boldsymbol{x}}_{lab}$ direction, with opening angle $2\theta$, while $\boldsymbol{Q}$ produces a cone about -$\hat{\boldsymbol{x}}_{lab}$U̇sing Equation 2.2, we see that the opening angle, $\beta$, of the $\boldsymbol{Q}$ cone is $\beta = \frac{\pi}{2} - \theta$.

We unite the rotating crystal with the scattering geometry by enforcing the Laue condition, $\boldsymbol{Q}= \boldsymbol{G}$ which requires the red and green cone of Figure 2.3 to intersect. We should emphasize that the $\boldsymbol{G}$cone is a physical vector that is moving as we rotate the sample, while $\boldsymbol{Q}$ is a theoretical construct used to illustrate the Bragg condition. Thus, the green cone maps out a surface on which $\boldsymbol{G}$ is constrained, but at any given instant $\boldsymbol{G}$ is a vector (not a cone). Alternatively, the red cone is just the locus of all vectors which satisfy the Bragg condition for a given $2\theta$ angle.

It is evident that if $\chi > \theta$, then the cones will intersect and Bragg condition will occur for two $\boldsymbol{G}$ orientations that are symmetric about -$\hat{\boldsymbol{x}}_{lab}$İf $\chi < \theta$, then we never satisfy the Bragg condition and no diffraction is ever present. This is true even if our camera covered a sphere surrounding the sample. Diffraction will not occur for this set of planes in this experimental geometry. Lastly, when $\chi = \theta$, we have exactly one $\boldsymbol{G}$ configuration that produces diffraction. When the Bragg condition is satisfied, we are at the rotations $\varphi = \varphi_1$ or $\varphi = \varphi_2$. By the symmetry about -$\hat{\boldsymbol{x}}_{lab}$ $\varphi_2 = 2\pi - \varphi_1$.

Finally, we note that the diffracted beam is described by three quantities, the Bragg angle ($2\theta$), the sample rotation angle ($\varphi$), and the detector plane angle from vertical ($\eta$) as illustrated in Figure 2.2. These values can be solved simulataneously by using the component form of $\boldsymbol{Q}= \boldsymbol{G}$. Solving the right side of the equation first, we note that $\boldsymbol{G}\cdot \hat{\boldsymbol{z}}_{lab}= |\boldsymbol{G}| \cos\chi$ and is constant. The $x-y$ plane projection of $\boldsymbol{G}$is $|\boldsymbol{G}| \sin\alpha$ and performs a clockwise rotation, $R(\hat{\boldsymbol{z}}_{lab},\varphi)$, such that $\boldsymbol{G}= |\boldsymbol{G}|(-\sin\chi\hat{\boldsymbol{x}}_{lab}- \cos\chi)\hat{\boldsymbol{z}}_{lab})$, when $\varphi = 0$. Applying the $\varphi$ rotation

$$\boldsymbol{G}(\chi,\varphi) = |\boldsymbol{G}| \begin{pmatrix} -\sin\chi\cos\varphi \\ -\sin\chi\sin\varphi \\ \cos\chi \end{pmatrix} \tag{2.8}$$

Solving for $\boldsymbol{Q}$ is similar. We use $\eta$ to quantify the rotation in the $y - z$ plane and define its zero when the $\boldsymbol{Q}_{yz}$ projection points in $\hat{\boldsymbol{z}}_{lab}$ as shown in Figure 2.2. Recalling that $\beta = \frac{\pi}{2} - \theta$

$$\boldsymbol{Q}(\theta,\eta) = |\boldsymbol{Q}| \begin{pmatrix} 1 & 0 & 0 \\ 0 & \cos\eta & -\sin\eta \\ 0 & \sin\eta & \cos\eta \end{pmatrix} \begin{pmatrix} -\cos\beta \\ 0 \\ \sin\beta \end{pmatrix} = |\boldsymbol{Q}| \begin{pmatrix} -\cos\beta \\ -\sin\beta\sin\eta \\ \sin\beta\cos\eta \end{pmatrix} = |\boldsymbol{Q}| \begin{pmatrix} -\sin\theta \\ -\cos\theta\sin\eta \\ \cos\theta\cos\eta \end{pmatrix} \tag{2.9}$$

Enforcing the Laue condition, $\boldsymbol{G} = \boldsymbol{Q}$, we arrive at

$$\begin{aligned} \sin\chi\cos\varphi &= \sin\theta \\ \sin\chi\sin\varphi &= \sin\eta\cos\theta \\ \cos\chi &= \cos\eta\cos\theta \end{aligned} \tag{2.10}$$

For a given crystal orientation, we can tabulate all four angles that define the geometry of scattering for a given collection of crystal planes. Specifically, if we know the orientation of a grain, we know the orientation of all the $\boldsymbol{G}_{hkl}$'s. From Bragg's law, we can calculate the $2\theta$ angle associated with its reflection. Our rotation about $\hat{\boldsymbol{y}}_{lab}$leaves $\chi$ constant,

$$\chi = \arccos\left(\frac{\boldsymbol{G}_{hkl}^{sam} \cdot \hat{\boldsymbol{z}}}{|\boldsymbol{G}_{hkl}^{sam}|}\right)$$

The remaining two variables must determined with careful consideration to their signs. $\eta$ measures the angle from the vertical and in a clockwise manner. From Figure 2.2, $\eta$ will be positive if the horizontal component ($\hat{\boldsymbol{x}}$) of the rotated $\boldsymbol{G}_{hkl}^{\phi}$ is positive, where

$$\boldsymbol{G}_{hkl}^{\phi} = R(\hat{\boldsymbol{x}},\varphi)\boldsymbol{G}_{hkl}^{sam}$$

We have two possible solutions due to the two possible $\boldsymbol{Q}$ - $\boldsymbol{G}_{hkl}$ cone intersections. We label these solutions $\omega_1$ and $\omega_2$, where these $\omega$'s determine the rotation intervals where we see Bragg diffraction. Since $\boldsymbol{G}_{hkl}$ points along -$\hat{\boldsymbol{x}}_{lab}$ at the $\varphi = 0$ configuration, we need to define a rotational offset, $\omega_0$. For consistency, we define this in the same convention as $\varphi$, so $\omega_0$ is measured clockwise from the -$\hat{\boldsymbol{x}}_{lab}$ directon.

$$\omega_0 = \arctan 2(-\boldsymbol{G}_{hkl}^{\widehat{sam}} \cdot \widehat{\boldsymbol{x}_{lab}}, -\boldsymbol{G}_{hkl}^{\widehat{sam}} \cdot \widehat{\boldsymbol{y}_{lab}}) \tag{2.11}$$

Thus, the rotations required to produce diffraction are

$$\omega_1 = \varphi - \omega_0 \quad \omega_2 = (2\pi - \varphi) - \omega_0 \tag{2.12}$$

When using Equation 2.12, care should be given to the sign of $\omega_0$. If $\omega_0 < 0$, it must be represented as $\omega_0 = \omega_0 + 2\pi$.

## 2.4 Example Diffraction Calculation

The previous sections have outlined a process that begins with a defined grain orientation and ends with a set of angles that describe the geometry of diffracted beam. These angles can used to define a vector, which when propogated to intersect the detector plane results in a Bragg peak. In this section, we provide a worked example of this calculation. Based upon personal experience, this should at the very least provide a step-by-step solution for the supplied orientation and can be used for beginners working with both nfHEDM and forward modeling. While not explicitly going through every last number, the important steps will be provided for each portion of the calculation.

Since the rotation axis defines a point in the measured sample plane, we can at most have one grain on axis. We will assume this condition, though note that the solved angles would admit the same result if we placed the grain off axis and had it sweep out a circle. It is only the implementation of the set of angles that makes the diffraction pattern different. For instance, the implementation of $\eta$ requires the projection of the grain center on the horizontal axis ($\hat{\boldsymbol{y}}_{lab}$) of the camera. For the on axis scenario, this projection never changes and is simply the rotation axis. Put more explicitly, the rotation about $\hat{\boldsymbol{z}}_{lab}$ is a proper rotation, so the length of the $\boldsymbol{G}_{hkl}$ does not change when translated off axis. From Equation 2.1 and 2.3, $\theta$ must be a constant during the rotation. Also, a rotation about $\hat{\boldsymbol{z}}_{lab}$ leaves the projection of $\boldsymbol{G}_{hkl}$ along that axis unchanged (and $\chi$ is then constant). Using the system of equations in (2.10) then enforces the remaining to angles $(\eta, \varphi)$ as constants. Our final results will mimic the collection protocol of our near-field experiments. Specifically, since we are solving for four angles $(2\theta, \eta, \omega, \chi)$, we implement certain limits that restrict the observed scattering.

The characteristics of the grain we wish to analyze are listed in Table 2.2. Euler angles have been chosen in the fundamental zone, where the Rodrigues-Frank vector has minimal magnitude. The grain is on-axis and its coordinates describe its center-of-mass when $\omega = 0$. The beam is defined as $z = 0$, and the rotation is about $\hat{\boldsymbol{z}}$ so as detailed eariler, the grain is always in the beam. We will assume that the sample is nickel for this calculation, which is one of the materials that has been measured in this thesis.

*Table 2.2: Sample Grain Properties*

| | |
|---|---|
| Material | Nickel (Ni) |
| Lattice Spacing | 3.52 $\AA$ |
| Crystal Structure | face-centered cubic |
| Orientation (ZXZ Eulers) | $(181.4410°, 12.8660°, 201.6690°)$ |
| Grain Center ($\omega = 0$) | $(0, 0, 0)$ mm |

We further simplify this measurement by considering only the first set of reflections that generate diffraction in the fcc lattice; the (111) set of Bragg peaks. When analyzing diffraction from a given grain, only a finite number of peaks are processed, which is determined by the Bragg angle ($2\theta$). Since $\sin^2(\theta) \propto h^2 + k^2 + l^2$, and face-centered cubic selection rules require $hkl$ to be all even or all odd, the first reflection will be the $\{111\}$ family of crystal planes, where $h^2 + k^2 + l^2 = 3$. Using Equation 2.4 for the (111) plane

$$\boldsymbol{G} = \begin{pmatrix} 1.7850 \\ 1.7850 \\ 1.7850 \end{pmatrix}$$

with the units of $\AA^{-1}$. This is the $\boldsymbol{G}$ vector of only the (111) plane, but it is known that other planes in this family will also produce scattering, such as $(1\bar{1}1)$. We can produce the $\boldsymbol{G}_{hkl}$ vectors for all of these reflections by applying the symmetry operators to $\boldsymbol{G}_{hkl}$. Specifically, $\boldsymbol{G'_i} = \mathcal{O}_i \boldsymbol{G}$, where $\mathcal{O}_i$ is one of the 24 symmetry operators. Table 2.4 omits these symmetry related $\boldsymbol{G'}$ vectors. Each component has a magnitude of $1.785 \AA^{-1}$, and possesses the same positive-negative configuration as the $(hkl)$. For example, $(\bar{1}11)$ corresponds to $(-1.785, 1.785, 1.785)$ $\AA^{-1}$ in the crystal frame.

We convert these crystal frame vectors to the sample frame by applying the rotation matrix associated with these Euler angles to the $\boldsymbol{G}_{hkl}$ list. Using Equation 2.6 for the listed Eulers,

$$\boldsymbol{U} = \begin{pmatrix} 0.9200 & -0.3919 & -0.0056 \\ 0.3832 & 0.8964 & 0.2226 \\ -0.0822 & -0.2069 & 0.9749 \end{pmatrix}$$

*Table 2.3:* $\boldsymbol{G}_{hkl}$ *vectors and scattering angles*

| $hkl$ | $\boldsymbol{G}^{sam}_{hkl}(\mathring{A}^{-1})$ | | | $2\theta$ | $\chi$ | $\varphi$ | $\omega_0$ | $\omega_A$ | $\omega_B$ | $\eta_A$ | $\eta_B$ |
|---|---|---|---|---|---|---|---|---|---|---|---|
| $(\bar{1}\bar{1}\bar{1})$ | -0.9326 | -2.6815 | -1.2240 | 6.9953° | 113.32° | 86.19° | 70.82° | 15.37° | -157.01° | 113.37° | -113.37° |
| $(\bar{1}\bar{1}1)$ | -0.9526 | -1.8868 | 2.2563 | 6.9953° | 43.13° | 84.88° | 63.21° | 21.67° | -148.09° | 43.02° | -43.02° |
| $(\bar{1}1\bar{1})$ | -2.3317 | 0.5187 | -1.9628 | 6.9953° | 129.41° | 85.47° | -12.54° | 98.01° | -72.93° | 129.50° | -129.50° |
| $(\bar{1}11)$ | -2.3517 | 1.3134 | 1.5176 | 6.9953° | 60.60° | 85.98° | -29.18° | 115.17° | -56.80° | 60.54° | -60.54° |
| $(1\bar{1}\bar{1})$ | 2.3517 | -1.3134 | -1.5176 | 6.9953° | 119.40° | 85.98° | 150.82° | -64.83° | 123.20° | 119.46° | -119.46° |
| $(1\bar{1}1)$ | 2.3317 | -0.5187 | 1.9628 | 6.9953° | 50.59° | 85.47° | 167.46° | -81.99° | 107.07° | 50.50° | -50.50° |
| $(11\bar{1})$ | 0.9526 | 1.8868 | -2.2563 | 6.9953° | 136.87° | 84.88° | -116.79° | -158.33° | 31.91° | 136.98° | -136.98° |
| $(111)$ | 0.9326 | 2.6815 | 1.2240 | 6.9953° | 66.68° | 86.19° | -109.18° | -164.63° | 22.99° | 66.63° | -66.63° |

These sample frame vectors are shown in Table 2.4.

The remainder of the table is dedicated to the geometry of the diffracted beam. The Bragg angle is equal for all the reflections because we are analyzing the same family of reflections and therefore their lattice spacings are all equivalent. Using Equations (2.1) and (2.3) admits a scattering angle of 6.9953°. The $\chi$ column is determined by taking the inner product of $\boldsymbol{G}_{hkl}$ with the rotation axis ($\hat{\boldsymbol{z}}_{lab}$), while $\varphi$ can be found using the first equation of (2.10). Finally, $\omega_0$ can be found with (2.11).

Determination of $\eta$ and $\omega$ requires more consideration due to the negative angle possibility. Specifically, when $\omega_0 < 0$, we represent $\omega_0 = 2\pi + \omega_0$. Then, since the rotation stage motor settings use the interval range $(-180°, 180°)$, we place all $\omega$ quantities within these bounds. Lastly, the magnitude of $\eta$ can be found from the second equation in (2.10). The sign is determined by the sign of the $\hat{\boldsymbol{y}}_{lab}$ component of $\boldsymbol{G}^{\omega}_{hkl}$, where $\boldsymbol{G}^{\omega}_{hkl} = R(\hat{\boldsymbol{z}}, \omega)\boldsymbol{G}^{sam}_{hkl}$. If this quantity is negative, then the peak is described by a positive $\eta$.

We enforce the limits of the nfHEDM setup to determine which peaks will be observed during the diffraction experiment. First, our rotation is about the $\hat{\boldsymbol{z}}$direction and our camera is configured such that the direct beam is at its base. This restricts visible peaks to those with a positive $\hat{\boldsymbol{z}}$component of $\boldsymbol{G}^{sam}_{hkl}$ (or $\chi < 90°$). The limitations on $2\theta$ are a result of the field-of-view of the CCD camera and the distance from the rotation-axis to the detector plane ($L$). Our current camera covers a $3.01mm$ square with $1.47\mu m$ pixels. If we assume the direct beam is at the base of this system, and the $L_1$ distance is $\sim 5mm$, we arrive at a $2\theta$ limit of $\sim 30°$. For the purposes of current nfHEDM, this is not a limitation in peak selection, especially since peaks of these large $2\theta$ values have intensities too weak to be feasibly imaged in our polycrystalline experiments. The $\omega$ rotation for the aluminum data in this thesis used two 45° contiguous intervals with centers offset by 90°, while the nickel used a single integration over 180°. Both collections had $\delta\omega = 1°$. The 100° coverage was used as a trade off between appreciable peak sampling and long readout times for the $LN_2$ camera, while 180° is the ideal case, where each reflection within a family should produce one visible peak. Of course, we might not be sensitive to that ideal peak due to the $\chi$ and $\eta$ constraints. In the current collection protocol, we limit $\omega$ to $[-90°, 90°]$. Finally, the $\eta$ restriction is due to the shape geometry of projected peaks. Peaks with a large $|\eta|$ have highly compressed scattering geometries, where they approach an infinite line as $|\eta| \to 90°$. Thus, we limit $|\eta|$ (somewhat arbitrarily) to 81° for peak analysis. We summarize these restriction in Table 2.4.

If we enforce these limits to Table 2.4 and label each reflection by it's row number and if it has the A or B reflection satisfying the restrictions, we see that only $2A, 4B, 6A, 8B$ will appear in our nfHEDM experiment.

A final set of figures illustrates how the distribution of peaks look upon a synthetic detector, shown in Figure 2.4. Here we take the same orientation from our example, only produce scattering for the on-axis and off-axis rotation. The off-axis rotation has the center of the grain at $\boldsymbol{r}(\omega = 0) = -0.146\hat{\boldsymbol{x}} - 0.091\hat{\boldsymbol{y}}$. We generate diffraction up to the $\{420\}$ reflections, which corresponds to $2\theta = 18.13°$. Our sample camera sits

*Table 2.4: Angle restrictions for nfHEDM*

| Angle | Restriction | Origin |
|---|---|---|
| $\chi$ | $\chi < 90°$ | Top plane imaging |
| $2\theta$ | $2\theta \lesssim 30°$ | Imaging distance and camera field-of-view |
| $\omega$ | $\omega \in [-90°, 90°]$ | Collection speed, maximal scattering range |
| $\eta$ | $\lvert\eta\rvert < 81°$ | Scattering geometry, beam attenuator |

$L_1 = 5mm$ from the rotation axis, and is composed of 2048 pixels that are $1.47\mu m$ square. The rotation axis projection on the camera is indicated by the × symbol and is at $(1024, 2010)$. Color points indicate the center of masses of peaks we expect to see in the actual experiment, while black dots do not satisfy at least one of the conditions in Table 2.4. For the off-axis configuration, the pixel address of the projection must also be checked, even if all conditions in Table 2.4 are satisfied. This is because the horizontal ($\hat{\boldsymbol{x}}_{lab}$) projection of the scattering center follows a sinusodial path, which defines the vertical axis from which $\eta$ is measured. When this projection is large in magnitude, a large $2\theta$ and/or $\eta$ can force the peak off the detector plane.

The main purpose of Figure 2.4 is to illustrate how scattering looks from a grain that is on and off the rotation axis. The on-axis case very clearly results in peaks that fall on rings, while the pattern is more complicated as we go off-axis. Since the forward modeling reconstruction requires precise knowledge of quantities such as $L$, and rotation axis projection onto the camera $(j_0, k_0)$, we use high purity, (approximately) single crystal samples, with small diameters that ideally reside on the rotation axis. This permits easy estimation of $L$ and $(j_0, k_0)$ by fitting peaks to rings.

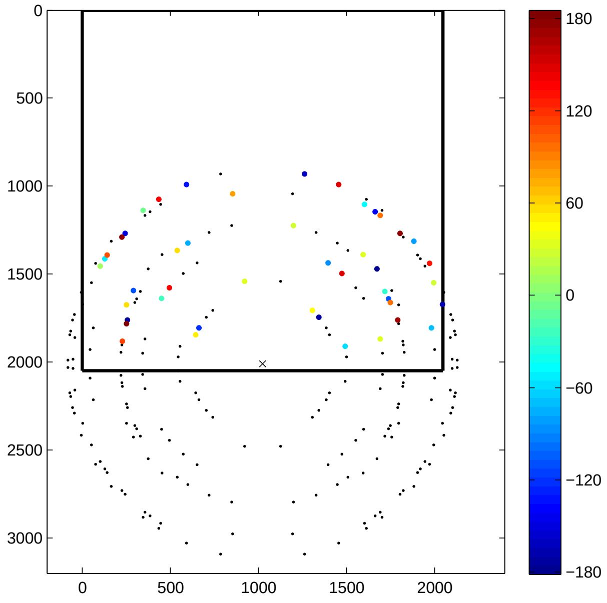

**On Axis**

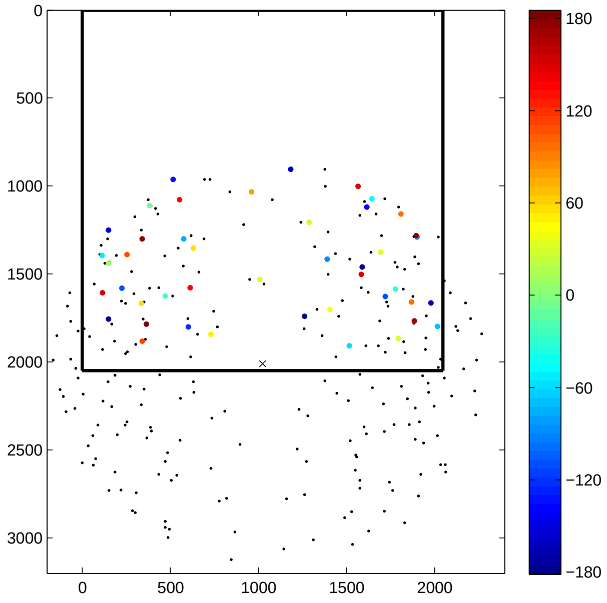

**Off Axis**

*Figure 2.4: All scattering generated by a grain of the orientation listed in Table 2.2. The scattering is shown when the grain is on the rotation axis and offset by the position* $[-0.146, -0.091, 0]$ *at* $\omega = 0$. *All peaks that are generated up to the* $\{420\}$ *reflection are shown, while a black box indicates the region that would be imaged in a nfHEDM experiment. Black dots indicate scattering that would not be seen due to violation of the angle restrictions itemized in Table 2.4. The points we are sensitive to are colored by their* $\omega$ *interval. Points in black that fall within our detector box are not observed due to their* $\omega$ *interval falling outside* $[-90^\circ, 90^\circ]$. *The projection of the rotation axis-direct beam intersection is marked with an* ×.

# Chapter 3

# Recovery in Polycrystalline Aluminum

## 3.1 Motivation

The overall theme of the following content is measurement of the annealing response in high purity metals. Using near-field high energy x-ray diffraction microscopy data. As has been emphasized, the use of nf-HEDM to monitor material response to external stimuli is ideal, due to its inherent non-destructive method of materials mapping. The results to be presented address the three main classifications of annealing response in polycrystalline material: *recovery*, *recrystallization* and *grain growth*. The measurements were accomplished with two separate materials, both high purity wires, but with differing initial states. Coarse grained aluminum, initially containing large defect content was used to illustrate the processes of recovery and recrystallization. Fully recrystallized nickel was used as the starting point for an *ex-situ* grain growth experiment. In both experiments, thermal energy provided the impetus for microstructure evolution and resulted in the properties of the final state microstructure, differing appreciably from the initial properties.

## 3.2 Aluminum

The first *in-situ* experiment using the forward modeling method of interpreting near-field high energy x-ray diffraction microscopy data was accomplished with an annealing experiment of high purity aluminum wire. The measurement produced 11 resolvable layers of microstructure that were repeatedly tracked as the specimen was subjected to low temperature anneals. Due to the large defect content in the initial microstructure and the combination of short time, low temperature anneals employed during the measurement, the annealing processes of polycrystalline recovery and recrystallization were the dominating observable responses. Here, we first outline the nf-HEDM experiment.

We discuss the reconstruction process that yielded orientation maps of the measured microstructure. Lastly, we put the results in the context of the annealing processes.

## 3.3 Experiment

The *in-situ* annealing experiment was performed in February 2007 and operated under the near-field experimental setup limitations of the 1-ID-B beam line at that time. Since then, significant upgrades have been made resulting in decreased collection times, better spatial resolution, and improved data collection protocols. The volumetric measurement of microstructure consisted of the collection of 11 distinct layers spaced 20 $\mu$m apart, along the wire axis. The spacing was selected due to both time restrictions and initial grain sizes. For both measurement consistency and sufficent intra-granular statistics, the presence of the same grains within multiple layers was necessary.

The sample for this measurement was a 1 $mm$ piece of high purity (99.999%) polycrystalline aluminum wire, purchased from Alpha Aesar. The initial sample state for the experiment was as-received aluminum and was simply cut from a 25 $m$ spool of material. There were no additional sample treatments prior to the measurement, aside from hand rolling to straighten the wire. The initial microstructure state was deformed, which was the result of extrusion used in production processing. The application of heat to this dislocation rich microstructure, and the resulting changes, are known as defect annealing and is the focus for this aluminum experiment.

Diffraction was collected using a liquid nitrogen cooled charged-coupled-device (CCD) camera, which imaged a scintillation screen composed of a Ce-doped layer on a single YAG crystal. The optics on the camera resulted in effective square pixel sizes of 4.11 $\mu$m. The scintillator was 15 $\mu$m in thickness, which is appreciable enough to produce weak 'tails' on diffraction peaks. The location of these tails were dependent upon the position of the spots on the detector. Tails above diffraction spots, as seen in this data set, correspond to focusing accomplished on the plane nearest to the sample. These tails turn out to not strongly affect the reconstructions since the simulation, with fixed lattice constants, cannot consistently put intensity in these detector positions.

The liquid nitrogen ($LN_2$) cooling system was the source of a systematic drift during the experiment. To maintain low background current, periodic replentishing of the $LN_2$ dewar was required every 8-12 hours, which is roughly the amount of time required to collect one 11 layer volume of microstructure. Due to the location of the dewar on the camera stand, a rigid body motion of the camera occured during the course of each volume measurement, leading to a change in the location of the imaging plane for each 2D layer of microstructure. This can be seen in Figure 3.1, where the edges of the beam shadow have been tracked over multiple layer measurements. The summary of reconstructions to follow in Section 3.3.1 discuss how these motions were resolved in the reconstruction. The drift was significant enough to be observed as changes in the beam position on the camera, which could be tracked with a shadow of the direct beam seen in every collected image. Diffraction from the tantalum beam attenuator can also be used

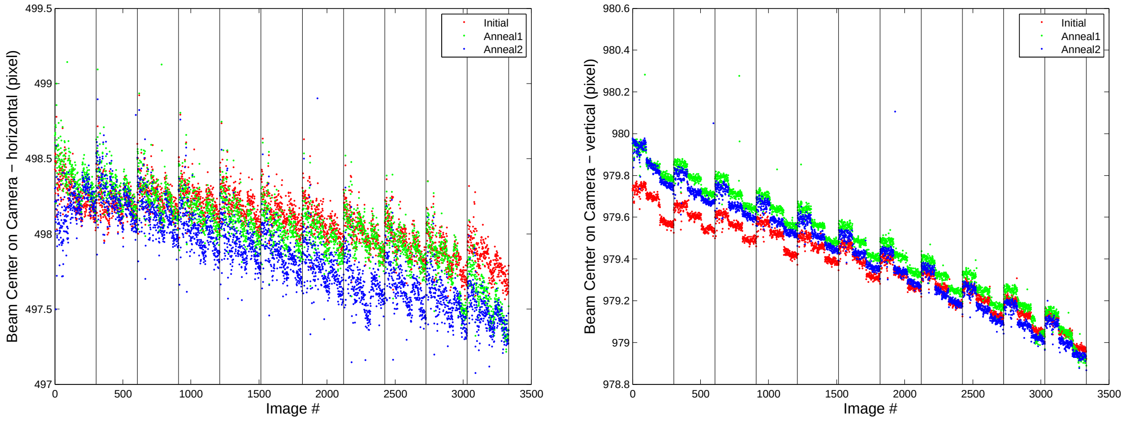

**(a)** **(b)**

*Figure 3.1: Plots monitoring the motion of the CCD camera as the $LN_2$ evaporates during the course of the 11 layer measurement. (a) illustrates the drift of the horizontal pixel position of the direct beam on the camera, while (b) shows the vertical position. The position is determined by fitting the 'direct beam shadow' to a gaussian, which appears on every camera image and is composed of a weak intensity that maintains a nearly constant profile during the data collection. The fit is conducted in both dimensions and the center is tabulated and plotted in these charts. Vertical lines on both plots indicate the location of a new layer of microstructure, and breaks the graph into 11 sets associated with each 2D cross-section that was measured. Within these vertical lines, three camera distances were used for the measurement and their clustering is also evident. Stray centers, outside of the trend can be attributed to poor fits to the image of interest, due to continued camera motion after translation or weak intensities in the diffraction image.*

as a fiducial mark for the tracking of both camera drift and intensity fluctuations. The beam block was placed between the sample and camera, with the purpose of attenuating the direct beam which was not diffracted by the sample. Given its close proximity to the sample ($\sim 1\ mm$) and its polycrystalline composition, diffraction spots from the beam block can be imaged on the detector. Further, with the beam block being held in a fixed configuration during the course of the measurements, the location of these diffraction spots are fixed in space. Therefore, changes in either the beam intensity or camera position can be tracked by monitoring of beam block diffraction.

The nf-HEDM data was collected using $5\ s$ exposure times for each 1° rotation interval ($\delta\omega$). The exposure time was selected to maximize the use of the dynamic range of the camera, with the criteria of observing weak peaks at high $\mathbf{Q}$, but also avoiding the saturation of peaks with large structure factors and therefore large intensities. Due to limitations in both readout times and the motor motions required to produce constant rotational speed during the image exposure, each image required $12.5\ s$ to collect and store. The necessity for both an appreciable sample volume for each sample state and the measurement of at least three distinct states forced a collection routine that covered two contiguous 50° wedges, where wedge centers were offset by 90°. While not generating the complete collection of top plane, the sampling of 100° produced sufficent diffraction to resolve both grain shapes and orientations, as illustrated in Section 3.3.1. Three camera-to-rotation axis distances were employed for all layers of the measurement, which was standard nf-HEDM protocol at the time of the experiment. This restriction has been relaxed since the time of measurement and typically two detector distances will suffice for a given measurement, with intermediate three distance collections used for experimental geometry calibration.

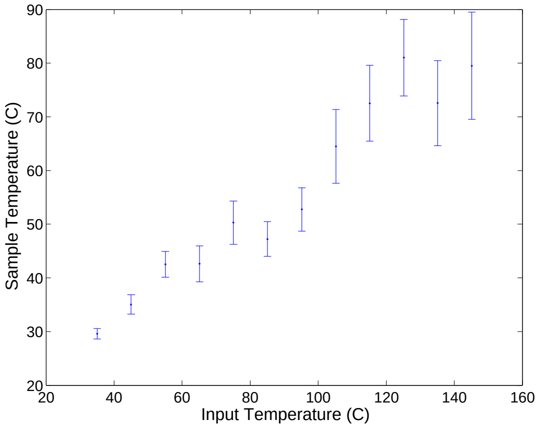

*Figure 3.2: Calibration curve produced for an aluminum sample of approximately the same dimensions as the one used for the nfHEDM experiment. Horizontal axis is the input temperature, while the response variable is the temperature of the sample measured at the approximately the same location as the aluminum microstructure (∼ 1 mm below the sample tip).*

The annealing for the experiment was performed with a fabricated boron nitride (BN) recepticle, which was resistively heated by passing current through Nichrome wire. The furnace design has seen several modifications, but the one used for this experiment was composed of two pieces: a solid container for the sample, which served as a spool to wrap the wire and a sleeve to cover these wrapped wires. The calibration curve for this furnace can be seen in Figure 3.2, which was obtained after the nf-HEDM measurement, using a piece of aluminum of the same dimensions and cut from the same spool. The same temperature settings used for the synchrotron measurement were produced for the calibration and the temperature at the analogous nf-HEDM imaging region was monitored. The annealing was done sequentially, with the first state collected at room temperature with no heat treatment performed to this point. The sample was then annealed for 2.5 hours at 40°C, 50°C, 60°C, and 80°C. During these thermal cycles, data was collected for a single layer at a single camera-to-rotation axis distance. Bragg peaks were monitored during this process to determine when the experimental diffraction signal had appreciably changed from the initial. Once the 80°C anneal completed, the sample was returned to room temperature and the same 11 layers of microstructure that were mapped in the initial state were collected for this first anneal. After collection, a second incremental annealing sequence was employed. The same single detector-to-rotation axis distance procedure was used, with furnace temperatures of 100°C for 2.5 hours, 120°C for 1.25 hours, and at the maximum furnace output for ∼ 15 minutes. Operating at maximum output was the result of an undetected detachment of the feedback thermocouple from the BN recepticle. The sample was returned to room temperature and two measurements were conducted. The first consisted of mapping the same 11 layers as we previously measured in the initial and post 80°C states. The second was a measurement of the opposite end of the wire, which had been embedded in the furnace. Though no one-to-one evolutionary tracking is possible with this 7 layer volume, deformation content can be quantified.

The alignment procedure for repeated measurement of the same 11 layers of microstructure was done through a monitoring of the sample tip position using a diode detector which sat ∼ 2 $m$ from the sample. By monitoring the counts in a fixed duration as the sample is moved vertically, the motor position of the sample tip can be determined. Because of the possibility of spatial displacement from thermal expansion and motor drifts, this tip measurement was repeated before each volume of microstructure was collected. Figure 3.3 displays the repeatability of this process. The sample tip returns to within ± 2 $\mu$m of its starting position (after each extended data acquisition period). This is is less than the width of the focused beam used for the measurement.

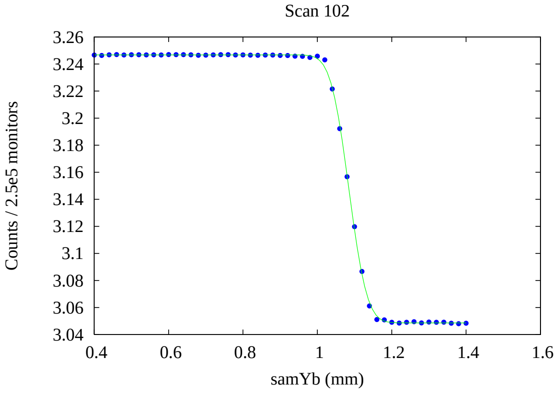

*Figure 3.3: Scan of the aluminum sample tip, prior to one of the measurement volumes. The graph illustrates the sample tip position through the measurement of absorption on a diode, ∼ 2m downstream of the sample. Fitting this profile to an error function yields a half-width of 27.2μm for the transition. This profile showed repeatability after thermal expansion during the heating process and after collection of layers, indicating that we have good agreement between our layer measurements for this experiment.*

### 3.3.1 Reconstruction

Reconstruction of the 33 distinct layers of microstructure ($11 \times 3$) was accomplished with the IceNine forward modeling software for nf-HEDM analysis. The process of orientation reconstruction for microstructure maps has been previously outlined, but will be briefly summarized in the context of this data for completeness. The relevant results concerning peak extraction, experimental parameters determination, and orientation reconstruction are also addressed.

#### Reduction of Experimental Data

The conversion of raw *.tif* images into a list of pixels illuminated through sample diffraction is a multistep procedure, as outlined in [66, 67]. Since all reconstructions are based upon the experimental diffraction content, extraction of peaks is a crucial process to producing both precise and accurate orientation maps. Considering the presence of beam block diffraction, scratches upon the scintillation screen, and a complex population of polycrystalline diffraction, the generation of a list of pixels illuminated by aluminum diffraction is challenging. The extraction is accomplished through the generation of a statistical background image produced at each camera-to-rotation axis distance. The intensity of each pixel (with a maximum of $65,535$ counts) is recorded in the 100 image time series for the single detector-rotation axis distance. The median intensity across all 100 images is tabulated for each pixel. A statistical (median) background image is thus created of the same dimensions as the diffraction images and is subtracted from each of the diffraction images to produce a background reduced image. This process not only removes the approximately flat background, but also eliminates static features on the camera, such as beam block diffraction, the approximately constant direct beam ‘shadow’, and imperfections on the scintillator. The background processing procedure continues with the subtraction of a baseline pixel count, which is the subtraction of a constant image from the background reduced image. This eliminates the retention of any anomolous intensities slightly above the median value. A baseline intensity of 25 was used for the aluminum reductions. The final step in the background treatment is the removal of ‘hot pixels’ using a 5×5 median filter. Simply explained, this is a 5 pixel window centered on the target pixel and assigned the median intensity of the 25 pixel intensities that are contained in this mask. This reduces sensitivity to small features, but the coarse grain microstructure leads to large diffraction peaks and therefore the 5×5 filter sufficed.

After removal of background from each diffraction image, a peak identification process is conducted, which retains the diffraction signal upon which the reconstruction will be based. Since the reconstruction is sensitive to spot locations and shapes, proper identification is sample’s diffraction signal is crucial. The 2D boundaries of grains are determined by fitting to the edges of peaks, so the existence of ill-defined objects can limit the sensitivity of the reconstructed orientation maps. Therefore, a method is required to produce well defined peaks that can generate geometrically accurate maps. Laplacian of

Gaussians (*LoG*) edge-detection filter accomplishes this with the nf-HEDM diffraction data [83, 84], by operating as a type of band-pass filter for diffraction spot edges. The segregated peaks have their intensities retained and are identified as individual peaks based on connected components. This labeling of peaks becomes advantageous when connecting features in the reconstructed orientation maps with the source signal in the experimental diffraction data.

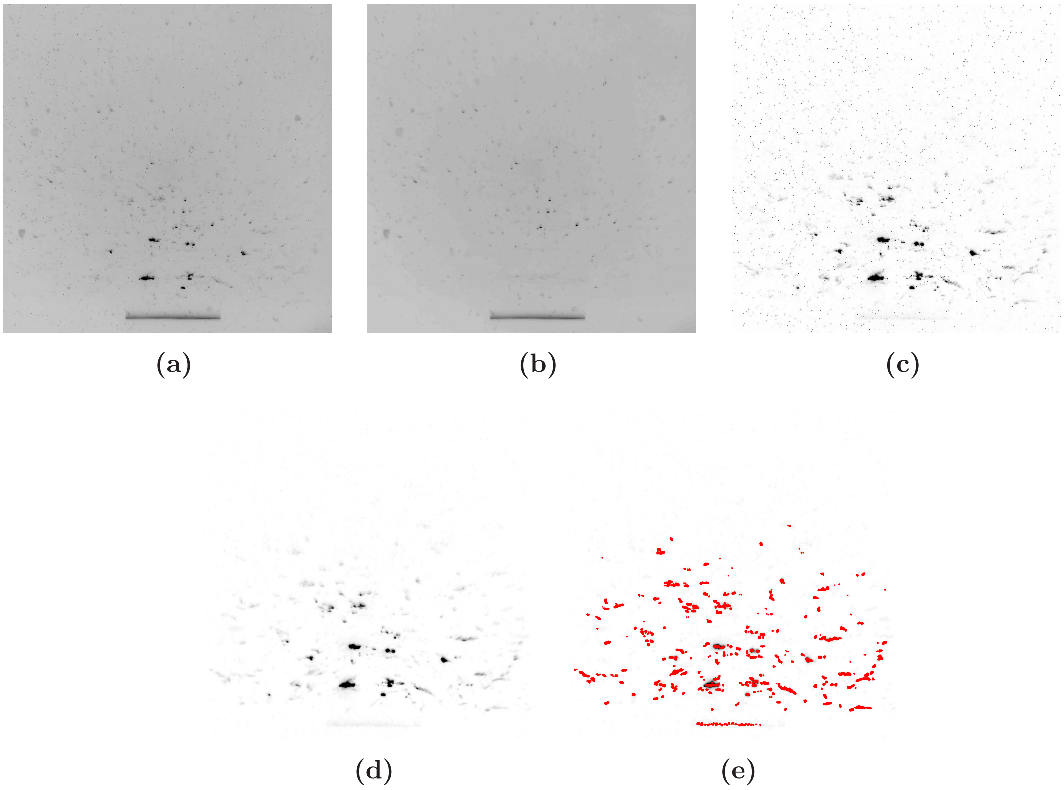

*Figure 3.4: The image processing routine for the aluminum data, illustrating each processing step. (a) illustrates a raw detector image that is associated with an integrated $\delta\omega = 1^\circ$ rotation, from the initial state microstructure. The image was collected at the $L_1$ detector-to-rotation axis distance. (b) displays the statistical background image, composed of the the mean intensity for each pixel in the 100 images used in the single detector distance collection. (c) is the first reduction, subtracting (a) from (b). A 5×5 median filter eliminates 'hot pixels' that are not associated with diffraction and is shown in (d). The pixels that are retained and serve as input to the forward modeling simulation are shown in (e). To better illustrate the diffraction signal, the color scale saturates at 3000 counts for images (a) and (b), while (c)-(e) saturates at 500.*

Figure 3.4 illustrates the steps towards producing the experimental data that is used as input for the forward modeling simulations. The first image is of a representative 1° $\omega$ integrated intensity image, as collected with the nf-HEDM experiment. The statistical background image generated for the detector-to-rotation axis distance which includes Figure 3.4(a) is shown in (b). The background reduced image is shown in (c), followed by the resulting image after the 5×5 median filter (d). The final image (e) is the binarized data, overlayed on the original image. The retention of beam block scattering at the bottom of (e) is due to the detector drift which makes the median background image inexact.

### Parameters Monte Carlo

The aluminum data was collected before the creation of a 30 $\mu$m diameter gold wire standard sample and collection protocol, which has served as the initial calibration measurement for nf-HEDM beam runs since 2008. While beneficial for determining the geometric parameters which are used as inputs for the forward modelling reconstruction, the gold wire measurement would be of little use for this experiment, due to the continual drift of the camera as the $LN_2$ evaporated during the course of the measurement. Even if available during this run, the gold wire would only be capable of providing experimental parameters for the first layer of the initial sample state.

To obtain the best possible experimental configuration for this measurement, the parameters optimization Monte Carlo was performed for each layer, which consisted of diffraction imaging at three detector-to-rotation axis distances. This data set has been continually analyzed for several years, using various versions of data reduction and forward modeling, which includes different parameter optimization processes and orientation reconstruction algorithms. The optimized experimental parameters are the progressive result of analyzing this aluminum data using available algorithmic resources as they reached maturation.

The underlying theme of all experimental parameter Monte Carlo (PMC) sequences was the selection of a set of voxels, perturbing the experimental parameters, then deciding if a cost function that rewarded overlap between simulated scattering and experimental diffraction was improved. All of these methods have evolved over time. The voxel selection procedure has been varied in regard to the spatial location of the PMC voxels (boundary voxels vs. grain interior voxels) and original fit quality through the restriction of minimum confidences for use in the PMC. The process for perturbing experimental parameters has varied many times, from deciding which quantities should be varied, if parameters at multiple detector distances should be coupled and by what amount, and the entire process of refining experimental parameters space. Lastly, the cost functions have changed not only with regard to parameters Monte Carlo, but also to the orientation reconstruction procedure.

Both the parameters Monte Carlo and the orientation reconstruction used a fixed x-ray energy of 50.062 keV and a fixed pixel pitch ($\gamma$) of 4.10974 $\mu$m (square pixels), which was determined through a rastering procedure of placing a small beam on the camera and horizontally and vertically displacing the imaging plane. A maximum scattering vector, $\mathbf{Q}$, of 8 $\mathring{A}^{-1}$, was used for both reconstructions and optimizations, which corresponds to fitting up to the {440} family of Bragg peaks. This corresponds to $\sim 35$ Bragg peaks per orientation. Fitting to higher $\mathbf{Q}$ values is possible, but these higher order peaks tend to have poor signal-to-noise qualities. Further, the increased time required for fitting in an expanded Q-space and the fact that fitting to $\sim 35$ already highly constrains the reconstruction, leads to the selection of 8 $\mathring{A}^{-1}$ as a good compromise.

This final parameter optimization was performed with 25 5.08 $\mu$m triangles for each layer, each with a minimum confidence of 0.2. A total of 2000 Monte Carlo iterations were performed on each of 512 processors, before checking for parameter improvement. This sequence was performed at least once and as many as ten times. The parameters separating $L$ distance were not coupled, which is justified due to the drifts exhibited by the detector over the course of the measurement.

#### Orientation Reconstruction

The 33 layers of microstructure were reconstructed using the IceNine forward modeling reconstruction software for nf-HEDM diffraction data. The maps consisted of fitting triangles with 5.08 $\mu$m sides, which was chosen to match the pixel size on the camera, which limits the spatial resolution. Each triangle was fitted independently of its neighbors. Reconstructions required approximately 4.5 hours per layer ($5\frac{voxels}{s}$) on 512 processors on the Texas Advanced Computing Center's Ranger super-computing cluster. The independent fitting of each voxel was used to ensure no biasing in orientation determination. As discussed in the sections to follow, the internal microstructure was coarse grained, with large orientation variations within each grain. As the annealing progressed, these internal distributions evolved. Therefore, the fitting of each voxel independently ensures sensitivity to subtle changes in orientations.

The orientation search for each voxel was performed first on a coarse grid, where each unique orientation is in the fundamental zone and is within 5° of all other orientations. Regions of interest in SO(3) were then gridded more finely until a final Monte Carlo optimization was done. The orientation was considered converged when a final grid resolution was achieved and optimized or when the confidence reached 0.95. Voxels with 0.1 confidence were retained in the fit, though this amounts to defining an orientation through the fitting of $\sim 3$ of 30 peaks. For the analysis that will be presented, a minimum threshold of $C = 0.25$ was employed. Once a voxel achieved $C = 0.95$, it was deemed converged and the orientation search concluded.

### 3.3.2 Map Results

The maps generated by the orientation reconstruction are shown in Figure 3.5. As stated previously, 11 maps were collected for each of three states. The orientation maps are colored according to the assigned voxel orientation, by mapping the Rodrigues vector representation of orientation to the red-green-blue (RGB) coloring scheme. The granular aspect of the microstructure is seen as regions of compact color. This coarse color scale does not illustrate the fact that each voxel has been fit independent of its neighbors.

To illustrate the internal variation, we use an expanded color scale that covers only the range of a single grain, which is shown in Figure 3.6. Here, instead of the RGB space spanning the entire fundamental zone of orientations, a small region of orientation space (2°) spans all of color space and local orientation variations are more evident. Specifically, it's seen that spatially localized regions within the grain have very similar orientation, while orientations far from this region can be significantly different (on this small scale).

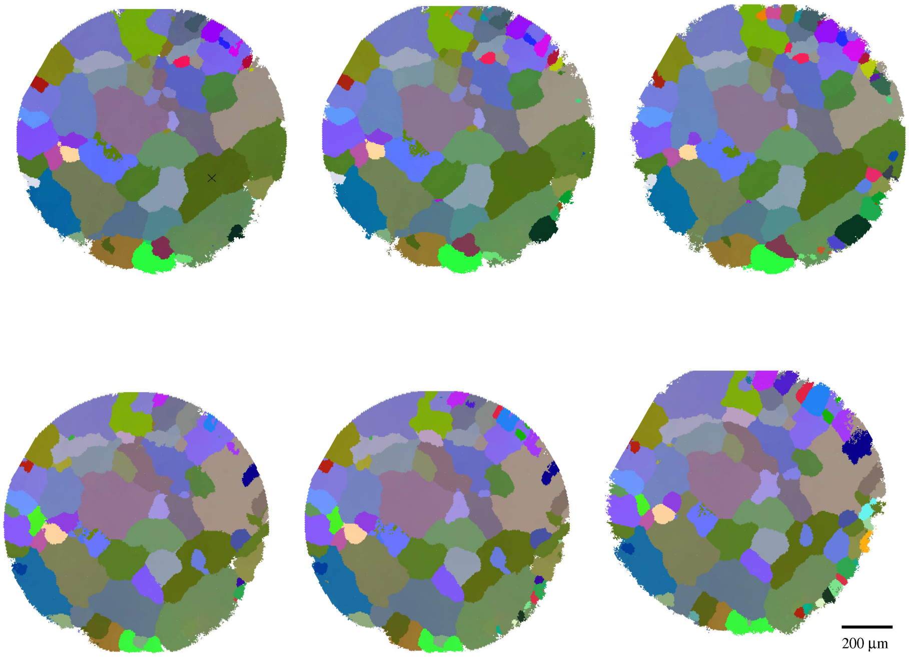

**Initial** **Anneal1** **Anneal2**

*Figure 3.5: Two layers of reconstructed orientation maps from the aluminum microstructure. Rows show maps from the same layer of microstructure, while the two set of maps are separated vertically by 80 µm. The columns indicate sample state. The same granular structure can easily be seen both across states and across layers, with the changes within a layer being more subtle than the vertical translation. Orientations were represented as Rodrigues vectors in a single fundamental zone, then mapped to red-green-blue space. Only voxels exceeding 0.25 confidence ($C = 0.25$) are shown.*

Confidence maps are produced for the same layer, through the anneal states, in Figure 3.7. The color scale minimum is 0.25. The confidence was used to gauge experimental parameters and determine when they were optimized. Specifically, Figure 3.8 shows a histogram of confidences for each layer of microstructure. Since each layer should be statistically equivalent, with roughly the same number of low confidence boundary voxels, we expect each distribution to be similar. This is evident in Figure 3.8. When

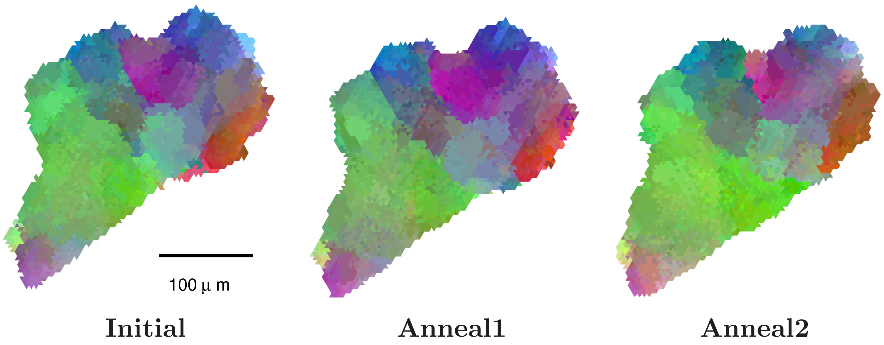

*Figure 3.6: Expanded color scale image of lower right grain found in Figure* 3.5*, colored dark green and indicated with a white ×, in the top left map. Instead of allowing the red-green-blue coloring scheme to cover all of fundamental zone of Rodrigues space, it only maps the portion that includes the voxels composing this grain. Therefore, orientation variations are more evident, as is the voxel-based reconstruction achieved with the forward modeling reconstruction. The evolution of these variations will be a point of emphasis in the material to follow.*

comparing each anneal state, an overall shift towards regions with higher confidence (more red) can be seen in both the confidence maps of Figure 3.7 as well as the histograms in Figure 3.8. One interesting feature is the increasing portion of microstructure that has large confidences and appears to be replacing the low confidence voxels in the 0.4-0.7 range. This will be discussed in the recovery discussion of this analysis.

One challenging aspect of this data set is the limited number of 2D cross-sections collected within the microstructure. With the coarse grained microstructure and only 200 $\mu$m of microstructure spanned along the wire axis, there are many grains that are not entirely encapsulated within the measured microstructure. Either their top or bottom is truncated in the measurement. Full encapsulation would mean that the target grain is absent in the first and last 2D cross sections in any of the anneal states. Grains exhibiting this property are ideal, for evolution analysis. For instance, grain initiation can be conclusively identified if the observation falls within the nine interior reconstructions. If the observation is in the top or bottom cross section, it is possible that the grain was initially outside the measurement window and therefore we have not observed a critical event.

We investigate the three annealing phenomena in the context of simply calculated quantities on the reconstructed orientation maps, these include metrics such as grain sizes, internal orientation variations, and voxel confidences. As stated earlier, we can look at these quantities on both a statistical and correlated basis. The number of grains in this data set is small compared to the nickel measurement, which will be presented in the next chapter, so monitoring evolution on a granular basis can be done without

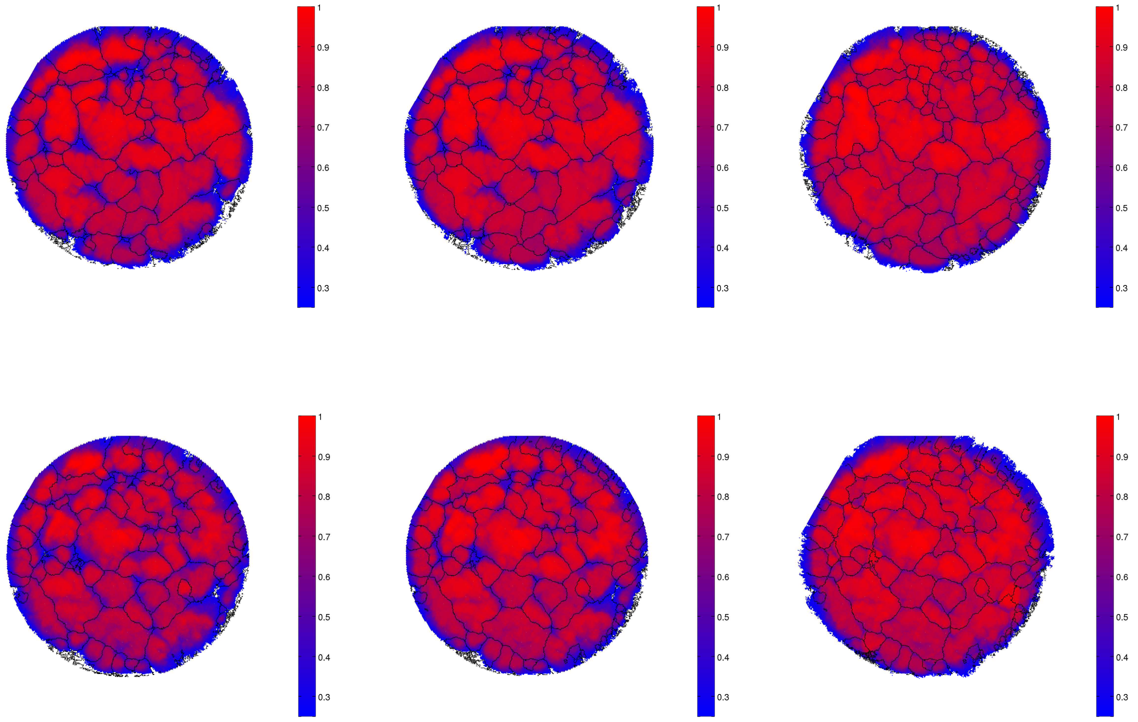

**Initial** **Anneal1** **Anneal2**

*Figure 3.7: Confidence maps corresponding to the orientation maps found in Figure* 3.5*. Black lines border all voxels where the neighboring voxel exceeds* 2° *in misorientation. Multiple lines fall over regions of white space, since the boundary map is created with a map containing voxels with confidences as low as 0.1, while these maps have 0.25 as the minimum. Superimposed on Figure 3.5, the black lines would outline the regions of visibly distinct colors.*

extensive data mining. The analysis presented will be based on investigation of both the reconstructed orientation maps (sample space), as well as interpreting the origins of the signal through diffraction images (detector space). Using these two domains affords complete evidence for the phenomena in question. This 'by hand' analysis should set the stage for future work on larger datasets that will require more automated approaches. Substantial algorithm and software development will be required. The aluminum data set, as analyzed here, can serve as a test bed for such development work.

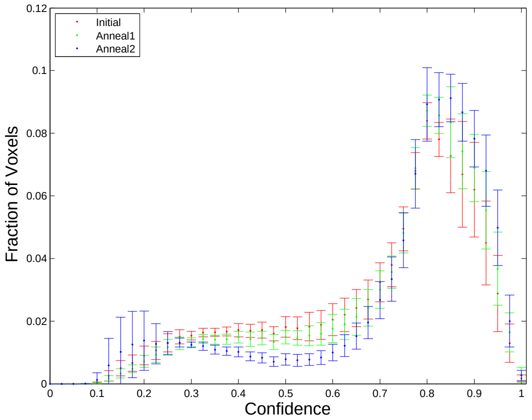

*Figure 3.8: Histogram of confidence values for the 33 maps measured in three distinct sample states. Confidence bin widths are 0.025. Each layer is individually histogrammed and normalized. The errorbars on each data point are the variation in the bin across the 11 layers composing that state's measurement.*

## 3.4 Recovery

### 3.4.1 Interpretation of Recovery through Diffraction

The recovery process is characterized by changes in dislocation density and distributions that result in the reduction of local orientation variations. Crystal orientation variations correspond to a distribution in the directions of local reciprocal lattice vectors, so recovery is observable as a sharpening of intensity distributions. The measurement of such orientation distributions is traditionally done using rocking curve measurements in single crystals [85], which is analogous to the nf-HEDM measurement, only done for numerous grains generating many Bragg peaks through polycrystalline diffraction.

In our spatially resolved measurements, as grains move toward more uniform orientations, diffraction peaks become more localized and uniform in detector space and approach the distribution associated with a single orientation crystal. For the diffraction emanating from a single grain, this can be interpreted in multiple ways in detector space. First, as the grain moves towards a uniform orientation, individual voxels also move towards a singular orientation. Diffraction from these singular voxels result in uniform intensity distributions within peaks, since the diffracted beams should now be moving in parallel. When imaged on a detector plane, the intensity profile of the diffraction peak from a grain of a single orientation will be the result of the cross-section geometry of the grain. Further, areal coverage by the diffraction peak on the camera will be as minimal as geometrically possible. This is because orientation spread leads to variation in the direction of the diffracted beam. Therefore, the 'smearing' should result in greater areal detector coverage (more pixels hit) than in the singular orientation configuration. Deviation in orientation also influences the $\omega$ coordinate, when diffraction is satisfied.

Uniform orientations result in small intervals in which the Bragg condition is satisfied. As orientations spread due to the presence of crystal imperfections (or dislocations), minor deviations in sample configuration (provided by rotating) lead to different regions of microstructure satisfying the Bragg condition. As grains move towards uniform orientations, the diffraction interval $\delta\omega$ over which some portion of the grain satisfies the Bragg condition is shortened. In the context of our aluminum experiment, this would result in Bragg peaks appearing in fewer $\delta\omega$ intervals.

Recovery in sample space is ideally suited for the voxel-by-voxel reconstructions accomplished with the forward modeling method. Since recovery amounts to the internal ordering of microstructure, sensitivity to *intra*-granular orientation changes is necessary. With each voxel's orientation assignment resulting from fitting many diffraction peaks appearing in many $\omega$ intervals, the resolved orientation is highly constrained. Monitoring how these assignments evolve with anneals serves as a method of quantifying the recovery signal in sample space. These voxels can then be used to generate simulated scattering onto the experimental detector images and permit data mining of the physical signal (Bragg peaks) during recovery.

We perform the analysis by first interpreting orientation variations as reconstructed in sample space through the three states, then use these assignments to monitor changes in detector space. Since the underlying feature of recovery is that it is a 'smoothing' of local orientations, we use two metrics to emphasize such changes. The first, kernel averaged misorientation or $KAM$ [66, 86], gives a measure of local orientation variations, while intra-granular misorientation or $IGM$ [86] is sensitive to larger length scale variations by measuring how regions of a grain deviate from the overall average.

### 3.4.2 Kernel Averaged Misorientation

$KAM$ tabulates the average misorientation between a voxel and its nearest neighbors. Since the in-plane spatial resolution (5.1 $\mu$m) is finer than that of the layer-to-layer spacing (20 $\mu$m), nearest neighbors are only considered in the measured plane. Additionally, since voxels adjacent to grain boundaries will produce artificially high $KAM$ values, we suppress $KAM$ voxels with $> 2^\circ$.

Figure 3.9 shows the spatial distribution of $KAM$, for the same layer of microstructure, through the three anneal states. Note that the gray scale is highly expanded. All voxels with sub-orientation resolution values ($KAM < 0.1^\circ$) are shown as white, while $0.5^\circ < KAM < 2^\circ$ are in gray scale. This gray scale allows identification of regions of relatively high disorder by noting the clustering of dark voxels in localized regions, as well as the observation of light regions with little short order disorder. In all three sample states, noisy regions as well as ordered one dimensional structures that correspond to low angle boundaries are observed. Some of these boundaries have ends that are disconnected from other boundary lines, implying a smooth orientation gradient around the end point. Many of these features can be correlated across the three anneal states of the sample, reinforcing the reliability of the reconstructions. One also finds regions in

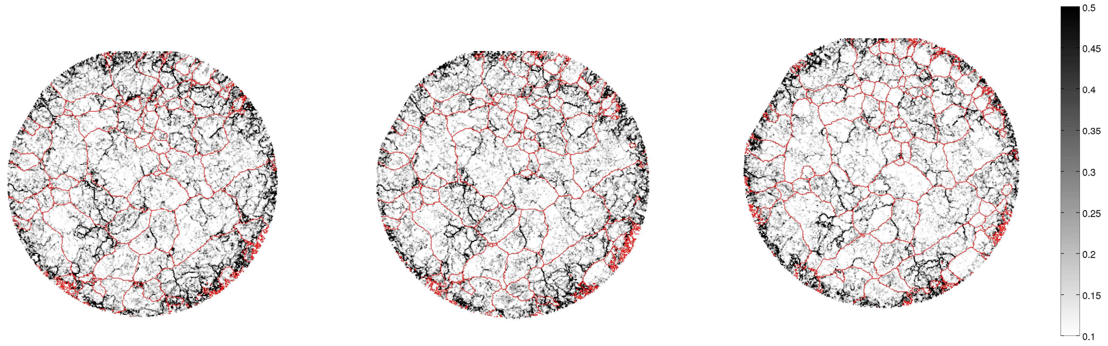

**Initial** **Anneal1** **Anneal2**

*Figure 3.9: Kernel Averaged Misorientation ($KAM$) maps of the same three layers of microstructure shown in Figure* 3.5*. The gray scale saturates at $KAM$ = 0.1° (white) and $KAM$ = 0.5° (black) degrees. All three maps use the same gray scale and have red lines outlining boundaries exceeding* 2°*.*

which ordered structure grows rather dramatically. The near-surface regions appear to be particularly active in this behavior, indicating the limitations of surface-based techniques in recovery focused experiments. We will investigate these further in Chapter 4.

While the $KAM$ maps in different anneal states are qualitatively similar, there is an overall lightening of the images as annealing progresses, implying decreased average $KAM$ within the sample. This is illustrated in Figure 3.10 as histograms obtained from the entire set of 11 measured layers in each state. The population in the sub-resolution ($< 0.1°$) bin grows significantly, while large $KAM$ values decrease in population. This growth of orientational order at short length scales is consistent with expected recovery behavior as noted earlier.

### 3.4.3 Tracked Microstructural Analysis

Figure 3.10 illustrates global changes over the entire microstructure, but does not make a one-to-one correlation through grain association. By connecting grains across states and monitoring their $KAM$ content, one can see if recovery is more dramatic in a specific set of grains with a certain orientation, or if the process is truly global and affecting all parts of the microstructure equally. Since $KAM$ can be used to quantify dislocation content, tracking the defective vs. non-defective grains over an annealing history can be used to identify growth patterns in the microstructure. We will return to this topic in Chapter 4.

Before characterizing grain evolution in the context of $KAM$ (and later $IGM$), we need to be explicit in defining our grains of interest. Analysis is restricted to grains which are present in all three sample states, which means grains must be correlated between

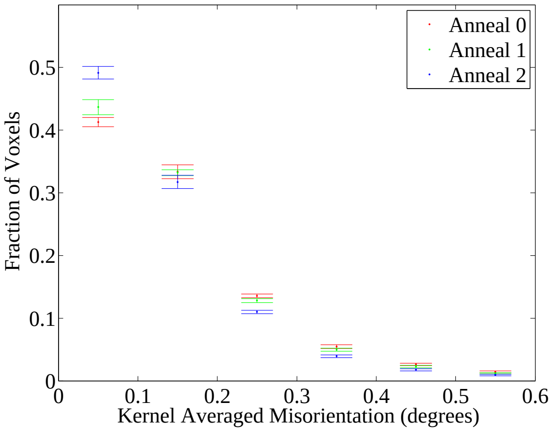

*Figure 3.10: KAM histograms for the three anneal states. Horizontal bin widths are* 0.1°*. Points are average values of histograms computed for each of the 11 layers and error bars are corresponding standard deviations.*

states. This is accomplished by minimizing both center of mass and verification that misorientation between the grain averaged orientations between states was less than a few degrees. A final visual inspection was performed since the system is manageablely coarse grained. Using these criteria, we track 117 'interior grains' in the measured microstructure. A restriction could be placed on forcing grains to be in 'interior' layers, meaning that the majority of the grain's voxels fall between layers $z_2$ - $z_{10}$. This would result in 60 tracked grains. Since the *KAM* analysis is focused on changes on the local scale, this restriction is not enforced.

A distribution of the volume of these tracked grains through the three states is shown in Figure 3.11. The data has been sorted by initial grain size. The grains associated with the initial state share the same ordinate axis value in the plot. A vertical red line serves to distinguish between 'large' and 'small' grains in the microstructure. The change in volume of the grains between the first and final anneal states are quite dramatic for the smaller grains, while larger grains tend to be rather static on a percentage of initial volume perspective. Grain growth and shrinkage can easily be identified in this plot as well.

The evolution of local disorder with annealing can be quantified with average *KAM*. Tabulated for each grain, average *KAM* is simply the arithmetic mean of the *KAM* of all voxels in a grain. For all anneal states, the average *KAM* per grain falls in a range between 0.04° and 0.24°. While there exists no strong correlation between average *KAM* and grain size, there is a correlation between anneal state and average *KAM*. The histogram in Figure 3.12 bins average *KAM* for the three states. The peak of the distribution remains at approximately the same average *KAM* value for all three states, though the final anneal distribution shifted towards a lower average *KAM*. It is the spread of the distribution that is most interesting. For the first two states, there

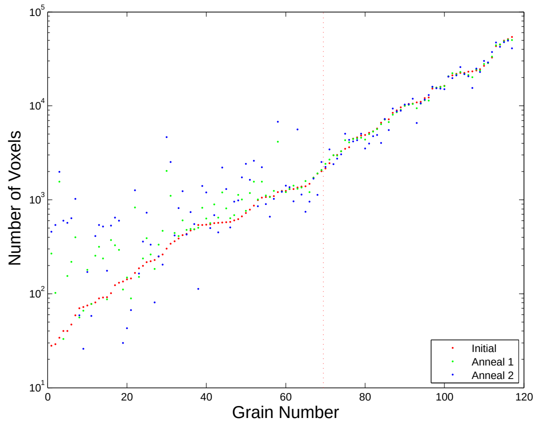

*Figure 3.11: Grain size distribution for tracked grains. Plot has sorted grains by their volume in the initial state. The first and second anneal state corresponding to this grain have the same value on the ordinate axis. The vertical red line shows the demarcation between 'small' and 'large' grains in the microstructure, based upon size variations through anneals.*

is a sizeable population high average $KAM$ grains, while in the final anneal state the distribution has a large population with average $KAM \leq 0.1°$.

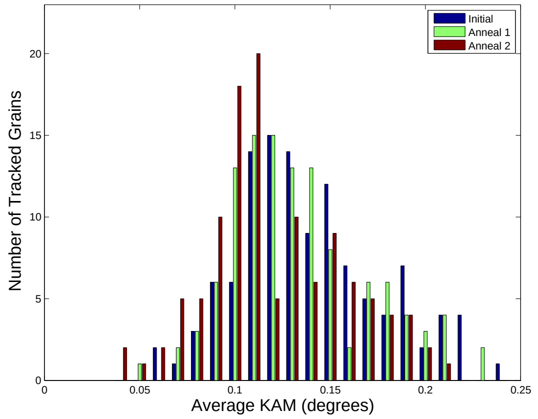

*Figure 3.12: Tracked grains histogrammed by average $KAM$ through the three anneal states.*

The distribution of average grain $KAM$ has been tracked, but recovery is associated with changes in $KAM$ as thermal energy is added to the system. With grains correlated between anneal states, *changes* in $KAM$ can be monitored. Figure 3.13 illustrates the relationship between changes in grain size with changes in grain averaged $KAM$. In general, the plot shows that most grains have decreased in grain averaged $KAM$ as the sample was annealed, while change in size has been equally distributed between growth and shrinkage. Specifically, Table 3.1 illustrates the number by quadrants.

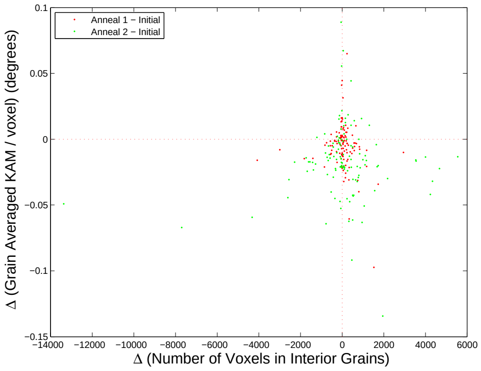

*Figure 3.13: Changes in grain averaged $KAM$ in comparison to growth/shrinkage of the grain size through anneals. This is a differential change plot of what was shown in Figure* 3.12*. Table* 3.1 *shows the distribution of points by quadrant. Red dots illustrate changes from the initial to the first anneal, while green dots move are differences between the first and final anneal averages.*

*Table 3.1: Distribution of Changes in Grain Averaged $KAM$ and Grain Size*

| | $\Delta N_{vox} < 0$ | $\Delta N_{vox} \geq 0$ |
|---|---|---|
| $\Delta KAM \geq 0$ | 18 \| 10 | 19 \| 11 |
| $\Delta KAM < 0$ | 31 \| 44 | 49 \| 52 |

*Table 3.1: Red numbers are associated with red dots in Figure* 3.13*, which are changes after the first anneal. Green are from the initial state to final anneal.*

Lastly, a histogram analogous to Figures 3.12 is shown in Figure 3.14. The distribution of $KAM$ changes is displayed in comparison to the initial anneal state. Effectively, this is a histogram that integrates over the horizontal axis of Figure 3.13. The plot clearly demonstrates a shift towards smaller average $KAM$ for grains in the microstructure.

Local variations in orientation have been quantified with the average $KAM$ for grains tracked through all three sample states. The observation echoes what was qualitatively displayed in Figure 3.9, the average $KAM$ in each grain decreases with anneal state. This process suggests a local ordering of microstructure, which can be associated with the recovery process in a polcrystal.

### 3.4.4 Global Microstructural Changes

$KAM$ is a useful metric for showing how microstructures evolve on highly localized length scales, since its tabulation is based on using only a few spatially connected voxels. Therefore, sensitivity to other microstructural features, such as orientation gradients, are un-noticable. This can be illustrated by imagining a grain with a perfect orientation

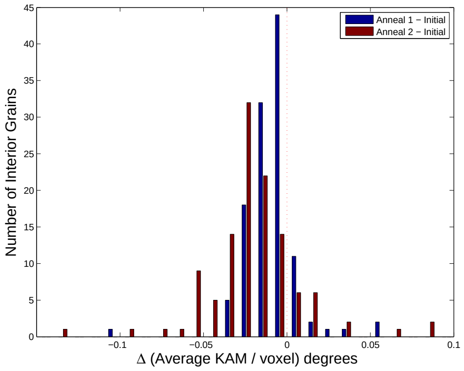

*Figure 3.14: Changes in grain averaged KAM for tracked grains through anneals. Blue shows the distribution of KAM after the first annealing, while red shows the results of the second anneal. The histogram is similar to* 3.12*, except now we show a one-to-one evolution.*

gradient, as could be seen in a bent crystal. Tabulating the *KAM* would result in a roughly constant *KAM*, which depending upon the magnitude of the gradient, results in a roughly constant *KAM* value. While finding grains with a finite and relatively constant *KAM* that is uniformly distributed throughout the volume could be used to identify orientation gradients, it is also possible that you just have a grain with uniform dislocation density producing random noise about a single uniform orientation. Instead, gradients can be identified by calculating a grain averaged orientation for all voxels composing the grain and then tabulating the misorientation between each voxel and this average orientation. We call this quantity the intra-granular misorientation or *IGM*. Subsequently, the *IGM* provides a means of determining longer range order for a grain and serves as an alternative to *KAM*, which is better for identifying short range effects. This calculation is dependent upon the definition of a 'grain'. The presented analysis defines grains with a 2° misorientation threshold, but smaller thresholds would define smaller regions with a smaller IGM.

### Grain Definition

Unlike the calculation of *KAM*, which is done with no underlying assumptions about a granular structure; the calculation of *IGM* requires a grouping of voxels that are both simply connected (in two or three dimensions) and of similar orientations to define a grain. Since most of the grains in this data set are measured in most, if not all layers, the question arises as to how to define an average orientation. Grains can be interpreted as a collection of voxels in 2D or extended to 3D via multiple layers. To address this issue, we take all grains, defined as containing at least 25 (connected) voxels and with a $\geq 2^\circ$ misorientation border and compare their average orientation as tabulated in-plane and as a volume. These quantities are plotted in the misorientation fundamental zone, as represented in Rodrigues-Frank space and shown in Figure 3.15. Colors have been used to represent the different layers in the microstructure. It is evident that no significant misorientation trend exists, suggesting that the analysis using grains as collection of voxels from multiple layers will suffice. If an overall rotation between layers was present, misorientations would cluster in some region of the fundamental zone that is separate from the origin. Specifically, dots of the same color in Figure 3.15 would be spatially compact and not the random distribution that is observed.

Additionally, Figure 3.16 shows the size distribution of grains in terms of the $log_{10}$ of the number of voxels composing the grain. This is used to illustrate the possibility of large misorientation spreads due to low statistics. It appears that the voxels that are furthest from the origin of the misorientation fundamental zone are still significant in size, containing thousands of voxels.

Figure 3.17 shows the distribution of misorientation angles between each layer's grain averaged orientation and the volume averaged orientation, through the three anneal states. This amounts to taking the one dimensional parameterization of the content in Figure 3.15. We have only included multi-layer grains in this histogram, since grains that exist in only a single layer would artificially inflate the contents of the 0° bin. Once again, no systematic shift in orientation between layers is observed.

Figure also 3.17 shows that the 0° bin becomes more populated with anneal, but this layer-volume analysis has not linked grains across states and has only attributed grains to voxels of similar in-plane coordinates and orientations across intra-state layers. Therefore, the number of grains (using the previous definition) is variable between states and, in fact, increases with anneal. This observation will be addressed in Chapter 4. Still, despite the lack of cross-state correlation for this presentation, there appears to be a strengthing of uniformity in orientation on a larger, granular scale.

### Intra-granular Misorientation

We have motivated the ability to analyze grains on a volumetric basis, which requires no further processing between reconstructed layers. Hence, calculating the *IGM* with voxels over multiple layers, within a given grain and state, is justified. Figure 3.18 displays the 'global' *IGM* distribution, which is analogous to the *KAM* presentation in Figure 3.10. The main difference is that correlation across layers has been performed, which was not used with the *KAM* due to the large distances between layers and the short range kernel used in the calculation.

The figure shows the *IGM* for all voxels which have been associated with 3D grains and how the distribution evolves with successive thermal treatments. Only voxels which exceed 0.25 confidence and occur in a spatially compact cluster with similar orientation (2°) were included. Further, only voxels within a defined radial center from the microstructure, determined by using voxel confidences, were used. This was also done for the *KAM* measurements. For each layer, a center is determined by averaging the $(x, y)$ coordinates of every voxel exceeding 0.5 confidence. A radius is then calculated by finding the maximum distance between this origin and an in-plane voxel $\geq 0.5$ confidence.

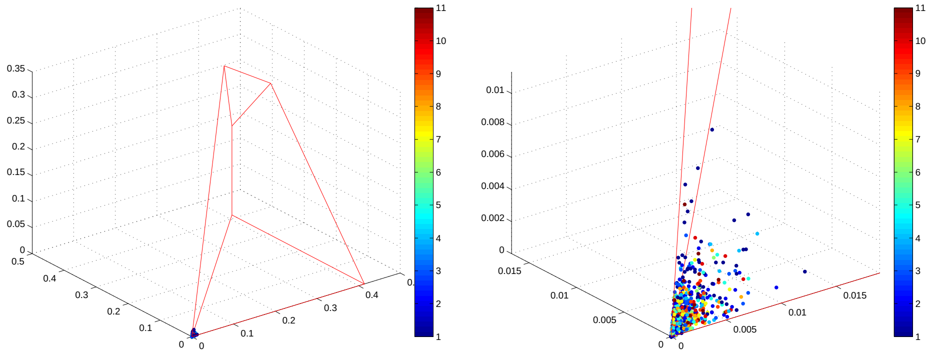

**Initial** **Initial**

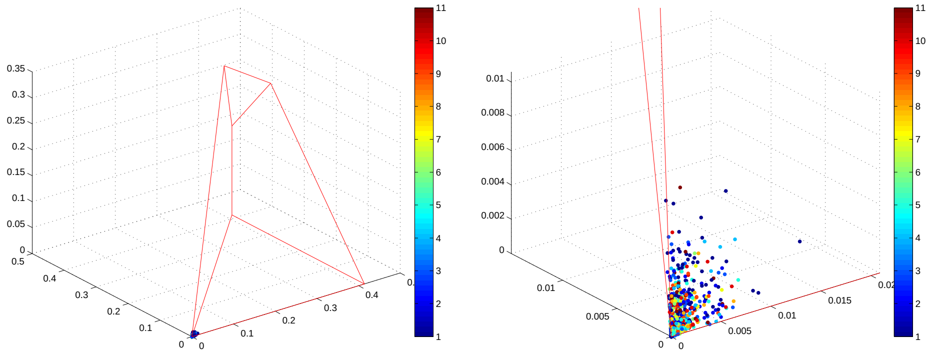

**Anneal 1** **Anneal 1**

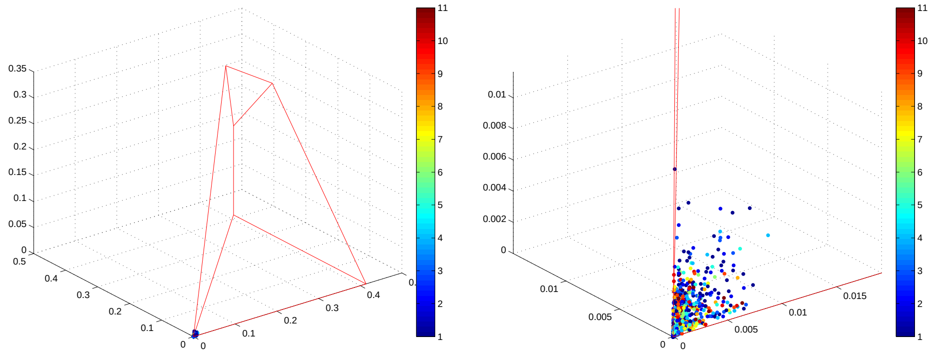

**Anneal 2** **Anneal 2**

*Figure 3.15: Rodrigues-Frank representation of misorientation between layer and volume for grains in the three sample states. Colors correspond to layers. Plots on the right display the (0,0,0) corner of the misorientation fundamental zone on an exaggerated length scale.*

All voxels that are associated with a grain and have a confidence exceeding 0.2 are used to populate the histogram.

Just like *KAM* the shift towards lower *IGM* values indicates an ordering that can be associated with recovery. But now, instead of highly localized changes (on the order

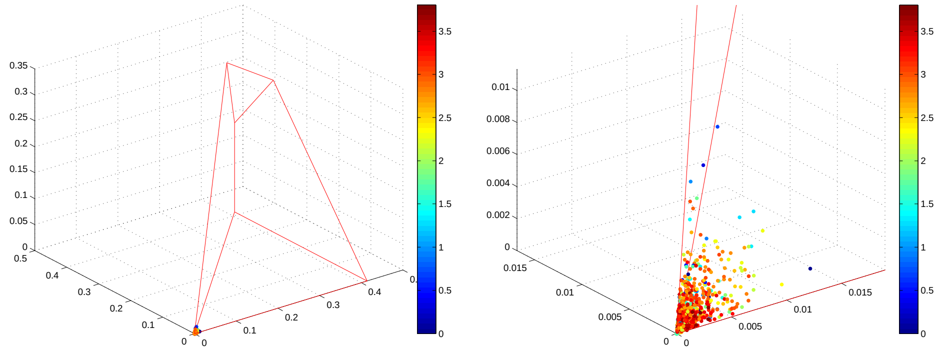

**Initial** **Initial**

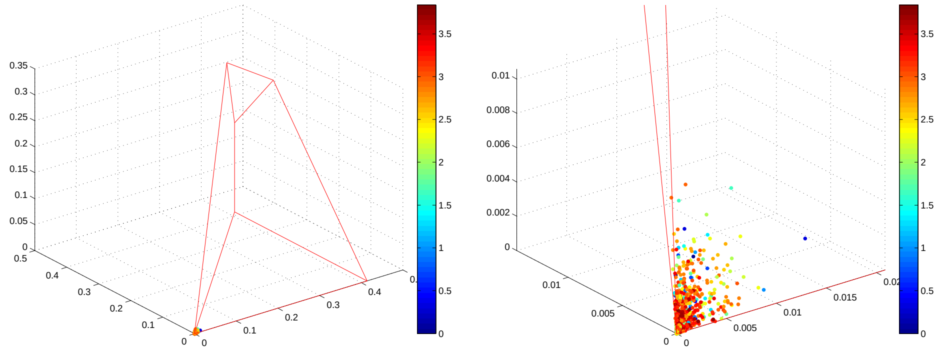

**Anneal 1** **Anneal 1**

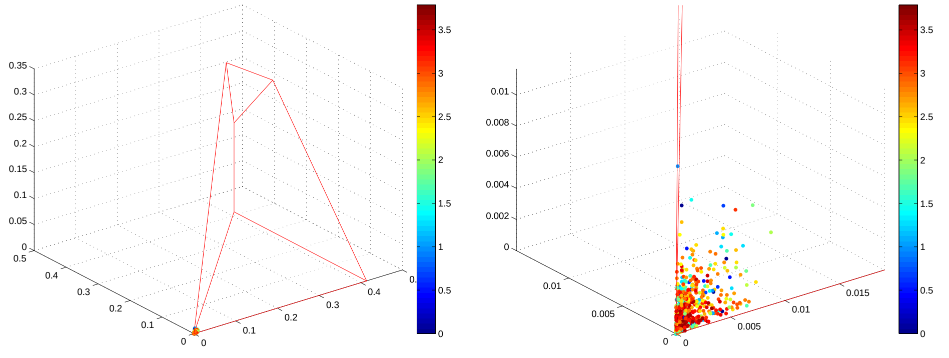

**Anneal 2** **Anneal 2**

*Figure 3.16: Rodrigues-Frank representation of misorientation between layer and volume for grains in the three sample states. Colors correspond to* $\log_{10}$ *of the number of voxels in a given 2D layer. Plots on the right display the (0,0,0) corner of the misorientation fundamental zone on an exaggerated length scale.*

of $\sim$ 10 $\mu$m), long range ($\sim$ 100s $\mu$m) ordering is observed. Grains, as a whole, are beginning to shift towards a more uniform orientation.

While simple monitoring of a global evolution of *IGM* on the full microstructure

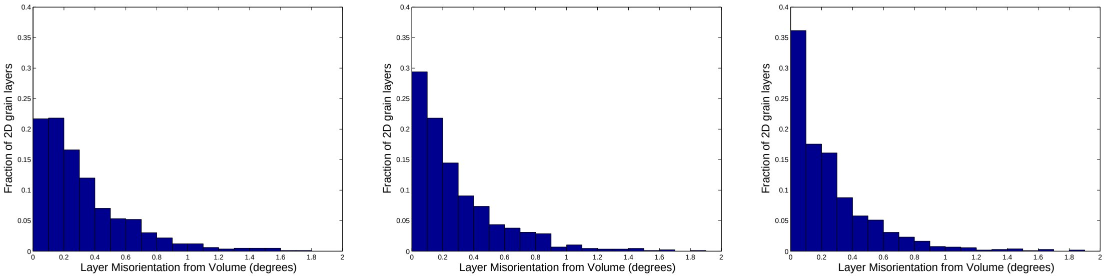

**Initial** **Anneal 1** **Anneal 2**

*Figure 3.17: Histograms of misorientation angle between volume averaged grain orientation and layer averaged grain orientation. Only grains that have cross-sections appearing in multiple layers are shown in this graph. Further, only grains containing at least 25 voxels are used in this histogramming.*

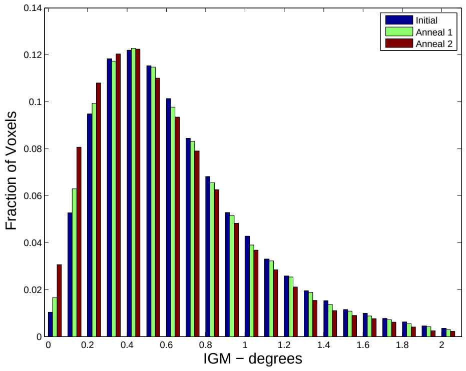

*Figure 3.18: Histogram of the distribution of IGM across the three sample states. The vertical axis is the fraction of voxels which are associated with grains and exceed 0.2 confidence in their orientation assignment.*

provides evidence for recovery, tracking the evolution on a granular basis can lead to a more localized understanding of how recovery takes place. Do all grains become more ordered or a select group of grains? How is the ordering spatially distributed within grains? Do the interiors of grains turn more ordered and in coherence with the grain's average orientation or is the ordering done independent of location, leading to a subgrain structure with low angle boundaries? Just like with the $KAM$, changes in the $IGM$ can be monitored for the same grain as a function of anneal.

Our grain based analysis of the $IGM$ begins with average $IGM$ for each grain. This is calculated by using all voxels with confidence $\geq 0.2$ to generate a grain averaged orientation, then measuring the misorientation between these voxels and that average. Each grain is assigned the average $IGM$ of its constituent voxels. The histogram in 3.19 shows the distribution of grains with respect to $IGM$. A grain must contain at least 10 voxels that exceed the 0.2 confidence criteria for use in this histogram. Consequently, grains that are very small or of indeterminant orientation are not processed. Further, the histogram shows fraction and not number of grains on the vertical axis. The number of grains within the microstructure is not constant, as grains can enter our measurement volume, grow or shrink to the 25 voxel threshold and therefore go uncounted. In many ways, the plot from Figure 3.18 contains the same information as Figure 3.19, except the way we classify our voxels has changed.

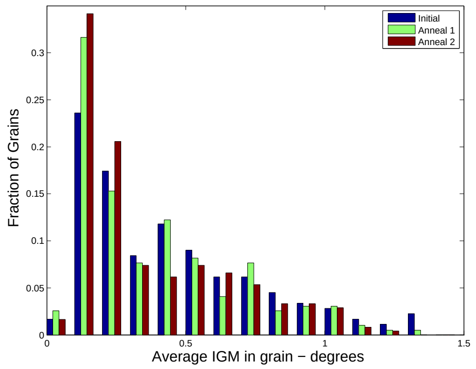

*Figure 3.19: Histogram of the distribution of IGM across the three sample states. The vertical axis is the fraction of voxels which are associated with grains and exceed 0.2 confidence in their orientation assignment.*

A one-to-one association of grains across states is shown in Figure 3.20, which histograms the change in *IGM* for a given grain. The majority of grains remain static in their overall *IGM* disorder, as evidenced by the peak at 0° for both distributions. The distribution broadens after the second anneal and the peak shifts slightly towards a decrease in *IGM* for grains, though the tails become pronounced as both increases and decreases in *IGM* are shown.

Thus far, the *IGM* has only been addressed as a global distribution, or confined to average *IGM* valus for single grains. While this is instructive in determining overall changes in the microstructure, orientation maps can be searched for spatial ordering in a manner similar to the *KAM* maps that were presented in Figure 3.9. This takes full advantage of nfHEDM measurements reconstructed with forward modeling: the orientation evolution of bulk grains after external stimulation. In Figure 3.9, we colored each voxel on a gray scale according to its *KAM* value. The same process is performed for *IGM* quantities. But unlike the local *KAM*, misorientations are taken with respect to a singular, average orientation over large spatial regions. Therefore, providing the full axis and angle information for *IGM* is possible. The maps shown in Figure 3.21 are *IGM* maps in the crystal frame. Boundary outlines show the same 2° boundaries that have been used to outline grains in earlier maps. These maps are similar to orientation maps, but are now colored by misorientation from a grain average orientation.

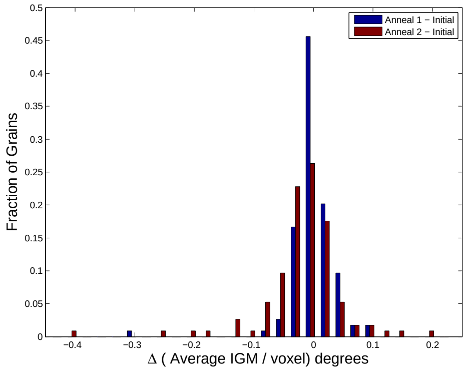

*Figure 3.20: Histogram of the distribution of the change in IGM across the three sample states. A total of 114 grains are tracked in this figure. Binning is done in 0.025° increments.*

While definitely rich in content, the *IGM* maps allow for the identification of both the existence and ordering of sub-grains, within a given grain. These can be identified as spatially localized regions of similar color. And while appearing random for some grains, their physicality can be verified by observing the existence of the sub-structure when looking at succesive layers and successive states of the same grain. This amounts to seeing the same colors occuring in the same in-plane position at multiple sample layers and in multiple sample states. We focus on two grains. Figure 3.22 shows each triangle converted into a single point, which is then colored by the full *IGM* quantity, the same as used in Figure 3.21. Just like compact regions of similar color in orientation maps suggest regions of similar orientation, regions of compact color in Figure 3.22 suggest microstructure that is similarly misoriented from the grain's average orientation. The clustering of these *IGM* colors can be interpreted as organized variation from a single average orientation, where distinct colors denote slight deviations from the average orientation.

Figure 3.22 shows the organization of subgrains within a larger collection of similar orientations, which we term a grain. While the subgrains are easily identified on both maps, there appears to be minimal evolutionary dynamics amongst the subgrains. To illustrate how annealing can result in subgrain evolution, Figure 3.23 shows a different grain from the microstructure. This 3D grain illustrates the physicality of the reconstruction by showing that features exist both through anneals and between layers.

The evolution that is most dramatic occurs in the top layer of the microstructure and is shown in Figure 3.24. Here, several metrics to illustrate that sub-grain evolution is present and evolving. Each row denotes a different anneal, with the initial state and final state as the top and bottom rows, respectively. The left column shows the 3-parameter *IGM*, all plotted on the same color scale. The area of particular interest is the yellow region in the bottom left that becomes more dominant in both order and size with anneal. The second column shows *IGM* as plotted by misorientation angle. Once

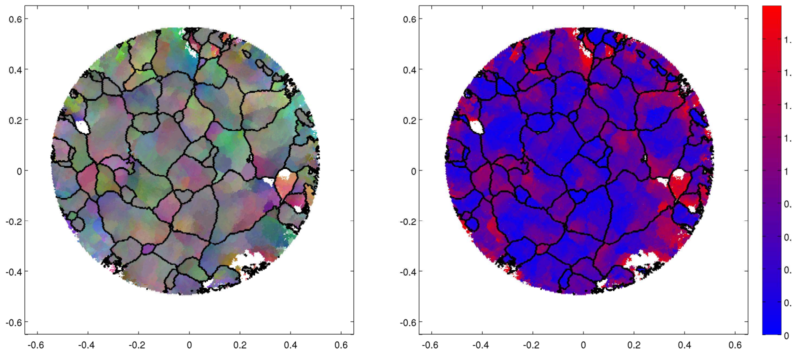

**Initial** **Initial**

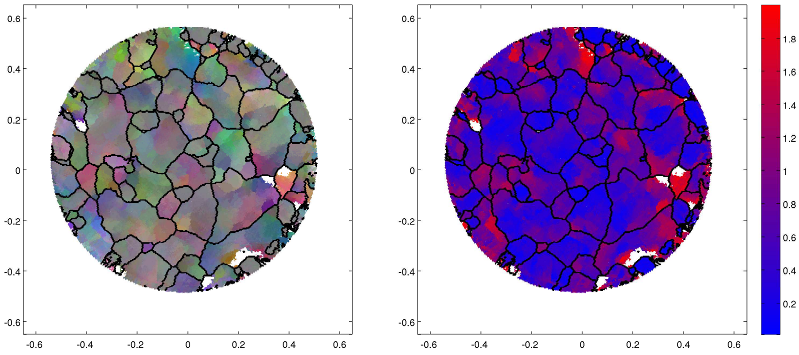

**Anneal 1** **Anneal 1**

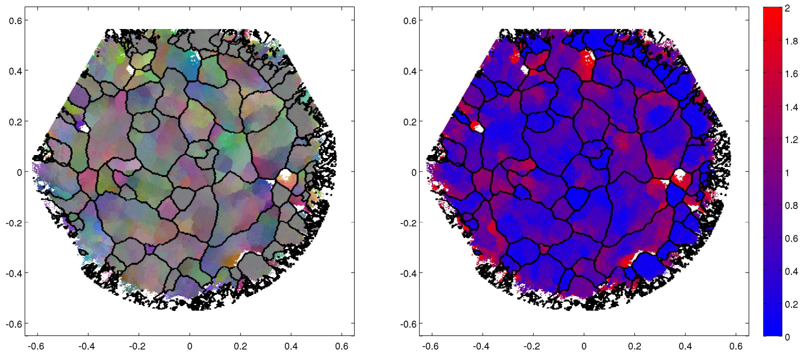

**Anneal 2** **Anneal 2**

*Figure 3.21: IGM maps of the top ($z_1$) layer of microstructure. Each row denotes a different sample state, while the left column shows voxels colored by the full 3-parameter IGM, where the grain averaged orientation is determined by averaging all voxels within a 3D grain (defined by the 2° boundary). Coloring is done by misorientation from this averaged orientation. The right column shows voxels colored by the 1-parameter IGM rotation angle (in degrees) from the averaged orientation. White regions in both maps indicate voxels that exceed 2° in IGM.*

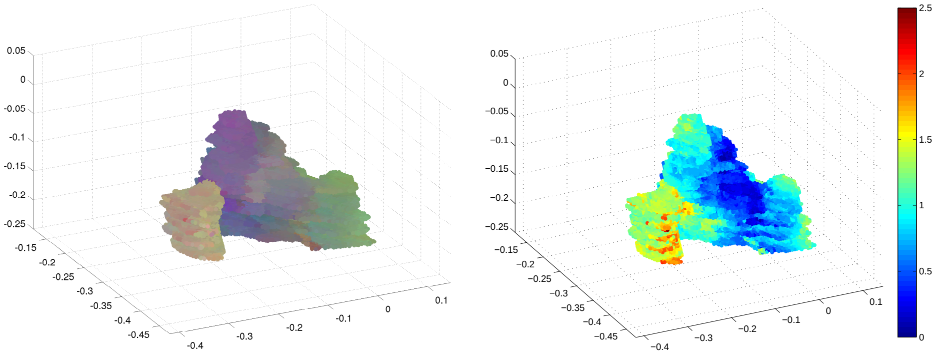

**Initial** **Initial**

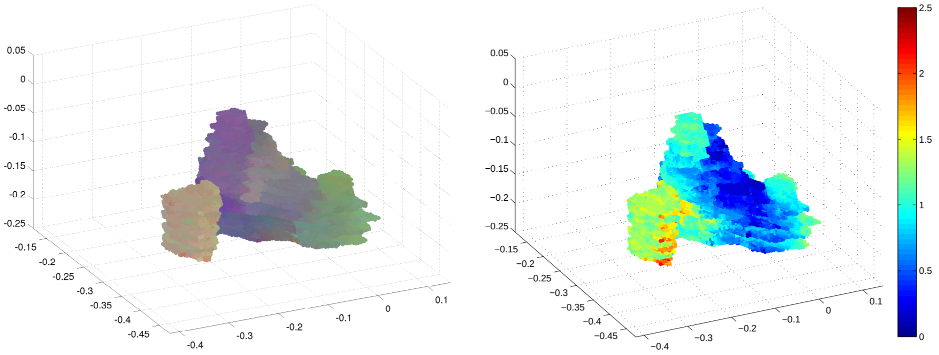

**Anneal 1** **Anneal 1**

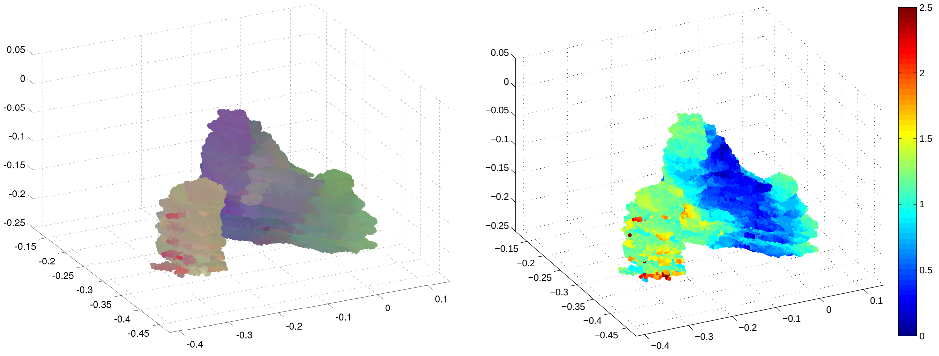

**Anneal 2** **Anneal 2**

*Figure 3.22: IGM maps for single grain in microstructure in the three anneal states. Left column shows voxels colored by the full 3-parameter IGM, while the right column shows the IGM angle in degrees. The figures show that within a given state, colors (and therefore misorientations from average orientation) are consistent between layers and are spatially localized. Further, that the same colors show up between states indicates that there is a physicality to this substructure within the grain and suggests the existence of subgrains with the microstructure.*

again, the region that is yellow also has a high *IGM* with respect to the grain average orientation. The third column plots the confidence metric that has been discussed earlier. The yellow region from the first column corresponds to a region that gets progressively more red with each anneal step. This suggests ordering, which would be evidenced by its diffraction signal producing intensity above background in the nfHEDM measurement. Lastly, the final column illustrates how local, in-plane disorder evolves in each anneal step in the form of a *KAM* map. The most interesting aspect of this is the black ring that confines the yellow region, which one would expect with a sub-grain. There is very high orientational order within the subgrain, but since it borders a parent lattice, with which it is misoriented, a high *KAM* border is formed. Emphasis should be placed on the color scale used to plot the *KAM*. Previous plots, like Figure 3.9 went from 0 to 0.5°, while this plot ranges from 0 to 0.4°.

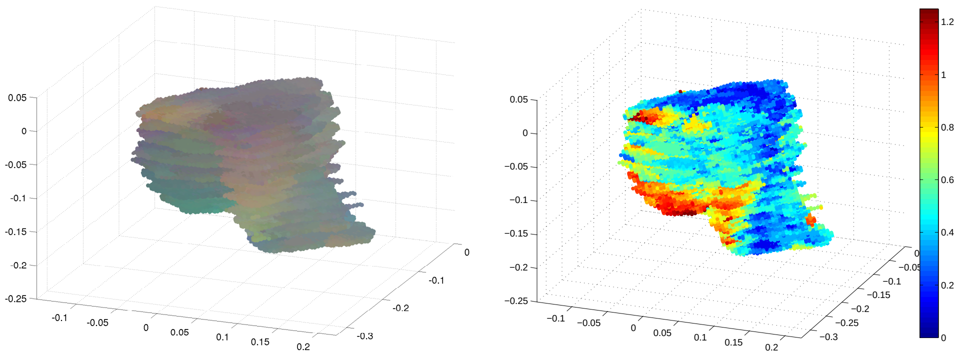

**Initial** **Initial**

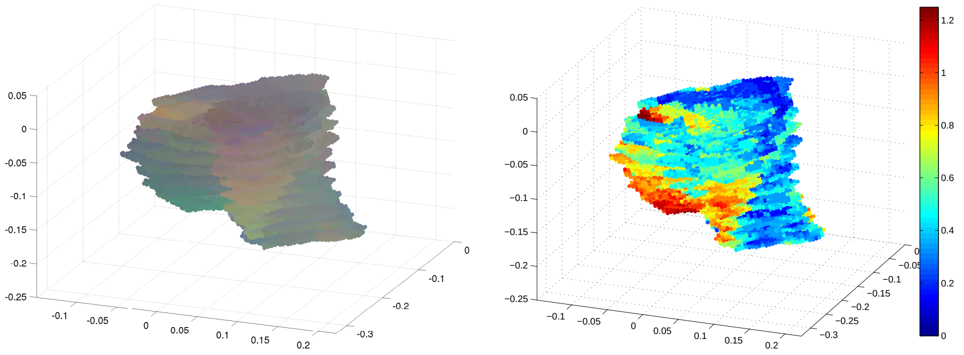

**Anneal 1** **Anneal 1**

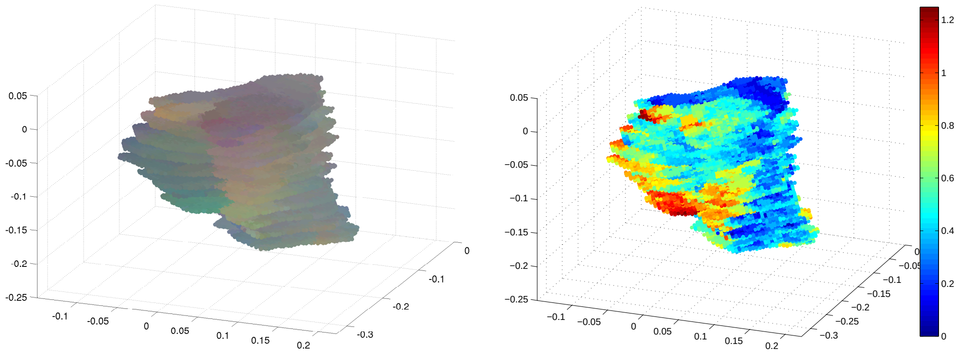

**Anneal 2** **Anneal 2**

*Figure 3.23: IGM plot like Figure 3.22, except for the focus grain of the following analysis. The plots are used to emphasize the layer-to-layer consistency in measurement as well as the repeatability of the underlying structure through anneal states.*

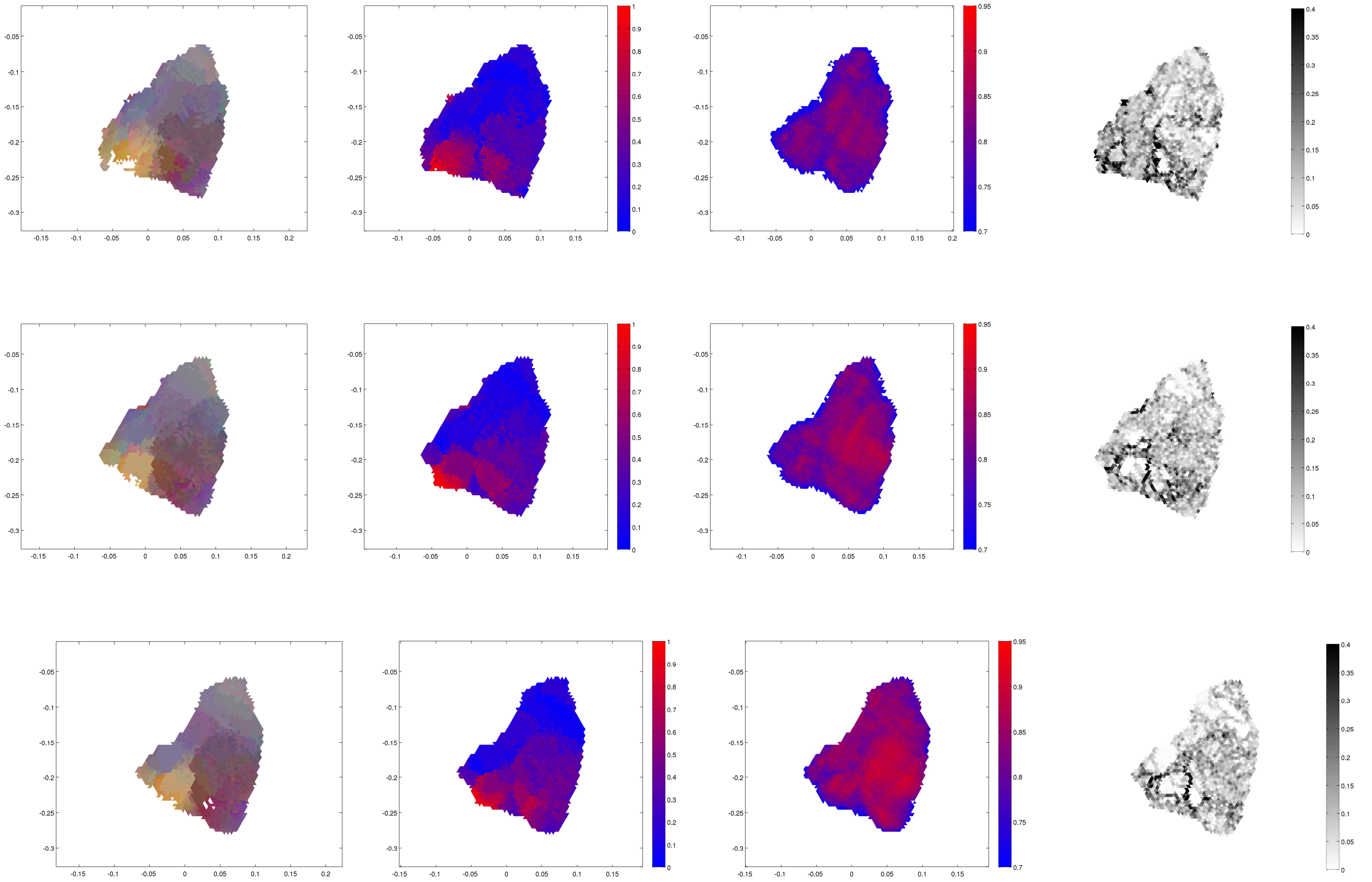

***IGM*** **IGM angle** **Confidence** ***KAM***

*Figure 3.24: Evolutionary description of the grain shown in Figure 3.23. The portion of the grain that is in the top layer ($z_1$) of microstructure is shown. The initial anneal state is shown in the top row, while the first and second anneals are rows 2 and 3, respectively. The left most column is an IGM map, showing the presence of sub-grains within the microstructure, which become more ordered after each anneal step. The second column is IGM parameterized by misorientation angle from the local, 3D lattice. The third column plots confidence, while the final column illustrates KAM.*

### 3.4.5 Recovery - Detector Space

The underlying theme of the previous section was the interpretation of microstructure maps in the context of recovery. This was illustrated in a sharpening of the local distribution of orientations, through the calculation of the short range, kernel averaged misorientation and on a larger length scale with the ordering of sub-grains that compose the larger, single color grains seen in the orientation maps of Figure 3.5. All of these processes amount to the reduction in defect content of grains as dislocations are 'annealed out' and migrate towards high angle boundaries, leaving more perfect local lattices.

The source of these orientation smoothing signals seen in sample space are changes in the properties of diffraction spots measured in each of the three states. Evidently, the peaks that are the signal for changes in the microstructure are undergoing an evolution that produces changes in both the shapes, sizes and orientations of grains. This section will address changes in the distribution of peaks in detector space by using the orientation maps to data mine what is happening on a spot-by-spot basis. As the confidence maps suggest, each voxel is the result of fitting $\sim$35 distinct peaks, so there must be a collaborative change in the majority of these signals to lead to the changes found in the previous sections.

As previously suggested, the process of recovery alludes to the removal of imperfections within a crystal lattice. If the process was permitted to continue *ad infinitum*, we would end up with a collection of grains that have every atom located at its theoretical position in the lattice. When such a crystal is configured so that a set of atomic planes satisfy the Bragg condition and are measurable on an area detector, one would expect the follow properties to be true of the signal:

- The intensity across the diffraction spot is smooth and uniform.
- The area of the spot is minimal for both the grain geometry and projection geometry producing the diffraction.
- The width of the peak is minimized in the $\omega$ dimension and approaches a $\delta$-function as the energy of the beam approaches true monochromicity.

Each of these instances result from the uniformity of $\boldsymbol{k_f}$, the diffracted beam emanating from the voxel. Once recovery has completed, we have a spatially significant collection of voxels in sample space that are of a single orientation and therefore have all their $\boldsymbol{G_i}$ vectors parallel. This results in a parallel collection of $\boldsymbol{k_f}$. Therefore, when these diffracted beams intersect a camera, the properties itemized will be present. Since each voxel in the recovered grain has the same orientation, the imaged diffracted peak will be as uniform in intensity as possible, given the diffraction geometry [87]. This leads to smooth distributions when diffraction is imaged on a 2D area detector. Further, the parallel direction of the diffracted beams mean that the areal coverage of the diffraction spot is entirely the result of the in-plane grain geometry and the resulting direction and magnitude of the parallel $\boldsymbol{G_i}$ vectors. Lastly, the minimization of the peak width in $\omega$ is the result of the uniform orientations only satisfying the Bragg condition for a specific configuration, dependent upon the bandwidth of the operating x-ray energy.

While the list above assumes the most ideal case of perfectly recovered grains, all of which are composed of single orientations, the reality is that our grains still have dislocation content, as can be seen the *KAM* maps produced in Figure 3.9. Specifically, we do not have voxels of single orientation within a grain, producing a parallel set of outgoing diffraction vectors. Instead, we have spatially localized voxels assigned orientations that become more tightly distributed around a single orientation as annealing progresses. This results in more parallel diffraction beams, which should produce diffraction signals that approach the ideal observations itemized above. One would expect for a grain that has undergone resolvable recovery to have intensity patterns that are smoother in later anneal states than in the initial states. For grains that have maintained an approximately constant shape in the measured plane of microstructure, one would expect the coverage of spots on the area detector to get statistically smaller, though the $\sim 4\mu$m pixels might make this observation difficult. Lastly, the partioning of $\omega$ space into 1° bins during data acquisition should result in peaks being observed in fewer consecutive images, if the move towards uniform orientation is physical. We explore these three detector space signals using a selection of grains from within the microstructure.

We begin the analysis of detector space by analyzing the general distribution of spots without correlation with both the microstructure, or states yet applied. While correlation in a one-to-one manner between peaks will be done in later analysis, looking at the size of peaks in the $\delta\omega$ partition can lend validity to the peak narrowing assumption. Figure 3.25 shows the width of peaks in each state. Peaks occuring from the same 3D grain, but in separate layers are classified as separate peaks. While the distribution appears to have possibly shifted to a broader peak width from the first two states to the final state, the population in the large $\delta\omega$ bins in the $7° - 18°$ widths seem to have decreased from the initial to final state. While the peak of the distribution appears to have shifted towards larger $\delta\omega$s, this can be deceiving in that we have made no correlation between the two microstructures and each peak is interpreted as an independent entity with no association betwen layers, among states or with the microstructure. Once peaks are correlated in these domains, interpreting the changes in the diffracted peak can be qualified.

It should be noted that this characterization of $\omega$ peak width is a preliminary characterization based an invalid assumption that peak widths in $\omega$ are equal for all reflections. In reality, there are variations in $\omega$ peak widths for different diffraction peaks emanating from the same grain. Specifically, the width in $\omega$ is influenced by the $\eta$ position of the peak on the detector [87]. This analysis does not make any correction for this effect. Instead, the analysis is based upon an assumption that by averaging over many peaks from a given grain, shifts in $\omega$ peak widths for different reflections should be comparable.

Aside from the generation of a background image, which is the statistical intensity across a single detector position of each pixel in the diffraction experiment, each peak is

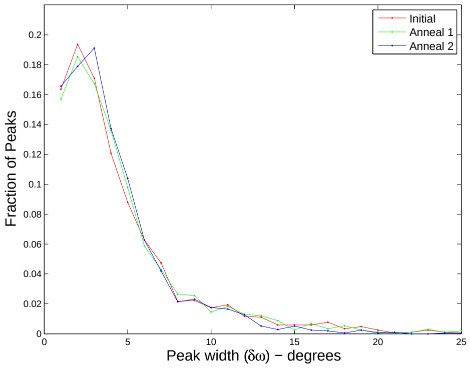

*Figure 3.25: Histogram of peak widths for the three states of the aluminum sample. Peaks from all 11 layers in each of the three states are listed. Width of peaks are determined by counting the number of distinct $\delta\omega$ intervals for a given diffraction spot. A peak is present in a $\delta\omega$ interval if the reduction program retains a pixel that belongs to a peak.*

determined independent of its neighbors in $\omega$ space. To get the full peak size in detector space ($(j,k)$,$\delta\omega$), we stack all images in a single, 50° $\omega$ wedge and look at connectivity across $\omega$. We look at the two wedges seperately, since the partitioning of $\omega$-space was not contiguous.

The possibility exists for the existence of a collection of small peaks that are connected by single pixels that would result in the assignment of a single peak ID. To avoid this connectivity problem, we erode each image (in a single $\delta\omega$ with a 3×1 and 1×3 window), which assigns zero to all illuminated pixels that do not have left-right, or top-bottom neighbors that are also illuminated. This effectively breaks any weak connectivity between a grouping of several peaks within a single $\delta\omega$ interval. Further, the possibility of having blatantly separate peaks weakly overlapping between adjacent $\delta\omega$ intervals should be minimized. The new collection of (eroded) peaks are then stacked into the 1024×1024×50 detector image and 3D peaks ($(j,k)$,$\delta\omega$) are identified through simple connectivity (pixels touch in at least one direction). This is how the peaks in Figure 3.25 have been determined. Peaks from all 11 layers are included in each anneal state.

We next use the reconstructed microstructure maps to gain insight into the sample space origins of each of these peaks. Our first requirement is to minimize changes in spots due to in-plane area changes that occur as a result of high angle grain boundary motion. For a given grain cross-section, we restrict the change in grain size as measured in voxels, to be between $95 - 105\%$ of the initial state grain size. Our second requirement is that the grain does not touch a free surface in any of the sample states, which amounts to a grain touching the surface of the cylinder. These restrictions result in 18 distinct grains and 57 different cross-sections, with each tracked through all three states. Using the IceNine forward modeling capabilities to simulate scattering from these sample regions onto the reduced detector images, we can associate points in sample space with their diffraction signal in detector space. With the 3D correlation in detector space, we can see how peaks change in $\omega$-space by searching for overlap among the simulated peaks and experimental peaks.

By finding peaks that overlap the simulated diffraction originating from these 18 grains and noting how the $\delta\omega$ peak width changes as we anneal, we get the the plots seen in Figure 3.26. These correlate peaks among states display how their widths in $\delta\omega$ space varies with anneal. All 11 layers are included in this plot, but the organization of the peaks vary, where Figure 3.26(a) simply histograms changes in adjacent peak widths in a single plot, (b) splits the contents of (a) into distribution changes during the first, then second anneal. Lastly, the plot in (c) shows differences in peak size when compared to the initial microstructure state. A general trend towards smaller $\delta\omega$ peak widths are seen in all three histograms, which would be consistent with the recovery assumption of narrowing peaks in the $\delta\omega$ partition.

Further emphasizing the changes in peak width distribution, Figure 3.27 illustrates the contents in Figure 3.26 (c), only colored by what happened with the $KAM$ distribution for the grain cross-section that was producing the observed diffraction peak. The histogram is stacked, with blue and cyan representing the change in peak width after the first anneal, while red and magenta are for changes between the first and final states. Blue and red histogram bars show changes in peaks that originate from grain cross sections that did not have their average $KAM$ per voxel decreases with each successive anneal, while the cyan and magenta peaks are from grains that average $KAM$ per voxel decreased after each anneal.

While changes in $\delta\omega$ interval width appears to be the most dramatic of the detector space changes associated with recovery, there are other diffraction signals which are associated with the ordering of the grains towards a more uniform orientation. In addition to $\omega$ tails shortening in detector space, the areal coverage of a peak on a single detector image should also be subject to changes. Viewing a grain as a composition of small volumetric elements, as is achieved with the tesselation in forward modeling, leads to having a single scattering vector for each unit. If the orientations of the grain become more uniform, these individual scattering vectors should become more parallel and therefore cover a smaller area on the camera. Hence, if one has a camera of sufficently high resolution, changes such as these should be observed, provided the diffracting grain remains constant in cross-section.

We first explore this behavior using the forward simulating abilities of IceNine and a representative grain from the aluminum microstructure. This is a grain from the initial state which exhibits a decrease in $KAM$ after each anneal. This grain has been used to produce simulated diffraction, which is shown in Figure 3.28. The image on the left is the simulated diffraction from the actual reconstruction, where variations in orientations are present within the grain, while the right plot shows the result of assigning each voxel the grain averaged orientation. The grain producing the diffraction for these images has 2607 voxels, so the left plot has 2607 unique orientations generating diffraction, while the right plot contains a single orientation spread across all 2607 voxels. The most dramatic

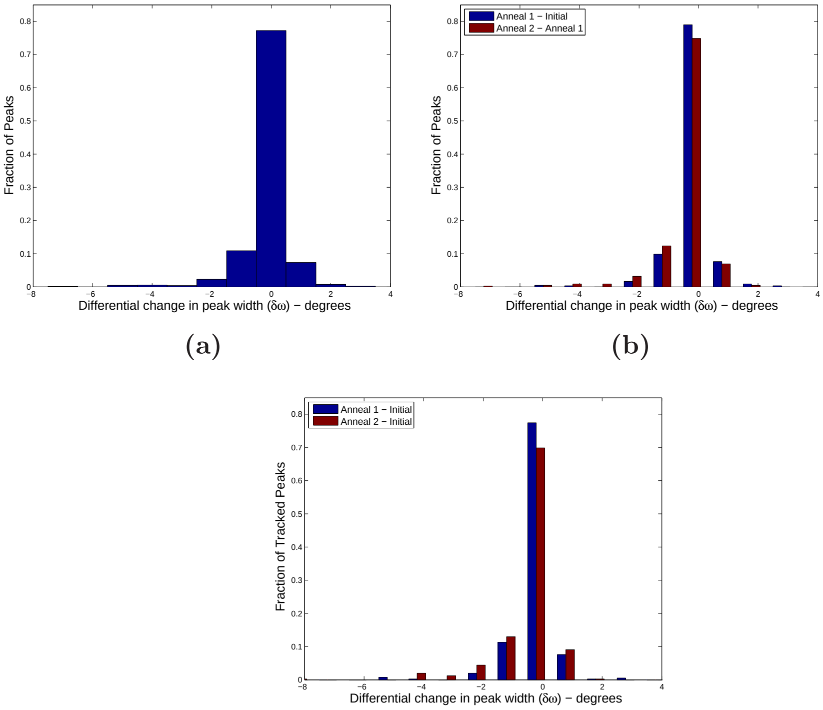

**(a)**

**(b)**

**(c)**

*Figure 3.26: Histograms illustrating the change in $\delta\omega$ peak widths for a subset of grain cross-sections which exhibited both minimal areal change during anneals and remained within the bulk of the wire. (a) displays all $\delta\omega$ width changes for peaks between sequential anneal states. A total of 1149 peaks are binned in this histogram, with 672 followed from the initial to 80C state and 477 in the next annealing sequence. (b) partitions the binning from (a) into the anneal progression from which it originated. (c) shows how peaks (which can be correlated among all three states) have evolved from the initial state. There are 409 of these tracked peaks, emanating from the 57 distinct cross-sections.*

feature of this plot is how narrow peaks are in $\omega$ for the singular orientation, as opposed to the reconstructed, multi-orientation grain. The single orientation diffraction image has every peak occur in a single $\delta\omega$ bin, while the left plot has peaks spread over as many as 10 intervals.

Since peaks are easily identified across multiple $\omega$ intervals, due to the sparsity of their population of detector space, we can further interpret how peak areas change, by collapsing a peak across multiple omegas and counting the number of unique (x,y) pixels that are illuminated. This removes the $\omega$ dimension associated with recovery and allows us to look at changes in peak area. Figure 3.29 illustrates the changes between peaks generated via a single orientation (or a completely recovered grain) and peaks that emanate from a grain containing dislocations. Here, the horizontal axis shows the peak area when a single orientation is used to generate the diffraction, while the vertical axis

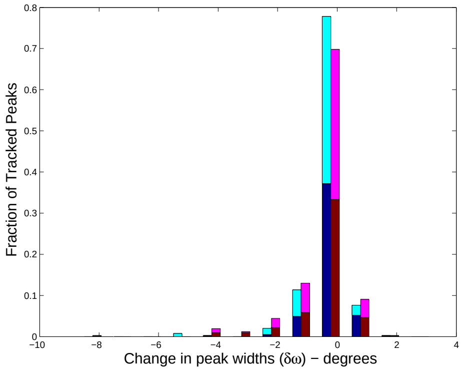

*Figure 3.27: Histogram of $\delta\omega$ changes from the initial peak width, after the sample has been annealed once and twice. The plot is the same as Figure 3.26(c), except peaks are now classified by their origins in the microstructure. Cross-sections of grains which exhibited a decrease in average KAM are illustrated in cyan and magenta, while 2D sections that exhibited an increase in KAM during at least one of the anneals are shown in red and blue. The red and magenta bars correspond to changes in peak width after the first anneal. The cyan and blue bars are from changes between the final and initial states.*

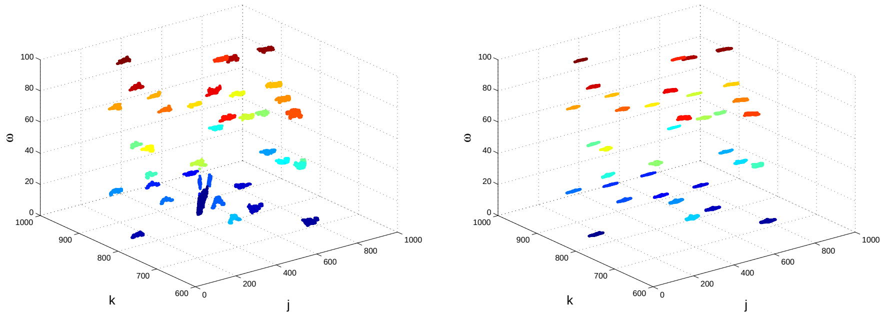

**(a)** **(b)**

*Figure 3.28: Three dimensional scattering picture illustrating the differences in peak geometry for a grain with orientation spread (left) and with a single orientation (right). The existence of tails in $\omega$ is clearly evident in the grain with orientation spread. Peaks have been colored by ID to make them visually distinct. The grain used to produce the diffraction is from the first layer of the initial state of the microstructure. $j$ and $k$ correspond to the horizontal and vertical camera pixel addresses.*

shows the peak area in the reconstruction. As already suggested, diffraction produced by a single orientation tends to yield smaller peaks (in area) than those generated by defect-laden microstructure. This is evident by the large number of peaks falling above the equality line, where a peak is of the same area in both the reconstruction and single orientation domains. The few reflections where the single orientation peak produces a larger area than the reconstructed peak are likely due to instances where diffracted beams on the grain edges are directed into the center of the spot. The assignment of the average orientation to these voxels would make the peak bigger since it simply expands the outgoing beam. While these instances are possible, the vast majority of peaks (30 of the 36) have peak coverage that is larger in the defective grain's peak geometry. Additionally, there is an extra peak in the reconstructed diffraction that is not identified with the grain averaged diffraction. Evidently, there is sufficent disorder within the grain to produce diffraction which does not overlap the grain average orientation's diffraction.

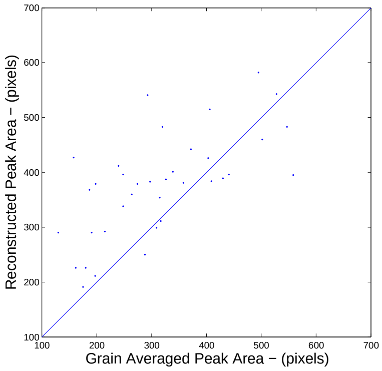

*Figure 3.29: Plot illustrating the differences in peak cross-section for a grain with orientation spread and the same grain with a single (grain-averaged) orientation assigned to the same set of voxels. The peaks are those shown in Figure* 3.28*. Areas have been determined by identifying individual peaks in detector space and collapsing them through $\omega$ space. This tabulation is done for both sources. The number of unique (x,y) pixels that remain are then counted and plotted on the axes. The majority of peaks have a larger area in the presence of orientation spread.*

Thus far, we have motivated the peak area change response to recovery in the context of simulated scattering from a structure. Now, we connect this information with the experimental peaks we see in the physical data set. Numerous difficulties exist in doing such a study. Specifically, the signal we are attempting to find, manifested as a peak losing area in the projection, would necessitate careful intensity analysis. Here we are only looking at a binary list of pixels that are simulated as either illuminated or not. With the current experimental system, seeing peaks begin to get smaller due to the ordering of the scattering origin is extremely difficult. Additionally, the use of pixels $> 4$ $\mu$m to monitor such small scale effects also makes resolving this recovery feature challenging. All these problems are coupled with the issue of grains changing in size as we anneal and therefore we have extra variables that contribute to spot size.

We use the same peaks as defined in the multi-state $\omega$ tracking seen in Figure 3.26. There, we had a total of 409 peaks that were monitored through all states. We then place a restriction that the peak can not change significantly in $\omega$ space after each anneal. The restriction placed on the peaks are that changes can not exceed 2° from state-to-state, which results in the retention of 335 peaks. These peaks are then collapsed in $\omega$ space and the pixels that are illuminated on the area of the detector are counted in each state. The number of pixels in a peak is then divided by the number of voxels in the microstructure that are responsible for generating that peak. Note, this is only using simulated scattering to find which experimental peaks overlap simulated peaks. By using the forward modeling simulator, we find which peaks can be associated with each grain. The simulated diffraction is only used for this experimental peak-microstructure map association and the number of pixels illuminated by the simulation is not used in this analysis. For each 'collapsed' experimental peak, we divide the number of pixels in the peak, by the number of voxels in the grain that has produced this peak. This is a means of separating the change in the area of spots due to the change in 2D grain sizes. Once these peaks are tracked, it is found that only 25 of the 335 peaks exhibit consecutive decreases in pixels per voxel after each anneal and 139 showed either a decrease in the pixels per voxel after the first or second anneal. This leaves 171 peaks (51 % of the 335 peaks), which became larger in a pixel per voxel basis, as annealing occured. Hence, we can conclude that for this annealing routine using this experimental setup, we are insensitive to the recovery response through areal spot changes. This is likely due to the large pixel sizes used on the detectors to capture a very position sensitive signal. Such a recovery measurement with a much finer pixel size would be of great interest in resolving this feature. Additionally, further anneals would also produce a more noticeable effect, as defect content continues to be reduced.

# Chapter 4

# Critical Events

Until this point, our discussion of the evolving aluminum microstructure has been dedicated to a global description of the ensemble of grains and how they have responded to the annealing process. With recovery, we saw that the microstructure, as a whole, moved towards a more ordered state, where dislocations that were present in the initial microstructure were gradually removed. The events were subtle in signal, but were clearly evident by a global increase in short range order as manifested in the decrease in kernel averaged misorientation. On a more granular scale, we saw that the orientation spread from the grain's average orientation ($IGM$) also decreased. Finally, the experimental origins of these orientation assignments were from peaks identified in the diffraction images, which became more defined (separable from background intensity), and this was identified as an increase in voxel confidences at each state.

We now turn our attention to the actual distribution of grains as the microstructure was annealed. Specifically, we look for changes in the actual ensemble of grains, which we label critical microstructural events. These are classified as the appearance or disappearance of grains as we move from state-to-state. In the instance of a grain appearing, we term this phenomena recrystallization and define it as the appearance of a new orientation in a region of microstructure, where the new orientation possess a significant misorientation with the initial neighborhood. Alternatively, grains that disappear from the microstructure have their physical volume supplanted by the neighboring grains. In the content to follow we will devote our attention to both the appearance of new grains within our microstructure in the recrystallization process and the disappearance of one grain as the result of grain growth. We will also interpret these results in the context of the reconstructed orientation maps as well as the experimental diffraction signal, similar to what was accomplished with the recovery presentation.

## 4.1 Tracking Statistics

For the identification of critical events it is mandatory that grains are tracked as a function of anneal state. This process was conducted earlier for comparative recovery statistics, but only grains that existed in all three states were analyzed. Minimal attention was also given to if the grain was fully encapsulated by the measured volume or if only a portion of the grain's volume was measured. For our critical events analysis, we must ensure that the grains we identify as either disappearing or materializing are indeed missing (or new) grains within the microstructure. Since the sample is coarse grained and was only sampled with 11 layers per state, elminating from the analysis any grain appearing in the top or bottom layer (and therefore possibly extended into unmeasured microstructure) is severely limiting. Instead, we develop a criteria that restricts grains to have a significant portion of their volume appear in the interior 9 layers measured in our experiment. Further, for grain nucleation and extinction, we require the event to occur within these interior layers. In addition to requiring that a grain is a spatially compact collection of voxels, we adjust our criteria such that (a) the grain contains at least 25 voxels, (b) at least one voxel exceeds 0.25 confidence or better, and (c) no more than 10% of the grain's total volume (measured in number of equal sized voxels) appears in the top or bottom layer of the measurement.

The existence of critical events immediately becomes evident when the number of grains in each state are counted. Using this modified grain definition, we have 134, 153, and 152, in the initial, first and final anneal state, respectively. Since the number of grains does not remain static, and actually increases in the final state, the appearance and disappearance of grains is suggested. We can analyze the origins of these grains more closely, since we have correlated grains between states by using misorientation, spatial centers, and a final by-hand verification. The results are summarized in Table 4.1, where we describe events by anneal state.

*Table 4.1: Number of Critical Events by Anneal State and Event Type for Aluminum*

| Event Description | Number of Grains |
|---|---|
| Nucleations | 39 |
| Nucleate and Persist (First) | 16 |
| Nucleate and Persist (Final) | 17 |
| Disappearances | 21 |
| Disappear (First) | 3 |
| Disappear (Final) | 12 |
| Exist Only in First Anneal State | 6 |

Table 4.1 counts each critical event and how it occurs within the microstructure. Obviously we can not determine if a grain nucleated in the initial state, since we have no prior information about the microstructure. We define a nucleation as the appearance of a grain in either the first or final anneal state, when the grain was not present in the initial microstructure, while disappearances require that the grain of interest does not exist in the final state. The 'nucleate and persist' classification is used to distinguish from the 'exist only in first anneal state'. Nucleate and persist means that a grain was

first identified in a state (given in parentheses) and was present through the remainder of the measurement. The two 'disappear' entries count the number of grains that were present in the initial microstructure and vanished in the state in parentheses. Lastly, six grains were found to materialize in the intermediate state, only to not be present in the final microstructure. In the end the number of nucleations is therefore the sum of the 'nucleate and persist' and 'exist only in first anneal state' quantities, while the 21 disappearances are the sum of the 'disappear' and also the six intermediate state only grains.

We should emphasize that is possible for some of these grains to have migrated to a region that was between measurement layers, since the layer spacing was very large for this experiment, at 20 $\mu m$. Yet with the repeated monitoring of the tip of the sample and its return to a few microns from its original position, insensitivity to such an event is unlikely.

We now focus on these new and disappearing grains to gain some insight into their development during the experiment. Figure 4.1 illustrates the position of the critical events in the microstructure, where states are denoted by color and event type (nucleation or extinction) by symbols. We only show the in-plane locations of these events and integrate over the nine layers that define the interior volume.

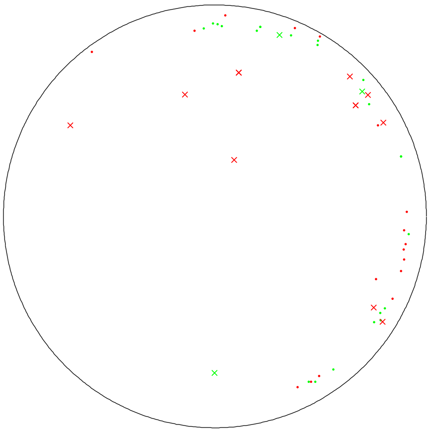

*Figure 4.1: Spatial location of critical events in the aluminum microstructure. Dots indicate the location of events that are the appearance of a new grain that was not present in the previous state, while × denote the disappearance of grains. Markers in red correspond to the event being seen in the final anneal state, while green is associated with the first anneal. The black outline gives a reference for the averaged edge of the sample for both the first and final anneal states.*

Immediately evident from Figure 4.1 is the inhomogeneous distribution of events within the microstructure, especially with nucleation. Nearly all nucleation events have been confined to the surface of the microstructure, which is consistent with the picture that nucleation on a free surface should take less energy than within the bulk. Therefore, we expect these events to initially occur on the surface of the microstructure before bulk recrystallization occurs. Not visible on this plot is a grain that we deemed to nucleate [3] within the bulk, which appears to have been measured just after the onset of recrystallization. We will discuss this bulk recrystallization event in Section 4.4, but first we devote our attention to the properties of the surface nucleated grains.

## 4.2 Surface Nucleation

The surface nucleation events we have seen in this measurement have resulted in numerous new grains developing (predominantly) upon the surface of the microstructure. We will interpret how these new grains relate to the remaining ensemble in the microstructure with the descriptive metrics that were established in the recovery portion of this work. This includes how these nucleated grains differ in confidence, kernel averaged misorientation (*KAM*), and intra-granular misorientation (*IGM*). Additionally, we will look at the relationship of this grain with the neighboring grains to see if any notable misorientation relationships are present. For instance, do the misorientations have a preferred misorientation with their parent orientation?

### 4.2.1 Kernel Averaged Misorientation

The kernel averaged misorientation (*KAM*) has been motivated as the short range disorder metric for our microstructural analysis. It is the result of determining the average misorientation angle between a voxel's orientation and its three, in-plane neighbors with which it shares a common edge. Earlier we established that in the process of recovery, an overall reduction in *KAM* as the global response to anneals. This would amount to regions of microstructure becoming more uniform in orientation as the local lattice becomes more 'perfect'. In the context of critical events, *KAM* also serves as an interesting metric in that there are expectations in regard to defect content and critical events. Specifically, as we anneal a microstructure and see recrystallization, one expects regions of high dislocation content to be replaced by a more ordered microstructure, or when viewed through the *KAM*, we expect regions of high *KAM* to be eroded and replaced with low *KAM* voxels. The disappearing, high *KAM* content regions can be removed through either the nucleation of a new grain (of uniform orientation), or it can be consumed by the surrounding neighborhood of microstructure, so that the region of high *KAM* is replaced through growth of a neighboring grain or grains.

Figure 4.2 summarizes how these surface events are related, which shows the average *KAM* in each state and its relation to grain size. We present the *KAM* distribution for each grain in the initial and final microstructures. These are shown as the black points in both plots and the errorbars are the standard deviation of the *KAM* for all voxels composing that grain. The critical surface events are illustrated with color, with blue points indicating grains that were deemed a critical event in the first anneal state and red points in the final state. Green points are also present in the initial microstructure distribution and indicate critical events that are in the bulk and associated with the disappearing grains that occured in first anneal state. The plot on the left illustrates $KAM$ for the initial microstructure, which was our most disordered state of measurement. The colored points, indicating the grains that were not present in the final microstructure admit two observations. The first is that vanishing grains were on the small side of the size distribution. This is not entirely unexpected, since small grains are expected to be those that disappear first in an annealing experiment, simply because the grain must be disassembled on the atomic scale and incrementally associated with its neighbors. The second observation is that the grains that vanish tend to have a larger than average $KAM$ and $KAM$ spread, indicating that they are composed of defective microstructure. Therefore, their elimination (by presumably ordered microstructure) agrees with the expectations of an annealing experiment. The right plot shows the final state $KAM$ distribution of grains and illustrates that nucleated grains are both small (because they have not been given appreciable time to grow) and possess a small $KAM$, which should be associated with a lower energy configuration than the dislocation filled microstructure.

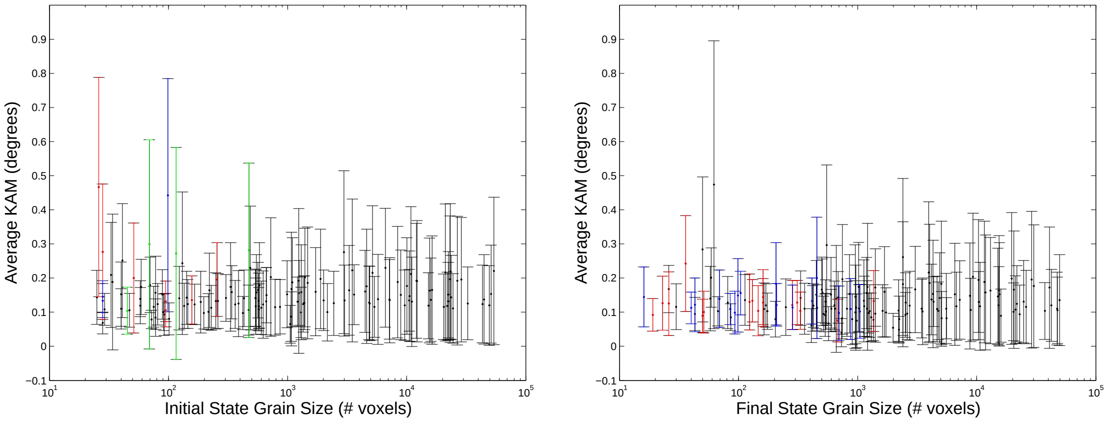

**Initial State** **Final State**

*Figure 4.2: KAM distribution for grains in the initial and final microstructure states. Horizontal axis shows the size of the grain in the given state as counted by the number of composing voxels (in 3D). Each point represents a grain in the interior microstructure that is described in the text. Each dot represents the average KAM of all voxels within the grain in the target state, while errorbars denote the standard deviation of these values. The colored points in the plot on the left indicate grains would eventually disappear from the measured microstructure, with red points indicating disappearing surface grains in the final state, blue points as those that disappear in the first anneal state and green points as grains that were in the bulk that vanished in the final anneal state. The red and blue convention indicating the final and first anneal state, respectively, are used in the the plot on the right to denote nucleation events and their distribution in the final state.*

We can emphasize these $KAM$ relations for the nucleating and disappearing grains by looking at the simple grain averages for the entire state and compare it with the special events. These are summarized in Table 4.2 for these surface events. First we note that the trend towards decreasing $KAM$ is present for the tracked grains with the average and spread decreasing after each anneal. For the initial state, we see that grains that eventually disappear have $KAM$s larger than the ensemble, while the same is true of the first anneal state grains that also disappear. Further, we see that the nucleated grains have a smaller $KAM$ and spread than the ensemble in the final state. The grains that nucleate in the intermediate state curiously have a larger $KAM$ than the ensemble, but also a larger spread, which suggests some anomaly in the distribution.

*Table 4.2: Distribution of Kernel Averaged Misorientation of Sample Surface Critical Events*

| Event Description | $KAM$ (degrees) |
|---|---|
| Initial State | 0.157 ± 0.13 |
| First Anneal State | 0.150 ± 0.13 |
| Final Anneal State | 0.133 ± 0.12 |
| Final Anneal Nucleation (Final Anneal) | 0.118 ± 0.075 |
| First Anneal Nucleation (First Anneal) | 0.180 ± 0.145 |
| First Anneal Nucleation (Final Anneal) | 0.125 ± 0.076 |
| Final Anneal Disappearance (Initial State) | 0.221 ± 0.16 |
| Final Anneal Disappearance (First Anneal) | 0.162 ± 0.091 |
| First Anneal Disappearance (Initial State) | 0.241 ± 0.20 |

Lastly, Figure 4.3 shows a $KAM$ map like those from the recovery section of this thesis, only with the nucleated and disappearing grains explicitly identified. A tighter $KAM$ scale than previous $KAM$ maps is used. The green lines outline grains that will no longer appear in the microstructure in the final state, while red indicates recrystallized grains. The highlight of this figure is the $KAM$ uniformity for the recrystallized grains in the final state, and to additionally show how defective (high $KAM$) the locations of nucleation are in the previous states. Of particular note are the triangular grain at the base of the map and the rectangularly shaped grain towards the bottom right (and closer to the center of the microstructure). Both these grains were initially in a region of high disorder, but have replaced it with a relatively uniform microstructure. The layer presented is simply a sampled layer of microstructure, where a high number of critical events were identified.

### 4.2.2 Intra-granular Misorientation

The presentation of $KAM$ and its relation to critical events showed that grains that nucleated within the microstructure had exceptional values when compared to the remainder of the microstructure. Specifically, the grains that disappeared were found to have high local disorder identifiable with large $KAM$ values, while the new grains that appear in the first and final anneal states had a lower than average $KAM$ in comparison

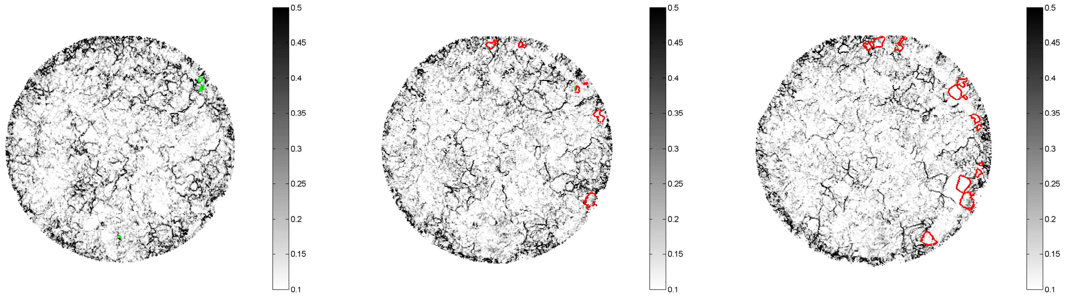

**Initial** **First Anneal** **Final Anneal**

*Figure 4.3: Reconstructed microstructure maps for the fifth layer of the aluminum microstructure, with voxels colored by their KAM. Colored outlines indicate the location of critical events within the microstructure, with red lines forming the boundary of recrystallized grains and green lines circling the grains that are not present in the final state.*

to the other grains in their anneal state. In our discussion of recovery, it was noted that $KAM$ provides our most local measure of disorder, by looking at adjacent voxels on the $5.04\mu m$ grid, and seeing how they are are misoriented with respect to their neighbors. In contrast, intra-granular misorientation ($IGM$) gives a more global picture of how orientations are distributed through operation on a granular level, by determining a grain averaged orientation and measuring the misorientation of each voxel in the grain with this average orientation. Like the $KAM$ analysis, where grains associated with critical events had differing $KAM$s than the remaining microstructure, we will echo that analysis, only using $IGM$ as the metric.

Figure 4.4 illustrates the $IGM$ for each grain in the initial and final state of the microstructure. Like Figure 4.2, we color critical events to indicate their relationship to the remainder of the grain population. The location of the critical events with respect to $IGM$ is similar to the $KAM$. Grains that have nucleated had a small spread in orientation as denoted by small $IGM$ values. Alternatively, the grains that disappeared had much larger orientation spreads, manifesting in a larger $IGM$. Yet for both these events, the orientation spread is less than the ensemble average for the state, as summarized in Table 4.3. This is not entirely surprising, considering the grains associated with the critical event were small, which does not lend itself to appreciable statistics to see the existence of orientation gradients. Thus, it is the localized orientation variation tabulated with $KAM$ that is more correlated with critical events than the $IGM$, which looks at longer range ordering.

Lastly, maps similiar to Figure 4.5 are shown, only using $IGM$ to color each voxel. Like our $IGM$ maps from the recovery chapter, we use two coloring schemes; one colors by misorientation angle, much like the $KAM$ maps colored by local misorientation angle. This is shown in the top row with the red-blue color scale, while the bottom row uses a coloring of the Rodrigues-Frank representation of misorientation, using all

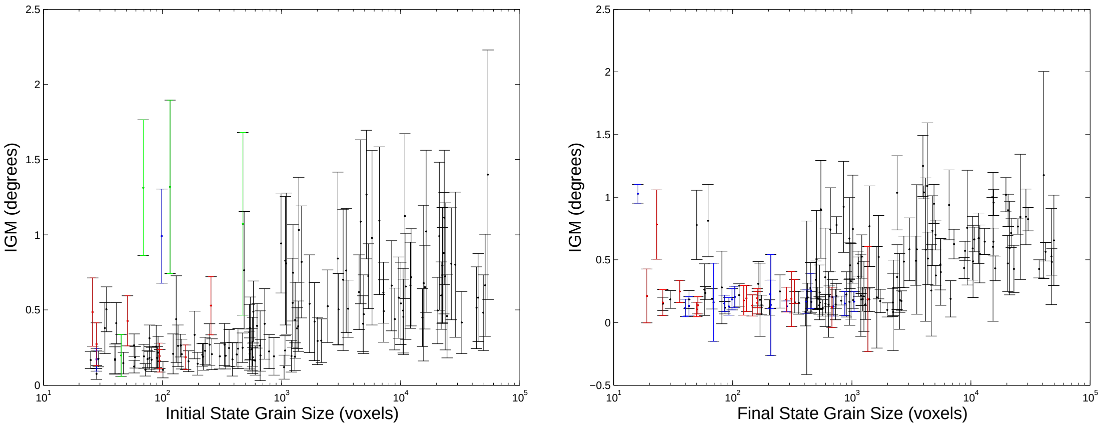

**(a)** **(b)**

*Figure 4.4: IGM distribution for grains in the initial and final microstructure states. Each point represents a grain in the interior microstructure , just like Figure 4.2, only now IGM is shown instead of KAM. Each dot represents the average IGM of all voxels within the grain in the target state, while errorbars denote the standard deviation of these values. The colored points in the plot on the left indicate grains that would eventually disappear from the measured microstructure, with red points indicating disappearing surface grains in the final state, blue points as those that disappear in the first anneal state and green points as grains that were in the bulk that vanished in the final anneal state. The red and blue convention indicating the final and first anneal state, respectively, are used in the the plot on the right to denote nucleation events and their distribution in the final state.*

three parameters. Just like the *KAM* maps of Figure 4.3 illustrated approximately uniform orientation distributions with low *KAM* in the nucleated grains, the *IGM* maps at the bottom row of Figure 4.5 show a uniform, grayish color, which suggests that there is no real orientation variation within the grain. Gray maps to points close to the Rodrigues-Frank space's origin and have color variations amounting to noise about a singular orientation.

### 4.2.3 Confidence

With the *KAM* and *IGM* analysis of these surface critical events, the differences in average quantities from the remaining ensemble have been of predominant interest. We now shift our attention away from measuring the critical events as entities within a distribution. Interpreting confidence with respect to the remaining ensemble provides little insight. Instead, the more relevant observation is to see how confidences evolve for these special surface grains. Obviously, nucleations result in a new scattering signals in the diffraction images, while grains that disappear have their signal vanish. Therefore, we expect nucleating grains to have an initially weak signal and therefore a low, but resolvable confidence. As these new grains grow (and fill more of the microstructure with

*Table 4.3: Distribution of Intra-granular Misorientation of Sample Surface Critical Events*

| **Event Description** | ***IGM*** **(degrees)** |
|---|---|
| Initial State | 0.464 ± 0.27 |
| First Anneal State | 0.419 ± 0.26 |
| Final Anneal State | 0.403 ± 0.24 |
| Final Anneal Nucleation (Final Anneal) | 0.222 ± 0.18 |
| First Anneal Nucleation (First Anneal) | 0.213 ± 0.15 |
| First Anneal Nucleation (Final Anneal) | 0.153 ± 0.08 |
| Final Anneal Disappearance (Initial State) | 0.346 ± 0.22 |
| Final Anneal Disappearance (First Anneal) | 0.280 ± 0.15 |
| First Anneal Disappearance (Initial State) | 0.444 ± 0.189 |

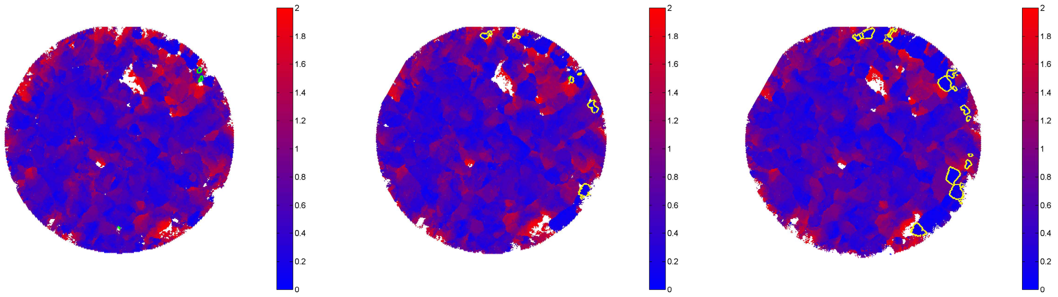

**Initial** **First Anneal** **Final Anneal**

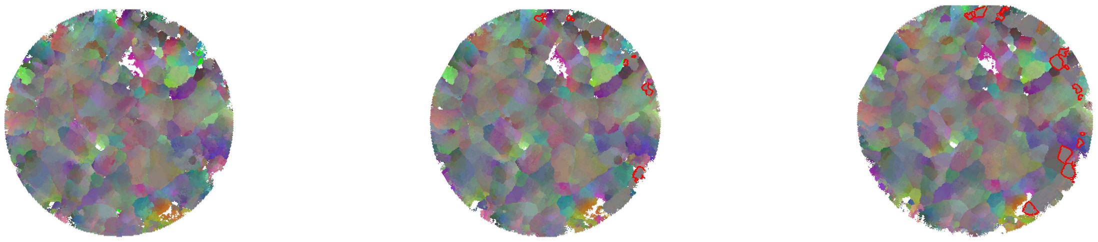

**Initial** **First Anneal** **Final Anneal**

*Figure 4.5: Spatial distribution of IGM with boundary lines enclosing the critical events. Top row has each voxel colored by its IGM angle (in degrees), while the bottom row shows the three component misorientation with a coloring scale that maps Rodrigues space to red-green-blue. Events outlined in green indicate grains that disappear in the final state, while those marked in yellow in the top row (and red in the bottom row), show nucleation events. This layer of microstructure is the same as shown for the KAM presentation in Figure* 4.3.

a well ordered lattice as evidenced by the *KAM* and *IGM* and capable of producing a well defined diffraction signal), we expect to see increased confidences for the grain on average. The opposite should be true for grains that disappear. Its diffraction signal should eventually vanish from the images and as such, and confidence in that orientation should go to zero. The simulated scattering should not overlap any experimental signal.

Focus will be limited to grains that are present in two of the three states for our confidence analysis, since more than one state is necessary for a confidence comparison. Tables 4.4 and 4.5 summarize grains that either vanished in the final anneal state, or nucleated in the first anneal state. Upon first inspection, it appears that the grain nucleation events follow the confidence trend we expect much better than grains that disappear from the microstructure. There are a few instances of a grain growing before vanishing from the microstructure. Due to the coarse spacing between sampled microstructure, it is quite possible that some of these critical events are the result of grains translating within the microstructure; into and out of the sampled diffraction layers. Alternatively, with the nucleated grains, the confidence picture agrees with our intuition. Grains get larger in both average and maximum confidence, since peaks become stronger and therefore separable from background. Additionally, these uniformly oriented grains should grow due to the energetics associated with their microstructural properties. To establish the validity of these signals, we explore detector space by identifying peaks associated with the nucleating grain $P$ and monitor its evolution through the three anneal states.

*Table 4.4: Confidence Statistics for Surface Grains that Disappear in Final Anneal State*

| | Average Confidence | | Maximum Confidence | | # of Voxels | | # of Cross-sections | |
|---|---|---|---|---|---|---|---|---|
| Grain | Initial | Anneal1 | Initial | Anneal1 | Initial | Anneal1 | Initial | Anneal1 |
| A | 0.52±0.07 | 0.49±0.10 | 0.64 | 0.64 | 95 | 148 | 1 | 1 |
| B | 0.40±0.08 | 0.56±0.18 | 0.54 | 0.85 | 101 | 291 | 1 | 1 |
| C | 0.48±0.02 | 0.46±0.03 | 0.51 | 0.50 | 51 | 53 | 1 | 1 |
| D | 0.20±0.03 | 0.22±0.02 | 0.26 | 0.26 | 414 | 145 | 6 | 2 |
| E | 0.33±0.03 | 0.34±0.03 | 0.39 | 0.39 | 54 | 32 | 2 | 2 |
| F | 0.36±0.07 | 0.36±0.12 | 0.51 | 0.59 | 279 | 326 | 2 | 2 |
| G | 0.52±0.11 | 0.48±0.11 | 0.70 | 0.65 | 157 | 145 | 1 | 2 |

### 4.2.4 Detector Space Analysis of Critical Events on Surface

We switch our focus from the orientation map analysis of sample space to the origins of these nucleation events as interpreted through the experimental signal collected as diffraction peaks in the nfHEDM experiment. Previously, we analyzed how evolving peak distributions were responsible for the recovery signal that was found in the orientation maps and was a result of shifts in peak distribution. These shifts included changes in peaks that were present through all three anneal states and included variations in spot

*Table 4.5: Confidence Statistics for Surface Grains that Nucleated in First Anneal State*

| | Average Confidence | | Maximum Confidence | | # of Voxels | | # of Cross-sections | |
|---|---|---|---|---|---|---|---|---|
| Grain | Anneal1 | Anneal2 | Anneal1 | Anneal2 | Anneal1 | Anneal2 | Anneal1 | Anneal2 |
| H | $0.67\pm0.04$ | $0.57\pm0.19$ | 0.75 | 0.86 | 64 | 1148 | 2 | 4 |
| J | $0.25\pm0.03$ | $0.23\pm0.03$ | 0.34 | 0.28 | 26 | 47 | 1 | 2 |
| K | $0.44\pm0.06$ | $0.53\pm0.08$ | 0.54 | 0.70 | 71 | 99 | 2 | 2 |
| L | $0.53\pm0.08$ | $0.48\pm0.14$ | 0.65 | 0.69 | 96 | 116 | 2 | 2 |
| M | $0.60\pm0.10$ | $0.64\pm0.08$ | 0.76 | 0.78 | 246 | 287 | 4 | 6 |
| N | $0.45\pm0.15$ | $0.47\pm0.20$ | 0.70 | 0.79 | 424 | 563 | 2 | 3 |
| O | $0.65\pm0.08$ | $0.64\pm0.11$ | 0.77 | 0.77 | 87 | 211 | 2 | 4 |
| P | $0.45\pm0.13$ | $0.62\pm0.19$ | 0.67 | 0.86 | 213 | 732 | 2 | 3 |
| Q | $0.60\pm0.05$ | $0.56\pm0.16$ | 0.69 | 0.84 | 34 | 892 | 2 | 4 |
| R | $0.39\pm0.07$ | $0.50\pm0.16$ | 0.55 | 0.80 | 146 | 422 | 3 | 4 |
| S | $0.66\pm0.07$ | $0.57\pm0.16$ | 0.76 | 0.76 | 59 | 96 | 1 | 1 |
| T | $0.33\pm0.02$ | $0.39\pm0.13$ | 0.37 | 0.62 | 26 | 251 | 1 | 3 |
| U | $0.40\pm0.05$ | $0.50\pm0.07$ | 0.49 | 0.61 | 42 | 104 | 1 | 1 |
| V | $0.39\pm0.05$ | $0.45\pm0.07$ | 0.46 | 0.56 | 31 | 86 | 1 | 1 |

shapes and peak widths ($\delta\omega$). With nucleation events, a more dramatic occurance in detector space is observed. Unlike recovery, where searches were performed for subtle differences in the same peak at each sample state, recrystallization or grain extinction events are associated with the appearance or disappearance of diffraction peaks. In a way, this is a much easier process than searching for minute variations in the peaks that was done with the recovery analysis, since the materialization of a peak in detector space is much easier to identify. Further still, we can understand what nucleation means in the context of forward modeling generated orientation maps.

For our analysis of detector space, one grain is selected from the microstructure and determine its associated scattering in detector space. Grain $P$ is selected from the nucleation grain list in Table 4.5 and extracted is a sampling of its peaks from detector space, which are shown in Figure 4.6. From the diffraction perspective, it appears that a diffraction signal is present in all three states, but only becomes resolvable after annealing has been performed on the sample. In the initial state, there is a collection of weak intensity at the eventual location of the peak, but this is not true for all the peaks generated by the grain. Specifically, the figure has the top row illustrating some measurable diffraction in all three states for this $(1\bar{3}1)$ reflection, while the bottom row shows extremely weak scattering at the initial state from the (024) peak. Hence, we do not identify the grain with our reconstruction because it is impossible to achieve a convergence in orientation with a small number of resolvable diffraction peaks in the initial state.

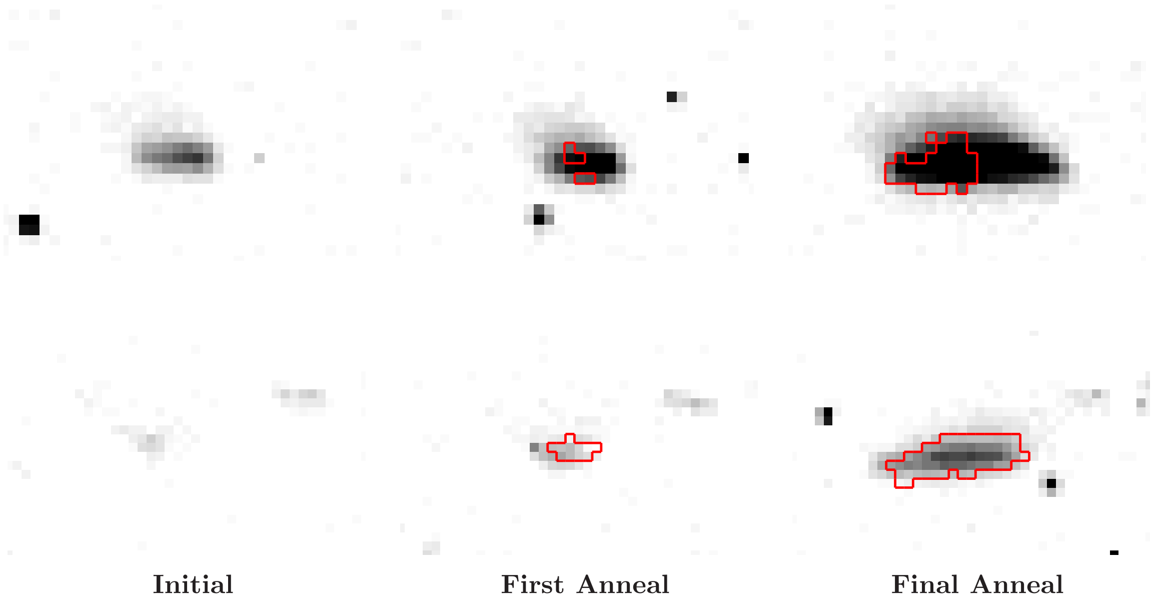

*Figure 4.6: Detector space images of diffraction emanating from Grain P found in Table 4.5. Diffraction is shown in each state for the $(1\bar{3}1)$ reflection in the top row, and $(024)$ reflection in the bottom row. The images have been subjected to background subtraction, but no median filtering or baseline subtraction, to retain the purest form of experimental data. The red outline illustrates where simulated scattering is placed on the detector from the nucleating grain. Evidently, there is some scattering from the nucleating grain in the initial state, but the lack of background separable peaks results in a lack of grain identification.*

### 4.2.5 Misorientation Relationships of Critical Events on Surface

Our last characterization of the critical surface events is to analyze the misorientation relationship between the critical event grain's orientation and the parent grain from which it nucleates. For each grain, we look at its neighborhood before nucleation or extinction, which means we interpret the neighborhood in the first anneal state since this is the microstructure where the disappearing grains are last seen or the nucleating grains first materialize. We inspect the misorientation of each grain with the surrounding neighborhood for both nucleation and extinction and search for special relationships in neighbor-to-neighbor misorientation as described by the coincident site lattice (*CSL*). These relationships are traditionally used to describe special configurations between adjacent lattices by quantifying the number of overlapping atoms if the two lattices were interwoven. The reciprocal of this fraction of atomic overlaps is classified as the $\Sigma$-value for that misorientation relationship. Hence, a value of $\Sigma3$ would mean that one third of the atoms in the interleaving lattices are coincident. We will discuss *CSL*s more extensively in our presentation of the nickel annealing experiment, but here we note that

*CSL*s have significance in being one of the necessary, but not sufficent, conditions for many special, low energy boundary configurations in a microstructure.

Only the misorientation relationships that are less than 5° from a *CSL* misorientation configuration are listed in Table 4.6. Grain labels are the same as used in Tables 4.4 and 4.5. The first four grains are disappearance events, while the remainder are nucleations. The grain neighborhood was determined by manual inspection of the maps to determine which neighbors were present. The misorientations listed in the table are quaternions and are the misorientation between the *CSL* operators and the misorientation between the two grains. Hence, this is a misorientation between misorientations. The final column, labeled ‘Special’, describes the relationship between the critical event grain and the neighbor of interest. Pairs with a 1 indicate that this grain pair has a parent-child relationship, which means the grain of interest is related to the critical event by being the explicit location of nucleation or the grain that appears to have engulfed the disappearing grain. Pairs with a 0 for this ‘Special’ category are grains that do not appear to be a dominating neighbor in that the critical event grain appears directly linked to another grain in the first anneal state and this other grain is an incidental neighbor. The table was generated by only looking at the misorientation with *CSL*s up to $\Sigma29$.

The relationships with *CSL*s admit some close relationships with special configurations, but overall there is no high precision special boundaries present. This is quantified in the final column of the table by envoking the Brandon criterion [41],

$$\nu_m = 15^\circ \Sigma^{\frac{-1}{2}} \tag{4.1}$$

which is nearness threshold for high angle boundaries to be associated with a *CSL* configuration. Hence, if the misorientation angle tabulated in the fourth column of Table 4.6 exceeds this Brandon criterion, then we really just have a random high angle boundary without some special configuration with its neighbor. Once we enforce this criteria, only three grain neighbors remain; two having a parent-child configuration. As we will see in the nickel analysis, to get a full picture of the evolution of a microstructure from the energetics associated with the boundaries, both misorientation *and* boundary plane are necessary. In this case, it does appear safe to state that the formation of a special boundary was not the driving force for the critical events, but instead the existence of a free surface.

*Table 4.6: Misorientation Relationships for Critical Events in First Anneal State*

| Grain | Misorientation | CSL ($\Sigma$) | Mis. from CSL(deg) | Special | Brandon |
|---|---|---|---|---|---|
| A | (0.8909,0.3108,-0.1029,-0.3150) | 25 | 2.38 | 1 | 1 |
| C | (0.9756,0.1159,0.1342,-0.1294) | 13 | 2.92 | 1 | 1 |
| F | (0.9169,0.0372,0.3634,0.1606) | 15 | 4.98 | 1 | 0 |
| G | (0.9374,-0.1532,-0.1389,-0.2802) | 21b | 3.94 | 0 | 0 |
| G | (0.9404,-0.0660,0.0930,0.3205) | 23 | 4.66 | 1 | 0 |
| J | (0.9404,0.2946,-0.1702,0.0003) | 27b | 4.88 | 0 | 0 |
| K | (0.9272,0.2370,0.1527,-0.2465) | 29 | 4.35 | 1 | 0 |
| L | (0.9591,-0.1239,-0.0148,-0.2541) | 27b | 3.11 | 1 | 0 |
| O | (0.9385,-0.1497,-0.2701,-0.1541) | 21b | 4.67 | 1 | 0 |
| Q | (0.8715,0.3355,-0.3251,0.1489) | 17 | 3.77 | 1 | 0 |
| S | (0.8990,0.0987,-0.2779,0.3236) | 25 | 3.71 | 0 | 0 |
| U | (0.9372,0.2791,-0.1453,-0.1506) | 21b | 3.79 | 1 | 0 |
| U | (0.9269,0.3151,-0.1451,-0.1433) | 21b | 1.81 | 0 | 1 |

## 4.3 Bulk Critical Events

The previous section was devoted to analysis of events that occured on the surface of the microstructure. While measurement of such events are possible using nfHEDM, it is the non-destructive monitoring of events occuring within the bulk microstructure that make this technique a special tool for materials characterization. We have shown that on the surface, a large number of critical events occured, which can make the quantification of bulk events based on surface measurements, such as electron backscatter diffraction (EBSD), misleading. The content to conclude this discussion of critical events will take the two occurences that were identified in the surface characterization (nucleation and extinction) and investigate their observation in the bulk, with a grain just after recrystallization in the initial state and one that vanished in the final state microstructure.

### 4.3.1 Bulk Extinction

The previous discussion of grain disappearance, or extinction, was focused on surface events where a grain that was present in the initial and/or first anneal state was no longer present in the final microstructure measurement. As outlined, there were many instances of this happening on the sample surface, which proved to be rich in critical event density. There, we classified grains through a definition that included misorientation among neighboring voxels and connectedness in three dimensions. The extinction event we observe in the bulk is more complicated that a grain shrinking to disappearance. Instead, we find reminants of a probable large grain from an earlier sample state, which we have not measured. This large grain has eroded into a non-connected object of similarly oriented voxels, but with intervening layers where no voxels from the grain are observed. The grain is presented in Figure 4.7 with orientation and confidence maps, where we illustrate the layer with the most voxels in the first two states. To emphasize the non-trivial 3D distribution with one image, Figure 4.7 is used with voxel centroids colored by sample state.

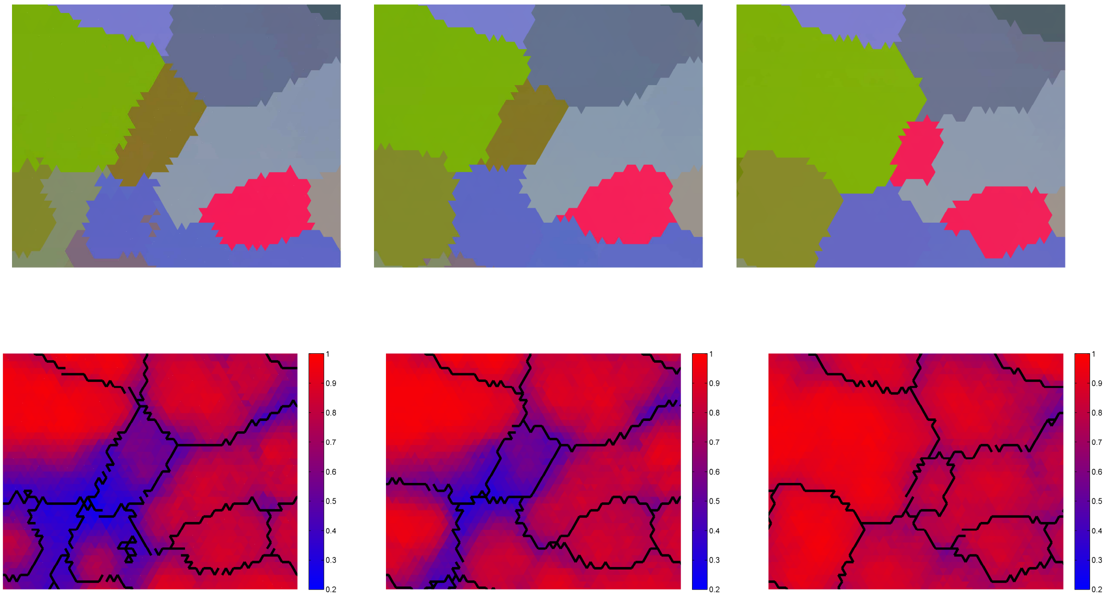

**Initial** **Anneal1** **Anneal2**

*Figure 4.7: Orientation and confidence maps illustrating the bulk interior grain that vanishes in the final anneal state. We show the sixth layer of microstructure ($z_6$), which has the most voxels present for this grain in the first two measurement states. The disappearing grain is in the center of the image and has been colored dark brown. The bottom row illustrates confidences associated with the maps in the top row. It is obvious that the grain is of low confidence in the first two states, then replaced by high confidence voxels associated with neighboring grains. The pink grain that appears near the location of the disappearing grain, in the final state, has the same orientation as the grain towards the bottom right corner of the image and is connected in the layer above the one presented here.*

We emphasize the difficulty in discovering such a unique grain within our microstructure. Our tools for microstructure tracking did not immediately identify this because of the criteria described earlier involving connectedness. Instead, this critical event was discovered through manual inspection of the orientation maps, followed by verification of similarly oriented voxels through multiple layers. The absence of the grain in some intevening layers proved the most problematic aspect of the correlation. With our grain idenitification routine, the initial grain is identified as four distinct entities due to both misorientation values and non-connectedness, while the first anneal state identifies it as three grains. The initial state grain is composed of 784 voxels, with all confidences

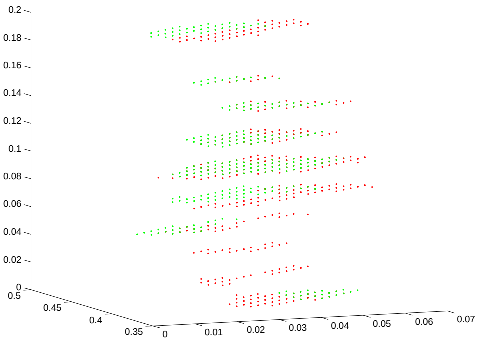

*Figure 4.8: 3D perspective of spatial location of the vanishing grain in the microstructure, shown in Figure 4.7. Red dots indicating voxels that are from the initial state and green dots from the first anneal. Gaps are evident in the microstructure by having given vertical locations without any voxels, specifically the first anneal state.*

exceeding 0.20, while the first anneal grain has 506 such voxels. The number of voxels in each layer as well as the average confidence per layer can be seen in Figure 4.9. The distribution of voxels within the grain are histogrammed with 0.025 bins for the two states. The histogram illustrates a remarkably static distribution of voxel confidences, though a slight shift exists in the first anneal state with voxels matching approximately half of their simulated peaks in the experimental data. We see from the number distribution of voxels, that this likely due to the weak confidence voxels being absorbed by the neighboring grains. Additionally, we see the consistency of the layers with the fewest number of voxels in the initial state have no voxels in the first anneal state.

### 4.3.2 Kernel Averaged and Intra-granular Misorientation

We interpret the distribution of voxels in the context of local misorientations with the *IGM* and *KAM*. Since this vanishing grain is actually a disconnected collection of voxels, we will analyze it in the context of both a 3D average and the more localized average confined to each layer. The layer-by-layer distribution of this local measurement of disorder is shown in Figure 4.11. While useful in illustrating the *KAM* spread from state-to-state and across layers, it does not supply the critical information as to why the grain is not present in the final anneal state. Instead, this is clearly identified by analyzing Figure 4.10, showing the spatial distribution of the target region of microstructure in all three states. It becomes readily evident that the grain that has disappeared has been replaced by a more ordered microstructure, as seen through the lighter shading in the final state region that once possessed our grain of interest. Two layers are shown to emphasize this dramatic *KAM* distribution.

*IGM* displays the global changes that are present in this grain that is disconnected over $200\mu m$ of microstructure. As we stated earlier, our grain correlation process iden-

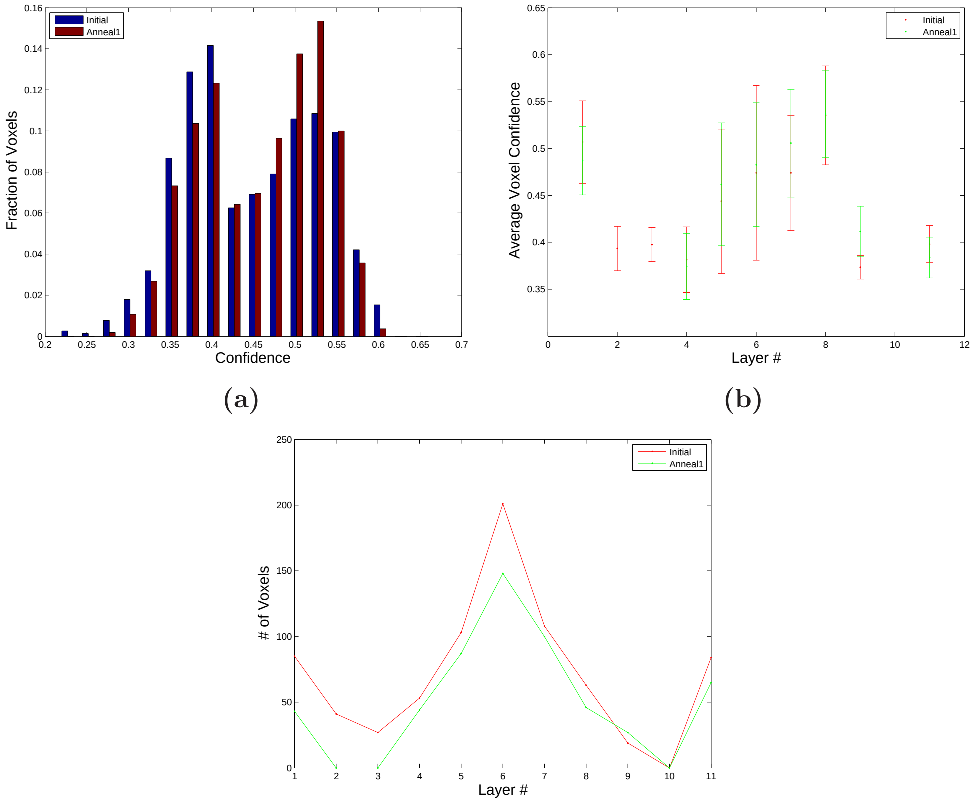

**(a)** **(b)**

**(c)**

*Figure 4.9: Statistical distribution of simple voxel quantities for vanishing grain in bulk microstructure, shown in Figure 4.7. (a) histograms all voxels composing the grain in the initial and first anneal state in 2.5° bins. (b) and (c) show the distribution of confidences and number of voxels by layer, respectively. The errorbars in (b) are tabulated by taking the standard deviation of voxel confidences in the given layer.*

tified this singular grain as four distinct grains in the initial state and three distinct grains in the first anneal state. The misorientation of these grains with respect to the grain averaged orientation are 0.33°, 1.70°, 2.05°, and 1.00° for the initial state and 0.08°, 1.36°, and 2.94° for the first anneal. Like the analogous *KAM* plot of Figure 4.11, the tails on the distribution are due to both disorder and small statistics. The voxels-by-layer distribution also indicates why we have an *IGM* drop around layers 6-8; the averaged orientation is dominated by this layer. In effect, it is the largest subgrain of the distribution. We illustrate the misorientation gradients by coloring voxels according to their misorientation from average in Figure 4.13.

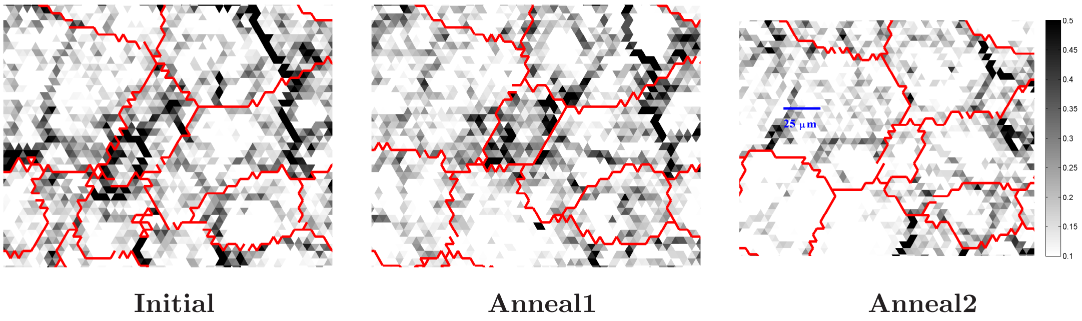

*Figure 4.10: Spatial distribution of the kernel averaged misorientation for the layer of microstructure presented in Figure 4.7. The maps are centered upon the grain that disappears, which clearly shows a disordered microstructure as evident by the dark voxels associated with large KAM values. The disorder is present in the first two states, but in the final state, the region is now part of an adjacent grain(s), with low KAM values. This suggests that the ordered microstructure is exhibiting grain growth in the vicinity of this weakly ordered grain and replacing it with a lower energy configuration.*

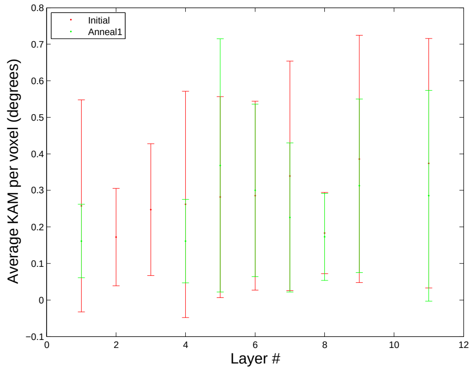

*Figure 4.11: Distribution of the average KAM per voxel as a function of layer in the microstructure. Errorbars are the result of KAM variation for the voxels within the given layer.*

### 4.3.3 Detector Space

Like our discussion of critical events on the surface, we analyze detector space to verify the extinction of this grain through the vanishing of its diffraction signal. Figure 4.14 shows the diffraction peak from the $(1\bar{1}3)$ reflection that shows no evidence of a diffraction signal, on that portion of detector space, in the final measurement state. Many other peaks illustrate this same feature, and this one has been selected simply as a simple illustration that verifies the physicality of this result.

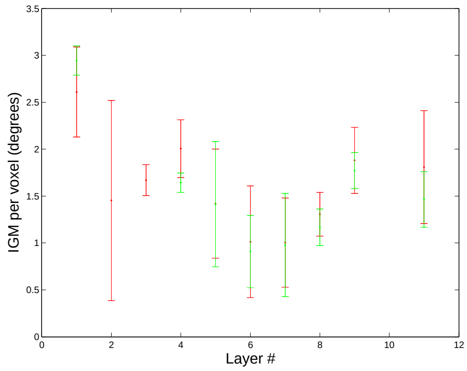

*Figure 4.12: Distribution of the average IGM per voxel as a function of layer in the microstructure. Errorbars are the result of IGM variation for the voxels within the given layer. The majority of voxels are populated in the sixth and seventh layer, which therefore dominates the grain averaged orientation.*

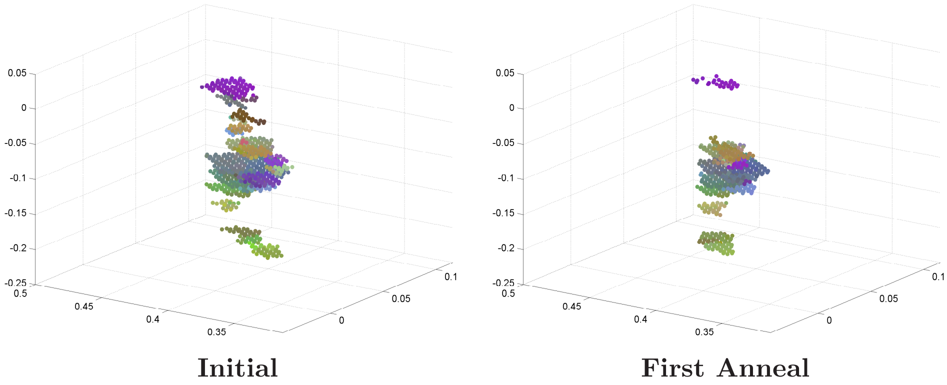

*Figure 4.13: 3D spatial distribution of the IGM for the grain that vanishes from the bulk in the final anneal state. As can clearly be seen, the grain is neither connected over all layers as well as having different layers misoriented with respect to each other. Voxels in each state are misoriented from the average by as much as 3°. This is quite reasonable for a grain elongated by deformation.*

### 4.3.4 Neighborhood Misorientation

In analyzing the neighborhood in which the grain disappears for any special misorientation relationships, as we did for the critical events on the surface, we find none of the resulting microstructure that replaces the grain to have a misorientation close to a *CSL*, or composed of a low-angle boundary. We use the grains in the first anneal state and confine our attention to the grain found in layers 4 through 9, admitting the average orientation of that grain for the misorientation tabulation, instead of the global average that includes pieces misoriented from the remaining bulk. The only misorientation from

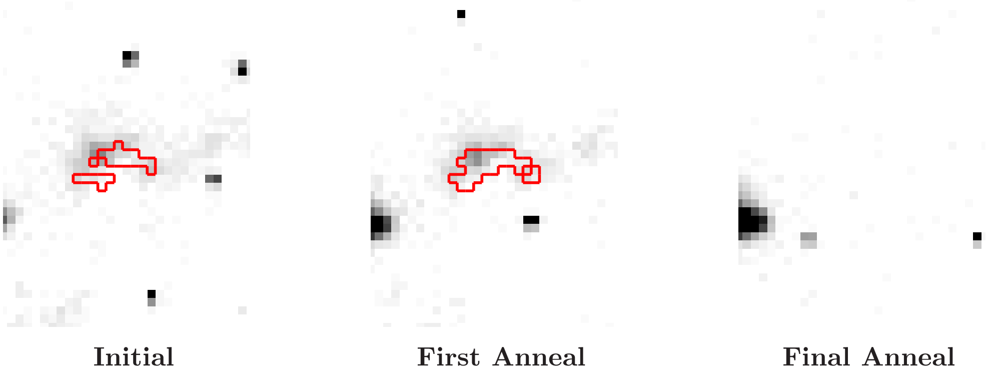

*Figure 4.14: Detector space scattering illustrating the vanishing signal emanating from the grain in the first two measurement states, but absent in the final anneal state. The diffraction is from a (1$\bar{1}$3) peak and the red outline illustrates the diffraction pixels that are generated by the grain via the forward modeling simulation. This peak comes from the sixth layer of microstructure and the disappearance of the peak has been verified by looking at neighboring $\delta\omega$ intervals, as well as the adjacent layers (5 and 7) in the final state diffraction images. In the initial and first anneal state, the peak occupies four contiguous $\delta\omega$ intervals; the middle interval with the most substantial intensity is displayed here.*

a CSL that is below 5° is a pair that is misoriented 3.01° from the $\Sigma$29b, which would not be associated under the Brandon criteria. On this basis, it appears that the cause of grain errosion is due to its high deformation content and supplying energy to replace it with a more perfect lattice is the driving force for microstructural evolution.

## 4.4 Bulk Recrystallization

Our final critical event concerns the observation of grain recrystallization, just after inception, in the bulk of this microstructure. This event was previously noted as an observed nucleation event [3], but after more tedious examination, it was found that there was a collection of voxels consistent with this grain's orientation and location, in the initial state. The conflicting picture was a result of multiple fittings done with maturing versions of both the reduction and forward modeling programs. Before the *LoG* method of peak identification in the reduction process, a simple baseline subtraction was used and evidently eliminated a sufficent number of peaks in the initial state that the forward modeling reconstruction never determined a converging orientation at the grain's location. Therefore, the region was populated by neighboring orientations, but with very weak confidences. After the new reduction program was implemented and new fits produced, the grain was found in an adjacent layer than the one where the nucleation event was deemed to have occured. This original layer was claimed as the nucleation site because the number of voxels in this layer in the first and final anneal was larger than any bordering layer. Figure 4.15 shows the difference between the two maps, illustrating the absence of the grain in the initial state with one fitting protocol and the newest fit illustrating the presence of the grain.

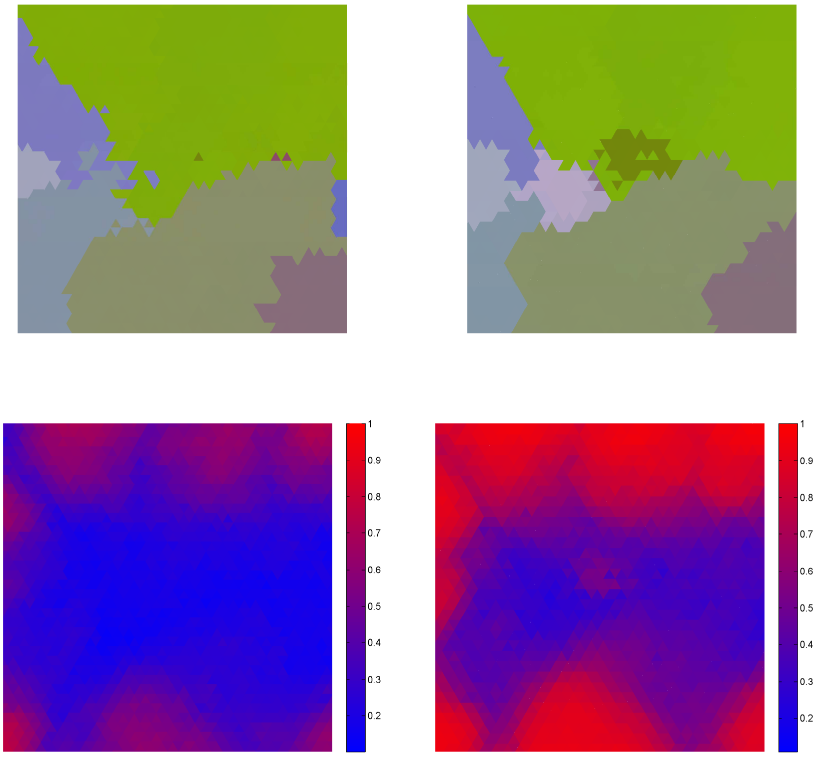

**Old Reduction** **New Reduction**

*Figure 4.15: Illustration clarifying the discovery of the nucleating grain in the initial microstructure, after improvements to the reconstruction and data reduction algorithms. The same portion of microstructure is magnified in the orientation maps in the top row. With the old software, the reconstruction was unable to find any resolvable orientation that was consistent with the experimental diffraction. (Appears we have one voxel with the correct orientation in the original map with $C \sim 0.2$, indistinguishable from noise.) The improvement in confidences is dramatically illustrated, showing that the new algorithms not only discovered a grain with a weak diffraction signal, but also improved the confidences of all voxels in general. The data that has been presented for the aluminum measurement are based upon these newer fits using improved reconstruction algorithms and the new data reduction program. Interestingly, another grain is also identified in the new fit, colored in pink.*

While unfortunate that we did not observe a true nucleation within the bulk, the location and properties of this grain suggest that it had recrystallized just prior to our measurement. Fundamentally, the science has not changed, just our claim that we have 'observed nucleation' [18]. We will summarize the results previously published [3], but also include a parallel analysis of the grain in the layer where it had always existed.

### 4.4.1 Reconstruction Maps

Figure 4.16 shows the region of interest where the grain of interest materialized within the microstructure. We illustrate both the orientation map and the confidence map adjacently, to show how the region evolves with each anneal. Of particular interest is the changes that occur with the confidences associated with the grain. Table 4.7 summaries the state-by-state properties of the grain, which includes a dramatic increase in grain size from the initial microstructure to the final anneal state. Further, the confidence distribution changes with a near constant confidence spread, yet increasing average voxel confidence with each anneal. As will be shown in our detector space images and as can be deduced from our discussion of reduction routines, it appears that this grain's diffraction pattern is becoming seperable from background with each anneal. In the initial state, more than half the peaks do not overlap extractable experimental diffraction. Further, the peaks that are being fit are rather weak and are only found using sophisticated extraction routines [83, 84]. The maps shown in Figure 4.16 have been spatially translated between states to ensure the field-of-view shown in the figure represents the same portion of microstructure. The application of in-plane translations by a single voxel was done between initial and the first anneal, while two voxel lengths in registering the first and final states. These translations were determined through minimization of misorientation between overlapping voxels in each state for the given layer.

*Table 4.7: Voxel Statistics for Bulk Recrystallization Event*

| State | Initial | Anneal1 | Anneal2 |
|---|---|---|---|
| Number of Voxels | 40 | 155 | 570 |
| Number of Layers | 1 | 2 | 3 |
| Average Confidence | 0.45±0.05 | 0.65±0.07 | 0.84±0.06 |
| Average KAM | 0.11±0.059 | 0.11 ±0.06 | 0.067±0.05 |
| Average IGM | 0.17±0.1 | 0.12±0.07 | 0.116±0.10 |

### 4.4.2 Internal Misorientation Distributions

Echoing previous analysis, we illustrate two properties of the nucleating grain, pertaining to internal orientation variation. The first is that the initiation site is a region of high local disorder. The second property is that the nucleated microstructure that replaces the current microstructure is much more ordered than what it is supplanting. Like all of our past discussion of disorder, we use both $KAM$ and $IGM$ to characterize defect content with the microstructure maps. We use the layer of microstructure adjacent to the one where the grain has nucleated ($z_6$) to characterize what the local disorder was probably like before the event occured. This is accomplished with $KAM$ in Figure 4.17, where the region prior to grain occupation has many dark voxels, indicating high $KAM$ values. Additionally, the new grain is composed of white voxels, characterized by low $KAM$ values and summarized in Table 4.7. $IGM$ is also summarized in the table and admits comparatively large spread in the initial state, which minimizes in the final two states to noise about an average orientation. This is commensurate with the low confidences, since the grain is determined through the fitting of a collection of weak peaks. The expanded color scale $IGM$ maps for the layer with the grain existing in all three states is shown in Figure 4.18.

We can infer that the portion of microstructure, which serves as the nucleation site for this recrystallized grain, was previously occupied by a disordered lattice. The grain that eventually replaces this dislocated microstructure is of nearly a perfect lattice, singularly orientated. This is evidenced by the low $KAM$ voxels in the final state supplanting those with high values in the initial. Further, we see that the grain has a very small orientation spread as determined through $IGM$ calculations, which is of the order of our orientation resolution for our reconstructions.

### 4.4.3 Detector Space Evidence

We can correlate the uniform orientation signal found in the microstructure maps with the diffraction signal that is their origins. Like our discussion of critical events on the surface of the microstructure and the disappearing grain that was found within the bulk in Section 4.3.1, we use the forward modeling simulator to identify regions of detector space responsible for the orientation assignments in the sample. Figure 4.19 shows scattering that originated from the layer where the grain was always present. Red lines outline the simulated scattering that originates from the nucleated grain in the sample. The top row displays the (133) reflection, which was used for sample space reconstruction and had extractable intensity, above background, in the initial state nfHEDM experiment. The second row illustrates scattering where the initial state peak was not resolved with our image processing and is scattering from the $(1\bar{3}1)$ reflection. Both peaks are isolated in the $\delta\omega$ partition of detector space. For the initial state, the same $\delta\omega$ interval is searched in the adjacent 2D measurement layers and no experimental intensity was founded in this portion of detector space. Figure 4.20 displays a collection of peaks from the layer where the grain is present in only the final two measurement states [3]. This is shown for completeness and to illustrate the absence of the grain in the adjacent layer, in the initial state.

To give a complete picture of scattering and the corresponding reflections, we take the initial state microstructure and record which peaks are overlapping experimental intensity as identified with our $LoG$ reduction routine, and then follow the distribution through the next set of anneals. While the grain size does change at each anneal state, we still have a large enough grain that peak overlap can be identified. This is summarized in Table 4.8 and we obviously only record reflections that should be present in our field-of-view. The number of peaks listed for the lower order reflections are complete, i.e. there is only one reflection from the {111} family for this grain that is observable in our experimental setup. The table clearly shows that as we increase the reflection order, more peaks become visible in the experimental images. We only report the peaks that were employed for the reconstruction, though if we go to higher $|\boldsymbol{Q}|$, we see many new peaks present. Specifically, the {442}, which is never found to overlap in the initial state has five peaks appear in the final diffraction state. Additionally, we see reflections as high as the {731} extractable from background.

*Table 4.8: Overlapping Peaks for Recrystallized Bulk Grain*

| Reflection Family | Initial | Anneal1 | Anneal2 |
|---|---|---|---|
| {111} | 1 | 1 | 1 |
| {220} | 4 | 4 | 4 |
| {311} | 5 | 5 | 6 |
| {222} | 2 | 2 | 2 |
| {331} | 4 | 7 | 8 |
| {420} | 3 | 6 | 6 |
| {422} | 1 | 4 | 6 |
| {511} | 3 | 7 | 7 |
| {333} | 0 | 2 | 2 |
| {440} | 0 | 1 | 2 |

### 4.4.4 Neighborhood Misorientations

Table 4.9 describes the relationship between the nucleating grain and its neighborhood in the final state microstructure. As is evident from the list of nearest CSLs, there is no clear origin for the orientation of the new grain, though the misorientation between the nucleated grain and the first and second grains are less than the 15° definition of a high angle grain boundary. Grain 1 has a misorientation of 14.3° with the nucleated grain, while Grain 2 has a 12.2° misorientation. Therefore, it is plausible that the nucleated grain was initially part of either of these grains. Still, this is on the high angle side of the spectrum of misorientation, which leaves this work somewhat consistent with earlier work. [51] The first six entries listed in the table are in-plane neighbors in our measurement, while the final grain was in an adjacent layer.

*Table 4.9: Misorientation relations of grains in the neighborhood of the nucleated grain.*

| Grain | Misorientation | Nearest CSL ($\Sigma$) | Misorient. from CSL (degrees) |
|---|---|---|---|
| 1 | (0.9922,-0.0687,-0.1026,0.0146) | 25b | 9.2 |
| 2 | (0.9943,-0.0621,0.0076,-0.0859) | 25b | 9.6 |
| 3 | (0.9558,-0.0765,-0.0154,-0.2833) | 27b | 7.2 |
| 4 | (0.9495,-0.0735,0.0189,0.3045) | 27b | 8.3 |
| 5 | (0.9568,-0.1612,0.0842,0.2270) | 27c | 11.1 |
| 6 | (0.9767,0.0005,0.0351,0.2117) | 13b | 4.42 |
| 7 | (0.9599,-0.0674,0.0037,-0.2720) | 27b | 7.9 |

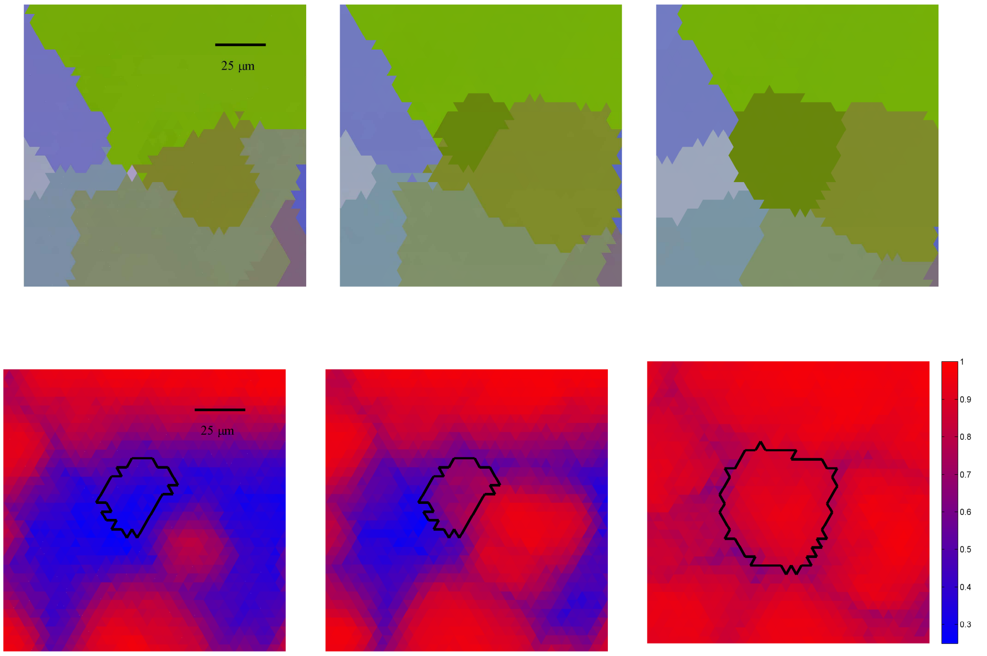

**Initial -** $z_6$ **Anneal1 -** $z_6$ **Anneal2 -** $z_6$

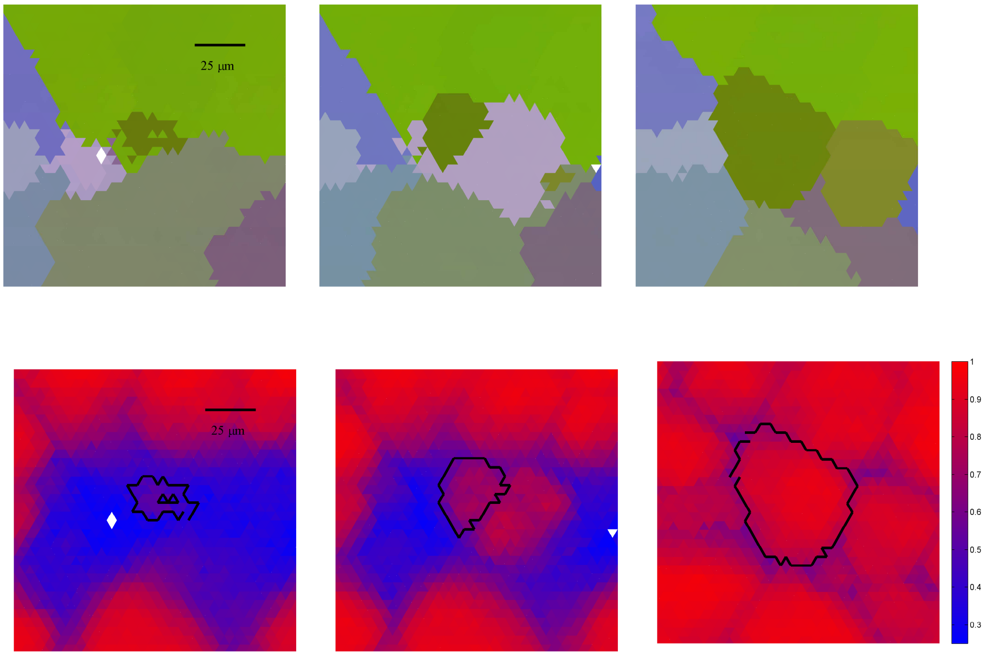

**Initial -** $z_7$ **Anneal1 -** $z_7$ **Anneal2 -** $z_7$

*Figure 4.16: Confidence and orientation maps from two layers of microstructure to illustrate the nucleation of a grain from a region of low confidence, associated with no strong scattering signal. The top two rows show the orientation and confidence map for the layer originally investigated and stated to be the location of the nucleation event. [3] The bottom two rows are from an adjacent layer, where the grain was found to be present in all three states, only with a weak confidence signal in the initial state. An outline of the grain boundary in each state is shown in black, while the confidence map for the initial state map where the grain is not present (row two, column one) has an outline of the first anneal state's grain boundary location.*

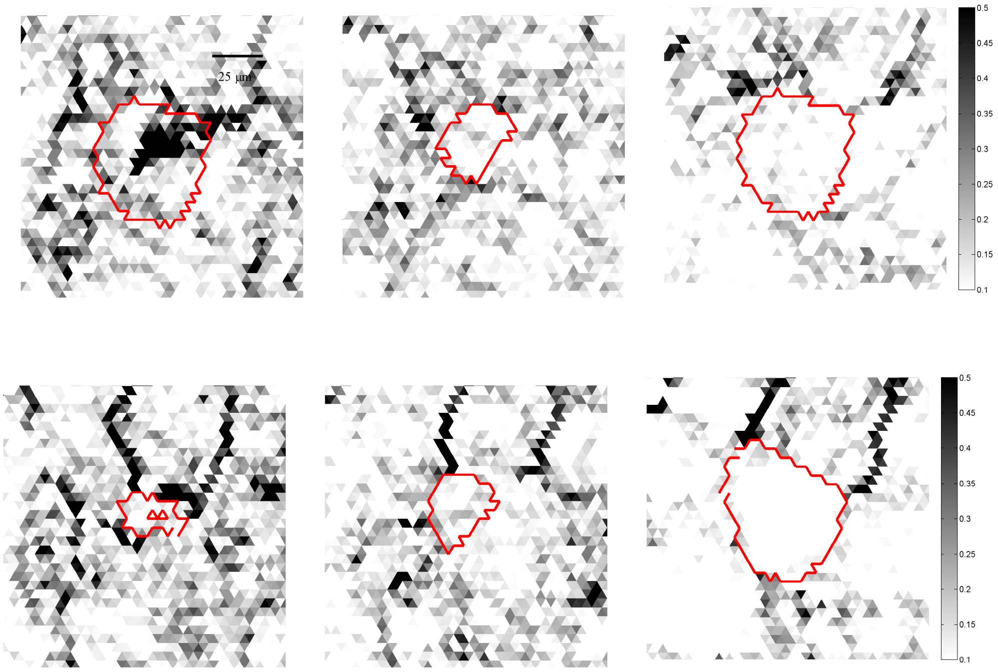

*Figure 4.17: KAM distribution of voxels for the two layers of microstructure shown in Figure 4.16. The color scale saturates at 0.5°. Outlines illustrate the location of the grain in the actual map, except for the first map, which has the same outline as the grain in the final state for that layer, simply to illustrate the region that is eventually engulfed by the nucleating grain. Both layers illustrate that the grain is highly ordered in the final state, as evidenced by its composition of low KAM voxels, while the initial state was composed of high KAM voxels in the region of nucleation.*

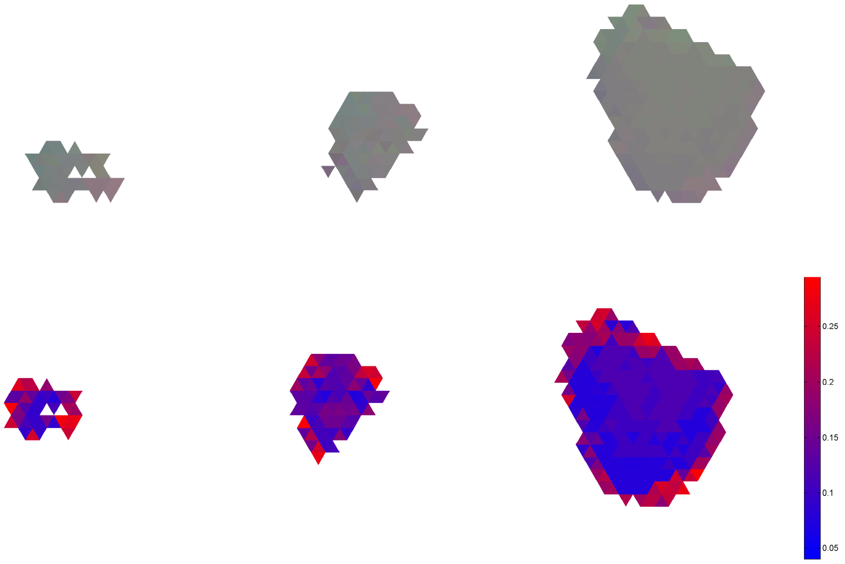

*Figure 4.18: IGM distribution for the recrystallizing grain in the bulk microstructure. Top row shows each voxel colored by the full three parameter misorientation from average, while the bottom row has voxels on a red-blue scale, colored by misorientation angle from average; the one dimensional parameterization of misorientation. Note the small rotation angle scale for the bottom row. This new grain is effectively composed of a single orientation, with noise about this singular value a result of the reconstruction resolution.*

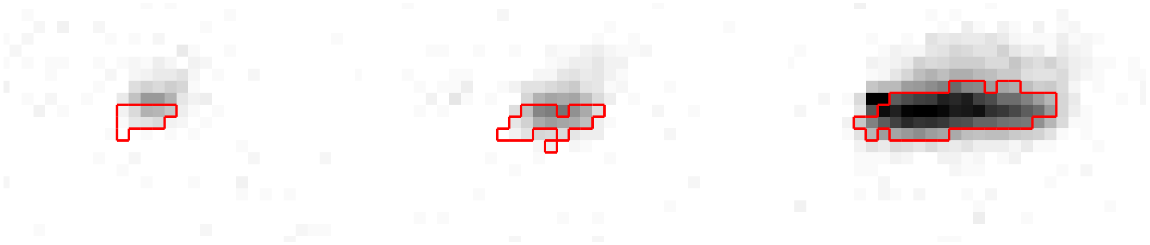

**Initial** **First Anneal** **Final Anneal**

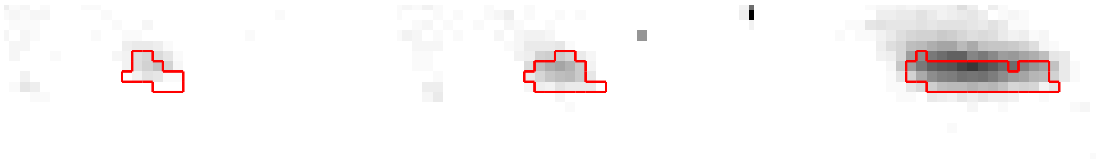

**Initial** **First Anneal** **Final Anneal**

*Figure 4.19: Scattering from the nucleating grain through the three sample states for the layer where the grain was aways present. Each row shows a different reflection, with the top row being the (133) reflection and the bottom row ($1\bar{3}1$). The top row had the experimental signal extractable in all three scattering states, while the initial state for the bottom row had the intensity too weak to be seperable from background with the newest reduction routine. Red outlines indicate the pixels that are hit by the nucleating grain in the forward modeling simulation.*

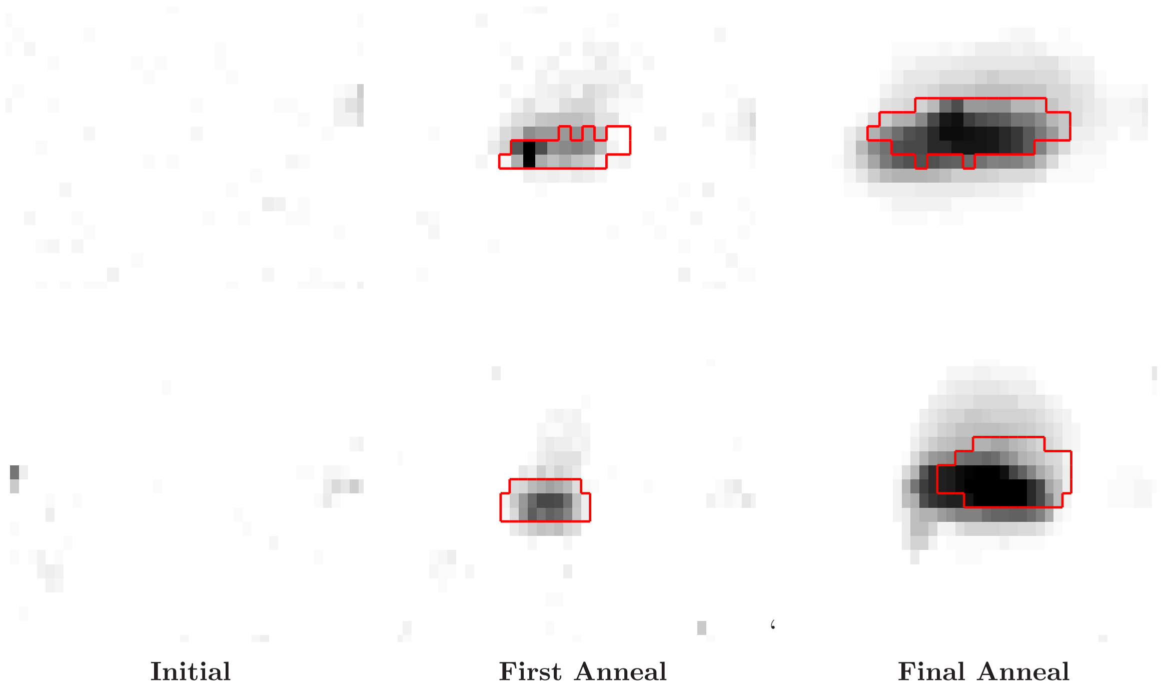

*Figure 4.20: Scattering from the layer where the nucleating grain is only present in the final two sample states. Each row consists of the raw detector images that have been background subtracted, but not subjected to a median filter. Peaks are isolated in $\delta\omega$ to this singular interval. Red lines indicate the simulated scattering signal that originates from the nucleating grain. Top row illustrates the (133) reflection, while the bottom row shows the ($\bar{2}04$).*

## 4.5 Discussion

We have presented the results of measurement on high purity aluminum using the forward modeling analysis of nfHEDM diffraction data. The sample was heat treated at low temperatures and the same small sampling of microstructural volume was measured with 2D maps of the cross-section. The initial state of the microstructure exhibited intra-granular orientation variations that are commonly attributed to the presence of defects or dislocations. Through the annealing process, we were able to discern two responses within the microstructure.

The first response was a global ordering of the microstructure, which can be attributed to changes in the spatial distribution dislocations such that localized regions of the microstructure approached a singular orientation with each anneal step. This was characterized in both sample space and detector space. In sample space, statistical analysis was conducted on two length scales, where the first measured extremely localized orientation variations through the kernel averaged misorientation or $KAM$. Here, it was found that orientation variations were minimized in each anneal step, within the bulk microstructure. On a larger length scale, intra-granular misorientation or $IGM$ monitored how voxels within a compact collection of similarly oriented voxels, classified as a grain, evolved. Here, observations including the formation of subgrains were realized and characterized. In both the context of $IGM$ and $KAM$, we see that the microstructure has become more ordered than each of the previous states and verified this through extraction of reconstruction's source signal in the experimental detector images. Peaks were associated with scattering within the microstructure and their shape evolution was tracked from state to state, illustrating common themes within recovery, such as the narrow of peak widths in the $\delta\omega$ partitioning of detector space.

The second observation was the existence of several critical events within the microstructure, which concern the appearance or disappearance of a grain in response to annealing. While a large number of such events were found to occur on the sample surface, there were two critical events that were monitored within the bulk. A disappearing grain was identified in the first two measurement states that was composed of a complicated geometry of several remnant grains, disconnected among different measurement layers. Consistent with expectations regarding the replacement of deformed microstructure with a uniform lattice, we noted that disappearing grain was composed of voxels of high $KAM$ and eventually replaced by the surrounding grains' highly ordered lattices. The diffraction signal confirmed the disappearance of the grain by identifying the disappearance of peaks in the final measurement state in regions of detector space previously occupied by diffraction from this grain.

We were also able to identify a grain just after the onset of recrystallization. The grain was composed of voxels of a nearly singular orientation through multiple measurement layers. Both $IGM$ and $KAM$ characterized such an ordering, with very low values for both quantities within the grain. The region in which this grain fills the microstructure was also investigated and displayed high local disorder through large $KAM$ values.

Detector space illustrated weak scattering associated with the grain in the initial state, but as annealing progressed and the grain became larger, peaks of higher order were distingushed from the background.

For both bulk and surface critical events, we discuss the misorientation of the grain with its neighborhood and found no clear occurances of special configurations that underlie many low energy boundary configurations. This is inconsistent with other works [88] that identify recrystallized grains as having a special orientation relationships with grains in surrounding neighborhood. Our observation also contrasts the understanding that 'nucleation' of a new orientation within a bulk polycrystal is energetically difficult [16]. With these comparisons, we should emphasize that our results are inconclusive at best, due to the coarseness of the vertical spacing leaving us unable to determine boundary orientation of the grain, which completely characterizes the boundary interface network, which is necessary for a full energy description of the initiation site.

While this data set was able to identify the signals of these two annealing phenomena, its scope was still limited by the experimental setup at the time of collection; most notably the camera capabilities. With pixels on the order of 4 $\mu m$ and collection times lasting nearly half a minute per image, the production of a statistically significant data set was impossible. The eleven layer microstructure with three anneal states was the best possible use of time to generate a data set that probed polycrystalline dynamics in response to annealing. Still, with few grains encapsulated within the interior volume of measured microstructure and many consisting of one or two cross-sections through the grain, content such as boundary plane were simply unresolvable. Further, the use of such low temperatures due to the *in-situ* design at the time of collection restricted the measurement to only the two of the three expected annealing phenomenon, with grain growth notably absent. Glacial movement of boundaries were probably observed during the measurement, but are on the order of our spatial resolution and therefore indiscernable. This is unfortunate, since questions pertaining to the movement of boundaries with respect to defect content would provide another signal in the annealing response. Do grains with small defect content (small dislocation densities) grow into grains with large dislocation densities? Answers to such questions would be of great interest to the materials community, especially when investigated with bulk microstructure.

The next section presents a similar annealing experiment only with significant advances made to the experimental microscope. Here, instead of measuring the annealing response of deformed microstructures, we begin our investigation after recrystallization of the full microstructure. Like this aluminum experiment, we apply differential anneals, except they are at much larger temperatures and encourage the motion of high angle grain boundaries in the grain growth process. With the amount of scientific content that this grain growth measurement has afforded, it seems that it would be beneficial to repeat this aluminum experiment to watch the complete effects of annealing on a high purity metal from the recovery of a deformed microstructure to coarsening in grain growth, as near perfect crystals evolve as an ensemble.

# Chapter 5

# Grain Growth in Polycrystalline Nickel

## Introduction

We present the results of a second annealing experiment conducted with high purity polycrystalline nickel. Much like the previous aluminum experiment, we apply heat to the specimen for a fixed duration, then measure the evolved microstructure at room temperature. While both measurements are based on the annealing response in a high purity metal, the observed signal was dramatically different. This was predominantly due to the initial state of the microstructure and the temperatures used for the anneals. Specifically, the nickel sample had an initial state that was fully recrystallized and did not exhibit the orientation gradients within its grains that were present with the aluminum. Therefore, the evolution was not influenced by the ordering of grains. Secondly, the temperatures used for this measurement were significantly higher than those applied to the aluminum experiment. In terms of homologous temperature $T$, the nickel measurement was performed at $\sim 0.6T_{Ni}$, while aluminum was measured at $\sim 0.35T_{Al}$. As such, the microstructural response is different and grain growth is the dominant signal, while recovery was the more overt process with our aluminum experiment.

The content to follow will be devoted to our study of grain growth in polycrystalline nickel and how its evolution through multiple microstructural states. Sections 5.1 - 5.3 presents experimental details including a description of how measurement practices have changed since the earlier work on aluminum, presented in Chapters 3 and 4. We first analyze, in this chapter, some simple statistics that are traditionally presented in grain growth studies. These include quantities of topological significance such as volumes, surface areas, and numbers of neighbors. The effects associated with parameters used to extract these quantities from experimental data are studied in detail. We then analyze how these quantities change with annealing. In the next chapter, we interpret the microstructure in terms of crystallographic orientation, misorientation and the evolution of these quantities with annealing.

## 5.1 Sample Preparation

The material used for the grain growth experiment was 99.999% purity nickel, which was purchased from Alfa Aesar in the form of a 5 $mm$ diameter × 50 $mm$ rod. The sample was electric discharge machined (EDM) from this stock into a 1 $mm$ diameter piece with overall length of 20 $mm$. The sample had an asymmetric cross-section geometry that permitted alignment which is a necessity for an *ex-situ* annealing experiment. Specifically, there was a square cut notch placed at the sample tip with a length of $1mm$ and radial depth of $500\mu m$. This geometry admits an ability for both rotational alignment of the sample and vertical volume displacement registration. For the experiment, the notch was imaged with an unfocused beam and is shown in Figure 5.1. The location of three feature points in the sample projection, within the broad beam, were recorded. The volume was then collected $1mm$ from the base of this notch, with adjustments to the volume size to account for grain growth outside of the initial imaged volume. A small protrusion is also present on the long side of the sample cylinder as a result of the EDM process. This feature provides a rotational reference when attempting to do one-to-one comparisons of maps between states. While this later feature was not originally intended, it was of great use during the on-line fitting process outlined in Section 5.3.

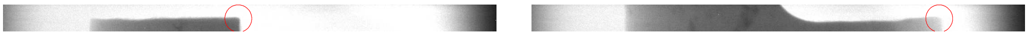
**(a)** **(b)**

*Figure 5.1: Profiles of the tip of the nickel sample in the transmitted beam. Images are the result of translating the sample vertically by $1mm$, with (a) as the top projection and (b) the transition region into a full cylinder. The red circles indicate the reference position that was used for determining geometrical changes in the sample as well as marking the vertical displacement required to collect overlapping sample volumes. In the fourth anneal state, the sample began to exhibit a bow, which resulted in the distance between the two recorded circles to expand. Hypotheses concerning the origin of this bowing are discussed in the text.*

The as received nickel microstructure had grain sizes of the order of a few microns, which is too small to be imaged. Thus, preliminary heat treatment was necessary.

The initial state of the sample used in the measurement was the result of an anneal at 750°C for 2 hours in a tube furnace setup equipped with a quartz tube, a vacuum pump, and a gas handling system allowing for use of a controlled atmosphere. Our annealing was done in forming gas ($97\%N_2, 3\%H_2$). The process for producing the forming gas environment is a flushing sequence, where the quartz tube is evacuated for 10 minutes, flooded with forming gas for 10 minutes (at a flow rate of 2 $cm^3$/second), then repeated. After the second forming gas cycle, the furnace is brought to the operating temperature and the sample is slid into the cavity, after beginning the process several inches upstream (and therefore not subject to heated gas). After the annealing duration is achieved, the sample is moved back to this upstream position, while forming gas continues to flow. In this configuration, it takes approximately 10 minutes to reach room temperature, where it is then removed from the tube.

This anneal schedule was adopted after extensive tests on specimens from the same sample stock. We produced $\sim 3mm$ long, $5mm$ diameter wafers that were mechanically polished to the extent that boundaries were visible on the surface using standard optical microscopy. Grain size estimates for different initial annealing sequences in $25°C$ and 15 minute intervals were obtained. Once the satisfactory initial grain size (of $\sim 40\mu m$) was determined, the test samples were then annealed multiple times and boundaries on the surface were monitored. When appreciable, yet differential changes in boundaries were seen, we established the annealing routine to be used in the experiment. Of course this entire preparation process is based upon monitoring events on the surface, so the liklihood of surface effects producing different grain dynamics behavior is a concern. Yet still, by noting that the sample is a small, free standing object and that the distribution of grain sizes on the surface (from the 2D images) follows the same size distribution as the bulk, we can safely assume the the motion of the bulk grains should be of the same order of magnitude as the observed surface motion. Lastly, no texture was obvious from previous measurements on this same sample stock by the Wynblatt group at Carnegie Mellon, as well as test measurements on the material conducted at the APS. If texture was present, a casting process would be necessary to generate as isotropic microstructure as possible.

## 5.2 nfHEDM Measurement

As in the previously outlined aluminum experiment, the nickel grain growth study was conducted at the 1-ID-B hutch of the Advanced Photon Source. Improvements to the experimental setup were realized between the times of these two experiments. Specifically, by the time this late 2010 experiment was conducted, a new Peltier cooled camera had been installed, with more stable collection software. In addition to the cooling system improvement, which does not require intermittent user intervention, read-out times on the camera also dramatically improved. While roughly 20 seconds of overhead time per image was required for the previous system, this new CoolSnap camera required only dead time due to the motion of motors required between images, which amounts to $1.7s$. The only regression with this camera was moving from a 16-bit dynamic range to 12-bit. Since the analysis presented is not reliant upon intensity fitting, this is a non-issue, though a larger dynamic range would allow for the imaging of weaker peaks while still not saturating those of high intensity.

### 5.2.1 Progress in Experimental Setup

Due to time constraints, the experiment was performed over two separate beam runs (October and December 2011). The second anneal state volume was split between these runs. Both measurements used the same setup with identical operating energies

($64.351keV$) and camera system equipped with the lutetium scintillator previously discussed. A new collection protocol was employed for these data sets, both in terms of collection routine and real time fitting. The former was implementing the full 180° rotation collection in $\delta\omega = 1°$ intervals. This results in an increased number of peaks (and therefore projection geometries) being imaged on the detector. The second process was the ability to collect data and reconstruct it 'on-line', meaning that fits were produced while the sample was present in the beam. With the development of a new, parallel generation of the forward modeling program [66], the ability to collect data and begin a fit has become standard. Like the aluminum experiment, $30\mu m$ gold wire was used as a calibration sample for determination of the experimental geometry of the setup, which was then left static after the sample was changed to the high purity nickel.[1]

Collection of images was done at an $L_1$ distance of $4.85mm$ for the October volumes, $4.81mm$ for the December volumes, and $\Delta L = 2mm$ for the detector spacings. This distance was a compromise between the need for imaging as many Bragg peaks as possible (and therefore a desire to be as close as possible) and the physical restrictions of the sample, beam block, and the highly complex collection of peaks due to the fine grained, polycrystalline sample. Hence, we avoid imaging too close because individual peaks become indistinguishable.

The direct beam and rotation axis were centered on the camera, so the $(j_0, k_0)$ address of the rotation axis - direct beam intersection was close to the horizontal center (pixel 1024) of the camera and as low in the vertical direction as possible, while still permitting the direct beam to be imaged. During the course of collection during both runs, no appreciable intra-volume beam drift was observed. Therefore, we assume the $(j_0, k_0)$ intersection to be the one measured for the nickel calibration layer (discussed later) and maintain this value for the duration of the experiment.

Since the optics on the camera are removed between runs, the pixel pitch was re-evaluated and found to be $1.48\mu m/pixel$ for both runs. This number is the result of placing a focused beam 20 $\mu m$ in width on the camera, which is translated over a $20 \times 20$ grid. Figure 5.2 shows an example of one of these raster scans, where the individual direct beam images have been stacked to illustrate the grid pattern. Since each position of the camera is recorded, the distance between camera collection points can be determined. By fitting the direct beam profile, a center and width of the beam (in pixels) was characterized. Our pixel pitch ($1.48\mu m/pixel$) is the result of determining the pixel displacement between all rastered points and their known displacement (via motor positions). Variation in pixel pitch was less that 1%, which is consistent with other nfHEDM measurements with this same setup. The image shown in Figure 5.2 is not from this specific data set, but is meant to be shown as an illustration of the process.

---

[1] We should emphasize that static means that not only is the camera not physically moved in the imaging plane, but the distances at which the gold data was collected is used for the target sample that is measured. If the experiment necessitates a change in the camera configuration, gold must be remeasured to effectively 're-zero' the experiment. This instance occured specifically during the December collection, when the nickel was taken out of the beam for a test sample that unfortunately required changes in the detector alignment. Thus, a remapping of the gold was necessary.

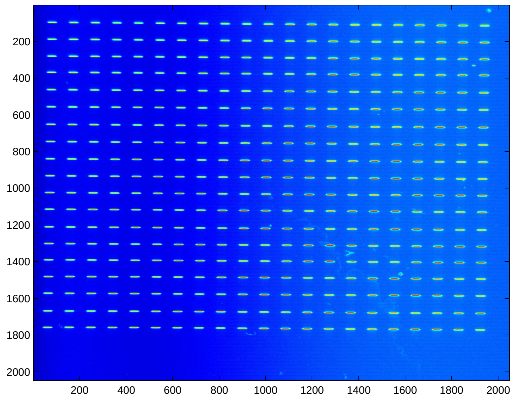

*Figure 5.2: Example pattern of a raster scan used to determine pixel pitch of the nfHEDM camera. In this image, a* $50\mu m$ *beam is placed on the camera, which is translated to produce the pattern seen here. In the event of distortions, such as spatial variation in the imaged beam, adjustments can be made to the camera mount to approach a flat imaging plane.*

Lastly, a coarse grained, tungsten beam attenuator was used for this experimental setup, in contrast to the polycrystalline tantalum attenuator used in the aluminum measurement. As discussed in Chapter 2, this new attenuator allows for the constant profiling of the direct beam on each image, which can be used to monitor both drift in the direct beam (by observing a temporal displacement in the vertical position of the direct beam), or a tilt in the camera (by observing a rotation in the projection of the direct beam on the imaging plane). Corrections for such drifts were unnecessary, unlike for the $LN_2$ cooled camera used for the aluminum experiment. This was verified with the parameters optimization program, where no systematic shifts to either pixel center $(j, k)$ or the camera's rigid body orientation were found. Simply, the camera was as perpendicular to the direct beam as is achievable with our setup.

In addition to beam attenuator's transmission feature, the limited number of grains in the beam attenuator's cross-section results in a lower probability of Bragg peaks being present on the detector, and when present, elimination can simply be achieved by either translation of the beamblock in the laboratory $\hat{\boldsymbol{x}}$ direction, or small rotations about the length of material. Figure 5.3 makes clear the improvement in beam block signal on the detector. While these spots are always static, and therefore should be eliminated in the generation of the statistical background image, uncontrolled motion of the beam block and intensity fluctuations in the direct beam can result in variations in the beam block diffraction and therefore poor background images. Thus, having as few beam attenuator peaks on the camera as possible is desired.

---

[1] Further, the more beam attenuator peaks that are present, the higher the likelihood that one of

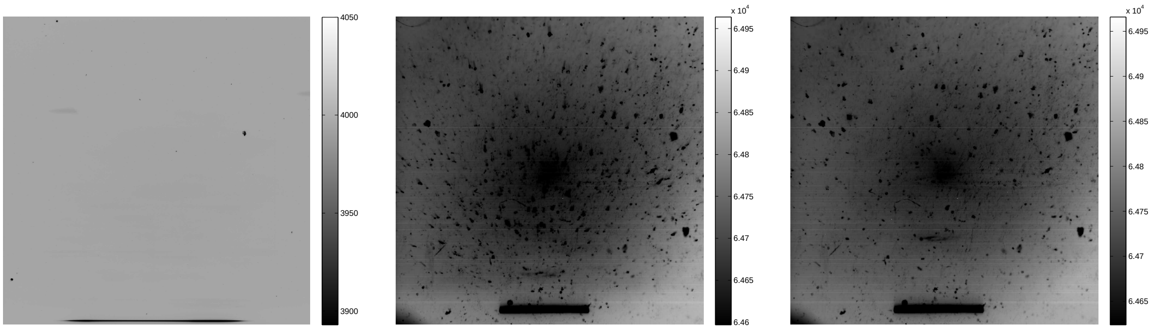

**(a)** **(b)** **(c)**

*Figure 5.3: Comparison between the two beam attenuators used during the course of development of the dedicated nfHEDM setup at 1-ID-B. The nominally single crystal tungsten beam attenuator used for the nickel experiment is shown in (a), while (b) and (c) are from the aluminum experiment using the polycrystalline tantalum beam block. The images produced here are the statistical background images that have been discussed previously, which has each pixel assigned the median intensity over the $\delta\omega$'s used for that single detector distance. (a) and (b) are from the first detector distance ($L_1$), while (c) is from the final detector distance and is used to further illustrate what is beam block and what is scintillator artifacts. Peaks that change spatial location, but move consistently, are due to beam attenuator diffraction. The features that look the same at $L_1$ and $L_3$ are due to imperfections on the scintillator, which was also changed for the nickel experiment to a free standing single crystal. Specifically, the fine, curved line features are imperfections on the Ce scintillator. The cameras used for these measurements were also different, with different number of pixels, pixel sizes, and dynamic ranges. Lastly, the shadow at the base of the aluminum images is not the direct beam, but diffuse scattering off the surface of the tantalum beam attenuator.*

### 5.2.2 Experiment

The nickel annealing experiment consisted of a total of six microstructure states, including the starting state, which we refer to as *Anneal0*. Due to unforseen constraints at the synchtrotron setup, the first two anneals were achieved without using a vacuum system and a different tube furnance than the one used for the production of the initial state and the final three anneals. Therefore, some variation is present in the anneal schedule, which is listed in Table 5.1. The description of each state is the annealing required to produce that state. Therefore, the long heat treatment for *Anneal0* describes the recrystallization anneal that takes the sample from the nanocrystalline state to a coarser grained polycrystal.

After the fourth anneal, the sample began to exhibit a bowing that made registration of different sample states challenging and we therefore limit our correlated analysis to the

---

these peaks will saturate the camera and produce a region on the detector where sample scattering can not be easily separated.

*Table 5.1: Annealing Schedule for Polycrystalline Nickel*

| Anneal State | Duration | Temperature | Environment |
|---|---|---|---|
| 0 | 2 h | 750°C | $97\%N_2, 3\%H_2$ |
| 1 | 23 m | 800°C | $97\%Ar, 3\%H_2$ |
| 2 | 30 m | 800°C | $97\%Ar, 3\%H_2$ |
| 3 | 25 m | 800°C | $97\%N_2, 3\%H_2$ |
| 4 | 35 m | 800°C | $97\%N_2, 3\%H_2$ |
| 5 | 25 m | 800°C | $97\%N_2, 3\%H_2$ |

first four. The origin of the bowing has yet to be conclusively diagnosed. The presence of a few large grains beginning to volumetrically dominate our measured volumes suggests that the onset of abnormal grain growth might have been present. If true, it is possible that for a sample of our dimensions, the growth of these abnormal grains and the high probability of abnormal shapes lead to structural changes in the sample geometry and the observed bowing.

Since these heat treatments were designed to produce grain growth in the sample, we expect average grain sizes to increase with each anneal. Therefore, the measured volume must be adjusted accordingly. With the exception of the first two states, where collection times were limited and the same number of cross-sections collected, each state had added 'layers' both above and below the previous measurement window. The number of contiguous (and distinct) layers are listed in Table 5.2. The camera exposure times required for each $\delta\omega = 1°$ collection interval was constant for all volumes and $1.4s$. Despite larger peaks as a result of larger grains, this count time was never long enough for appreciable peak saturation, which would distort the image data. While count times could have been slightly lower, the $1.7s$ overhead of motor motion for each image and the ability to get significant signal from weak peaks resulted in the use of this constant collection time.

*Table 5.2: Volume Collection of Polycrystalline Ni*

| Anneal State | Number of Layers | Number of Volumes |
|---|---|---|
| 0 | 70 | 4 |
| 1 | 71 | 5 |
| 2 | 87 | 2 |
| 3 | 86 | 2 |
| 4 | 101 | 2 |
| 5 | 104 | 1 |

The notched sample tip was used as the macroscopic fiducial mark for alignment of volumes during nfHEDM data collection. Since the production for one of these optimized maps would be on the order of 3-6 hours using the available computing resources and online optimization abilities, it was necessary to ensure that we were measuring the same volume without having to fit a layer and make adjustments. The monitoring of fiducial layers is also necessary because this experiment is done *ex situ*, unlike the previous aluminum experiment. Before the collection of each volume, we measured the projection of the tip in a wide, unfocused direct beam ($\sim 1.5mm \times 300\mu m$). The sample was rotated so that the vertical edge of the notch was as parallel to the beam as possible, using 0.1° steps. We recorded these projections and manually adjusted any tilts from vertical that maybe be present and would make registration using 2D sections more difficult. Images of this projection, as well as a projection of the base of the cut (which is parallel to the beam), were collected at the same $L$ distances and motor positions were recorded (specifically those relevant for rotation and vertical sample translation). This imaging process was done both before and after collection of a nfHEDM volume. Evidenced by near identical images (to within a couple pixels) for these temporally separated measurements, we were assured that sample and motor drifts were not experienced over the course of nfHEDM data collection. Images of these two projection configurations are shown in Figure 5.1.

In addition to the transmitted beam imaging of this ‘fiducial’ region, nfHEDM mapping also was used for registration among sample states. The justification behind this process was to get a more specific indication of the vertical location we are mapping in each 2D measurement. Three layers were collected in the region where the sample transitions from a half cylinder into a full cylinder (notch), with the objective of capturing the location where this transition occurs. The three layers were spaced $4\mu m$ apart. One unintentional benefit of this fiducial region was the presence of a bump along the flat region on top of the full $1mm$ cylinder. Therefore, the reconstructions of this region show two compact regions; the half cylinder and this island of microstructure. The size of this island further aided the interpretation of spatial location along the sample.

The first collected volume of eventual 3D microstructure was $1mm$ below this fiducial transition. Spacing between consecutive layers of microstructure was $4\mu m$, which was based on the $4\mu m$ FWHM of the focused beam and the need for at least 5 cross-sections through each grain in the microstructure for faithful 3D grain shape determination. After each annealing treatment, additional layer measurements were added both above and below the previous state’s extremum layers. Since the anneals were designed to produce differential and not dramatic volume changes, the increase in number of measured layers from state-to-state was more for ensuring overlap between measurements than accounting for expected grain volume shifts. To further complicate the data collection, the singular nfHEDM volume that represents each anneal state is actually the composition of several subvolumes (see Table 5.2) that were collected due to variable issues including problems with data collection software (*Anneal1, Anneal4*), hardware problems involving the fast shutter-rotation stage triggering (*Anneal0*), time constraints (*Anneal2, Anneal3*). The time constraints actually forced the sample off the x-ray microscope and therefore an intra-state rotational discontinuity exists, which adds an additional complication to the sample registration. It should be noted that each volume is composed of the number of layers indicated in Table 5.2, but these are *distinct* layers. When a new subvolume was necessary, a layer from the previous subvolume was collected to ensure overlap. Lastly, each subvolume contained at least one 3 detector distance measurement, which was collected for the intent of parameters optimization. Three detectors constrain the measurement more than two, so using a three detector mapping is better served for this purpose. At least one of the fiducial region measurements also used a three detector collection.

## 5.3 Forward Modeling

### Reduction

The collected diffraction data was reduced by generation of a statistical background image for a given layer and camera distance that was subtracted from each individual $\delta\omega$ file. The image was thresholded with a baseline of 3 counts and all pixels in a peak in excess of 5% of the maximum peak intensity were retained. This is a more simplified process than the edge detection sequence used for the aluminum data. The newest reduction program was developed later than both of these experiments. Since the aluminum data set was sufficently small that re-reduction and re-fitting of the data was feasible, it implemented the newest reduction algorithm and yielded improved results and when coupled with changes to the reconstruction software, its fit quality dramatically improved. While re-reduction of the nickel data is possible, re-fitting the data would be prohibitive given the currently allocated computational resources. When resources are available, re-reconstruction of this data set should be explored, considering that test fits using the old and new reductions indicate a higher population of the twin signal, which we introduce later in this chapter. Still, for the purposes of this thesis, the reduction used for the orientation reconstruction is sufficent for extracting the signals of interest.

### Parameters Optimization

For each subvolume of microstructure, satisfactory parameters optimization and reconstruction of the calibration ($30\mu m$) gold wire worked as the starting point for a second optimization on the actual nickel data set. Parameters optimization were only conducted on three detector nfHEDM measurements. The optimization permitted de-coupling of the camera spacing, so the distance from $L_1$ to $L_2$ was not fixed to the same $L_2$ to $L_3$ spacing. The only parameters that were variable during the optimization were the projection of the direct beam on the camera $(j_0, k_0)$, $L$ distance, and rigid body camera orientation. The beam energy and pixel pitch of the camera were fixed to the calibration constants of $64.351keV$ and $1.48\mu m/pixel$. The optimization was done iteratively, where parameters were confined to smaller and smaller intervals until the process failed to produce a better configuration for the experimental geometry. As noted in the description of the collected volumes, $3L$ data was collected for the fiducial layers and intermittently for layers within the probed volume; typically the last layer of a subvolume. These layers were also tested with the optimized parameters from the fiducal layer. Optimizations did not result in a change in rigid body camera orientation and $(j_0, k_0)$ shifts were sub-pixel, so no systematic shifts were implemented in the reconstruction.

## Reconstruction

A sample reconstruction from one of the *Anneal4* state layers is shown in Figure 5.4, which includes both the confidence and orientation maps. The data was fit with triangles with $2.81\mu m$ sides, which given the state of the reconstruction software at the time of fitting, was the highest resolution possible for a sample of this size. This is approximately one generation coarser than the limiting resolution of the camera ($1.48\mu m/pixel$). The map clearly illustrates the teardrop shaped feature we noticed along the length of the macroscopic sample.

Upon first inspection, the most noticable feature in the microstructure is the presence of many flat boundaries. Further, many of these flat boundary grains display an alternating color pattern, normal to the flat boundary. These are prevalent in Figure (a). Such a pattern indicates an specific misorientation relation between a sequence of grains. As was described in Chapter 1 and will be investigated in Chapter 6, these grains possess the twin orientation relation, which is a special type of boundary that is known to develop with increasing frequency during the annealing of nickel [31, 32].

The confidence map appears more dramatic in its uniformity within grains, in constrast to the aluminum data set. This is due to the well ordered microstructure, which has minimal orientation spreads within grains. We will quantify this later. Also of note is the thin blue ribbon that surrounds each grain in the confidence map. This is indicative of a high quality fit, since the blue region occurs at grain boundaries and amounts to the fitting of peak edges. These edges are even more dramatic when the reduction has perfectly extracted peak shapes. Peaks that are too small would be the result of thresholding peaks too high and the mapped microstructure would have compact grains of high confidence, surrounded by low confidence regions that are due to the removal of peak edges in the diffraction data. Alternatively, thresholding too low would allow the boundary to be blurred and the transition between grains to be obscured. Since a large portion of the results to follow are dedicated to the dynamics of grain boundaries, having fits with reasonable grain boundary delination is imperative.

To compare how different the fits would be with the different reduction routine, we show the same layer fit with the same parameters in Figure 5.5, with one fit using the reduction we used for this thesis, while the second shows a fit with the log of Gaussians *(LoG)* reduction process [84, 83]. The main feature is the extraction of additional twin-related grains or orientations. As we will see in Chapter 6 to come, these types

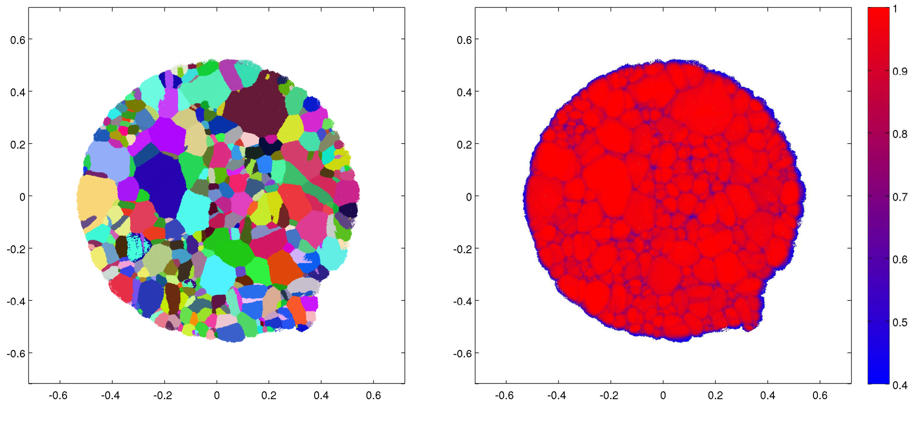

**(a)** **(b)**

*Figure 5.4: Orientation and confidence maps from a layer of the Anneal4 state of the nickel microstructure. Triangles in the map have* $2.8\mu m$ *side widths. Axis dimensions are in millimeters.*

of boundaries are a dominating signal in the experiment and therefore a comparative analysis to the one presented should eventually be completed.

To illustrate the uniformity in quality of the maps, Figure 5.6 is a graph of the confidences distribution within each map for each of the sample states. The expectation is for the majority of the maps to be composed of high confidence voxels, which correspond to being within a grain. There should exist some low confidence regions which are due to the grain boundaries that outline grains as discussed above. The distribution peaks around the 0.98 confidence value and with each voxel generating $64 \pm 3$ peaks (with $49 \pm 2$ peaks falling on multiple detectors), we are therefore seeing roughly 63 peaks accounting for the orientation of each grain. This large overlap is shown in Figure 5.7, which illustrates the experimental peaks (black), simulated peaks (green) and their intersection (red) for a single $\delta\omega$ diffraction image from the initial state measurement.

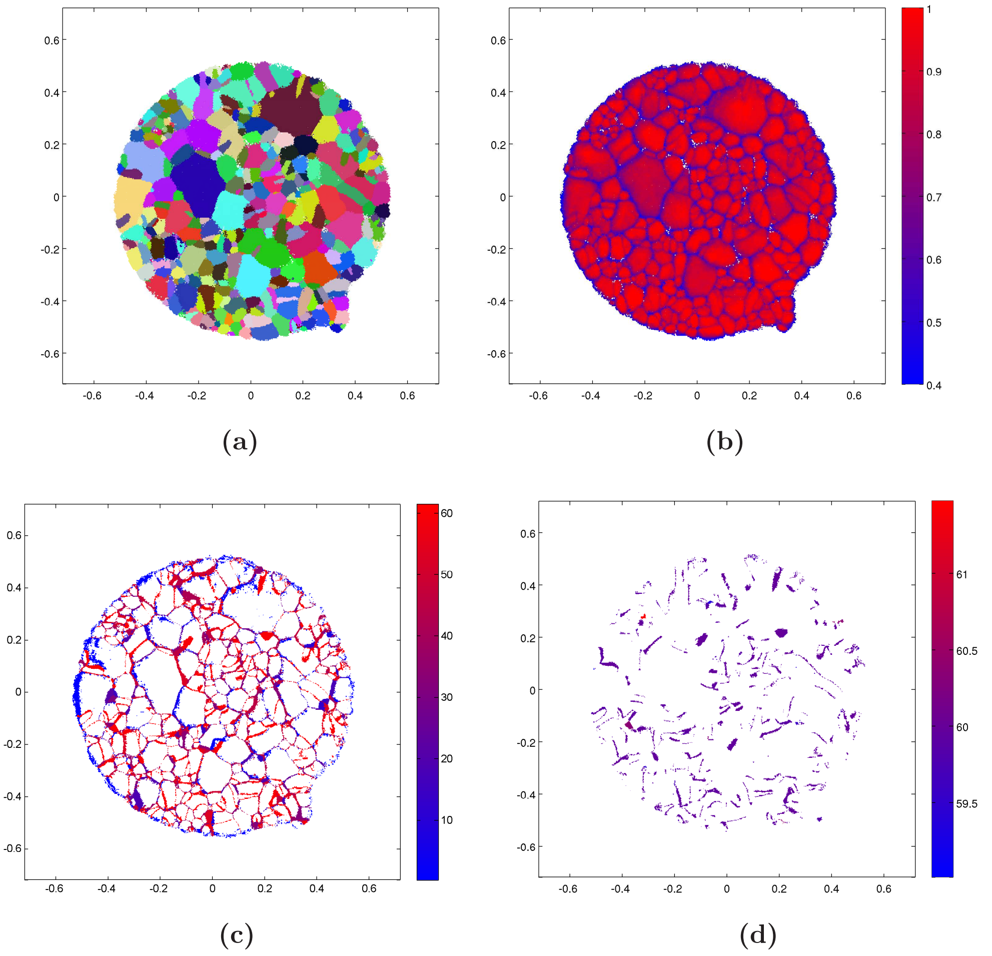

**(a)** **(b)**

**(c)** **(d)**

*Figure 5.5: Orientation and confidence maps using the new LoG reduction routine. The reconstructed layer is the same as that in Figure* 5.4*, with only the reduction having changed. Parameters have not been optimized using this new reduction. Confidences are slightly reduced as can be seen by using the same confidence scale as the earlier figure. (c) shows a point-to-point misorientation between the maps produced by the two different reductions. Here, the misorientation between voxels in the same location in each map is tabulated and colored by the misorientation angle. While boundary widths show differences between the fits, which is expected as edges of peaks are changed between the two diffraction image reductions, the appearance of several new grains is also evident. Specifically, many of these new grains have a twin misorientation with the neighboring grain(s). (d) illustrates this twin relationship by only displaying the voxels within* 60° *of the twin misorientation.*

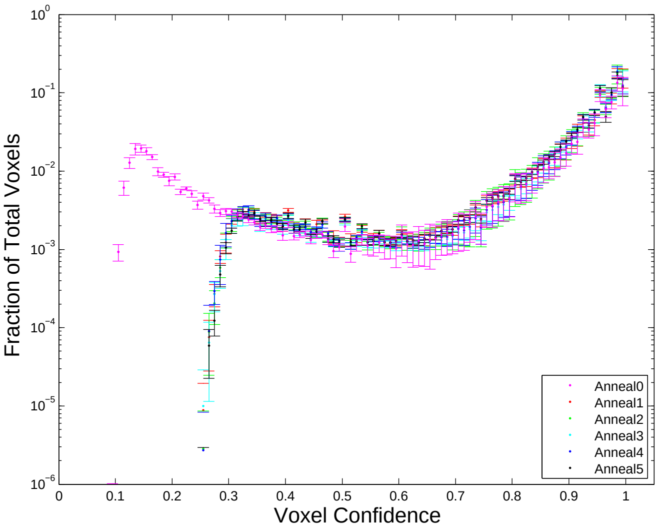

*Figure 5.6: Confidence histograms for all states of the nickel microstructure. Voxels in each layer populate a* $0.01°$ *binning scheme. This is converted to a fraction of total voxels for the layer. This normalized histogram is then averaged over all layers composing a volume and produces the points seen in the histogram above. The error bars are standard deviations within the layer for the given bin. The repeatable distribution of confidences through the anneals shows that the quality of fit is repeatable. The initial state has a population below* $0.3$ *because its fits permitted voxels with a confidence of* $0.1$ *to be retained, while the final five states moved this lower bound to* $0.3$*. These low confidence voxels occur on the perimeter of the sample and are not associated with poorly fit grains within the bulk. This is suggested by noting that the .mic files used for Anneal0 had an average of* $320k$ *voxels per layer, while the later anneals average* $269k$ *voxels per layer.*

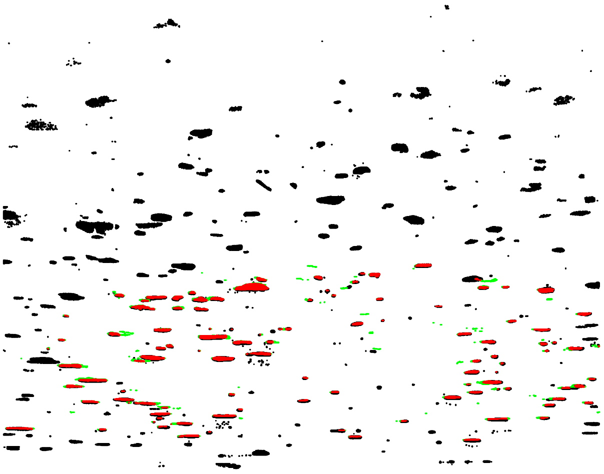

*Figure 5.7: Single $\delta\omega$ interval diffraction image from the Anneal4 microstructure. Black pixels illustrate experimental scattering that is not matched by the forward modeling, while red pixels indicate overlap between simulated and experimental diffraction. Green pixels show simulated peaks which do not hit experimental intensity. Fits were conducted to a maximum $|\boldsymbol{Q}| = 10\mathring{A}^{-1}$, which explains why the unfit peaks near the top of this image do not overlap the simulation. They fall beyond the simulated diffraction range. The large peak sizes are representative of the large grains that are present in the microstructure in this state. Fitting to higher order peaks ($|\boldsymbol{Q}| = 12\mathring{A}^{-1}$) would further improve positional and orientational resolution, but at a substantial computational cost.*

## 5.4 Volumetric Data

By the method of collection, nfHEDM is a technique that provides two dimensional maps of a section of microstructure that can reside in the bulk of a sample. It is the sequential collection of many cross sections that allows the three dimensional picture of the microstructure to be deduced. Still, moving from the 2D maps like those shown in Figure 5.4 into a volumetric map is challenging, since connecting adjacent layers is a non-trivial procedure. Further still, registering these three dimensional maps among different sample states adds another layer of difficulty. The analysis to follow operates on the three dimensional meshes generated though the compositional stitching of the two dimensional maps reconstructed with forward modeling. The mesh generation that these maps are built from is due to the intensely dedicated work of S.F. Li [66]. His thesis provides details into the principles of meshing used to generate the nickel volumes that are to follow, but we will briefly outline the big picture of how we get from cross-sectional maps to volumetric datasets.

The microstructure maps produced with the forward modeling reconstruction utilize an equilateral triangular grid for the spatial representation of the physical sample. While manageable when left in this form, maintaining this tesselation for the generation of a three dimesional microstructure is limiting. Therefore, we overlay the mapped microstructure onto a square grid, which can take advantage of pre-existing computational geometry algorithms for generation of 3D objects. The new spatial assignments are based upon the overlap of square pixels on the equilateral grid, where majority rules are used for the assignment. While the choice of the square pixels is an adjustable parameter, we use squares smaller than the resolution of the triangular grid, to minimize the loss in resolution in going from one representation to the other. With our current software, the change to a square grid is done as an intermediate process to generating a volumetric picture of the microstructure. Thus we read in multiple 2D maps and output rectilinear voxels that fill space.

Since the eventual meshes are based on association of neighboring voxels into a grain, average orientations are tabulated into a list of grains and the grid voxels are assigned IDs. This grain association and orientation averaging are controlled by parameters which restrict the minimum confidence for voxels to be used and a maximum misorientation threshold for their association. Since it is possible that a small population of voxels within the bulk are not associated with an orientation (low confidence) and therefore are assigned the ID of no microstructure (air), a majority filter can be run through the grid to fill in such gaps and assign the voxel to its most frequent neighbor. The completed product of this grid interpolation is a three dimensional representation of the volume of microstructure where voxels possess IDs that correspond to grain averaged orientations. The resulting file of grain IDs is customarily called a *.dx* file.

The *.dx* files provide the coarsest three dimensional representation of the measured microstructure; essentially a sugar cube model. While useful for crude estimates of volumes, surface areas, and number of neighbors, a representation of the microstructure that is more physical is necessary. This is especially true if one would like to determine things like the surface normals of grains. Using a rectilinear grid would admit only three unique directions, which is unsatisfactory. Therefore, this *.dx* file is passed through a meshing program to smooth and interpolate boundaries into a physically realistic map that more closely resembles an actual microstructure.

The surface and tetrahedral meshes we show are generated by implementing the CGAL package in C++ [89]. The process entails a Delaunay triangulation routine to produce meshes that attempt to faithfully represent the boundary surfaces that exist between grains of differing orientations (or different IDs when viewed as *.dx* files). The main principle of this meshing process is to restrict the displacement of quadruple points (locations where four grains meet) and triple lines (three grains) as sampled in the original structure. The mesh is generated by limiting the deviation away from these high information density regions of microstructure. Further limitations are put on the quality of the mesh elements, so undesirable geometries (triangles with acute angles $\leq 20°$ or tetrahedrons with large aspect ratios are avoided. These restrictions are realized through the use of protecting Delaunay balls [66], which are centered around these triple lines and quadruple points and limit the insertion of new nodes into the mesh. The resulting product is a triangular surface mesh or tetrahedral volume mesh that represents the measured microstructure.

Mesh generation is a constantly evolving field and new implementations with specific criteria are continuingly being developed. The work presented in this thesis is not intended to be a study in computational geometry or meshing, but instead an instance of implementation of a specific type of meshing, which produces our three dimensional microstructure. We will present several mesh related results and how they influence the science we are after, but we should emphasize that this work uses the meshing process as a means to an end and not an end in itself. For more detailed explanations regarding the specifics of the meshing process used to generate the microstructures in the sections to follow, we refer the reader to a more detailed explanation of mesh implementation on our microstructures [66, 89].

The meshed microstructure from this process is illustrated in Figure 5.8. The first four sample states are shown, with anneal state increasing from left to right. A cutaway of the initial state has been performed to illustrate the interior grains in the microstructure.

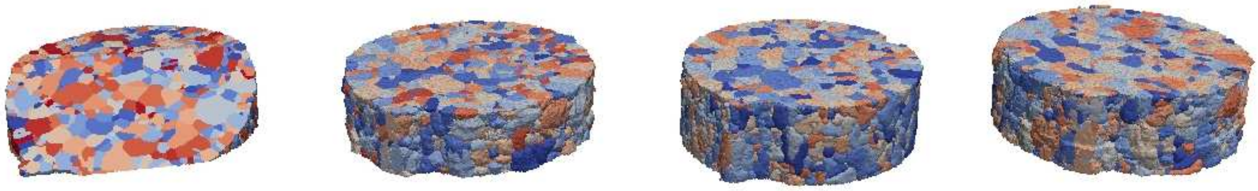

*Figure 5.8: Mesh microstructures from the first four sample states. Anneal state increases from left to right, with the initial state obliquely cut to illustrate the interior microstructure. These meshes are based of a rectilinear grid with in-plane elements of* $1.2\mu m$ *side-widths.*

## 5.5 Roadmap

The content that follows is microstructural analysis on the nickel anneal states, interpreted as a three dimensional entity. On many levels, this analysis is in stark contrast to the aluminum data presented in the previous chapters. There, we were able to monitor the evolution of a coarse grained microstructure. Most of the interesting science was confined to the interaction within grains, most predominantly recovery. There, we saw thermal energy used to produce greater order within each grain's atomic lattice. The onset of recrystallization was hinted at as ordered microstructure developed from regions without definite orientation. These two responses were the only ones that were definitively evident.

In contrast, this nickel measurement provides a different challenge. The initial state has already been subject to a recrystallization anneal, so thermal input resulting in ordering of deformed microstructure was not seen during our nfHEDM measurement. Further, the generation of new grains via recrystallization was also absent. Instead, the dominating feature was grain growth or coarsening, which resulted in the motion of grain boundaries, causing changes in the interfacial network that permeates through the polycrystal. Changes in these boundaries amount to geometric changes in the ensemble of grains. Hence, tabulation of changes in simple quantities, such as grain volumes and number of neighbors, is of interest. These classical grain growth metrics will be interpreted for the same 3D ensemble of grains and will compose the sections to immediately follow.

While topological changes are certainly present in the microstructure, the origins of their motion requires attention to the properties that distinguish one boundary from another. We build upon the language of the previous chapter to measure the evolution of the orientation and misorientation distributions within the polycrystal. The observation of large populations of crystallographically similar boundaries will motivate the use of the coincident site lattice (CSL) and the grain boundary character distribution (GBCD), both of which describe the properties of the interfacial network and will conclude the present analysis of this nickel dataset.

## 5.6 Grain Growth Topology

This section will be devoted to conceptually simple statistics which describe the distribution of grains within the microstructure. In this formalism, grains are thought of as compact objects possessing a single orientation. The analysis to immediately follow will not explicitly look at grain orientations, but instead will interpret bulk statistics about the microstructure. Quantities like grain volume, number of neighboring grains, and their relative changes will be the primary metrics. Still, grain orientation underlies all this analysis due to the discussion in the previous section. The passage from a collection of triangular voxels into a three dimensional microstructure results in an orientation averaging process. With the aluminum data, we saw that spreads about this average orientation were reduced with anneals and this was a salient feature of the data set. Prior to our discussion of topological quantities, we will first motivate the use of grain average orientations for this data set.

### 5.6.1 Orientation Spread

To confirm that intragranular orientation effects are not the dominating feature for this ensemble of grains and that the use of grain averaged orientations is justified, we select 10 contiguous layers from each state and evaluate their intragranular misorientation distributions. The results are shown in Figures 5.9 and 5.10. Like the aluminum intragranular evaluations of the previous chapter, we restrict the voxel confidence to exceed 0.2 (though 0.7 or greater would produce similar results as is discussed in Section 5.6.2). We reiterate our definition of a grain as a compact collection of voxels (that can bridge several layers) with at least 50 voxels having a confidence exceeding our defined threshold. Further, the misorientation of adjacent voxels are never in excess of 2°. The grains we present for this intragranular misorientation analysis are not one-to-one; we are not looking at the exact same collection of grains. Instead, we are simply conducting a statistical sampling of a volumetric cross-section of the sample. The extent of the volume is the same in each state (10 layers), but the number of grains can obviously vary. Further, we have only enforced the 50 voxel criteria for identification of a grain and therefore the possibility of capturing only a fraction of the total number of voxels composing a grain is both possible and probable. Still, the statistics shown below are consistent and display the characteristics of a well ordered microstructure.

As discussed in the aluminum chapters, intragranular misorientation is tabulated by defining a grain by a specific criteria (2° boundaries, 50 compact voxels, $> 0.2$ confidence), averaging the orientation of all these voxels within the grain, then calculating the misorientation between each voxel's orientation and the grain averaged orientation. Table 5.3 shows the voxel and grain distribution for the analyzed 10 layers. The small number of both voxels and grains are notable in the initial state (*Anneal0*), but is likely due to the 50 voxel threshold being close to the average grain size in the distribution. The grain size distribution also appears to be non-monotonic, but is likely due to the sampling of the volume. Evidently, we choose 10 layers in *Anneal4* that have fewer small grains than our volume selection for *Anneal5*.

*Table 5.3: Ten Layer Statistics For Polycrystalline Ni*

| Anneal State | Number of Voxels | Number of Grains | Average Grain Size (Voxels) |
|---|---|---|---|
| 0 | 631k | 529 | 1194±2030 |
| 1 | 2.96M | 745 | 3968±8253 |
| 2 | 2.95M | 704 | 4188±8738 |
| 3 | 2.92M | 744 | 3923±8307 |
| 4 | 2.96M | 549 | 5391±11688 |
| 5 | 2.93M | 670 | 4377±8484 |

Quantities characterize intragranular variations and
do not signify a global coarsening signal associated with grain growth

Our evaluation of intragranular misorientation uses two methods of parititioning the data. The first method looks at the distribution of all voxels without considering their grain association. This is shown in Figure 5.9. The second method does consider how voxels are associated with grains, allowing us to look at the intragranular misorientation on the coarser, grain scale that is in Figure 5.10.

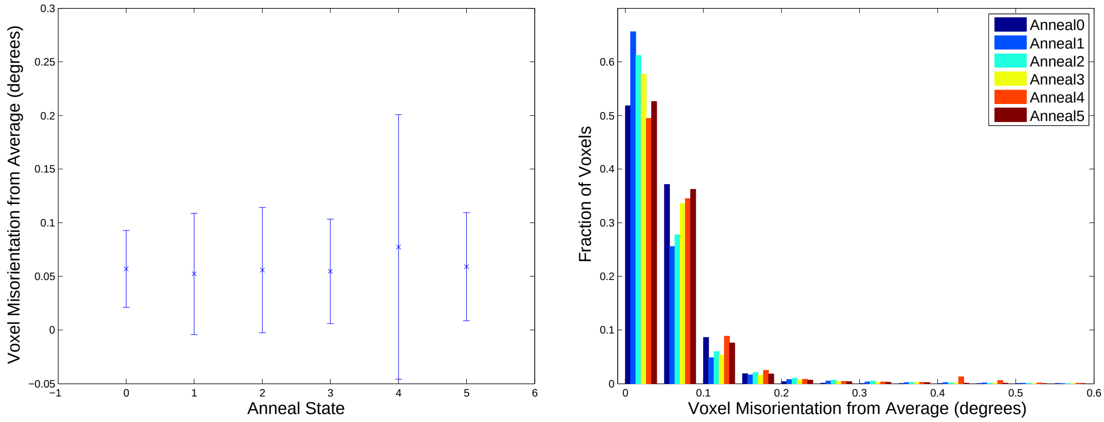

*Figure 5.9: Intragranular misorientation distribution as interpreted on the voxel scale. Plot on left shows how the distribution of all voxels that are associated with grains (fitting our criteria) vary from state to state. The histogram shows the fraction of voxels in the given volume by partitioning by both anneal state and intergranular misorientation value. The number of voxels in each state is shown in Table* 5.3*.*

Figure 5.9 is composed of two plots showing the voxel distribution of the intragranular misorientation through the initial and five anneal states. The histogram shows the fraction of voxels in a given state binned by intragranular misorientation, while the scatter plot shows the average intragranular misorientation for each state. The errorbars on this figure are voxel standard deviations of the voxel's intragranular misorientation within the state. Both plots suggest a very small intragranular misorientation (effectively noise near our orientation resolution) that does not appreciably change as we anneal. The one curious feature is some slightly larger variations in the later anneal states, which most likely are due to an anomoly in the orientation averaging procedure, where points are at or near the edge of the fundamental zone and therefore create an average that is between the bimodal orientation distribution. In other words, a more sophisticated orientation averaging algorithm should remove these outliers, which identifies these orientations on the edges of the fundamental zone.

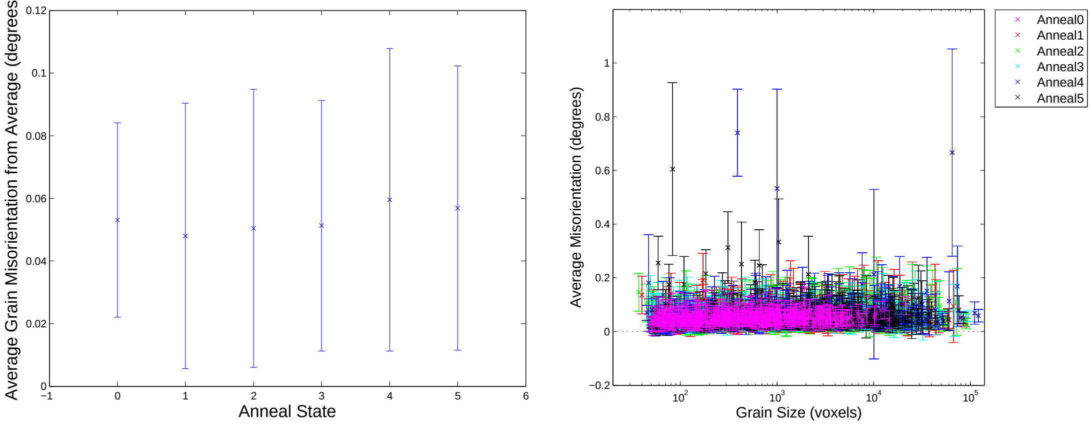

*Figure 5.10: Intragranular misorientation interpreted on the grain scale. The first plot is similar to the plot on the left in Figure* 5.9*, only now the averaging is done over grains. Specifically, an intragranular misorientation average and deviation is determined by averaging this quantity for all voxels that compose a grain. This is then averaged to produce the distribution seen. The right plot shows how voxels are distributed within each grain in each of the anneal states. The large, outlier points are explained in the text and are due to fundamental zone edge effects.*

Figure 5.10 also shows two plots, but now a grain association is the classification metric. The first plot is much like the first plot of Figure 5.9, except now a grain-averaged intragranular misorientation is plotted and the variation in this quantity among grains is used for the errorbar. Once again, the small variation that was seen in the voxel based analysis is present. This has to follow, since the grains are simply collections of these voxels. We illustrate these results on a more individual basis in the second plot. Here, each grain shows up as a point in the plot, where error bars are standard deviations of the intragranular misorientation quantities within the grain. We plot against grain size to display its independence in intragranular misorientation. Grains that are large have approximately the same intragranular misorientation distribution as those that are small. As stated earlier, the few anomalous grains with high intragranular misorientation values are due to orientation averaging issues within the fundamental zone and would fold back into the general population if corrected.

The main message from Figures 5.9 and 5.10 is that the spread in the internal orientation distribution of grains remains static and small through the course of this experiment. This constrasts with the aluminum experiment, where variations in orientation within grains was the strongest signal and was associated with the recovery process due to annealing. For this nickel data set, the stage where recovery is the dominant feature has already passed and while probably still present as we do each anneal, the signal is below our resolution limits. Thus, since the voxels composing a grain display a noise in orientation about an average value, we are safe to interpret each grain as an object with a single crystallographic orientation.

### 5.6.2 Meshing Parameter Study - Rectilinear Grid Results

In passing from a stack of 2D *.mic* files, where orientations are assigned on a triangular grid, to the 3D gridded and smoothed microstructures that we analyze in the sections to follow, data can be altered. Specifically, quantities like boundary information can easily be changed through the re-sampling on the new space filling tesselation. Further, small features can be eliminated if certain mathematical restrictions are placed on the 3D outputs. Selecting proper values for the parameters that dictate the passage from 2D orientations into 3D grains is critical. Here, we will discuss two such gridding parameters in relation to this nickel microstructure – misorientation for grain definition and in-plane grid resolution.

We do not explore the confidence parameter for grid inclusion, though strongly suggest its investigation in future work. Only triangles above a given confidence threshold are maintained for the mesh. The value we use is 0.7 and is based upon the spatial distribution of low confidence voxels. Figure 5.11 illustrates the use of this threshold in a layer of the first anneal state. The outline images in (a) and (b) display the voxels which have a confidence below 0.5 and 0.7, respectively. We can see that voxels of low confidence are associated with the edge of the sample and are due to the simulation hitting some collection of peaks, but not as many as interior microstructure. Therefore, we raise the threshold confidence to the point where interior boundaries begin to appear (0.7 from (b)) and use this as our grid acceptance confidence. Determination of this value is qualitative and should be studied further, but its use is based upon these surface *vs.* interior arguments.

We also note that our intra-granular misorientation discussion of Section 5.6.1 used 0.2 confidence as the minimum for analysis. The conclusion there was spread in orientation within grains was minimal and therefore increasing our confidence criteria should produce a similar result.

Lastly, we recall that a majority filter is passed through the 3D structure to eliminate grid elements that might have null assignments due to sampling of a low confidence voxel in the *.mic* maps (see Section 5.4). This process is performed twice and its influence on the microstructure has yet to be characterized. Its intention is to remove artifical 'holes' in the microstructure that can lead to undesirable artifacts in the mesh, but unintentional consequences might still be present.

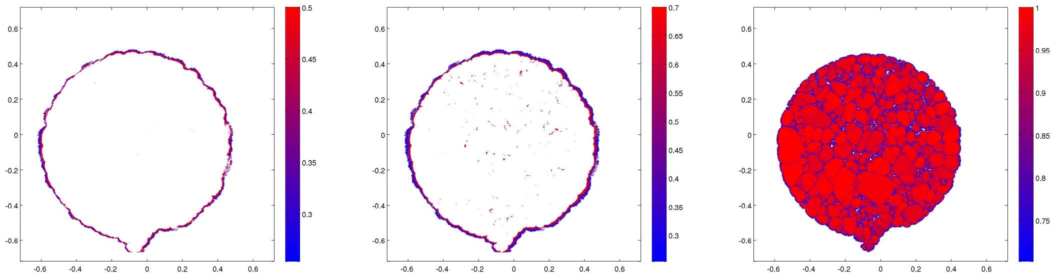

**(a)** **(b)** **(c)**

*Figure 5.11: Confidences maps of a representative layer of microstructure from our measurement. The maps illustrate the spatial distribution of low confidence voxels, which is used populating the rectilinear grid. Only voxels with confidences less that* 0.5 *and* 0.7 *are shown in (a) and (b), respectively. (c) shows voxels that are in excess of 0.7.*

Therefore, we note that the grid characterization with grain misorientation threshold and in-plane resolution (presented here), along with mesh characterization through mean width [66] serve as preliminary investigations on the mesh generation toolbox introduced in S.F. Li's thesis [66]. Understanding the effects of parameter tweaks in producing the gridded (*.dx*) and smoothed (mesh) from the initial (*.mic*) reconstructions is a continuing process. Still, our intention with this measurement is to discuss topological quantities that evolve in the annealing experiment, so determining how some of these parameters alter the measured microstructure is of importance. We use the number of grains as the response variable, so decoupling the misorientation threshold and in-plane resolution can not be accomplished. Instead, we will first interpret how the misorientation threshold influences a fixed grid size, then fix this threshold and vary the mesh grid resolution.

### Grain Misorientation Threshold Parameter

The 2D maps are originally assigned individual orientations on a triangular grid, but this is reduced to multiple elements assigned a single, grain averaged orientation as the microstructure is extended to 3D. Figure 5.12 shows how different misorientation thresholds influence the number of grains that are found in the rectilinear grid. In many ways, this analysis is a pre-cusor to the work presented in Table 5.3. There, we defined a grain as a compact collection of voxels that had no neighbors in excess of 2°. The main conclusion from interpretation of this plot is that using a threshold of 0.1° is infeasible due to the orientation noise evident in Figures 5.10 and 5.9. At such a threshold, we are at the orientation resolution of the experiment and therefore expect many singular grains to be subdivided, simply due to the high probability of neighboring voxels exceeding the noise baseline of the reconstruction. The remaining misorientation thresholds that are used fluctuate by a few percent, but exhibit no dramatic difference.

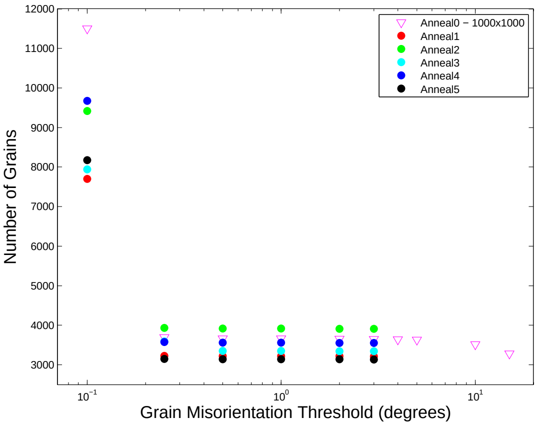

*Figure 5.12: Number of grains in rectilinear grid as a function of misorientation threshold in grain orientation averaging. Data is presented from tesselating each of the volumes differently to see how the distribution changes. Obviously, since the microstructures vary in number of layers collected, the number of grains will be variable between states. The same grid resolution was used for the study and was composed of voxels with an in-plane resolution of* $0.923\mu m$ *square, except for Anneal0 that used* $1.2\mu m$ *square, which is the grid resolution used in the tracked microstructure analysis.*

Figure 5.12 also shows that as we move to smaller and smaller misorientation thresholds, the number of grains in the grid increases, which is intuitive. The results use $0.923 \times 0.923 \times 4\mu m$ elements, which are actually larger than the resolution used for the bulk of the work to follow ($1.2 \times 1.2 \times 4\mu m$). A grid of this working resolution is shown for the initial state with triangles in the figure and follows the same pattern as the higher resolution mesh.

For the analysis in the coming sections, 3° is the misorientation angle threshold used to define grains. Without any dramatic distribution differences when thresholding from 0.25° to 10° we are at liberty to make a section anywhere within this range. Specifically, the $1.2\mu m$ grid and a 3° threshold results in 3648 grains. Moving to a threshold of 0.25° would only result in 46 more grains, while 10° would produce 131 few grains. In both cases, this is only a few percent change and we can therefore be satisfied with our 3° choice.[2] Conversely, since 0.25° can be achieved without changing the distribution, this would be ideal. Low angle boundaries prove to have different properties than high angle, as was discussed in Chapter 1 and their identification is important. We should further clarify that 3° was used for the significant results of Chapter 6 that involves mesh-to-mesh registration. The correlation was performed before both this misorientation and in-plane resolution study.

---

[2] The second half our our analysis is devoted to the evolution of the grain boundary character distribution *(GBCD)* and the dominant signal (the $\Sigma 3$ boundary) has a misorientation angle, $\Delta\theta = 60°$, and is therefore not influenced by this misorientation thresholding.

To present a visual as what each of these different misorientation thresholds means in the context of the actual reconstructions, Figure 5.13 overlays boundary lines of different misorientation angle thresholds. Figure 5.13(a) uses two of the larger misorientation thresholds, where boundaries in excess of 15° misorientation are shown as black lines, while boundary lines between 5° and 15° are presented in green. While the majority of boundaries are painted black, there does appear to be some lower angle boundaries present. Since our color scheme covers all of orientation space, regions with low angle boundaries (and therefore similarly oriented) are displayed as the nearly the same color. Thus, the green lines, which represent a small orientation, appear to cut through seemingly single orientation grains. The purple grains at the top half of the image display such low angle boundaries.

Figure 5.13(b) magnifies a region of the microstructure in (a) and uses misorientations in excess of 0.25° to color boundaries black, while those between 0.1° and 0.25° are in green. Here, the noise in orientation resolution is displayed as a random scattering of green lines are seen embedded within grains and having not apparent spatial organization.

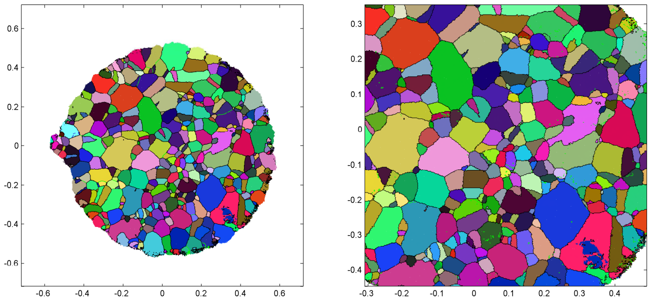

**(a)** **(b)**

*Figure 5.13: Boundary maps from the final state microstructure. In (a), black lines outline boundaries in excess of* 15° *in misorientation angle, while green lines fall between* $[5°, 15°]$. *A finer misorientation scale is used for (b), with black lines showing all boundaries greater than* 0.25°, *while green is in the* $[0.1°, 0.25°]$ *range. The pink-blue coloring of a grain near* $[0.35, -0.35]$ *mm is due to the grain's orientation falling on the edge of the fundamental zone in orientation space (as discussed in Section 5.6.1). Despite the dramatically differing colors, this is actually a single grain of minimal orientation variation, like the remaining ensemble.*

### In-plane Grid Resolution

Figure 5.14 uses the 3° misorientation threshold and then varies the size of the voxels used to compose the rectilinear grid. It is immediately evident that as we make our grid finer and finer the number of grains increases. In fact, the plot is monotonically increasing across the entire range of rectilinear voxel sizes. Obviously, this number should converge to the number of unique grains found in the microstructure maps (*.mic* files), as defined by the 3° boundary. While we do not observe the convergence for all anneal states, the initial microstructure appears to contain a static number of grains as represented by the three finest resolution points. This observation is only evident by monitoring the two smallest resolution points, which unfortunately have not been generated for the other five anneal states due to computational limitations. Still, a convergence is suggested.

The convergence to a constant number of grains is suggested work that should be further explored and only recently hypothesized as a possible consequence of a sub-resolution sampling and the majority filter, which is used twice on each microstructure. Considering that our reconstructions were performed at resolution of $2.8 \mu m$ , using any grid elements larger than this will fail to capture small features in the microstructure, which are of interest. Specifically, if critical events are a driving force for microstructure evolution, we must be sensitive to them in our representation of the microstructure. As our grid resolution approaches the size of our triangles, we should still expect to lose small features due to the operation of the majority filter. Small grains will be eroded in this process. It is only when each voxel is represented by many grid elements that all small features will be protected. Yet going to as small a grid as computationally possible is not a final solution to faithfully representing the microstructure. Information about boundaries are also important in characterizing a microstructure and too fine a grid can result in a tesselation that requires significant smoothing to remove artifacts of the grid.

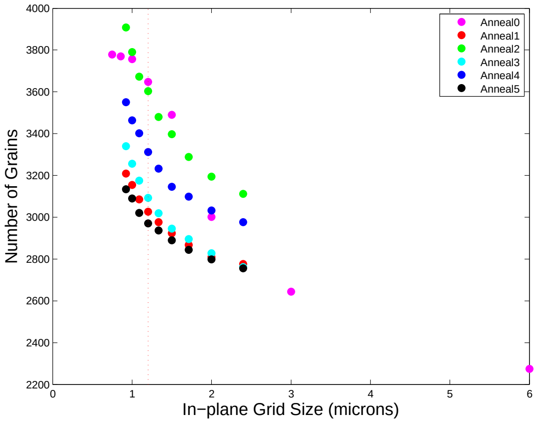

**(a)**

*Figure 5.14: Number of grains as a function of in-plane grid sizes. The vertical line indicates the $1.2 \mu m$ resolution used for the grain boundary tracking measurement. Horizontal axis shows the (square) in-plane resolution of the grid. Convergence appears to be present for the fine resolution initial state points.*

With a grid resolution illustrating convergence in grain number has not been observed, we are forced to select a resolution based on other factors. We have settled upon $1.2\mu m$ as our grid resolution, which is represented in our figures with a vertical line. This is based upon three considerations. The first is that the largest square that will fit inside one of our equilateral triangles (at measurement resolution) is $1.3\mu m$. We can think of this as the best approximation to our reconstruction resolution. Second, in Chapter 6, we find that varying the grid resolution and monitoring an intrinsic experimental signal (coherent twin peak distribution) results in an optimal grid resolution between $0.9\mu m$ and $3\mu m$ (based upon meshed grids). Finally, grids with in-plane resolution that is larger than our reconstructions will needlessly coarsen our measurement and therefore we place an upper limit of $2.8\mu m$ on our in-plane grid resolution. Hence, we select $1.2 \times 1.2 \times 4\mu m$ and a misorientation threshold of 3° for our rectilinear gridding and advocate continued investigation into grid resolution artifacts.

### 5.6.3 Meshing Parameter Study - Tetrahedral Mesh Results

In passing from the rectilinear grid to the smoothed mesh, we begin to remove the sugar cube features inherent in the tesselation and move closer to an accurate representation of the microstructure. While extracting information such as grain volumes and number of neighbors is not crucially affected by the volumetric representation that we use (rectilinear grid *vs.* tetrahedral mesh), the resulting *GBCD* that will be discussed later is dramatically influenced by the building blocks of the volume. The *GBCD* is a five parameter description of the grain boundary interface network, where two of the parameters describe the geometry of the boundary normal (with a unit vector). If we were to exclusively use the rectilinear grid representation, we would be forced to accept only three possible directions for the interface normal, which is much too coarse for investigating a distribution that should cover a sphere. We use the mesh to alieviate this problem and we therefore must investigate the influence of our grid parameters on the resulting mesh. We exclude the geometrical meshing parameters (aspect ratios, etc.) [66], but note that they are implemented to produce a mathematically reasonable representation of the microstructure. Changes to these parameters will influence the outputted microstructure, but are kept constant for our study.

Figure 5.15 performs the same comparison of number of grains in the 3D structure with variable grid parameters that were achieved in Figures 5.12 and 5.14, only here grains in the tetrahedral mesh are counted. Since the mesh is based upon the grid, the results are comparable. The number of grains as a function of misorientation threshold and grid resolution in (a) and (b), respectively mimic those found for our grid. The increasing number of grains is expected for the mesh with finer resolutions, since small features are represented by more grid elements. Eventually, this distribution should converge to the number of grains in the grid.

A direct comparison between the two 3D representations are found in (c) as the ratio of mesh grains to grid grains is plotted. Here we see that for a coarse gridded object, the two representations are equivalent, as should be expected. If the only additional process that is performed on the 3D grid is the smoothing during meshing, we expect large features to always be present. It is when we move towards a fine grid that the discrepancy between grid and mesh begins to develop. Specifically, we see that numerous fine grid grains are lost at fine resolution. We explore this with grain size distributions in Section 5.7.1, where it is (not surprisingly) small grains that are lost in the mesh process. This is likely due to a problem inherent to the meshing procedure, where small grains are not being identified due to sampling frequencies [66]. We do note that there appears to be a convergence for the initial state, where approximately 75% of grains are retained in the mesh.

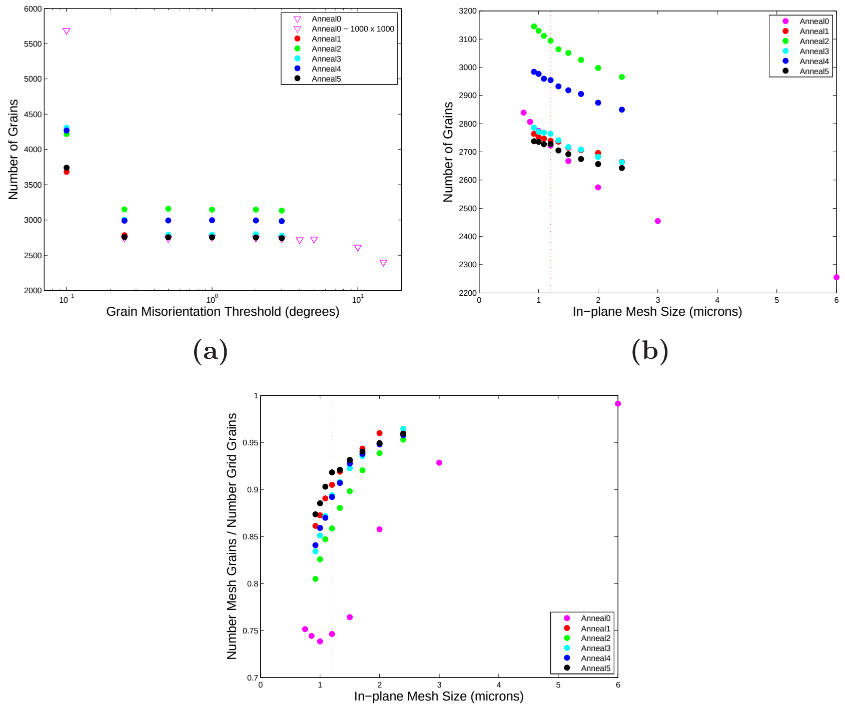

**(a)** **(b)**

**(b)**

*Figure 5.15: Number of grains in smoothed mesh as function of (a) misorientation threshold in grain orientation averaging and (b) in-plane mesh resolution. Data is in comparison to Figures 5.12 and 5.12, which used the straight rectilinear grid for grain counting. (c) takes the ratio of grains in the tetrahedral mesh to those in the .dx file from which it originated. Variation in number of grains between meshes is due to changes in the volume of measured microstructure in each sample state.*

## 5.7 Coarsening in Nickel Microstructure

The most direct measure of coarsening is growth of the average grain size. Note that, in a given volume of material, the only way for the average size to change is through the disappearance of grains. This is because average grain size is simply the volume of a grain ensemble divided by the number of grains. Here, we first address the influence of the above considerations on the computation of average grain size. Next, we (finally) present our first characteristic of coarsening: the evolution of the grain size distribution and the average grain size.

### 5.7.1 Grain Size Distribution

Figure 5.16 illustrates the grain size distribution for the *Anneal0* state as we vary processing parameters. Without loss of generality, we use only a single state so as to minimize the confusion in presentation. Figure 5.16(a)-(b) illustrate the effect of varying grid resolution on the grain size distribution. A Gaussian distribution is shown centered about grain sizes of $\sim 10^4 \mu m^3$ in (a).

Deviation between the grids begins to develop around the $10^2 \mu m^3$. Specifically, we see that as we go to finer and finer grids, the fraction of grains composed of a single volume element increases, but approaches a common fraction. This picture is consistent with the observation in Figure 5.14, where an increasing number of grains was observed with the fine grid microstructures, but eventual convergence was seen in the two finest resolution points. Evidently, these added grains are small in size.

This confirms our hypothesis for the origins of the increasing number of grains with finer grids found earlier. Grains containing only a few voxels in our reconstructed maps are converted into an increasing collection of volume elements as our 3D grid becomes finer. Subjecting these grains to two majority filters will erode them from the microstructure when grid sizes are large. This can be seen for the $\geq 3 + \mu m$ curves in (a). We do not see any small grains in our distribution because our building blocks are too large. Once our grid becomes fine enough to fit multiple building blocks in each reconstructed voxel, then the majority filter will cease to eliminate these very small grains. At some fine resolution (near $1 \mu m$), we will see a convergence where the majority filter will not remove any small features and the number of grains will be static. This is when our grain number and grain size distributions will converge.

Figure 5.16(c)-(d) demonstrates both the number fraction and volume fraction when misorientation threshold is varied. The graphs emphasize that we have few low angle boundaries in the $0.25°$ to $\sim 15°$ boundary segmentation.

Figure 5.17 repeats the analysis with *Anneal0*, but uses the tetrahedral mesh as the entity that is investigated instead of the *.dx* representation of the microstructure. We have presented the distributions using both the tetrahedral mesh and the rectilinear grid to illustrate the difference in small grain distribution, which was seen in the grain number distributions of Figure 5.15. Comparing the plots in Figure 5.16 with Figure

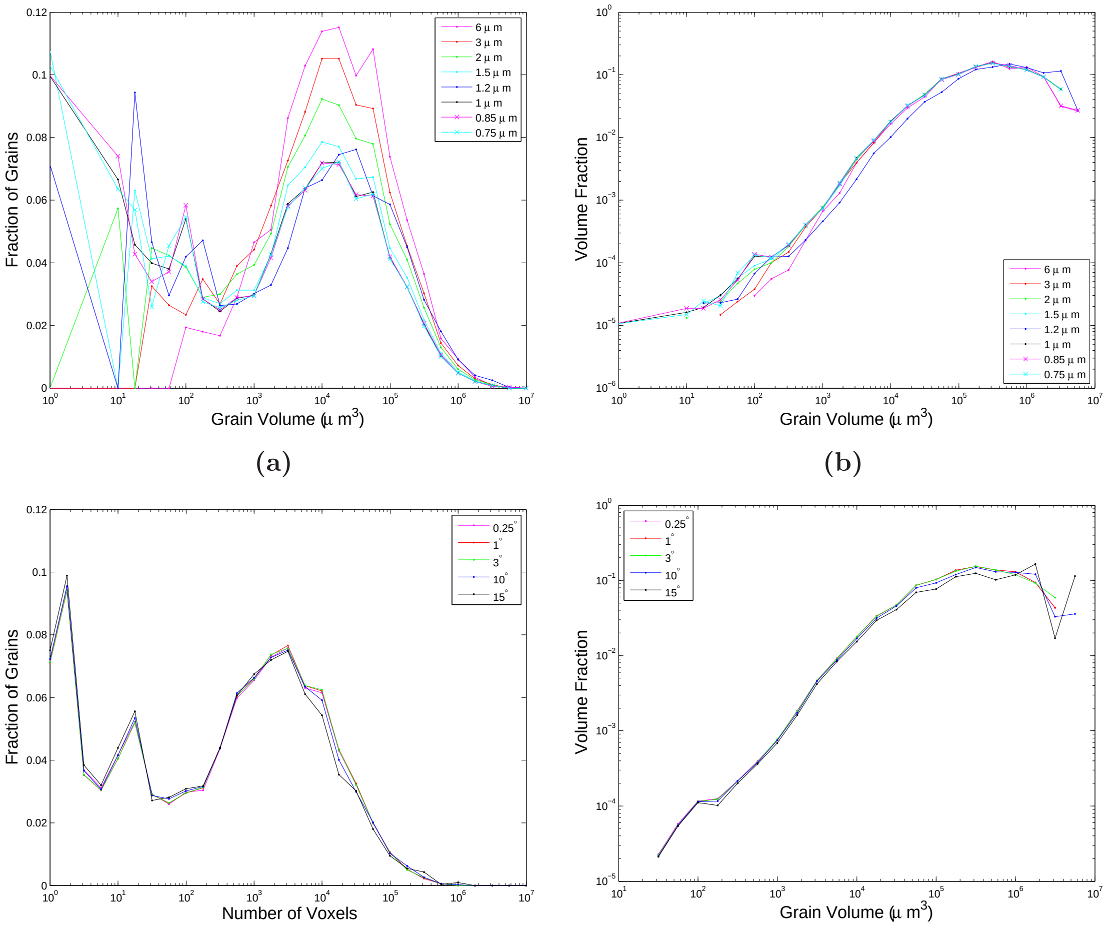

**(a)** **(b)**

**(c)** **(d)**

*Figure 5.16: Grain size distributions for Anneal0 state, using the rectilinear grid with variable in-plane resolution (a-b) and misorientation threshold (c-d). Grain sizes (represented as both number of grid elements and grain volumes) are plotted on the logarithmic scale. The plots using grain volume as the dependent variable (a,b,d) are the result of multiplying each grid element by the constant building block volume of that grid. For the mesh resolution study (a-b), the grid elements are variable, while in (d), we have used elements with volumes of* $5.76\mu m^3$ *that correspond to the* $1.2\mu m$ *grid. (c) histograms by the grain size as number of voxels in a grain. Plots (a,c) illustrate fraction of grains in the microstructure with a given size, while (b,d) uses volume fraction of the measured microstructure as the bin value.*

5.17, we note a significant number of small grains lost in processing from *.dx* file to mesh. We must keep this in mind when we investigate topological quantities later, since items such as number of faces and critical events like grain disappearance are clearly influenced by meshing. We also note the convergence towards a constant fraction for small grains in (a), just like was observed in (a) of Figure 5.16.

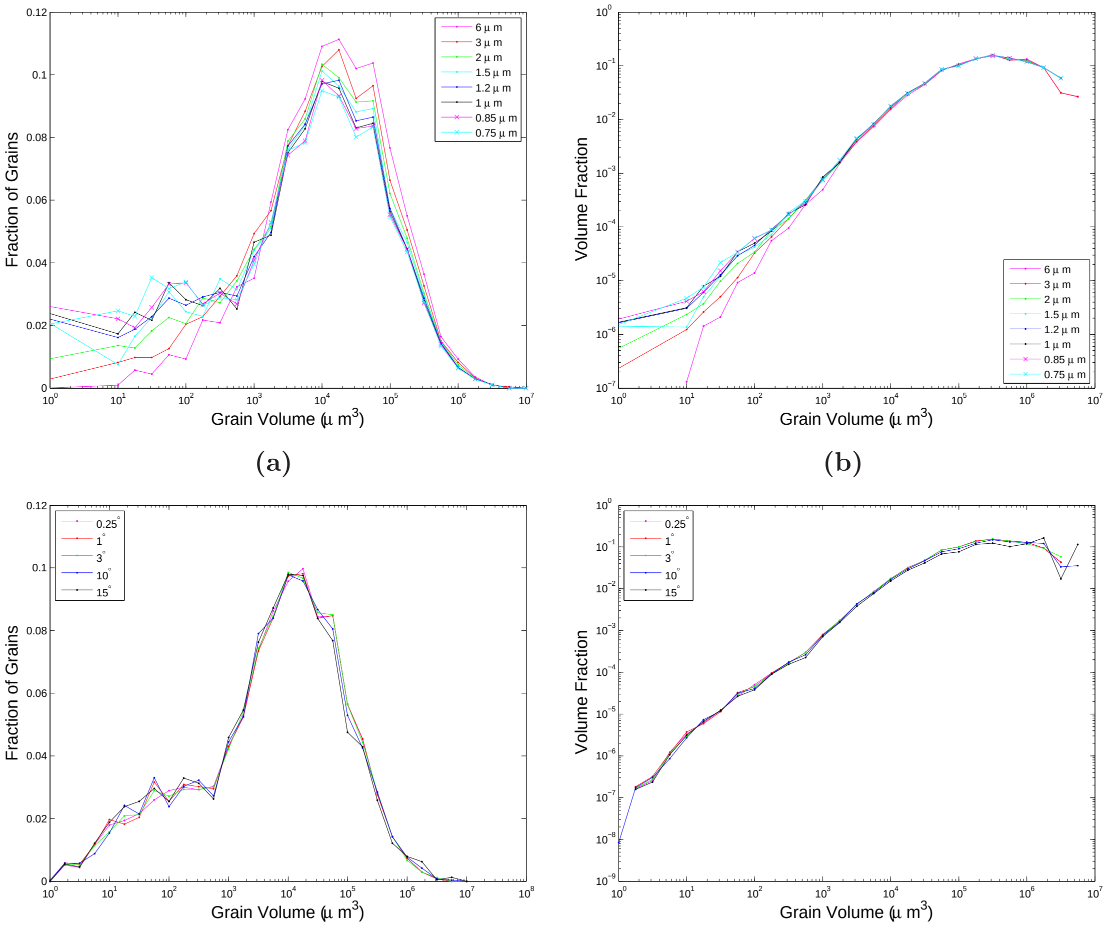

**(a)** **(b)**

**(c)** **(d)**

*Figure 5.17: Grain size distribution's using the tetrahedral mesh with variable in-plane resolution (a-b) and misorientation partitioning (c-d). Plots display the same quantities as Figure 5.16, except we use the smoothed tetrahedral mesh instead of the rectilinear grid.*

### 5.7.2 Microstructure Evolution with Annealing

Having laboriously detailed the effects of producing 3D generated microstructures from our reconstructed maps, we can now look at the evolution of the microstructure in response to annealing. All the 3D representations to follow will be based on 1.2$\mu m$ in-plane resolution and the 3° misorientation threshold, unless otherwise specified. Our characterization of the annealing response will be conducted with two traditional statistics – grain volume and number of neighbors. The bulk of the analysis presented in the remainder of this chapter will be based upon analysis of the gridded microstructure, and not the mesh, due to the established insensitivity to small grains in the latter microstructure's representation.

We will begin with a broad characterization that performs no correlation between grains and simply compares grain size through anneal states. This is akin to the type of quantities that can be measured with other orientation imaging techniques, except unlike those destructive techniques, we are looking at (approximately) the same volume of microstructure (as detailed in Section 5.2). Therefore, many of the same grains are present in the six sample states, though the expanding sample volume sizes (see Table 5.2) will introduce composition variation in the grain ensemble.

Next, we use the one-to-one correlation between microstructures, which will be described in Chapter 6, to look at the evolution of grain size distributions and number of grain boundaries on a granular basis. It is this type of analysis that uses nfHEDM to its full capacity. Monitoring how the exact same grains and boundaries, deep within the bulk material, respond to thermomechanical processes can not be accomplished with other orientation imaging techniques. We take full advantage of nfHEDM's evolution capabilities.

As will be detailed in the next chapter, the registration of volumetric grain maps across multiple states was performed by S.F. Li. Presently, only the first four sample states have been registered and our statistics will be based upon thier correspondence. Additionally, software for the indentification of critical events (grain extinction) has not reached a maturation level that can produce reliable results. Therefore, we limit our analysis to the $1,307$ grains that are identified in all four states. Further, since our focus is on bulk properties of the microstructure, we restrict these grains to be interior in *all four states.* This leaves 976 grains for our analysis of bulk statistics. One of these tracked grain is illustrated in Figure 5.18.

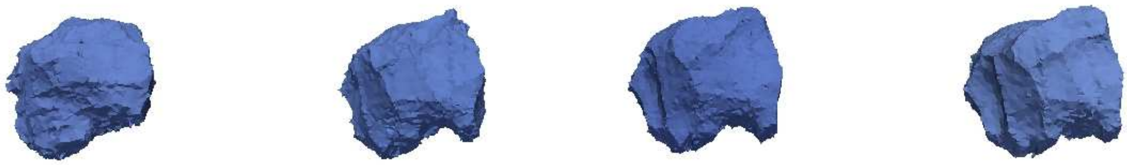

*Figure 5.18: Single grain extracted from the meshes in Figure 5.8. The anneal state increases from left to right, with the initial state on the left. The grain increased by 25% in volume from the initial to third anneal state and is one of the larger tracked grains with $\bar{R} = 109\mu m$ (see Section 5.7.2).*

### Grain Size Evolution - Uncorrelated

As a microstructure is annealed, grains grow at the expense of their neighbors, which results in an increasing average grain size for the ensemble. We illustrate the average grain size, $\bar{R}$, for our six sample states in Figure 5.19. $\bar{R}$ is calculated by taking the sphere equivalent radius based upon the volumes of each grain in the ensemble. Except for an anomalously large number of small grains are present in *Anneal2* measurement volume (leading to a decrease in $\bar{R}$), we see the expected coarsening relation: a linear increase in average grain size with each anneal. Average grain sizes grow from $V \sim 1700\mu m^3$ to $V \sim 2900\mu m^3$, a volumetric increase of 70%.

Both the tetrahedral mesh and rectilinear grid representations of the microstructure are illustrated. The average sphere equivalent radius for the mesh is larger than the grid because of the loss of small grains in process, as suggested in Figure 5.17. Since the grains that are omitted are small, the volume in both representations is approximately constant, yet the grid will have more grains and consequently a smaller average radius.

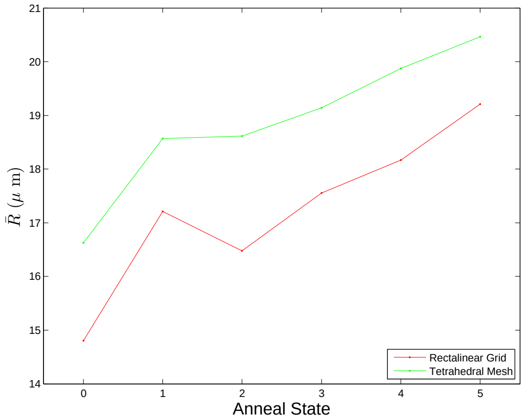

*Figure 5.19: Scaled grain size distribution across all anneals, using a grid elements of* $1.2 \times 1.2 \times 4\mu m$*. For each grain in the rectilinear grid representation (a) and tetrahedral mesh representation (b), a sphere equivalent radius is calculated for the grain's volume,* $\bar{R}$*, and scales the distribution.*

In Chapter 1, we noted that if the distribution of grain sizes remains unimodal with anneal, we have normal grain growth. This is in contrast to abnormal grain growth, where a selection of grains begin to grow faster than the remaining population. Figure 5.20 confirms that normal grain growth was observed in this nickel measurement. We plot distribution of grain sizes, scaled by the average radius for that state ($\bar{R}$). As we anneal the spread around the average grain size remains constant and centered about this average grain size, $R = \bar{R}$. If abnormal grain growth was present, we would see a bimodal distribution of grain sizes develop, instead of the observed single log-normal distribution.

### Grain Size Evolution - Correlated

Figure 5.21(a) is the grain size distribution for the 976 tracked grains from the first four anneal states. The distribution is similar in content to Figure 5.20, except there now

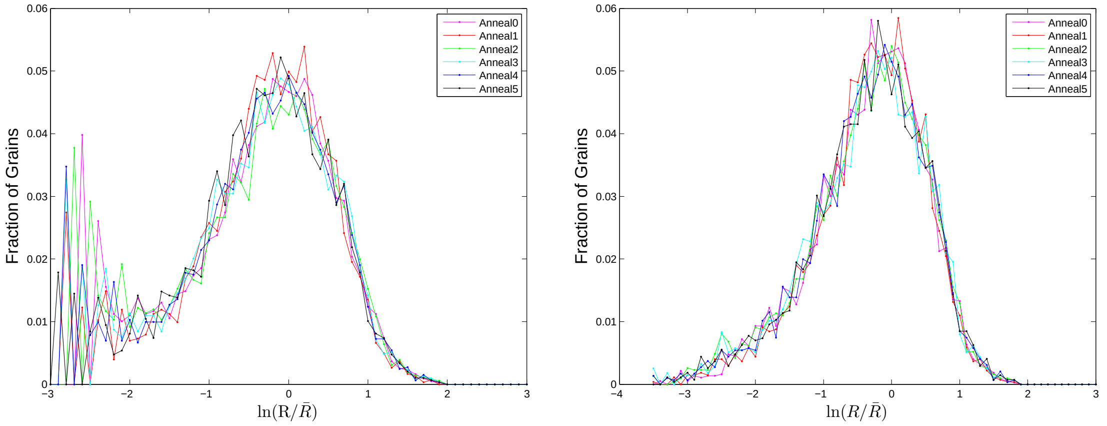

**(a)** **(b)**

*Figure 5.20: Scaled grain size distribution across all anneals. For each grain in the rectilinear grid representation (a) and tetrahedral mesh representation (b), a sphere equivalent radius is calculated for the grain's volume, $\bar{R}$, and scales the distribution.*

exists a one-to-one correspondence between all grains in the distribution. Grain sizes are measured by number of rectilinear grid elements, which are $5.76\mu m^3$ in volume. The distribution remains static with anneal, though a slight shift towards larger grain sizes is noticable in the last two anneal states. Specifically, near the large grain size tail, we see an increasing population with anneal state.

Changes towards larger grain sizes were observed in (b) and (c), where the relative change in volume, $\frac{dV}{V}$, with anneal state was presented. The change in volume is incremental in (b), while with respect to the initial state grain sizes in (b). Both of these volume change plots suggest that our anneals resulted in a gradual coarsening process. In (b), the change in volume is rather small between consecutive anneal states, with the distribution centered around zero and no discernable change in distribution shape between each anneal step. The incremental changes are shown to cumulatively result in larger grain sizes in (c), where there is a distribution shift relative to the initial grain sizes. In *Anneal3*, we see that most grains are larger than they were in the initial state, evidenced by the blue curve's peak at $\frac{dV}{V} > 0$. Additionally, we see that there is a population of grains that have shrunk from the initial to third anneal state, which is consistent with the process of coarsening.

### Number of Neighbors Evolution - Correlated

While grain sizes illustrate the coarsening process in polycrystals, other metrics can be used to give a picture of how grains are evolving. As a complement to grain size distributions, we show the number of neighbors distribution and like the grain sizes, we interpret its evolution with anneal. For our analysis, we simply count the number of

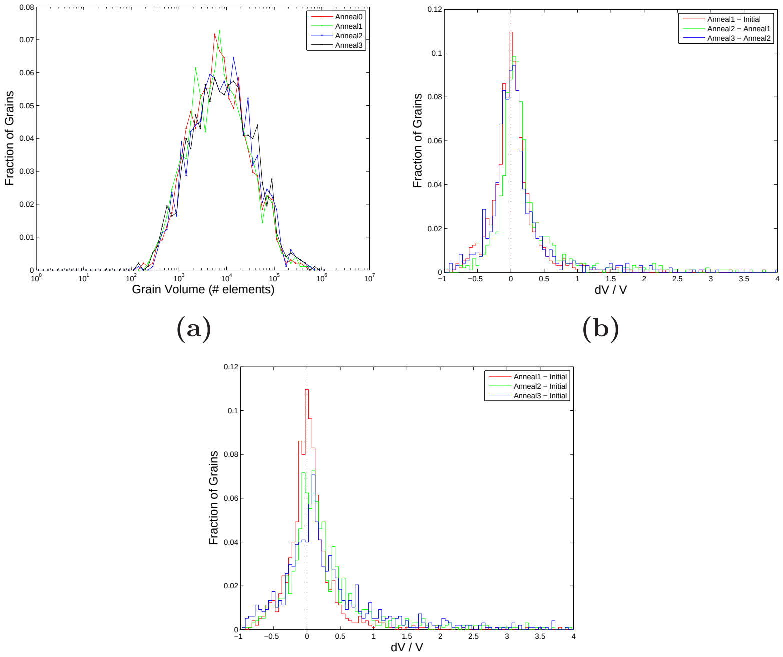

**(a)** **(b)**

**(c)**

*Figure 5.21: Grain volume distributions for* 976 *tracked grains through the first four sample states. The volume of grains is shown in (a), where volume is represented as number of* $5.76 \mu m^3$ *that compose the grain. (b-c) show the changes in volumes of individual grains, plotted as incremental changes* $\frac{dV}{V}$*. Changes in grain size between consecutive states is shown in (b), while the evolution with respect to the initial grain size is shown in (c). The red line in (b-c) illustrates the 'no size change' position.*

unique grain IDs that border our tracked grains. We used this process to identify grains which are on the surface, by having one of the neighboring IDs associated with air. No restrictions have been placed upon the properties of grains which border our tracked grains. Specifically, in counting the number of neighbors for one of our tracked grains, we include those grains which are not among the 976 which are tracked. Of course, in our grain size distribution, the coarsening or shrinking of tracked grains is evolving among the untracked grains.

In Figure 5.22, we show the distribution and evolution of number of grain neighbors (boundaries). Like Figure 5.21(a), where a roughly constant distribution of grain volumes was seen in each anneal state, 5.22(a) shows an approximately constant neighbor distribution. The plot is truncated to only show the location of the peak and note that there are several large grains with many boundaries in this collection of tracked grains. The grain volume-number of neighbor distribution is presented in Figure 5.23 and illustrates that many boundary grains are large in volume.

Differential changes in number of neighbors are shown in (b-c), with changes relative

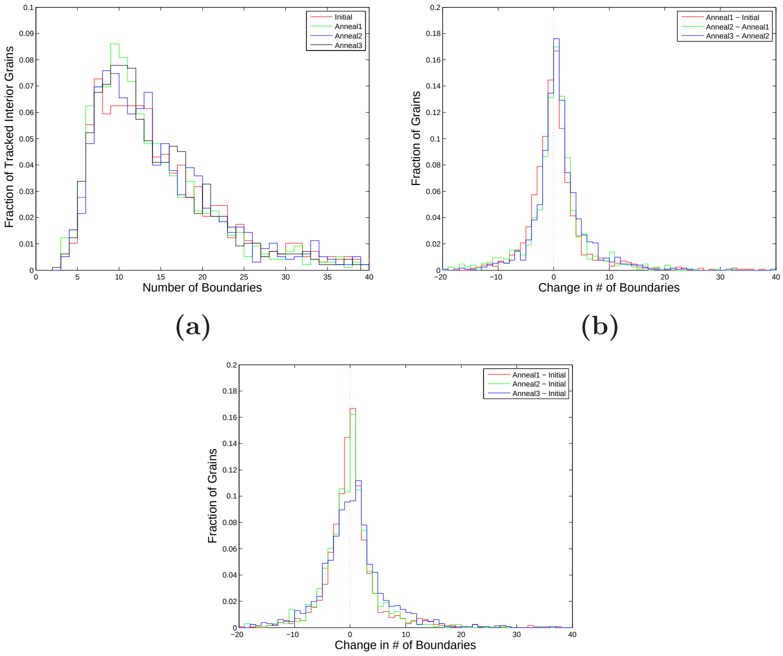

**(a)** **(b)**

**(c)**

*Figure 5.22: Number of neighbor distributions for* 976 *tracked grains through the first four sample states. (a) illustrates the number of grain neighbors through each state, while (b-c) look at differential changes for each grain. (b) shows changes incremental, between consecutive anneal states.*

to the initial state shown in (c). The histogram in (b) is similar to Figure 5.21(b), showing each anneal does not result in dramatic changes in the number of neighbors for a given grain. The cumulative shift in number of neighbors (c) does not show the steady shift towards larger quantities that was apparent with grain volumes. Grains have changed number of neighbors, as indicated by the broadening of the blue curve in (c), but distribution is still peaked about zero. Since grain growth is a process that is driven by the reduction in energy associated with grain boundaries, the broadening of the distribution should be expected. Presumably, high energy boundaries shrink in area and are replaced with lower energy configurations. This process can lead to critical events, like grain extinction, which will influence this neighbor distribution. Since the process is continual, the number of neighbors should also be evolving, which is what is suggested by Figure 5.22(c). It is this evolving distribution of grain boundaries that is our focus of Chapter 6.

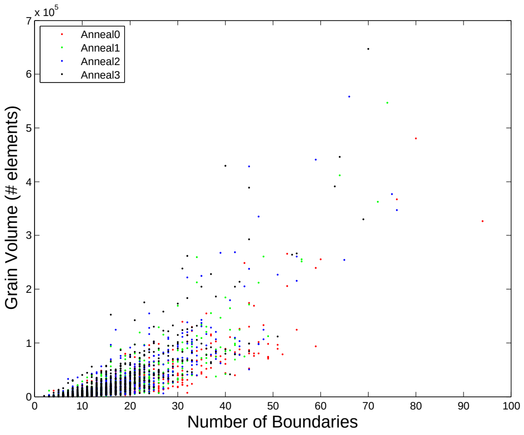

*Figure 5.23: Correlation between grain sizes and number of neighbors for the tracked grains. The coarsening process, leading to larger grain sizes, is easily seen by the black points (Anneal3) falling above the red points (Anneal0) in the plot.*

# Chapter 6

# Microstructure Evolution in Nickel

## Introduction

We now focus on the orientations of the individual grains composing the polycrystal and the misorientations describing their network of interfaces. In what follows, the dominating signal for this experiment will be found to be crystallographic in nature, and its evolution provides a new look at microstructural response to annealing. Our discussion of misorientations will be put in the context of the five parameter grain boundary character distribution (*GBCD*), which has proven to be a useful metric in characterization of interfaces of polycrystals. Its use will motivate analysis of a dominanting peak in the distribution, known as the coherent twin boundary, and our analysis will track how it evolves through incremental anneals to the microstructure.

## 6.1 Orientations and Misorientations in Nickel Microstructure

### 6.1.1 Orientation Distributions in Rodrigues-Frank Space

Unlike the aluminum data, where the measured coarse grain sample contained a few hundred grains in each anneal state, the nickel measurement contains several thousand grains. Our first anneal state contains approximately 2000 grains, which is an order of magnitude larger than the any previous x-ray coarsening experiment. Therefore, we are able to better quantify such statistics as the grain size and orientation distributions and expect their numbers to give a good description of a bulk polycrystalline system.

In Figure 6.1, the orientation distribution in Rodrigues-Frank space is displayed. The initial state orientation distribution is shown with black dots, while the third anneal is compared with green dots. We choose to use the grains that are present in the mesh for this display, since the mesh will be used for description of interfaces in the *GBCD* and the misorientation distributions to follow. Here, each point represents a single, orientation averaged grain. Initially, we will interpret the microstructure as a statistical distribution of orientations without performing grain-to-grain correlation. Since the anealing measurement was performed *ex-situ*, the macroscopic sample configuration will not be replicated between states. This results in a change in the sample coordinate system and consequently the orientations. Therefore, a global rotation is applied between anneal states for sample registration. The influence of this rotation is shown in the displacement between green and black dots in Figure 6.1, where orientation-to-orientation associations can be made between states, but they do not overlap. Evidently, the distribution of grain orientations is largely static. Qualitatively, we do not see any significant difference between the distribution of orientations in the initial state and those present after three anneals. In fact, the vast majority of grains in the initial state remain in the microstructure throughout the measurement.

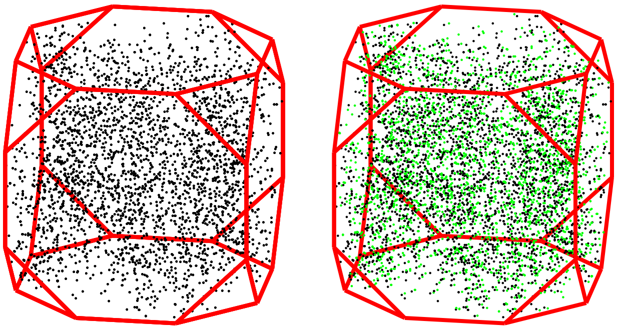

**(a)** **(b)**

*Figure 6.1: The orientation distribution of the initial nickel microstructure is shown in (a). (b) shows both the initial and third anneal state, with the third state represented with green points. Each point represents a single grain in the microstructure, extracted from the tetrahedral mesh. We can deduce that while the orientation distribution remains static as we anneal, we do have an anisotropic distribution of orientations in our microstructure, as evidenced by regions of orientation space that remain empty through the entire experiment. Specifically, orientations near the octahedral faces of the fundamental zone space remain absent.*

Several properties of the orientation distribution of Figure 6.1 hold special microstructural significance. Globally, instead of uniformly filling the truncated cube, as would happen with a truly random microstructure, there are clusters of similar orientations in the Rodrigues-Frank representation. In the language of materials science, this anisotropy is termed ‘texture’ and is used to describe a preferred orientation within a microstructure. The type and amount of texture in a material is influenced by the preparation history of the sample.

The orientation clustering is clarified in Figure 6.2, where the fundamental zone has been rotated to illustrates the localization of orientation points from Figure 6.1. A projection of the zone into the $RF_x - RF_y$ plane clearly displays clustering near the origin as well as four clusterings near the edges of the square. The orientation points near the origin are uniformly distribution along the z-axis of Rodrigues-Frank space. Recalling that our orientations are described with the Z-X-Z Euler angle convention (see Chapter 2) and in our coordinate system $RF_z$ is parallel to our sample's z-axis, we can conceptually visualize these orientations as cubes rotated about the cylinder axis. This observation is common with fcc materials that have been prepared into cylindrical shapes (wires, rods) [90]. During processing, the crystal's {100} axis preferentially aligns with the cylinder axis, forming a bias in orientations termed the fiber texture.

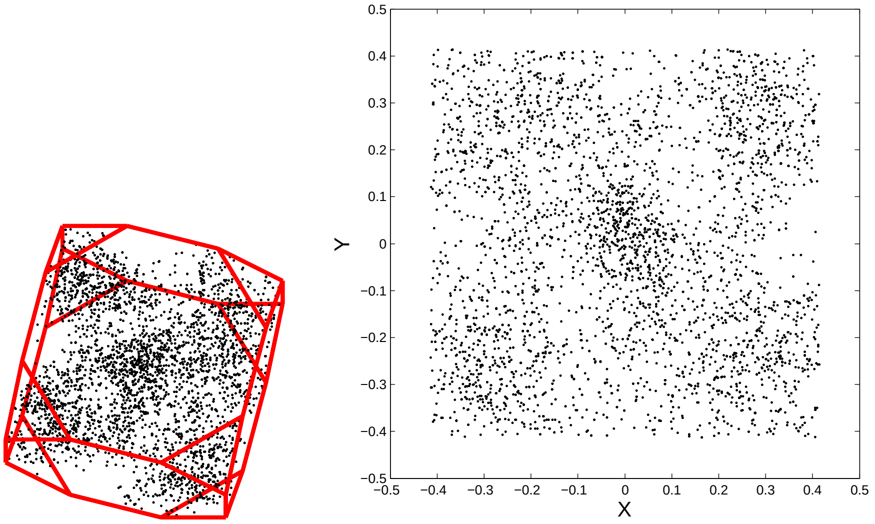

**(a)** **(b)**

*Figure 6.2: Plots of the orientation distribution from the initial microstructure shown in Figure* 6.1*, only rotated (a) to illustrate the non-uniform distribution of grains in orientation space. (b) shows the $x - y$ plane projection of the fundamental zone and permits easy identification of the five regions with significant orientation density. This anisotropy in orientation influences the evolution of the microstructure as we anneal and is part of the dominant signal in this experiment. In technical terms, this distribution of orientations describes a* {111} *and* {100} *fiber texture.*

The remaining orientation clusters are near the corners of the fundamental zone, in the vicinity of the truncating triangles. They are associated with large rotations about the body diagonal axis of the cube ({111} direction).

The observation of a non-uniform orientation distribution suggests than an anisotropy will be important in annealing phenomena. Therefore, enforcing theories which are built upon assumptions regarding orientation isotropy will be challenging at best. This immediately suggests that this measurement is far from an ideal specimen for following the assumptions of the Macpherson-Srolovitz theory of grain growth [22], which has been explored [66]. This grain growth theory has an underlying assumption that a geometrical quantity is the driving force for microstructural evolution and assumes that all boundaries have comparable energies and mobilities [42, 2]. This is not present in nickel, where the misorientation between neighboring grains and the crystallographic plane that composes their grain boundary is highly anisotropic[2, 31].

### 6.1.2 Misorientation Distribution

The orientation distribution illustrated that a non-random collection of grains are present within this nickel sample. While this distribution is certainly non-trivial, it is how these grains are spatially organized and how that influences the distribution's annealing evolution that is of greatest scientific interest.

We determine the misorientation distribution of the interfacial network by using a surface mesh that is composed of triangular elements [66]. These triangular 'patches' serve as planes of delineation between the two separate lattices and capture the unique boundary shapes that are shown as lines on the 2D maps. Each patch contains information about the neighborhood and orientation of the interface. Area, the crystallographic orientation of the grains on either side of the patch, and the patch normal (in the sample frame) are retained for analysis. To standardize the language that will be used in describing this collection of elements in the surface mesh, we classify *patches* as the individual triangles that capture the most local geometry of the interface and are our fundamental building block of interface space, while *boundaries* are collections of patches that describe the surface between the same two grains. Since grain averaged orientations describe this microstructure, a boundary is a collection of patches that have the same orientation pairs and are connected in sample space. Restrictions have been placed on these triangles so that the geometry of the mesh is regular. Patches are not permitted to have extreme geometries, which typically means one of the three angles within the triangle is very small ($< 20°$). This process is outlined in [66].

#### Misorientation Angle Distribution

The misorientation angle distribution of the grain boundary interface network is shown in Figure 6.3. The distribution is weighted by both patch area (a) and number fraction (b-c). All plots are normalized. Like the orientation distribution, the entire measured microstructure is presented from each state with grain-to-grain correlations. This will contribute to bin variations across states. The histograms use 0.25° bins for the partitioning of the misorientation angle. (a) displays the complete misorientation angle distribution and ranges from 0 to 62.8°, which fully describes a system with cubic symmetry. Immediately apparent is a large percentage of boundary misorientations that have very specific angles that dominate the distribution. There is a pronounced spike at the 60° bin and several weaker peaks that separate from background. The histogram in (b) displays the distribution by weighing each boundary by unity. This eliminates the possibility of large area boundaries dominating the distribution. The number of distinct boundaries in the microstructure varies from $19,510$ in the initial state to $13,957$ in the final state. Binning by number of boundaries makes the peaks around 32°, 35°, and 39° more pronounced.

The underlying misorientation angle distribution from (b) is magnified in (c). The black line indicates the Mackenzie distribution [77], which describes the misorientation angle for randomly arranged cubes (or alternatively the angle distribution if Rodrigues-Frank misorientation space was uniformly filled). It appears that the boundary distribution of the nickel follows this random distribution, except for those select bins that have a disproportionately large number of boundaries. The underestimation can be attributed to the large population at a select few bins.

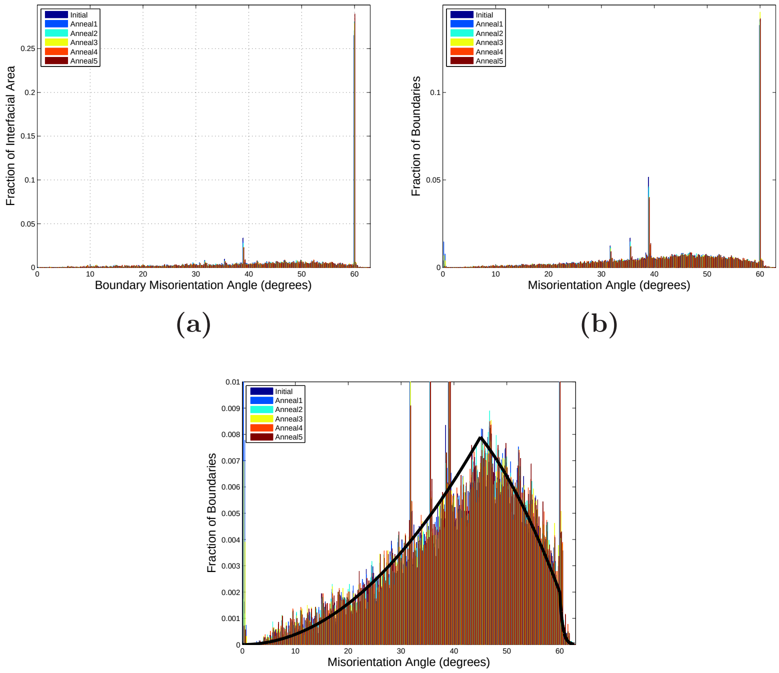

**(a)** **(b)**

**(c)**

*Figure 6.3: Misorientation angle distribution for nickel microstructure through all sample states. Histogram is partitioned with 0.25° bins in misorientation angle and the distribution has been weighted by patch area or number of boundaries, then normalized. (a) illustrates the area weighted distribution for all states and all possible misorientation angles. (b) shows the distribution of boundaries by misorientation angle, with each boundary given a weight of unity. (c) shows the same results as (b), but changes the vertical scale to a maximum of 1% to display that the underlying distribution of misorientation angles is random. The Mackenzie curve for randomly oriented cubes is shown as a heavy black line.*

The large bin populations seen in Figure 6.3 can be attributed to the heavy twin population that exists within this microstructure and leads to a significant number of misorientations with a rotation angle of 60°. The other peaks and most notably the one about ∼ 39° are a consequence of this twin population. We focus more directly upon these special misorientation relations, by expanding the peak through a finer binning scheme using 0.01°.

Figure 6.4 illustrates the two most dramatic peaks of the angle distribution and are both related to the twin. The twin misorientation is described as a 60° rotation about the $\{111\}$ axis, while a 38.94° rotation about the $\{110\}$ axis describes a configuration that is frequently observed due to the assembly of a boundary network containing many twins[91].

The sharpness of the peak is quite pronounced, with nearly 10% of the entire interfacial area of the initial state polycrystal having a misorientation angle within 0.005° of twin misorientation angle. The asymmetry in (a) of the peak at 60° is due to symmetry. It is shown below that essentially the entire population of this peak corresponds to a 60 degree rotation about the $\langle 111 \rangle$ direction. In a cubic structure, a rotation by $60° + x$ is equivalent to rotation by $60° - x$ and imposition of symmetry in our analysis puts all such rotations at or below 60 degrees.

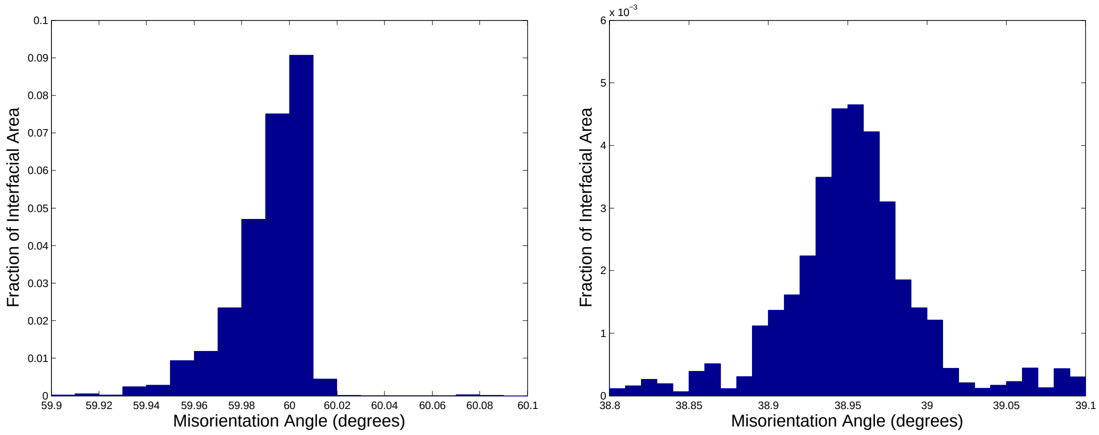

**(a)** **(b)**

*Figure 6.4: Expanded view of the two peaks in Figure 6.3, binned with 0.01° resolution in misorientation angle. The peak distribution is shown only in the initial state, though the later anneal states illustrate the same behavior. The peak on the left indicates that ∼ 10% of the interfacial area has a misorientation angle of* $60 \pm 0.005°$. *The peak is asymmetric due to the physical origins of the responsible misorientation and is clarified in the text. A symmetric peak about 38.95° is shown in (b) and accounts for ∼ 0.5% of the interfacial area.*

### Misorientation in Rodrigues-Frank Space

To this point, only the nickel's misorientation angle has been characterized, which is a single parameter description of misorientation. The full parameterization of misorientation is now demonstrated with the misorientation fundamental zone in Rodrigues-Frank space. This is shown in Figure 6.5 for the initial state microstructure, previously used for the orientation distribution in Figure 6.1. The unique geometry of the misorientation fundamental zone space makes it difficult to clearly identify regions of clustered misorientation. For better visualization, Figure 6.6 breaks the misorientation fundamental zone into nine slices along the $RF_z$ axis and uses a 2D histogram in $RF_x - RF_y$ to indicate the distribution of misorientations in the fundamental zone.

While the misorientation angle distribution is useful as a first pass characterization of the microstructure, the full three parameters gives us the complete picture of misorientation space. At first glance, the distribution of points appears random (as was also suggested by Figure 6.3(c)), but there exist clustered collections of boundaries that can be found through rotation and investigation of these plots. These are emphasized with black circles in Figure 6.6.

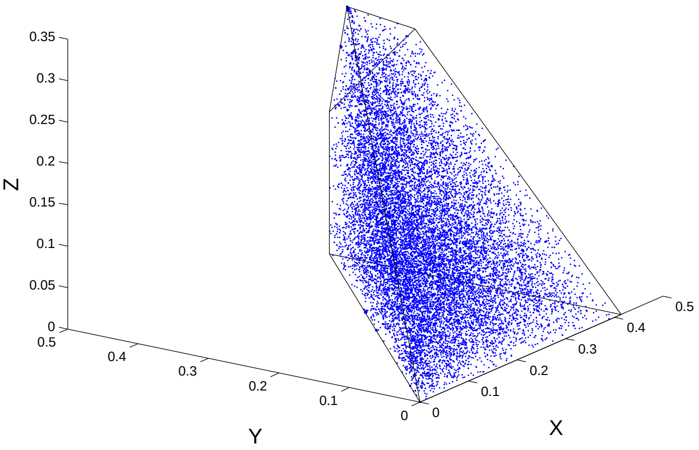

*Figure 6.5: Initial state misorientation distribution of the nickel microstructure, represented in the Rodrigues-Frank misorientation fundamental zone. Each dot corresponds to a different boundary within the microstructure, $\sim 19k$ in all. The plot shows the 3D distribution of the zone, with several clusters present, but not immediately apparent. Figure* 6.6 *shows integrated slices along the vertical axis to better illustrate such high density regions.*

### Misorientation Distribution and Special Boundaries

The misorientation distribution in nickel has been fully characterized in Figures 6.5 and 6.6. It was found that certain regions have high local density in misorientation space. We will interpret these in the context of the *CSL* model discussed in Chapter 1 and employ the $\Sigma$ notation for describing specific boundary types. The analysis associates each patch in the microstructure with a nearest *CSL* misorientation [32, 28]. The calculation follows from Equation 1.4, only now misorientation operators associated with the boundary and *CSL* configuration are employed, respectively.

$$\Delta g = (\Delta g_{CSL})^{-1} \Delta g_{boundary} \tag{6.1}$$

where $\Delta g$ is our boundary's misorientation ($\Delta g_{boundary}$) from the *CSL* configuration, represented by the operator $\Delta g_{CSL}$. The list of these *CSL* operators are readily available [32, 28, 36, 35]. Only the $\Delta g$ misorientation that is in the Rodrigues-Frank fundamental zone is retained for both misorientation angle and axis determination. The calculation of $\Delta g$ is performed for different *CSL* configurations. The boundary is associated with the *CSL* producing the minimum misorientation angle with the boundary's misorientation.

The presented data is based on *CSL*s up to $\Sigma 133$, though as the distribution will show, only a select few $\Sigma$s have unusual populations. Specifically, those that can be represented as $\Sigma 3^n$. In fact, since the $\Sigma$ value of a misorientation explains the density of atomic position overlap between two interleaved lattices (see Chapter 1), arbitrarily large $\Sigma$s should not be expected to be special in terms of energetics.

Figure 6.7 displays the *CSL* association of boundaries by fractional interfacial area within in the initial state polycrystal. A large portion of the microstructure is associated with $\Sigma 3$ and $\Sigma 9$ misorientations, while the remaining *CSL*s appear to be uniformly populated. The second plot utilizes the Brandon criterion [41] for characterizing the *CSL* association, with quantities in cyan being associated with the *CSL* under the Brandon criterion for misorientation from the $\Sigma$ configuration. While $\theta_{Brandon} \sim \frac{1}{\sqrt{\Sigma}}$, there still exist several boundaries with large $\Sigma$ associations that fall below $\theta_{Brandon}$.

While Figure 6.7 illustrates that there are some collection of boundaries that fall within a given misorientation angle criteria from certain $\Sigma$ values, it does not give a complete picture as to how close we are to certain *CSL* configurations. For instance, the $\Sigma 3$ and $\Sigma 9$ bins have nearly all entries satisfying the Brandon condition, but that indicates they are misoriented by less than $8.66°$ and $5°$, respectively. This is a liberal restriction and while not plotting precisely the same quantity, Figures 6.3 and 6.7 shows that our misorientations are rather sharply defined.

Figure 6.8 uses a $0.25°$ association criteria instead of $\theta_{Brandon}$ for *CSL* classification. The plots are area weighted fraction of the distribution for the two classifications. The first (red dots), show the area fraction within the $0.25°$ distribution. Therefore, the $10^{-1}$ value for the $\Sigma 9$ point indicates that 10% of the microstructural area that is within $0.25°$ of a CSL is associated with the $\Sigma 9$. The green dots look at the fraction in the entire microstructure, without restrictions placed on distance from a *CSL*. Thus, $\sim 13\%$ of the entire interfacial area in the microstructure is within $0.25°$ of the $\Sigma 3$ misorientation.

Demonstrated in Figure 6.8 is that we have a large set of boundaries associated with a small set of *CSL* points: $\Sigma 3$, $\Sigma 9$, $\Sigma 27a$, $\Sigma 27b$, $\Sigma 81a$, $\Sigma 81b$, $\Sigma 81c$, and $\Sigma 81d$. Since it is possible to have the same density of overlapping atomic positions for different misorientation configurations, letters are used for distinction. Interesting, these 8 *CSL*s can be represented as $\Sigma 3^n$ and are likely due to the configuration properties of the microstructure. For instance, three grains in a polycrystal typically form a triple line, which is the junction of three crystalline interfaces. If two of these interfaces have a $\Sigma 3$ misorientation, the misorientation of the third interface is constrained and satisfies the $\Sigma 9$ misorientation [91]. Similarly a $\Sigma 3$ and $\Sigma 9$ misorientation results in the third boundary of a $\Sigma 27$ type.

Exploring how close these distributions are to exact coincidence is of interest, since the previous arguments were insufficent (Brandon and randomly chosen 0.25°). To demonstrate variations with our misorientation threshold angle, we look at the area distribution within each $\Sigma$ bin as a function of misorientation angle from that *CSL*. This distribution is displayed in Figure 6.9.

The curves illustrated in Figure 6.9 present an interesting pattern that is replicated in each grouping, including the four $\Sigma 81$ *CSL*s that are not illustrated. An error function-like distribution is present for small misorientations, followed by a plateau where increasing the misorientation angle from the exact *CSL* adds few new boundaries, then an increase to unity for larger misorientation angles. The interpretation of this distribution is that the step function region describes boundaries that can be characterized as possessing the descriptive *CSL* configuration, while the tail to unity is composed of 'random boundaries' that are attributed to the target *CSL*. These boundaries are present because the analysis requires *some* $\Sigma$ association. If we made our CSL distribution denser, these interfaces would most likely be associated with a new *CSL* point. For instance, the $\Sigma 3$ does not illustrate this random tail, but if we limited our collection of *CSL*s to a smaller set, it would be present.

The distribution of Figure 6.9 is an interesting display of an intrinstic signal within our microstructure. We will investigate the error function property associated with the *CSL* configuration by fitting to the functional form

$$\alpha + \beta erf(\frac{\theta - \theta_0}{\sigma}) \tag{6.2}$$

where $\theta_0$ in the center and $\sigma$ are the width of the distribution. The results of the fit are displayed in Figure 6.10, with (a) and (b) illustrating the center and width, respectively. The points in Figure 6.10 are the result of averaging the distribution for each anneal state (i.e. averaging the different color lines in Figure 6.9. The center of the distribution is constant in $\Sigma$, with a mean of $0.29 \pm 0.02°$. The width of the peaks sharpens with lower $\Sigma$ values, as the distribution illustrates a small, but finite broadening with increasing $\Sigma$.

### Orientation and Misorientation Conclusions

Through analysis of both the orientation and misorientation distributions of this nickel microstructure, several conclusions can be drawn about the underlying orientation properties of the polycrystal. The distribution of orientations in the polycrystal is non-random, but instead exhibits a clustering in the fundamental zone that can be interpreted as texture. It was found that annealing does not significantly alter the orientation distribution. This was shown in Figure 6.1(b), where the orientation of grains in two different anneal states was presented.

Since orientations do not change, the misorientation distribution is also found to be static. The distribution was explored using two parameterizations: misorientation angle and Rodrigues-Frank misorientation vectors. While static, the misorientation distribution was quite unique, with a large fraction of boundaries having a very specific misorientation relation. Figure 6.3(d) demonstrates this distribution with the misorientation angle parameterization. These select boundaries could be described (almost exactly) in the language of coincident site lattice theory as $\Sigma 3^n$ misorientations (Figures 6.8 and 6.9.

The dominant misorientation is the $\Sigma 3$, which is commonly referred to as the twin misorientation and is described by a 60° rotation about the crystal's $\langle 111 \rangle$ axis. Nearly 30% of the interfacial area in the microstructure is associated with this configuration. The heavy twin population saturates the interfacial network to the extent that other misorientations, constrained by the presence of two twin related boundaries, produce other special misorientations that are also appreciably populated ($\Sigma 9$, $\Sigma 27$, $\Sigma 81$).

While changes in the misorientation distribution appear as an unlikely response to the annealing of this microstructure, evolution can still occur with the grain boundaries through changes in the crystallographic plane that composes the interface. In the presentation to follow, investigation of the boundary interface plane will be performed and how its distribution evolves as a function of anneal. Since a large portion of interfaces can be described with a small subset of misorientations, we can restrict our analysis to those configurations and monitor boundary plane evolution. By combining the grain boundary plane description with the misorientation, we arrive at the full five parameter description commonly referred to as the grain boundary character distribution or *GBCD*.

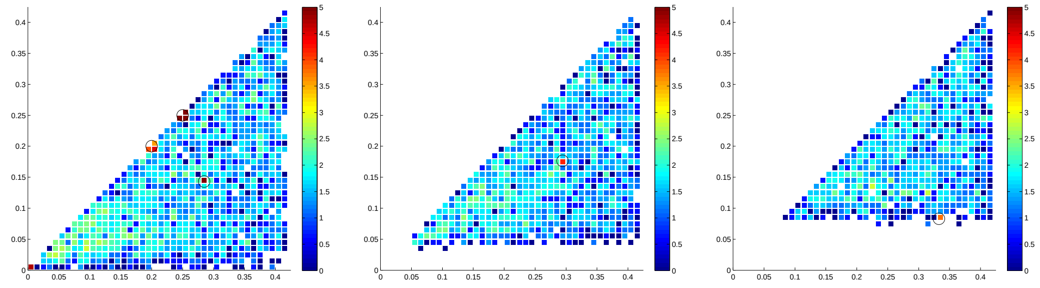

$RF_z < 0.0370$ $0.0370 \leq RF_z < 0.0741$ $0.0741 \leq RF_z < 0.1111$

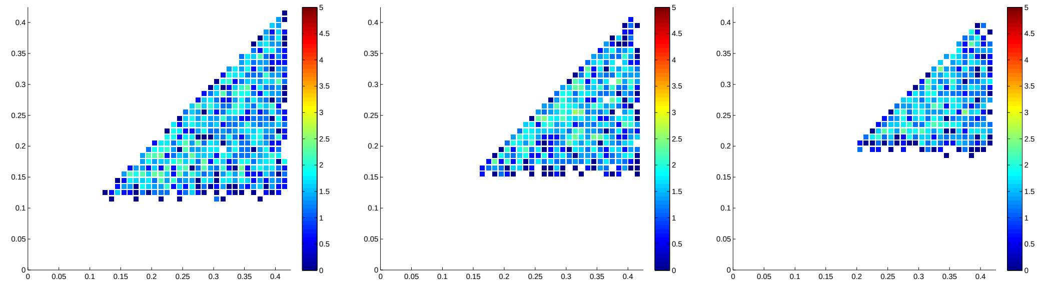

$0.1111 \leq RF_z < 0.1482$ $0.1482 \leq RF_z < 0.1852$ $0.1852 \leq RF_z < 0.2223$

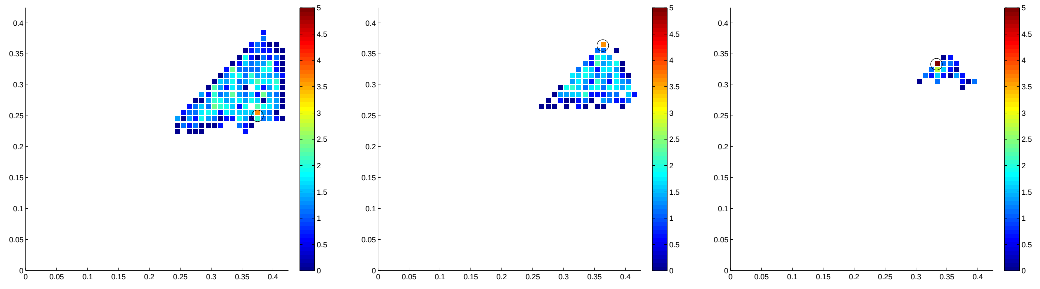

$0.2223 \leq RF_z < 0.2593$ $0.2593 \leq RF_z < 0.2964$ $RF_z \geq 0.2964$

*Figure 6.6: Collapsed sections of the misorientation distribution displayed in Figure 6.5. Each two dimensional plot is an projection of points falling with in a different cross-section of misorientation space, where integration is done over the z-axis. All of the fundamental zone is captured in these images and easily illustrates the clustering that is not readily apparent in the 3D representation shown earlier. Here, a 2D histogram with bin widths of 0.01 in* $RF_x$ *and* $RF_y$ *are populated by the number of boundaries falling in that* $RF_z$ *slice of misorientation space. The bins are colored by the number of boundaries in a given partition of misorientation space. The color scale uses the natural logarithm to illustrate the distribution of boundaries. Most of misorientation space is uniformly filled, which is colored in blue and corresponds to a population of only a few boundaries (*$\sim 5$*). Regions with a large number of boundaries (*$\gtrsim 100$*) are colored red, with the largest population occuring in the bottom right slice, with over 1000 boundaries in a single bin. Black circles indicate the location of special misorientation relationships related to the twin misorientation and can be described by* $\Sigma 3^n$ *in coincident site lattice theory.*

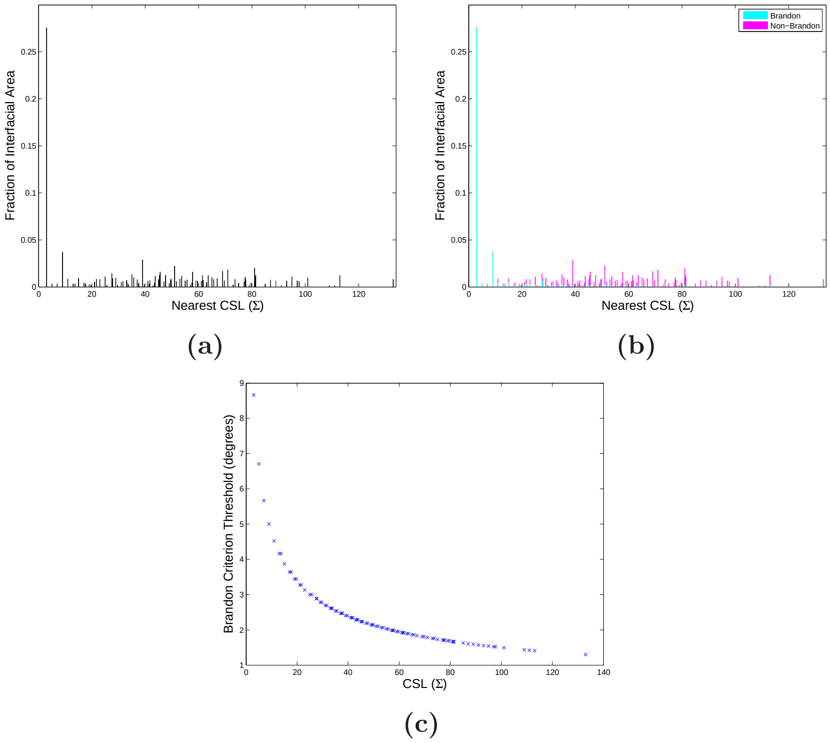

*Figure 6.7: (a) Distribution of interfacial area in the initial microstructure obtained by classifying misorientations with the nearest coincident site lattice point. 98 distinct $\Sigma$ values are used for this classification, ranging from $\Sigma3$ to $\Sigma133$. For the population in a bin, the misorientation of the patch must be closer to that $\Sigma$ value than the remaining 97 configurations. No consideration of the misorientation angle from the associated $\Sigma$ is used in (a), while (b) invokes the Brandon criterion for misorientation, only counting those patches that fall within the Brandon angle of the associated $\Sigma$. The Brandon threshold angle, $\theta_{Brandon}$ is shown in (c). All boundaries that fall within the Brandon critierion for a given $\Sigma$ are colored in cyan, while pink illustrates the remaining boundaries. Since the Brandon angle scales as $\frac{1}{\sqrt{\Sigma}}$, the distribution expectedly satisfies the small $\Sigma$ configurations, but there are still a collection of large $\Sigma$ values that fall within the threshold angle.*

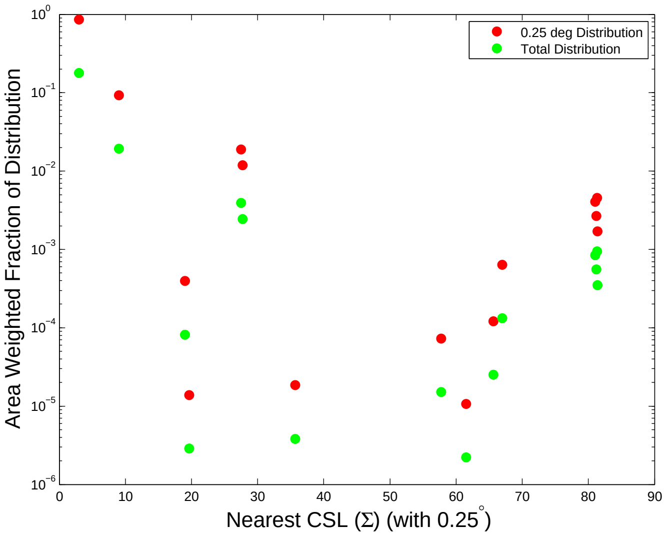

*Figure 6.8: Area fraction of microstructure as associated by* $\Sigma$ *value. The red and green points indicate two different populations in the data. Red dots are based upon the subset of boundaries that are within* $0.25°$ *of a CSL misorientation. The green dots relax this distance-from-CSL restriction and looks at the area fraction of boundaries associated with a given CSL (regardless of misorientation from this CSL point). Simply, its a measure of the fraction of boundaries that are closer to the given CSL than any other CSL point in the utilized list. To clarify, the* $\Sigma 3$ *red dot has a value close to unity, indicating that of all the boundaries within* $0.25°$ *of a CSL, approximately all of them are of the* $\Sigma 3$ *misorientation. The green dot for* $\Sigma 3$ *is* $\sim 0.2$*. Therefore, 20% of the interfacial area in our polycrystal is closer to the* $\Sigma 3$ *misorientation than any other CSL in our list. The plot shows that the largest values in both distributions are associated with* $\Sigma 3^n$ *misorientation configurations.*

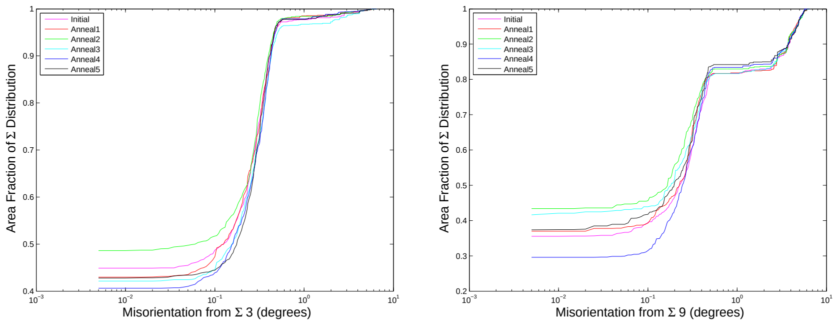

$\Sigma 3$ $\Sigma 9$

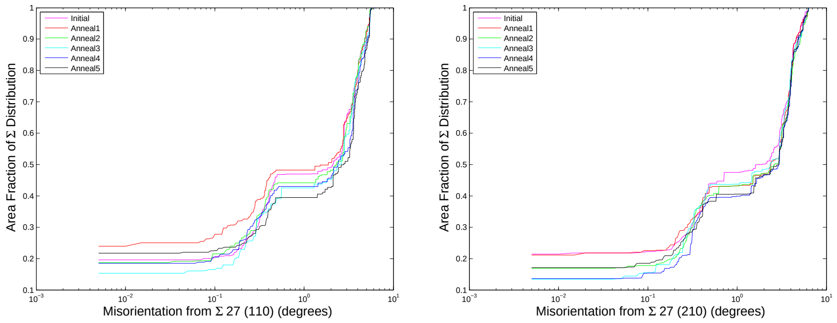

$\Sigma 27a$ $\Sigma 27b$

*Figure 6.9: Integrated area distribution as a function of misorientation from CSL configuration. The horizontal axis shows the misorientation from the CSL configuration ($\theta_{CSL}$), while the vertical axis indicates the fractional area (of patches associated with this $\Sigma$) that have a $\theta < \theta_{CSL}$.*

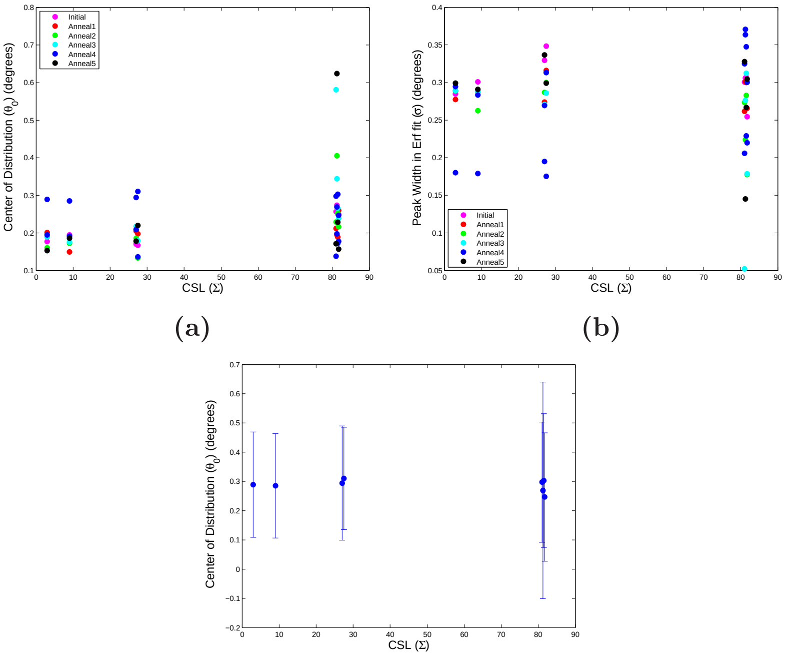

**(a)** **(b)**

**(c)**

*Figure 6.10: Results of fitting the rising edge portion of integrated area distribution of Figure 6.9 to Equation 6.2. The horizontal axes show the Σ number, with only $\Sigma 3^n$ displayed, and for configurations with the same Σ, points are offset ($\Sigma 27, \Sigma 81$). (a) illustrates the center of the distribution, while (b) shows the width. The information is combined in (c) to illustrate the peak distribution.*

## 6.2 Grain Boundary Character Distribution

Our discussion until this point has been devoted to the interpretation of microstructures as a spatial distribution of crystallographic orientations. We have quantified how these orientations have varied both within and among grains, where grains have been defined as clusters of similarly oriented voxels from the forward modeling reconstruction. Chapter 3 analyzed grains with respect to internal variations, while also interpreting the local orientation environment of nucleation and extinction events. There, a movement towards more uniform orientations was found to be the dominant signal and the microstructural response to the application of annealing sequence.

This analysis method has been furthered in Section 1.4, where this fully recrystallized nickel microstructure has minimal orientation variations and a unique, yet static distribution of interface misorientations (though the total area composed of certain misorientation configurations was seen to increase in Figure 6.3). If our analysis was to conclude with misorientation, we would have little justification and explanation for the dynamics that characterized the anneals, which saw grains grow and others shrink and obviously a microstructure with different properties from the one that was initially measured. Since the changes in interfacial area appear to be associated with a small set of special misorientation configurations, we isolate those boundaries and ask what other physical variables capture their evolution. This motivates a parameterization known as the grain boundary character distribution, which was introduced in Chapter 1.

The grain boundary character distribution ($GBCD$) is a five-parameter description of the crystallographic properties that describes the interface between adjacent grains. Three of the parameters describe the misorientation relation, explored in Section 1.4 for this nickel sample. The remaining two parameters are a description of the atomic planes that compose the boundary and is typically represented as the boundary normal vector in each of the crystal frames. Since the misorientation describes the rotation required to go from one lattice to the other, determining the boundary plane in one grain will implicitly specify that of its neighbor.

The motivation for the $GBCD$ is that neither misorientation nor boundary plane normal, by themselves, give the full picture of grain boundary properties, such as mobility or energy. In fact, molecular dynamics simulations [2] demonstrate large variations in these quantities for a given misorientation or boundary normal. This is displayed in Figure 6.11, which is from the aforementioned simulations. The plots illustrate the dependence between boundary plane, misorientation, and energy.

Evidenced by the plot is the existence of a very low energy boundary configuration associated with the $\Sigma 3$, when the boundary plane is the $\{111\}$ family of planes. This coherent twin and is the result of a 'mistake' in the stacking of atoms on the boundary. For face-centered cubic materials, the $\{111\}$ plane is closed packed and is built through an $ABCABCABC...$ stacking routine, where $A,B,C$ distinguish between different in-plane positions of atoms. Annealing twins occur when there is a disruption in this sequence, described by $ABCA\boldsymbol{B}ABC....$ This disruption forms a $\{111\}$ plane of atoms,

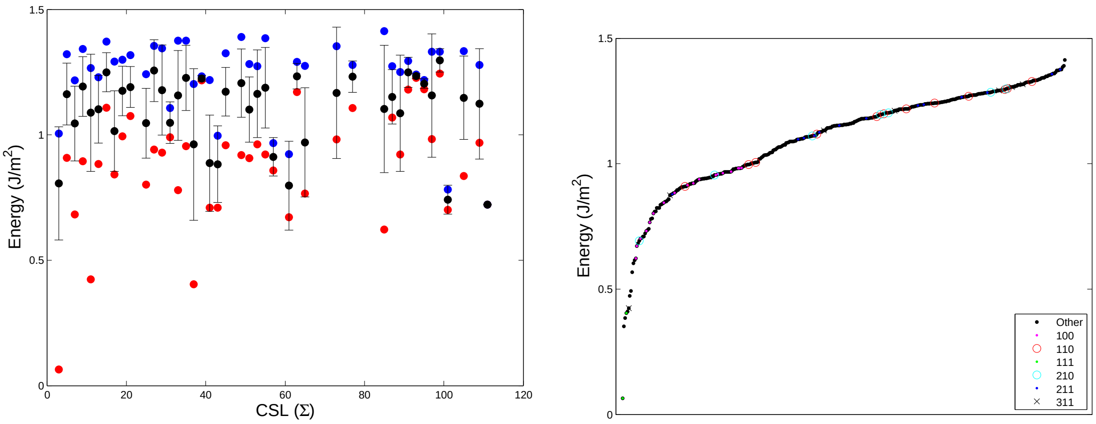

(a) (b)

*Figure 6.11: Molecular dynamics simulation results from [2], for nickel, illustrating the dependence of grain boundary energy on misorientation (a) and boundary plane (b). A total of 388 distinct points in GBCD space were investigated and their results reproduced here. The misorientation plot takes all Σ values and shows the variation associated with changes in boundary plane orientation. The error bars are the standard deviations associated with different boundaries within the misorientation, while the blue (red) dots indicate the maximum (minimum) energy observed for a given configuration. Energy as a function of boundary plane is shown in (b). All points in GBCD space are sorted by increasing energy (horizontal axis in (b)) and a selection of specific boundary plane types are shown with colored dots.*

but rotated by 60° from their nominal position in the standard stacking configuration. Thus, this instance can be described as being composed of a 60° rotation about the [111] axis, with the boundary normal along the rotation axis. This twin is labeled ‘coherent’, because the $B$ layer of atoms is correct for both sides of the lattice. The generation of such stacking faults has an intrinsic energy associated with it that is material dependent.

In addition to describing the energy associated with the stacking mistake, the stacking fault energy can also qualitatively describe dislocation mobility [13]. For materials with high stacking fault energy, dislocations can move readily and therefore slip (shearing of a plane of atoms) is more present when a stacking fault is present. This results in the entire crystal shifting by several atomic positions, but maintaining the same crystallographic orientation across the boundary. Alternatively, materials with low stacking fault energy (such as nickel), have dislocations that are relatively immobile. Therefore, instead of having the stacking fault result in a lateral shift of the crystal, a twin is formed, with an orientation (very specifically) different than the parent grain. For comparison, the stacking fault energy of nickel is less than half that of aluminum, which explains the lack of twins seen in the aluminum microstructure and their prevalence in this nickel.

## 6.3 Calculation and Representation of the Grain Boundary Character Distribution

While a usefully descriptive metric for characterizing the *GBCD* of a microstructure, visually illustrating the five-parameter space is non-trivial. Figure 6.13 displays the method traditionally used for representing the *GBCD*, as developed by the Carnegie Mellon University MRSEC program. Here, a portion of misorientation space has been isolated and the distribution of normals are symmetrized and plotted on a stereographic projection of the unit sphere. The $\{111\}$ direction is shown as the location of the peak for the $\Sigma3$ plot, while the origin of all these maps is the $\{001\}$ direction. For consistency and comparison, we use their method of producing *GBCD* quantities which we will briefly summarize, though we eventually deviate in the binning process of misorientation space to fully capture our sharpness in that space. A more rigorous mathematical explanation of the binning procedure can be found in publications produced by the Carnegie Mellon University group [10, 26].

### 6.3.1 Microstructure tesselation in GBCD space

The *GBCD* is generated by using the surface mesh, composed of individual triangular patches that contain information about the patch orientation in sample space and the crystallographic orientations describing the grain averaged orientation on either side of the boundary. Since the local lattice orientation is known, these sample frame normals can be converted into the crystal frame, which results in all five parameters necessary for the *GBCD* tabulation.

For this calculation, misorientation is represented by Euler angles, defined in Chapter 1, and boundary normals by (two) spherical angles. These quantities populate a 5D histogram by finding the symmetrically equivalent representations of the misorientation and boundary normal. Since exactly three fundamental zones of misorientation can be fitted into Euler angle space $(\phi_1, \Phi, \phi_2)$ if it is limited to $[0-90°, 0-90°, 0-90°]$; we use this partition (in 10° bins), though $\Phi$ is partitioned by $\cos\Phi$, unlike the other two Euler angles. The 10° partition was also used for the boundary normal space; binned as $(\cos\theta, \phi)$, where $\theta$ is the polar angle and $\phi$ the azimuthal. This binning scheme ensures that for a random polycrystal, composed of uniform misorientations and random direction boundaries, each bin is equally populated. For our *GBCD* histogram, the binning quantity is the patch area.

Once the area weighted *GBCD* histogram is produced, a normalization is performed, where bins are converted from interfacial area to multiples of a random distributions (MRDs). This entails dividing each bin by the average total binned area. Since each patch has 36 symmetrical equivalents that fall into our binning requirement, this means our normalization constant is $\frac{36\times Area}{9\times9\times9\times9\times36}$, where *Area* is the total interfacial area of the polycrystal. The use of MRDs is an alternative to a strict normalization, since it serves as a reference to a random polycrystal. Therefore, any anistropy in the polycrystalline interface network can be easily interpreted. Specifically, for a given bin, $MRD \gg 1$ would indicate a five parameter grain boundary type that occurs much more frequently in the given microstructure than a random one, while $MRD \ll 1$ would mean a deficit of such boundaries, compared to random.

Visual representation of the *GBCD* is accomplished with stereographic plots that fix misorientation and display the distribution of grain boundary normals. In a way, this produces a much more informative picture than either the misorientation alone (as shown in Figure 6.3 or 6.5), or boundary normal alone, displayed in Figure 6.12.

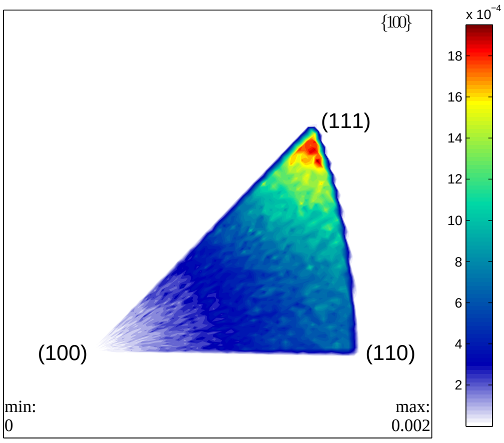

*Figure 6.12: Distribution of all interface boundaries in the crystal frame for the initial state microstructure. Here, each patch populates the standard stereographic triangle, which uses 1° bins in spherical normal. The distribution is normalized by the total interfacial area, with red regions indicating large population.*

While instructive in indicating a large population of {111} boundaries and a deficiency of {100}, combining both misorientation and boundary type is most instructive. This is typically accomplished through the selection of a *CSL* misorientation and producing an equal area grid in boundary normal space. The grid is filled by determining which *GBCD* histogram bins populate each point. Since we saw that $\Sigma 3^n$ configurations were associated with a large portion of the interfacial area, this process can effectively present the *GBCD* in a highly anisotropic material, such as this nickel. Figure 6.13 displays the $\Sigma 3$ (with two different color scales) and $\Sigma 9$ boundary normal distributions from the initial state microstructure. It is analysis involving these five parameter distributions that will be of interest for the remainder of this work.

### 6.3.2 Boundary Resolution and Meshing

The generation of the *GBCD* requires knowledge of both the grain misorientation distribution and grain boundary normal distribution. As has already been illustrated in

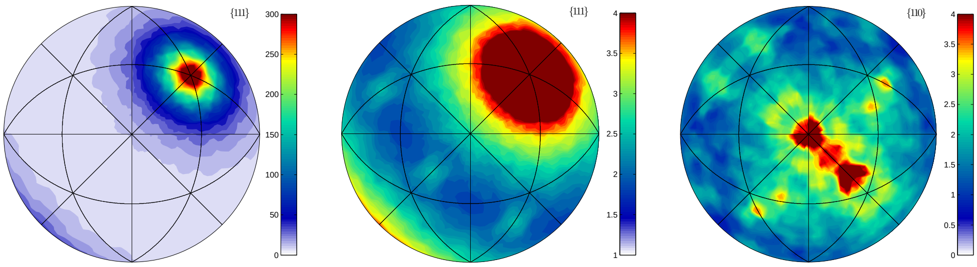

**$\Sigma 3$ - linear** **$\Sigma 3$ - logarithmic** $\Sigma 9$

*Figure 6.13: GBCD plots for the initial state nickel microstructure. The procedure for producing such maps is detailed in the text. Here, the $\Sigma 3$ and $\Sigma 9$ are illustrated, with the $\Sigma 3$ represented on a linear and logarithmic color scale, to illustrate both the sharpness of the $\{111\}$ peak and the distribution of normals in the tails. The $\Sigma 9$ distribution is also illustrated (on a linear MRD scale) and displays the prevalance of tilt boundaries, perpendicular to the $[110]$ misorientation axis. The colorbars indicate MRD values, except for the second $\Sigma 3$ plot, which is shown on a $\ln(MRD)$ scale.*

Section 5.6.1, the nickel microstructure exhibited minimal intra-granular orientation variations, on the order of tenths of a degree. This is due to the high orientation resolution of the technique, predominantly attributed to over-constraining orientations through the fitting to multiple diffraction peaks per voxel. Since intra-granular misorientation can be neglected for this sample, we were able to describe each grain with a single orientation. This translates to a sharp misorientation distribution, which we saw in misorientation angle with Figure 6.3 and full representation in Rodrigues-Frank misorientation space in Figure 6.5. This leaves the resolution of the boundary normal as the remaining characteristic of interest.

Chapter 5 explicitly detailed the conversion of 2D *.mic* files into volumetric meshes. Also outputed in this process is a surface mesh, composed of triangular elements that approximate the interface between grains. Hence, the determination of our grain boundary normal is highly dependent upon the 2D to 3D processing. We will explore how boundary resolution is influenced by changing the in-plane grid size. Our response variable will be the width of the $\Sigma 3$ peak, an intrinsic property of the sample. With coarser interpolations, we expect to have fewer and fewer unique directions to describe boundary planes and consequently a broader peak. We explore this for the initial microstructure state, using different grid sizes.

Figure 6.13 illustrates the boundary normal distribution for a given coincident site lattice misorientation and was the result of meshing with a rectilinear grid composed of $1.2 \times 1.2 \times 4\mu m$ voxels (the latter being the spacing between measured layers). The coherent twin peak in (a) is clearly present, but changes in-plane distribution can change its shape as shown in Figure 6.14, where in-plane resolutions of $6\mu m$ and $0.6\mu m$ are illustrated. Not surprisingly, changing the resolution of the grid has great influence on the boundary normal distribution.

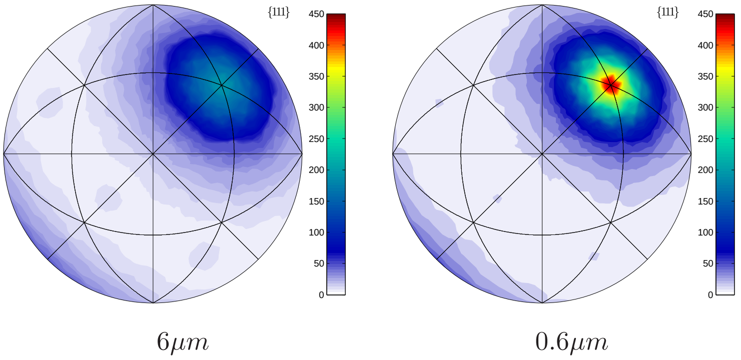

*Figure 6.14: Σ3 distribution illustrated with variable in-plane grid resolutions. The coherent twin peak exists for all grid resolutions, but the maximum and width are highly sensitive to the grid resolution.*

To quantify our distribution we use three methods of statistical characterization, the first two introduce evaluation of statistics on a sphere. To the best of our knowledge, this is the first time *GBCD* peaks have been analyzed in this manner. One approximates the peak as a Gaussian distribution on a sphere, which is termed the von Mises-Fisher distribution [92]. The second method introduces the concept of an orientation tensor, which can be used to describe a collection of area weighted normals and quantify their spread [93, 5]. Lastly, while both of these methods can describe the distribution, their ability to fully characterize the peak distribution is lacking. We fit the area weighted histograms in boundary normal space to a Lorentzian function and use that to estimate the width of the coherent twin peak. We will use these three methods to first investigate the peak characteristics as a function of rectilinear grid resolution, and then to describe the evolution of the peak through anneal states.

### Partitioning of data

We have established that the Σ3 peak is highly localized in misorientation space and has an appreciable number of patches within fractions of a degree of the coherent twin relation in five parameter *GBCD* space. To determine the shape of the peak, individual patches within 0.75° of the Σ3 are used. This threshold is based on Figure 6.9. It ensures that entire Σ3 distribution is captured, but random high angle boundaries associated with the Σ3 are not. Figure 6.15 describes how this selection criteria influences the portion of microstructure that is retained for this mesh resolution study.

With patches selected, boundary normals must be determined in the crystal frame. It should be noted that the peak in Figure 6.13 is symmetrized. On the full sphere, the same peak distribution would be present at eight locations; one for each of the axes in the {111} family. Realizing this symmetry, only positive component boundary normals

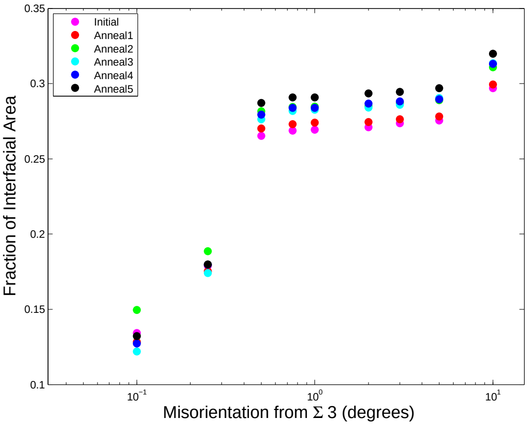

*Figure 6.15: $\Sigma 3$ distribution illustrated by fraction of the interfacial area of the microstructure. The plot is analogous to Figure 6.9, except we eliminate the CSL association and determine every patch's distance from the $\Sigma 3$, as judged by misorientation angle. The horizontal axis indicates the misorientation angle threshold (all boundaries less than this angle are counted), while the vertical axis indicates the fraction of the total interfacial area of the present state's microstructure.*

will be used. Through all the symmetry related representations of the normal, three copies of each patch satisify this requirement and are symmetrically arranged about the $\langle 111 \rangle$ direction.

Since each patch has a different area, a weighted distribution is produced, which can be fitted to the functional form in Equation 6.4. We create a 2D histogram where bin quantites are $\cos\theta$ and $\phi$, which produces an equipartition of this portion of boundary normal space. There are 90 bins in each dimension, which has the range $\cos\theta \in [0, 1]$ and $\phi \in [0°, 90°]$. This grid is populated by boundary areas and then normalized so that all bins sum to unity. Hence, the *MRD* scale is not utilized in this study.

### Von-Mises Fisher Distribution

The von Mises-Fisher distribution [92] is the spherical analog to the Gaussian distribution

$$f((\theta,\phi);\alpha,\beta,\kappa) = \frac{\kappa}{4\pi\sinh\kappa}\exp[\kappa(\sin\theta\sin\alpha cos(\phi-\beta)+\cos\theta\cos\alpha)] \qquad (6.3)$$

where $\theta$ is the polar angle describing in the inclination with respect to the $x-y$ plane, $\phi$ is the azimuthal angle, and $\alpha$, $\beta$ are the centers of the distribution. The parameter $\kappa$ provides an estimate for the dispersion of the data around the mean direction ($\alpha$,$\beta$). The larger the value of $\kappa$ the more tightly peaked the function becomes. For our peak fitting procedure, we model Equation 6.3 with the function [94]

$$f((\theta,\phi);\alpha,\beta,\kappa,a,b) = a + b\exp[\kappa(sin(\theta)sin(\alpha)cos(\phi-\beta) + cos(\theta)cos(\alpha))] \tag{6.4}$$

Determination of the the parameter set $(a, b, \alpha, \beta, \kappa)$ is accomplished with non-linear regression. Once the parameters are determined for the distribution, the FWHM of the peak can be calculated

$$\theta_{FWHM} = \arccos(\frac{log(\cosh\kappa)}{\kappa}) \tag{6.5}$$

### Von-Mises Fisher Distribution Results

Rectilinear grid resolutions of variable sizes for the initial state microstructure are used for this study. The vertical dimension of the voxels has been kept constant at $4\mu m$, consistent with the resolution of the measurement. The in-plane resolution is square and ranges in side length from $0.6\mu m$ to $6\mu m$. The peak in $(\cos\theta, \phi)$ for the extreme resolutions is shown in Figure 6.16 with both the raw 2D histogram and the fitted von Mises-Fisher distribution. The functional form captures the general shape of the peak, but the peak maxima are underestimated, and therefore peak widths (Equation 6.5) will be overestimated. Despite these observations, it is still instructive to monitor how the peak evolves using this distribution since it should be sensitive to general trends in peak character.

Evident from Figure 6.16 is that the peak shape clearly changes with grid resolution. These differences are explored in Figure 6.17, where both the maximum bin and FWHM of the peak are plotted against mesh resolution. The center of the peak in $\theta$ and $\phi$ are not displayed and varied by less than 0.001° from the optimal $\phi = 45°$ and within 0.001 of $\cos\theta = 0.9553(\theta = 54.736°)$. Under-estimation of the peak maximum is shown in the plot of resolution versus fit maximum, with the fit in black and the histogram maximum in red. Consequently, the width of the distribution is over-estimated, which is shown in (b). The error bars on the distribution are from a 95% confidence interval placed on the $\kappa$ parameter and then evaluated with Equation 6.5.

Despite the under-estimation of the fit to the coherent twin peak, it appears that fit properties reach an equilibrium with in-plane resolutions between 0.9 and $1.5\mu m$. Therefore, the $1.2\mu m$ resolution used in Chapter 5 and for our correlated boundary study is an acceptable representation of the microstructure. For resolutions that are larger than these in-plane lengths, the representation is too coarse and the peak is broadened. For grids finer than $0.9\mu m$, the peak also broadens. While not presently understood, it is hypothesized that this is due to difficulties in the smoothing of fine features.

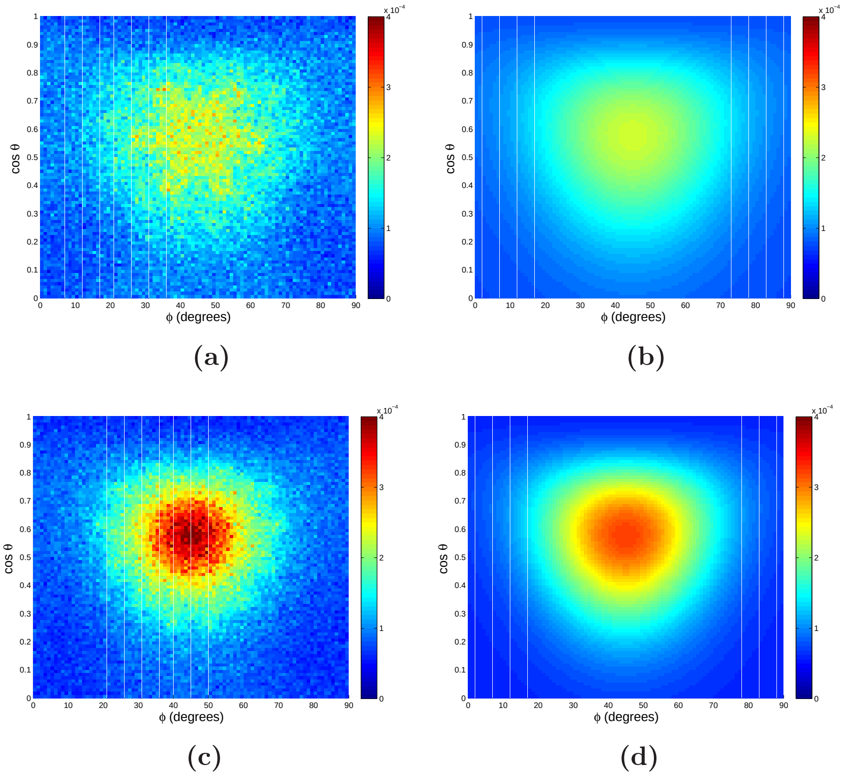

*Figure 6.16: Grain boundary normal distribution for patches with a misorientation angle within* $0.75°$ *of the* $\Sigma 3$*. The plot is parameterized as* $\cos\theta$ *vs.* $\phi$ *and illustrates the peak for the* $6\mu m$ *resolution grid in (a) and the* $0.6\mu m$ *grid in (c). Fits to these area weighted histograms are shown in (b) and (d). The histogram is area weighted and normalized to unity. The color scale is the same for all four plots.*

### Distribution Characterization via Orientation Tensor

Fitting the coherent twin peak to the von Mises-Fisher distribution has two drawbacks. First, it assumes that the functional form for approximating the peak is correct. It was found that fits both underestimated the peak height and overestimated the peak width. This suggests using a functional form that is closer to the Lorentzian distribution on a sphere than the Gaussian. The second disadvantage is that the data must be histogrammed for the regression.

Therefore, an alternative method of analyzing distributions on a sphere is proposed. It is analogous to determination of the moment of inertia tensor of classical mechanics [82], where the spatial distribution of mass in a system describes its inerti qualities in the context of rotation. The construction is called the *orientation tensor* [93, 5] and analyzes the spatial distribution of boundary normal directions and uses the patch area, instead of mass, to weight the distribution. This is shown in Equation 6.6

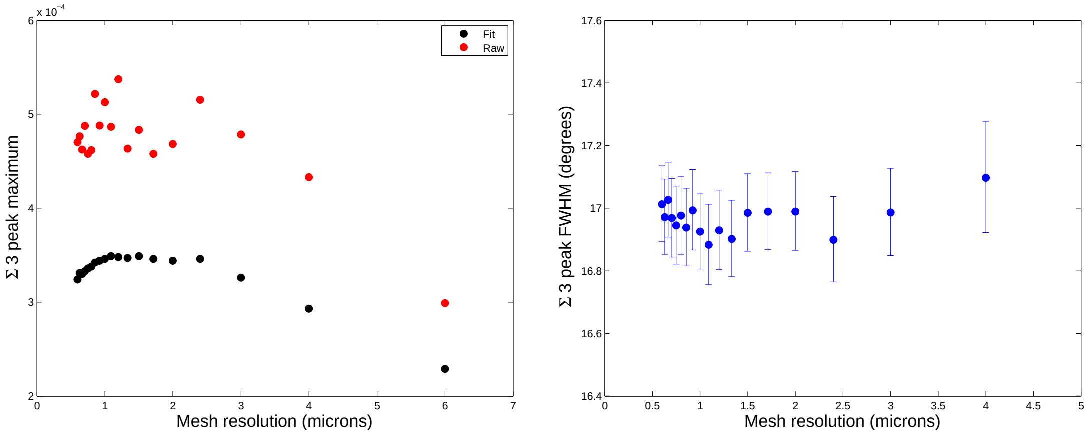

**(a)** **(b)**

*Figure 6.17: Results from fitting the $\Sigma3$ boundary normal peak to the von Mises-Fisher distribution. (a) illustrates the maximum value of both the fit (black) and the raw 2D histogram. The fit underestimates the maximum found in the data set, shown in red. (b) displays the peak widths of the distribution, which is a FWHM estimation. Error bars are estimated from the 95% confidence intervals on the fit parameters.*

$$\boldsymbol{T} = \frac{1}{A}\begin{pmatrix} \sum A_i x_i^2 & \sum A_i x_i y_i & \sum A_i x_i z_i \\ \sum A_i x_i y_i & \sum A_i y_i^2 & \sum A_i y_i z_i \\ \sum A_i x_i z_i & \sum A_i y_i z_i & \sum A_i z_i^2 \end{pmatrix} \tag{6.6}$$

where the summation is over each patch with an area, $A_i$, and a crystal frame normal direction $(x_i, y_i, z_i)$. Like the inertia tensor, the orientation tensor is real and symmetric and therefore can be diagonalized, with eigenvalues $(\lambda_i)$ along the diagonal associated with an eigenvector $(\nu_i)$, analogous to principal moments and axes for an inertial distribution. Our normalization constant, $A = \sum A_i$, forces $\sum \lambda_i = 1$. Eigenvalues are sorted, such that $\lambda_1 \geq \lambda_2 \geq \lambda_3 \geq 0$, and their associated eigenvectors are numbered the same way. We interpret $\nu_1$ as the principal axis, which is the direction of the peak of the boundary normal distribution. The larger the value of $\lambda_1$, the more peaked the distribution, since having $\lambda_1 \gg \lambda_2, \lambda_3$ would suggest a uni-axial distribution, while all three eigenvalues $\sim \frac{1}{3}$ would suggest a uniform distribution, since all eigenvectors are orthogonal and no axis is preferred.

Obviously, the eigenvalues of this orientation tensor should give us some understanding about how the data is distributed in boundary normal space, and more specifically, how variation occurs around a peaked direction like we have with the coherent twin. We employ Woodcock's [5] eigenvalue ratio parameterization to characterize the peak. By plotting the ratio of eigenvectors $(\ln \frac{\lambda_1}{\lambda_2} vs. \ln \frac{\lambda_2}{\lambda_3})$, the directional distribution of boundaries can be identified. Values with $\ln \frac{\lambda_1}{\lambda_2} \gg \ln \frac{\lambda_2}{\lambda_3}$, the distribution is clustered in a single direction, such as would be the case with a flat boundary and similar to what we see with the Σ3 boundary normal. $\ln\frac{\lambda_1}{\lambda_2} \ll \ln\frac{\lambda_2}{\lambda_3}$ indicates a distribution of normals that are rotationally symmetric about a fixed direction, as would be seen on the surface of a cylindrical object. Lastly, the further a distribution is from the origin in the $\ln\frac{\lambda_1}{\lambda_2} vs. \ln\frac{\lambda_2}{\lambda_3}$ plot, the stronger the distribution type. This can be estimated by a third eigenvalue ratio, $\zeta$, known as the strength parameter.

$$\zeta = \ln(\frac{\lambda_1}{\lambda_3}) \tag{6.7}$$

Since the boundaries we are examining are clustered, increases in the strength parameter correspond to decreases in the spread of boundary normals in our distribution. Since the $\ln\frac{\lambda_1}{\lambda_2} \ll \ln\frac{\lambda_2}{\lambda_3}$ plot ranges from a clustering about a single direction on the vertical axis to a belt-like distribution of normals, as would describe the surface of a cylinder, on the horizontal axis, the use of a polar angle to describe this distribution shape is appropriate. This polar angle, appropriately termed the shape parameter, $\tau$, is defined as

$$\tau = \frac{\ln(\frac{\lambda_1}{\lambda_2})}{\ln(\frac{\lambda_2}{\lambda_3})} \tag{6.8}$$

$\tau$ ranges from zero for the belt-like (or girdled) distribution to infinity for the clustered distribution.

### Mesh Resolution as Interpreted with Orientation Tensor

Evaluating the orientation tensor for the coherent twin boundary normal distribution yields the principal eigenvector in the $\langle 111 \rangle$ direction, while the other two eigenvalues are exactly equal and therefore have arbitrary eigenvectors that are mutually orthogonal. This means that the peak is symmetric about the $\langle 111 \rangle$ and only the strength of the peak is relevant. Figure 6.18 shows a plot of $\zeta$ as a function of mesh resolution for the initial state microstructure. The relationship between strength and resolution is similar to that of peak maximum and resolution found in Figure 6.17. For resolutions between 0.9 and $2\mu m$, the strength is maximal and constant, which is in agreement with the findings of the von Mises-Fisher fits that illustrated a peak maximum and width convergence between 0.9 and $1.5\mu m$.

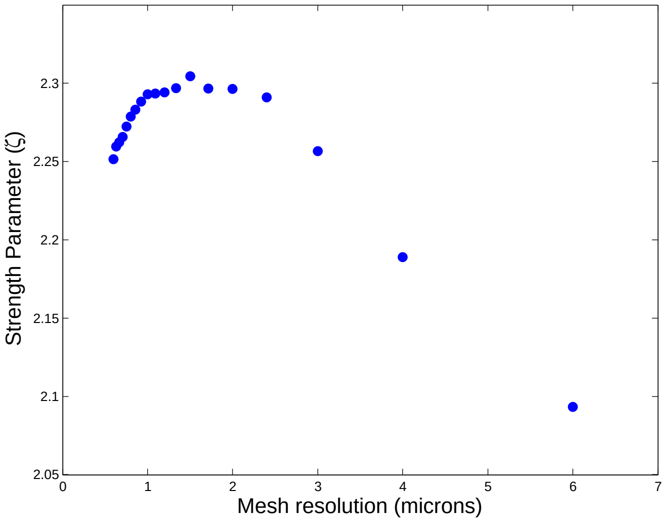

*Figure 6.18: Strength distribution parameter as determined with the orientation tensor analysis for the initial state microstructure of variable in-plane resolution. Only two unique eigenvalues were found for the distribution, indicating the peak is symmetric about the principal direction ([111]). The strength parameter quantifies how strongly peaked the distribution is.*

### Mesh Resolution and the Lorentzian Distribution

The final quantification of peak distribution is a fit based upon the 2D area weighted histogram that was employed for the von Mises-Fisher approximation. Here, the two boundary normal variables $(\cos\theta, \phi)$ are separately evaluated by integrating the distribution across the complementary histogram dimension. A sample of this distribution is shown in Figure 6.19, along with the 2D histogram over which it was integrated. The appearance of the distribution immediately suggests fitting to a Lorentzian functional form

$$f(x; y_0, B, \Gamma, x_0) = y_0 + \frac{2B}{\pi} \frac{\Gamma}{4(x - x_0)^2 + \Gamma^2} \tag{6.9}$$

where the FWHM of the distribution is given by $\Gamma$ and the distribution's center is at $x_0$. Here, $x$ will be $\phi$, when we integrated over $\cos\theta$ and vice versa.

The fit to the distribution is shown as a red line in Figure 6.19, which is representative of all plots of these types for variable mesh resolution. The $\phi$ distribution is well matched to the Lorentzian, while $\cos\theta$ is also well approximated by the Lorentzian, but the asymmetry for large $\cos\theta$ results in a poor fit near extremes. Since the purpose of this Lorentzian fit is to estimate the width of the peak, this descrepancy near the tails is inconsequential. The fit parameters are illustrated with 95% confidence intervals on each

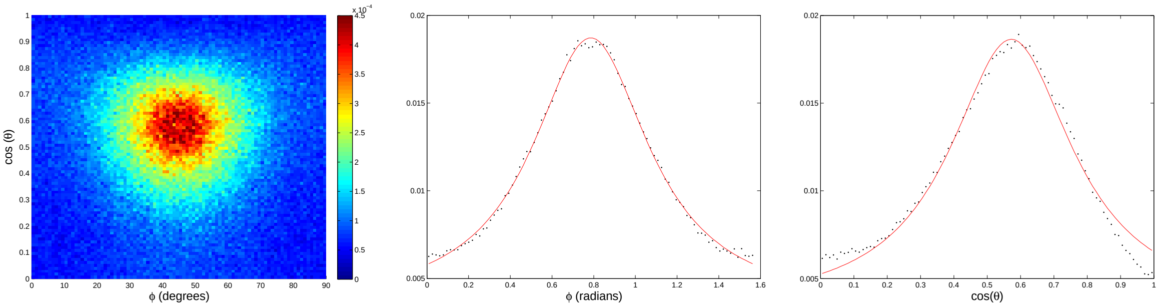

**(a)** **(b)** **(c)**

*Figure 6.19: Results of fitting each dimension of the 2D area weighted histogram of boundary normals to a Lorentzian functional form. (a) is the normalized, area weighted boundary normal histogram for the initial state microstructure with an in-plane grid resolution of* $1.5\mu m$*. The plots in (b) and (c) are the results of integrating across one histogram dimension and fitting the distribution (shown in red). (b) is the* $\phi$ *distribution, which is produced by integrating vertically in (a), while (c) is the result of integrating horizontally.*

parameter, which is displayed as error bars. The evolution of the peak as a function of mesh resolution is summarized in Figure 6.20. The center of the distribution for each parameter agrees with the coherent twin direction ( $(\cos\theta, \phi) = (\frac{1}{\sqrt{3}}, 45°)$ ), with a narrowing of the confidence band with finer grid resolutions. Its static distribution is not displayed here.

Finally, peak widths in $\cos\theta$ and $\phi$ can be expressed as $d\cos\theta d\phi$, which is simply the differential formula for a solid angle on the unit sphere. Equating this product to the solid angle swept out by a cone that intersects the unit sphere gives

$$d\Omega = d(\cos\theta)d\phi = 2\pi(1 - \cos\theta_{cone}) \tag{6.10}$$

Here, $d\Omega$ is the cap on a cone with a basal radius of $\sin\theta_{cone}$. The full width of the cone can be defined as $2\theta_{cone}$. We use the widths of both $\cos\theta$ and $\phi$ to define this angular width of our peak distribution and employ the 95% confidence intervals on these two quantities to produce error bars. This peak width, as a function of mesh resolution, is illustrated in Figure 6.21.

Interpreting the results of the Lorentzian fits to both $\cos\theta$ and $\phi$, we see that peak amplitude reaches a maximum in the range of $1.5 - 2\mu m$ in-plane resolution, then broadens for both coarser and finer grids; just like the observations in the other two characterization methods. For in-plane resolutions between 0.9 and $1.2\mu m$, a minimum in distribution width is observed. Therefore, the choice of an in-plane resolution of $1.2\mu m$ should suffice for analysis of the distribution across anneal states.

While not explicitly determined, the decrease in peak quality for both very coarse and very fine grids makes intuitive sense: reconstructions were performed with a 2D grid

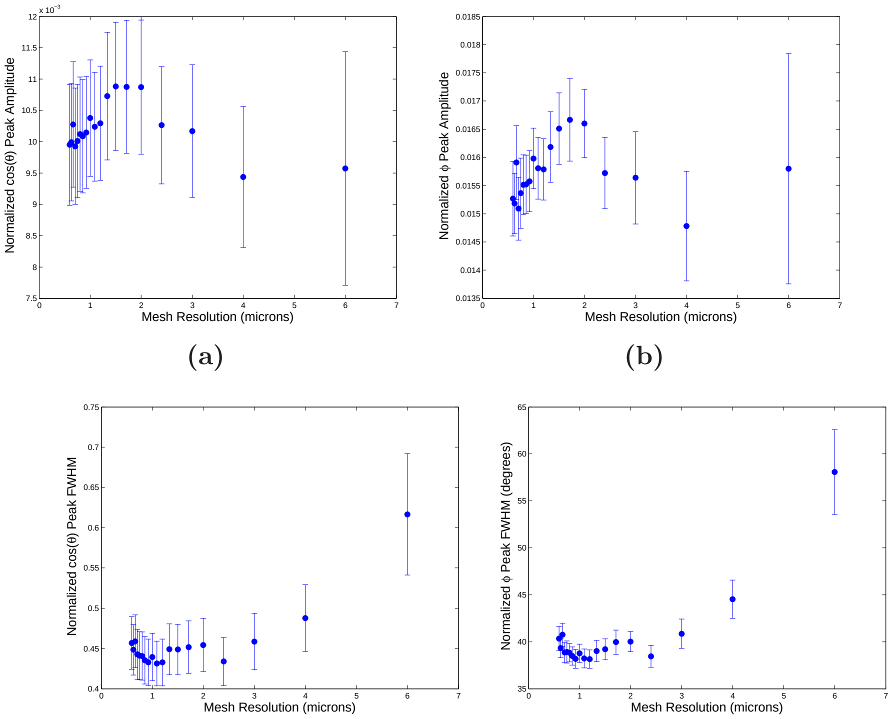

**(a)** **(b)**

**(c)** **(d)**

*Figure 6.20: Results of fitting a Lorentzian function to the coherent twin peak of the* $\Sigma 3$ *distribution in the initial anneal state. The evolution of the* $\cos\theta$ *distribution((a),(c)), and the* $\phi$ *distribution ((b),(d)) are shown as a function of variable mesh resolution. The top row illustrates the amplitude of the normalized distribution, while the bottom row displays the peak's FWHM.*

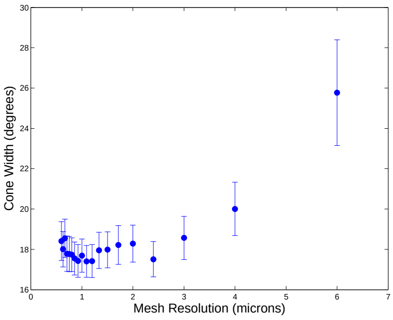

*Figure 6.21: Width of the coherent twin as defined by the* $\theta_{cone}$ *quantity from Equation 6.10. Error bars are described in the text.*

of $2.8\mu m$ equilateral triangles. If resampling of this grid with rectilinear elements that are much larger than these triangles, the mesh will be insensitive to subtle features in the microstructure and therefore our boundary normal distribution will be coarse. Alternatively, if we sample with elements that are much smaller than our measurement's spatial resolution, artificially fine features are introduced into the interface network which can negatively influence mesh smoothing and accurate representation of the microstructure.

### Resolution Conclusions

The coherent twin peak for the initial state microstructure has been quantified with variable rectilinear grid resolutions. Characterization of the peak has been accomplished with three methods, each with variable success. The first method approximated the peak with a functional form on the unit sphere, known as the von Mises-Fisher distribution, which is used to describe a normal distribution on the unit sphere. Using this approximation, we found the coherent twin peak to be underestimated, which leads to overestimation of the widths. These are displayed in Figure 6.17 and illustrate that for in-plane grid resolutions in the interval $[0.9, 1.5]\mu m$, the peak profile is relatively stable. The fitting process does suffer from assuming that the coherent twin peak is both normally distributed and fits must be produced by histogramming the boundary normals. The Lorentzian analog to the von Mises-Fisher distribution would be ideal for characterizing the peak.

The second method for peak characterization used the concept of an orientation tensor. Determining the eigenvectors and eigenvalues of the distribution provided a method of describing the shape and qualitative clustering of the peak. Only two unique eigenvalues were found for the orientation tensor of each mesh, indicating a symmetric peak was present. This is expected due to the inherent use of symmetry operators to determine the boundary normal directions of the distribution. Actually, since our method of determining boundary normals confines the discussion to positive components of the three cartesian directions, the $\langle 111 \rangle$ will always be an eigenvalue. Still, even with this attribute, a large magnitude for the other eigenvalues indicates a broad distribution away from the coherent twin direction. Hence, the strength parameter was used for describing the distribution of normals, only with different in-plane resolutions. Like the von Mises-Fisher analysis, the orientation tensor interpretation of the data suggests that the $\Sigma 3$ peak is stable over element sizes in the $[1, 3]\mu m$ interval.

Lastly, we noted that the functional form of the $\cos\theta$ and $\phi$ distributions for this collection of boundary normals follows a Lorentzian distribution. Estimating the distribution with this function illustrated great agreement with both peak amplitude and width. The two independent analysis were then converged to estimate the solid angle covered by the peak on the unit sphere and by equating this with a cone, an angle was provided to estimate the width of the coherent twin distribution. It was found that mesh resolutions between $[0.9, 2]\mu m$ showed minimal variation in the peak properties.

With this resolution study, we settle on using the 1.2 $\mu m$ grid for the remainder of our analysis involving the *GBCD*. A fixed resolution now allows us to probe the experimental response to the annealing sequence applied to the microstructure. We repeat this same analysis with the three fitting methods, only now use anneal state as the dependent variable, instead of initial state mesh resolution.

## 6.4 Coherent Twin Distribution through Anneals

Having established the misorientation threshold and grid resolution for the Σ3 distribution, the evolution with respect to anneal can be investigated. The Σ3 peak for all six measured states is illustrated in Figure 6.22. The same color scale and binning procedure have been used for all plots. The comparison is not exactly one-to-one in that the size of the measured volume is variable, as was previously noted. Still, the *GBCD* histogram used to produce these plots was normalized, so if the coherent twin distribution is a global description of the sample state, varying the volume size should not influence these plots. Immediately evident from these plots is that the Σ3 peak distribution becomes sharper with each anneal step. The peak is narrower and the maximum increases. It is investigation of the sharpening of the coherent twin with annealing that will conclude this thesis.

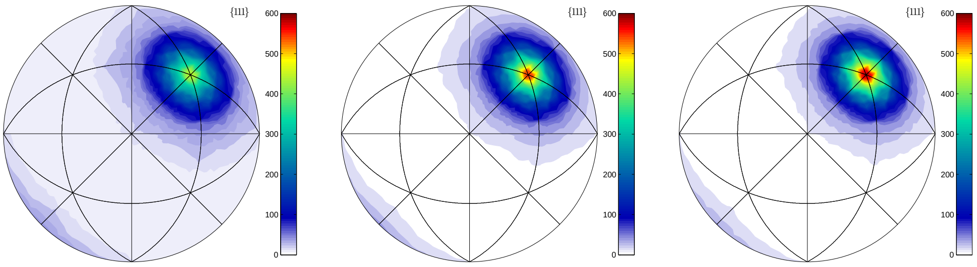

**Initial** **Anneal1** **Anneal2**

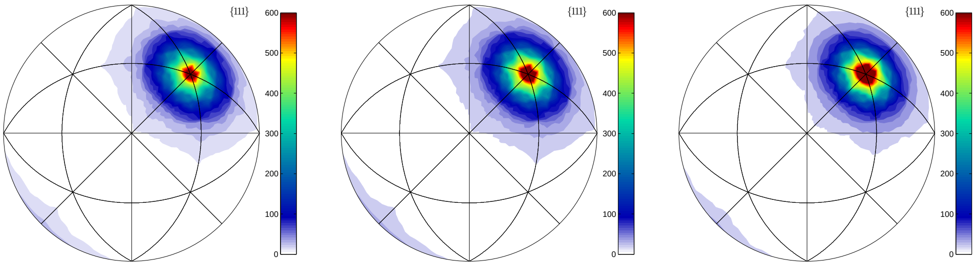

**Anneal3** **Anneal4** **Anneal5**

*Figure 6.22: Grain boundary normal distribution for the Σ3 misorientation partition of GBCD space. Color scale is the same for each plot and maximizes at an MRD value of 800.*

The metrics used to characterize the peak shape in Section 6.3.2 are replicated in Figures 6.23, only now anneal state is the dependent variable. Two in-plane resolutions of

1.2 and 0.92$\mu m$ are used, simply for comparison. The work that uses tracked boundaries will be based on the 1.2$\mu m$ mesh. The von Mises-Fisher analysis of (a) and (b) in Figure 6.23 shows what would be characterized as a sharpening of the peak, with both the monotonic increasing of the peak maximum and a decreasing of the peak's FWHM.

Like the mesh resolution analysis using the orientation tensor, the distribution admits only two unique values for the eigenvalues. This should come as no surprise, since the earlier investigation looked at the peak in the initial state, which should be the broadest of all states. Figure 6.23(c) shows the strength parameter, which is the only physically meaningful quantity for our orientation tensor study. The distribution is shown to strengthen with each anneal, indicative of a more 'peaked' distribution and consequently confirms the von Mises - Fisher analysis that the distribution is sharpening with anneals.

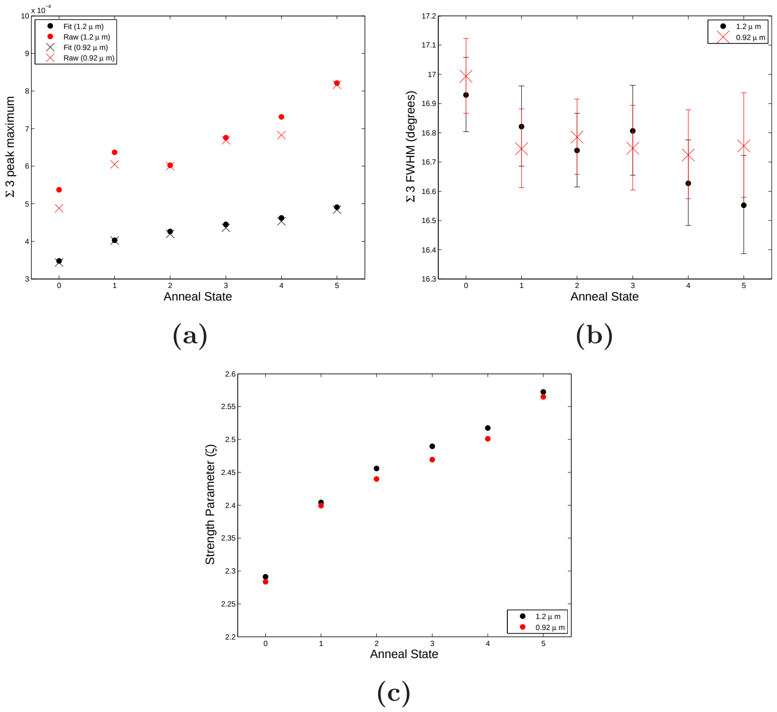

**(a)** **(b)**

**(c)**

*Figure 6.23: (a) and (b) show the results of fitting von Mises - Fisher function to the* $\Sigma 3$ *patch normal distribution peak for each of the six sample states, while (c) illustrates the result of using the orientation tensor to determine the strength paramter, defined in Equation* 6.7. *Results for both* 1.2$\mu m$ *and* 0.92$\mu m$ *in-plane resolution are presented. (a) shows the maximum of the coherent twin peak as determined from the raw 2D histogram, like that shown in Figure* 6.16*(a),(c) and from the von Mises-Fisher fit. (b) displays the FWHM of the peak, with errorbars determined from the* 95% *confidence interval around the* $\kappa$ *parameter of Equation* 6.4. *All three plots indicate a sharpening of the* $\Sigma 3$ *with each successive anneal.*

Lastly, we replicate the Lorentizan analysis that was previously used to investigate mesh resolution to determine the evolution of the $\Sigma 3$ peak with anneal state. Like the previous two characterization methods, we fix our in-plane resolution to $1.2\mu m$ for our generation of meshes. The distribution of fit parameters is displayed in Figure 6.24, where both amplitude and peak width are indicated. It is clearly evident that the coherent twin distribution is getting sharper as we anneal, shown with an increase in peak amplitude and a decrease in width. This is present in both the $\cos\theta$ and $\phi$ parameterization. The opening angle $\theta_{cone}$, shown in Figure 6.25, also illustrates a sharpening of the distribution, suggesting that as we anneal the population is dominated by coherent twins.

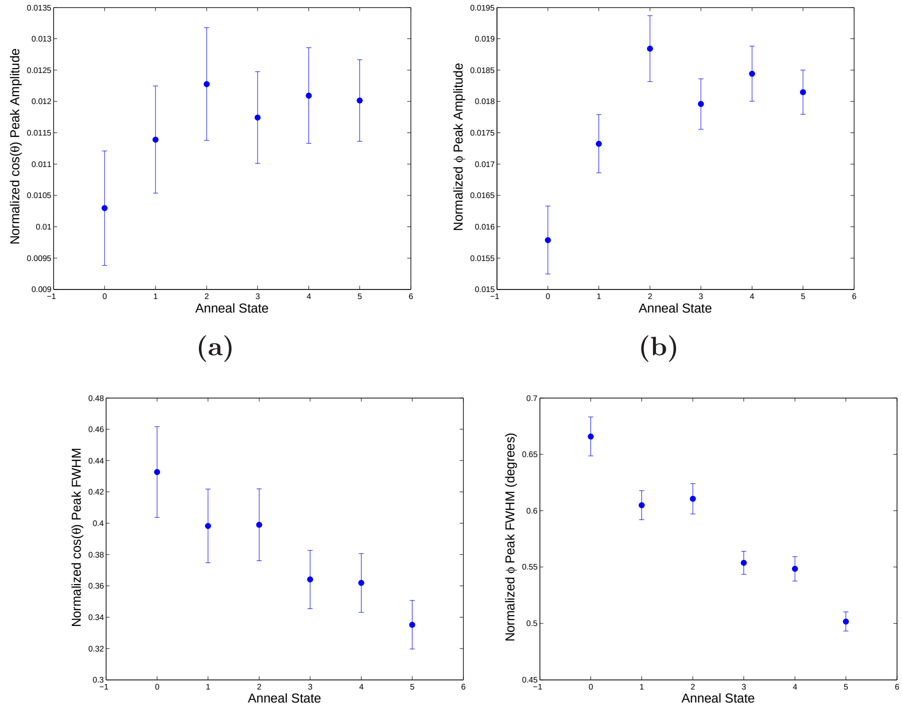

**(a)** **(b)**

**(c)** **(d)**

*Figure 6.24: Analogous set of plots to Figure* 6.20, *only now anneal state, instead of in-plane mesh resolution is the dependent variable. Volumetric grid elements are* $1.2 \times 1.2 \times 4\mu m$ *for all six sample states. (a) and (b) show how the peak amplitude changes with anneal for the* $\cos\theta$ *and* $\phi$ *distributions, respectively. (c) and (d) show peak width changes with anneal, with (c) as the* $\cos\theta$ *width and (d) the* $\phi$ *width.*

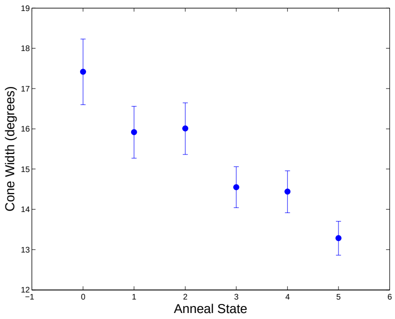

*Figure 6.25: Annealing evolution of the $\theta_{cone}$, obtained by determining peak widths of $\cos\theta$ and $\phi$ using Lorentzian forms. This quantity gives an estimate of the breadth of the $\Sigma3$ peak in boundary normal space as a single angle.*

## 6.5 Sharpening of the $\Sigma3$ distribution

The previous results have characterized a high purity nickel microstructure subjected to a sequence of anneals. It was found that a large population of interfacial boundaries were associated with a very specific *GBCD* point: the coherent twin boundary. With such a large portion of boundaries possessing the misorientation of the coherent twin ($\Sigma3$), the habit of the interface plane can be measured with appreciable statistics.

The large population of coherent twins is expected from energy considerations, as the coherent twin boundary has been identified as a very low energy configuration, with a deep cusp compared to the local energy landscape, which was shown in Figure 6.11. A plot similar to our *GBCD* type plots is shown in Figure 6.26 [6], which displays the inverse relation between boundary energy and boundary population, which has been repeatedly observed [11, 31]. The figure clearly exhibits this inverse relationship. Interestingly, the $\Sigma9$ shows a local maxima near the energy minima, but the global maximum is along the tilt axis (boundary normal perpendicular to misorientation axis) for the $\langle 110\rangle$ misorientation, despite having a local energy maxima in the vicinity. It is believed that this relationship is due to the large number of $\Sigma3$ boundaries that are present in the microstructure. A three grain neighborhood, where two boundaries are coherent twins results in the third boundary being a $\Sigma9$ with the tilt boundary configuration. Therefore, it appears that the global minimum of the coherent twin in energy space is responsible for the evolution of the $\Sigma9$ boundary and not the local energy minima for that boundary misorientation.

While we can confidently state that one of the experimental responses to the annealing process is this sharpening of the coherent twin distribution, the question arises as to the mechanism for such an observation. Hypothetically, the change in distribution could be attributed to any combination of several factors:

- Re-orientation of grains into the $\Sigma3$ configuration, with coherent twin boundaries.

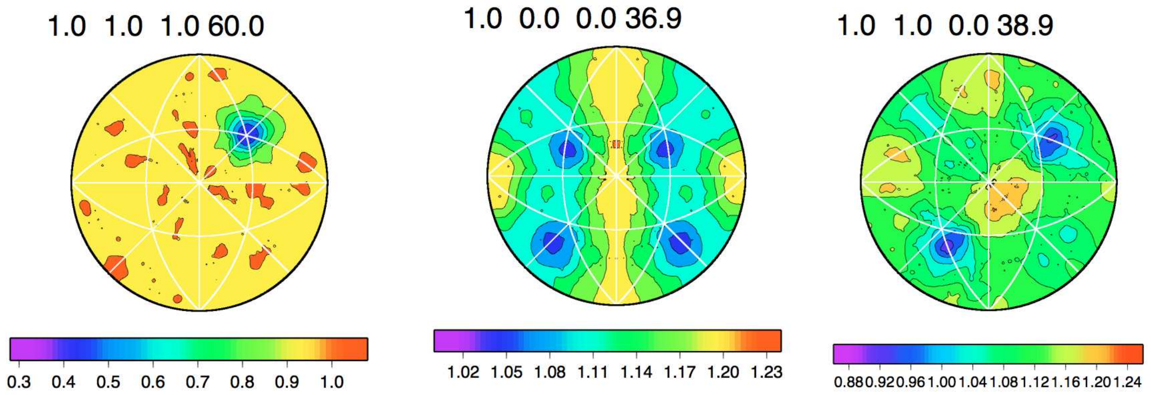

**Σ3 - Energy** **Σ5 - Energy** **Σ9 - Energy**

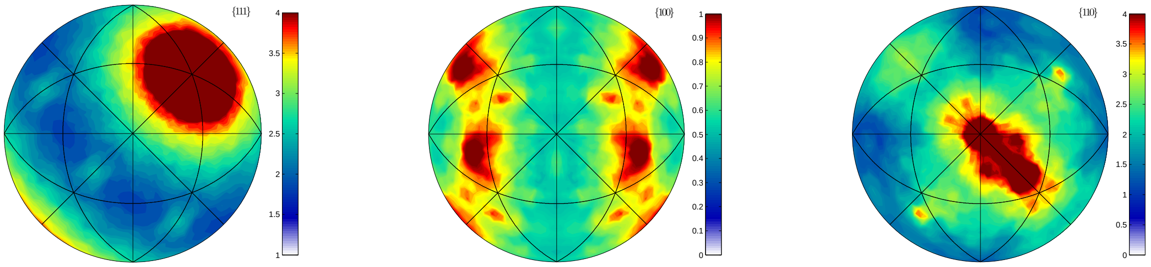

**Σ3 - Population** **Σ5 - Population** **Σ9 - Population**

*Figure 6.26: Comparison illustrating the inverse relation between grain boundary energy (top row) and grain boundary population (bottom row) for the initial state microstructure. The inverse relation is apparent for Σ3 and Σ5, but not the Σ9, with a peak in population near the energy maxima. This is attributed to the close relationship between Σ9s and the coherent twins. Simply, the global energy minima of the coherent twin dominates the local energy maxima for the Σ9 misorientation. See the text for further details. The energy plots are based on molecular dynamics simulations for nickel [2] and are reproduced from [6]. Here, each point in GBCD space was subjected to interpolation so that the entire boundary normal space could be associated with an energy for a fixed misorientation type. The interpolation is based upon energy values for 388 distinct boundary configurations [2]. The bottom row illustrates the GBCD for the configurations shown in the top row. The color scales are different for each plot and selected to fully illustrate the grain boundary normal distribution for a given misorientation. The color scales are* $\frac{J}{m^2}$ *for the energy plots and MRDs for the population plots. The Σ3 population is colored via* $\ln(MRD)$ *to illustrate the coherent twin boundary minima.*

- Changes in interfacial area of Σ3 misoriented boundaries, where boundaries exhibiting the coherent twin configuration grow faster than those off the coherence condition.

- Re-distribution of pre-existing boundaries towards the {111} direction.

- Nucleation of new interfaces possessing the coherent twin configuration.

In the work to follow, we attempt to resolve the origins of this evolution. We will explore the changes in the context of the four explanations provided above and offer supporting or refuting evidence for each mechanism, as observed in the volumes of spatially resolved orientations.

### 6.5.1 Microstructure Correlation

The merit of nf-HEDM is as a non-destructive tool for characterizing a microstructure, and in our case, monitoring the evolution of the same ensemble of grains. This is particularly relevant for investigating the origin of the coherent twin sharpening. Past studies [31] have shown that increased annealing treatments have lead to a sharpened coherent twin distribution, like we have observed, but the measurements were conducted with destructive microscopes (such as EBSD) and therefore the cause of the evolving distribution can not be conclusively determined.

We eliminate the variability associated with statistical measurement of a microstructure by performing a cross-state correlation on the grain boundary level. This process was accomplished by S.F. Li through the construction of registration software and its difficulty should not be understated [66, 62]. Since the experiment was performed *ex-situ*, registering across states is a difficult task that requires a configuration minimization process that measures alignment after a succession of rotations and translations have been applied between two states. Further complicating this registration is that the measured microstructure has evolved from anneal to anneal (which is the signal we are investigating), so the shape and location of grains has changed after each anneal. Even with the differential changes, we see in the microstructure, this task is non-trivial. The end result of this process is a patch-to-patch correlation across sample states. Each patch is associated with a mesoscopic boundary composed of many patches, so the inherent noise in the one-to-one mapping of patches can at least be restricted by acknowledging an upper threshold on validity: a given grain boundary should map to that same grain boundary, though its consituitive components might not map to its exact representation in the second state boundary.

For this study, correlation has been mapped between the initial state and the first three anneal states. The final two measurements (*Anneal4, Anneal5*) will be neglected for the remainder of this thesis. The lack of registration is due to the topological difficulty associated with the development of an anomolous bow along the length of the sample. Additionally, we should note that some boundaries among these anneal states were not included because they were simply unable to be correlated. This is especially true for grains falling near the top and bottom 2D cross-sections in each volumetric measurement. Our analysis will be restricted to boundaries that were measured through all four registered states and therefore let us fully interrogate what is occuring within the microstructure. It is with this correlation that we begin our investigation of the origins of the coherent twin evolution.

### 6.5.2 Description of Tracked Microstructure

In determining the origins of sharpening of the coherent twin peak, we use only boundaries that are tracked in each of the first four microstructural states, while ignoring all other boundaries. This is a strict method of determining evolution, but it is also the most direct procedure for identifying the origins of the sharpening of the coherent twin distribution. From our hypothesis list, the use of a tracked ensemble of boundaries should clarify the first three points, while the formation of coherent twins through nucleation can not be provided by this analysis method. Nucleation is a critical event and therefore filtered in our tracking requirements.

The coherent twin peak for these tracked boundaries is shown in Figure 6.27. Since the peak strengthen with each anneal for a consistent set of boundaries, we know that the distribution sharpening is at least partially due to non-nucleation. This does not exclude their possibile presence and mechanism for the coherent twin sharpening, but it is deduced that it is not the only mechanism. The statistics of the tracked microstructure are summarized in Table 6.1. A total of $131,392$ patches have been traced through all four states, and are associated with $5,294$ distinct boundaries. It has been found that some patches are tracked in early states and later states, but absent in the interim. These patches are omitted in this analysis.

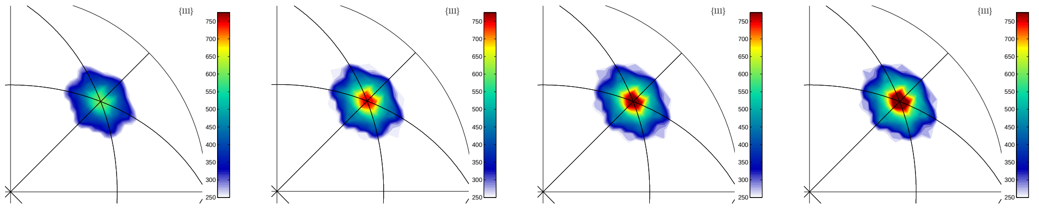

**Initial** **Anneal1** **Anneal2** **Anneal3**

*Figure 6.27: GBCD map of the Σ3 misorientation using only the tracked microstructure, consisting of* $5,294$ *unique boundaries. The location of the coherent twin has been expanded to illustrate that sharpening is present. The color scale is in MRDs and is the same scale for each plot and only locations above* $250$ *MRDs are illustrated.*

We begin our discussion of the tracked microstructure by analyzing the interfacial distribution and the alignment through crystallographic quantities such as average orientation and misorientations. The interfacial area of tracked microstructure shows a large increase ($\sim 25\%$) in the first anneal, and then a relatively static distribution, varying by less than $1\%$ in the subsequent states. The total area of these tracked boundaries actually decreases in the final state, which would be consistent with a system moving towards a lower energy configuration, since each boundary has some associated interfacial energy ($\gamma$) and a reduction in this total area would result in a lower energy state. While this is certainly possible, we should be reminded that the system is not closed and it is possible that other boundaries (that were not tracked through the four states) could be influencing this area distribution.

*Table 6.1: Statistics for Tracked Boundaries in Nickel Microstructure*

| | Initial | Anneal 1 | Anneal 2 | Anneal 3 |
|---|---|---|---|---|
| Interfacial Area ($\times 10^6 \mu m^2$) | 4.368 | 5.493 | 5.492 | 5.448 |

The registration of the microstructure requires the sample to be both rotated and translated by finite amounts, so that the geometry is as consistent as possible with the initial microstructure, and all changes are the annealing response and not sample handling. Translations will influence quantities such as distances swept out by boundaries in the coarsening process, but nothing concerning the crystallographic nature of the microstructure. The rotation required to align the initial state with all later states does influence the orientations because of our defined coordinate system. Hence, a rigid body rotation of the microstructure will result in a global change in grain orientations (as seen in Figure 6.1, but since the misorientation is a local quantity, it will be uninfluenced by this transformation.

We first classify the changes of rotationally registered microstructures of the first three anneal states with their counterparts in the initial state. This is produced in Figure 6.28. Here, the $5,294$ unique boundaries have been analyzed by taking the evolution of the two grains composing the boundary. Each boundary consists of two initial state orientations, and the boundary is tracked through the next three states. We have calculated the misorientation angle between the grains that compose the tracked boundaries and have produced a histogram with 0.01° bins to illustrate the distribution via sample state. With each successive anneal, the misorientation from the initial state accumulates. This is simply used as an illustration to show the uniformity of the registration and anomolous outliers in the tail of the distribution. Specifically, there are a select few grains that have higher misorientations than the distribution averages and they remain large after each anneal.

While grain-to-grain orientation across states exhibit changes introduced through registration, it is the boundary misorientation which is of greatest interest. This space should be independent of macroscopic sample rotation, since misorientation is a relative and not coordinate system dependent, like grain orientation. To determine evolution with respect to misorientation, we calculate the misorientation between boundary misorientations in the initial and first three anneal states. Effectively, we are determining the misorientation between two misorientations. This analysis is accomplished in the misorientation fundamental zone of Rodrigues-Frank space and is illustrated in Figure 6.31. Since the registration simply took the physical sample and applied an overall rotation and translation, there should be no misorientation distribution changes introduced by the correlation process, since each grain is rotated by the same amount. Therefore, the changes that are illustrated in the misorientation distribution should be interpreted as changes introduced through the annealing process.

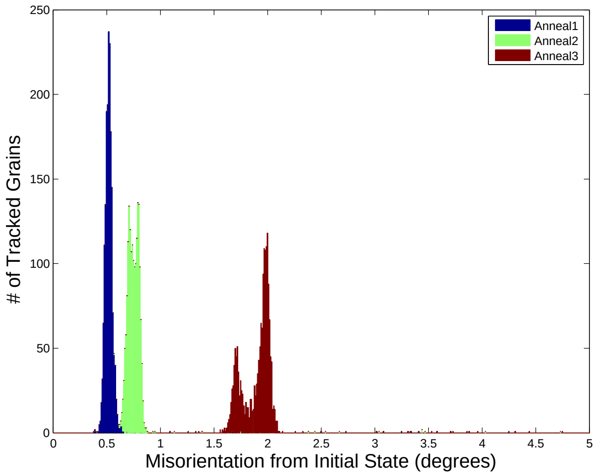

*Figure 6.28: Grain-to-grain misorientation introduced through sample registration via macroscopic rotation. The distribution is binned by misorientation angle in* $0.01°$ *increments.*

### 6.5.3 Misorientation Evolution

Determination of the origins of the coherent twin sharpening begins with misorientation space changes attributed to annealing. We have already illustrated that some changes are occuring with the misorientation angle plot in Figure 6.29. With some of these angle changes exceeding intragranular orientation variations, it is important to quantify the evolution. It should be emphasized that a broad binning of 10° in *GBCD* used for our peak illustrations in Figure 6.27, but our Σ3 angle width measurements indicate a much sharper peak in misorientation space.

We first partition this data space into the Σ3 peaks, like in Figure 6.9. The misorientation of every patch with the Σ3 misorientation is determined and then integrate the areal and number distribution of the tracked microstructure over this angle, which is shown in Figure 6.30. The plots are similar to our earlier exploration, using area fraction within the *CSL* bin as our vertical scale.

The analomous *Anneal3* distribution is also replicated, which does not follow the approximately static trend that is admitted to the remaining three states (overlapping curves). It seems apparent that this variation with *Anneal3* is due to sample registration, and not an annealing response. A vertical red line is drawn to illustrate the 0.75° distribution that was used earlier (see Section 6.3.2) to approximate our discussion of the Σ3 distribution, but that results in the omission of a small collection of boundaries (15 of the $1,034$ boundaries). If we push our misorientation threshold from Σ3 out to 4.28°, we reach a configuration where the same set of boundaries are included in all four states, which is illustrated by the blue line in (b). Since we wish to accomplish a true one-to-one tracking of the coherent twin evolution, we will use this as our threshold for

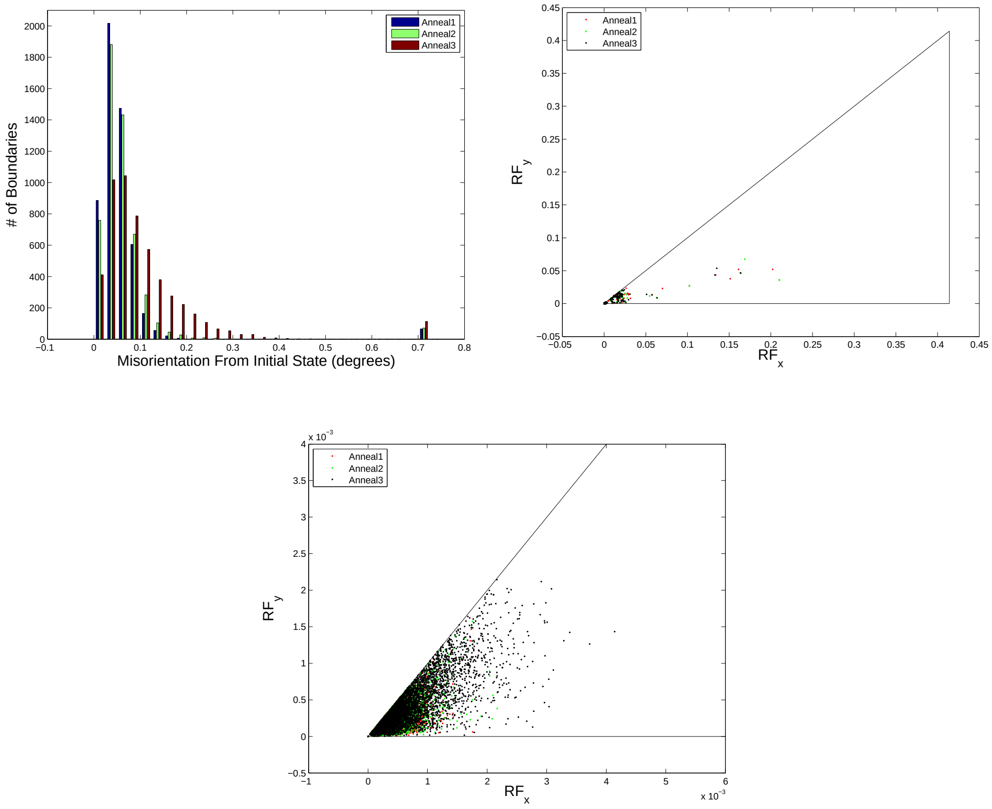

*Figure 6.29: Misorientation-to-misorientation distribution of tracked boundaries within the microstructure, compared to the initial state. (a) bins the misorientation angle between the initial state and later anneal state misorientations. All boundaries in excess of* $0.7^\circ$ *are placed in the last bin, which contains 66, 71 and 112 boundaries, for the three anneal states, respectively. (b) and (c) show the full three parameter misorientation in Rodrigues-Frank space. The zone is projected into the* $RF_x - RF_y$ *plane and contains all misorientation points (*$RF_z \leq 0.027$*). Each point in the distribution is colored by the second misorientation state, with comparisons always being performed with respect to the initial state. The majority of misorientations are at the origin of the fundamental zone, which is magnified in (c), but there does exist several outliers.*

investigation of the coherent twin peak.

We previously noted that this analysis will not capture the origins of the sharpening of the coherent twin, because bin width in misorientation space from our *GBCD* plot is much larger than the observed changes in misorientation with anneals. Still, we analyze this distribution to see if any misorientation changes can be viewed in the context of coherent twins.

Referring back to the Rodrigues-Frank misorientation space distribution among boundary misorientations in Figure 6.29, we define a threshold magnitude of 0.005 for Rodrigues-

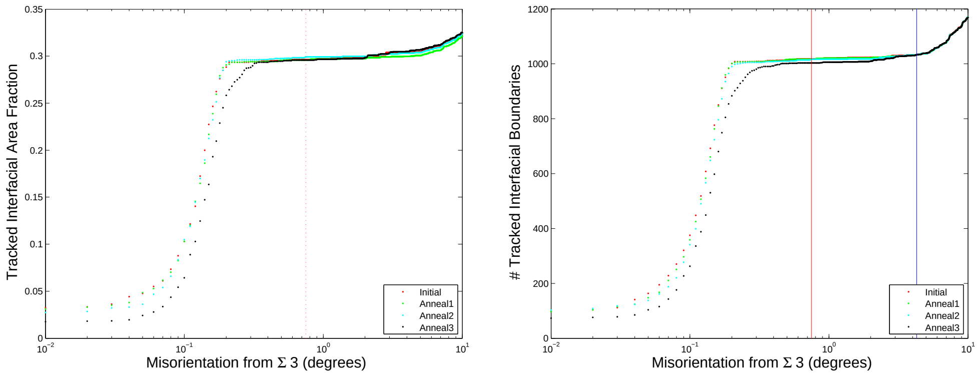

**(a)** **(b)**

*Figure 6.30: Misorientation from the* $\Sigma3$ *configuration for patch misorientations across the four tracked states. Figure is the tracked analog to Figure* 6.9*, except now we look at area fraction for the entire microstructure, not just within the CSL association. (a) illustrates the distribution integrated over interfacial area, while (b) is over number of boundaries. Vertical red line indicates a misorientation angle of* $0.75°$*, while vertical blue line is at* $4.28°$*.*

Frank vectors which partitions our data into two classifications: 'no misorientation' and 'finite misorientation'. These are made in comparison to the initial state. Such a partitioning results in 66, 71, and 112 unique boundaries falling in the finite misorientation grouping. Since each point is associated with a boundary that has been correlated, we can search for consistency present through all three state comparisons. Of these finite misorientation boundaries, 30 were found in all three anneal states, which are associated with five grains of unique orientations (i.e. one of the grains composing the boundary is from a set of five). Finally, of these 30 boundaries, three are associated with the $\Sigma3$ misorientation; two belong to a common grain. Table 6.2 summarizes these three boundaries, which is actually listed as four because Boundary 3 and 4 represents the same grain neighbor pair, but is split in the tracking in *Anneal1*.

If we associate tracked boundaries with their constituent grains, we can determine if anything is special about the $\Sigma3$ boundary, such as exceptional area in comparison to the grain's other boundaries. For Boundary 1, we have the 'rotated grain' (Grain 1) occur in five boundary pairs, with an initial interfacial area of $4.24(6) \times 10^3 \mu m^2$ and final interfacial area of $4.89(3) \times 10^3 \mu m^3$. This is composed over 118 patches. Hence, the area of this $\Sigma3$ boundary is $\sim 45\%$ of the grain's total tracked interfacial area. Similarly, Grain 2 has 26 distinct grain boundaries consisting of 932 patches. These boundaries cover $3.37(0) \times 10^4 \mu m^2$ in the initial state and $3.94(6) \times 10^4 \mu m^2$ in the final state. Hence, Boundary 2 accounts for $\sim 40\%$ of the interfacial area, while Boundary 3-4 is 10% of the tracked surface area. Interestingly, these two boundaries are the two largest (of the 26 boundaries) associated with this grain.

Probing this analysis further and investigating the grain boundary normal domain, a

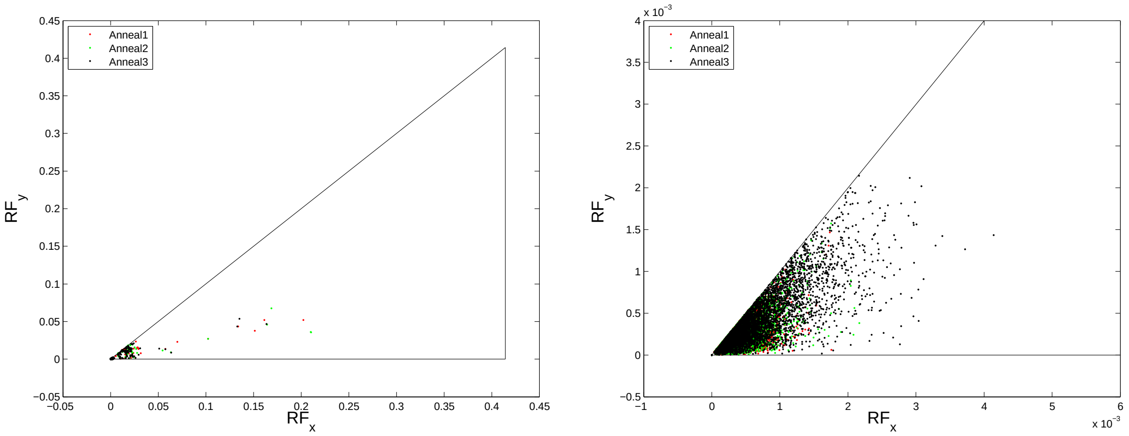

*Figure 6.31: Misorientation distribution in Rodrigues-Frank space of boundary-to-boundary misorientation with respect to the initial state. Each boundary has a misorientation in each state. Here, we compare this misorientation with that of its corresponding boundary in the initial state. The space is projected into the $x, y$ plane ($RF_z \leq 0.027$). The majority of points are at the origin of the fundamental zone, which is magnified in (b), but there exists a few boundaries that are far from this origin.*

*Table 6.2: Statistics for Σ3 boundaries with changed misorientations*

| | Boundary 1 | Boundary 2 | Boundary 3 | Boundary 4 |
|---|---|---|---|---|
| Associated Grain | 1 | 2 | 2 | 2 |
| Number of Patches | 49 | 319 | 22 | 89 |
| Area of Interface ($\times 10^4 \mu m^2$) | | | | |
| *Initial* | 0.19(0) | 1.34(9) | 0.04(4) | 0.33(7) |
| *Anneal1* | 0.21(6) | 1.46(7) | 0.07(3) | 0.34(1) |
| *Anneal2* | 0.22(0) | 1.53(5) | 0.07(9) | 0.37(6) |
| *Anneal3* | 0.22(4) | 1.58(0) | 0.08(0) | 0.30(8) |
| Misorientation from Σ3 (°) | | | | |
| *Initial* | 1.13(8) | 2.82(7) | 2.82(2) | 2.82(2) |
| *Anneal1* | 0.13(7) | 0.11(4) | 0.15(4) | 0.15(2) |
| *Anneal2* | 0.06(0) | 0.07(7) | 0.10(7) | 0.10(7) |
| *Anneal3* | 0.12(2) | 0.15(7) | 0.17(1) | 0.17(1) |

rather unique result is found that would be difficult to discern with any other technique. Specifically, it appears for Boundary 1 and Boundary 2 (the two dominant boundaries that we have investigated) that the boundary normals become more $\{111\}$ oriented. The distributions are illustrated in Figure 6.32 and 6.33. These are similar to the histograms shown in Figure 6.16, except we do not have sufficient statistics to populate all of boundary normal space. Instead, the histogram is filled by patch areas for the singular boundary and monitoring the distributions distance from the coherent twin position. Like Figure 6.16, the 2D histogram uses an equal area partitioning in boundary normal space, with a bin width of 1° and 0.011 for $\phi$ and $\cos\theta$, respectively. Bins are colored by summing the area of all patches in a given bin. The normalization of Figure 6.16 is not performed for these figures. It seems evident that we observe an annealing driven event where both the misorientation and boundary normals of the given grains move towards the low energy coherent twin configuration.

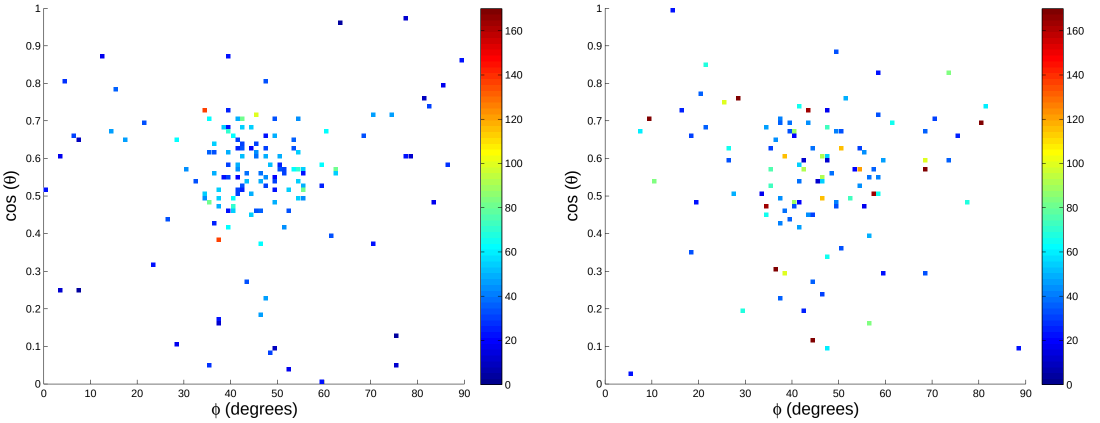

**Initial** **Anneal1**

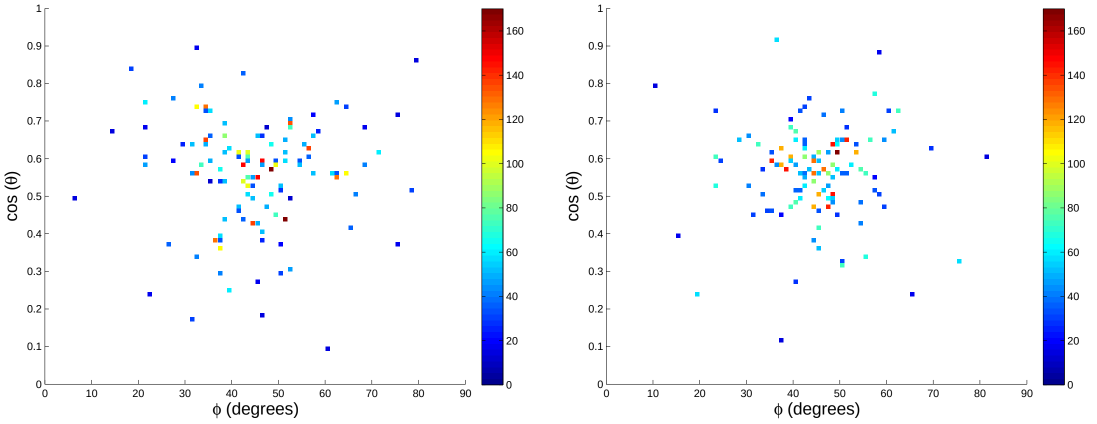

**Anneal2** **Anneal3**

*Figure 6.32: Distribution of boundary normals for Grain* 1 *from Table* 6.2*. Boundary normals are represented in the crystal frame of the grain that has exhibited a 'rotation' towards the coherent twin misorientation. The collection of patches composing the boundary, as evolved through the four sample states are presented in a* 1° *binning. Colors indicate the sum of patch areas (for this one* Σ3 *boundary) falling in the given boundary normal space bin. The color scale is in* $\mu m^2$.

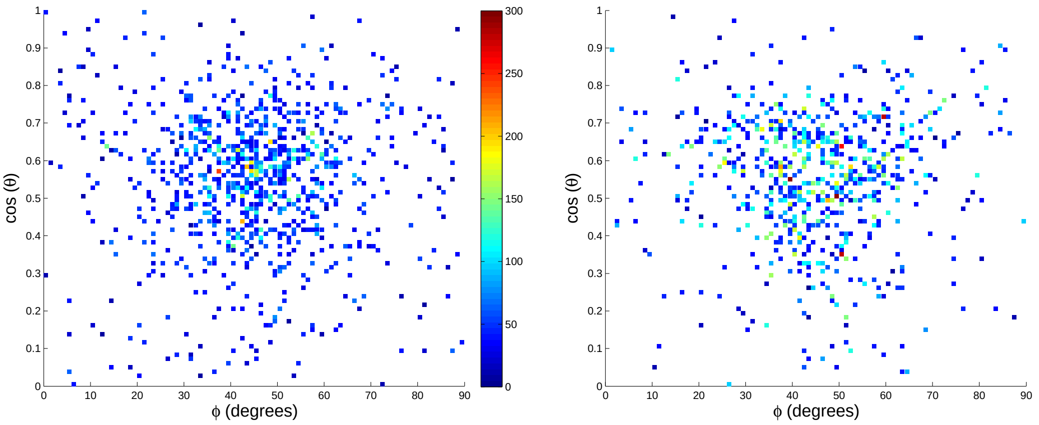

**Initial** **Anneal1**

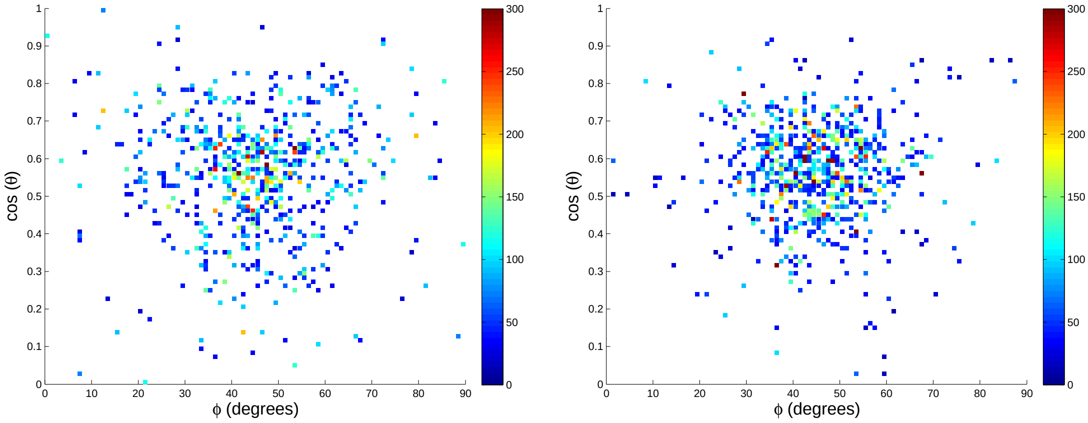

**Anneal2** **Anneal3**

*Figure 6.33: Distribution of boundary normals for Grain* 2 *from Table* 6.2*. Boundary normals are represented in the crystal frame of the grain that has exhibited a 'rotation' towards the coherent twin misorientation. The collection of patches composing the boundary, as evolved through the four sample states are presented in a* 1° *binning. Colors indicate the sum of patch areas (for this one* Σ3 *boundary) falling in the given boundary normal space bin. The color scale is in* $\mu m^2$.

While this is certainly a dramatic result and could be labeled a critical event, these were only 2 boundaries in the microstructure accounting for 0.3% of the total interfacial area. Further still, our plots of Figure 6.27 would be insensitive to such a misorientation change, since the boundary remains in the same (broad) misorientation bin in all four pictures. This observation suggests that grain rotation is a possible mechanism for microstructure evolution [95]. For this sample, grain rotation is not a dominating mechanism for coherent twin sharpening (only two observations), but it is observed and could play a much larger role in other systems.

### 6.5.4 Coherent Twins and Interfacial Area

The misorientation contribution to the coherent twin sharpening effect will now be separated from our investigation. We note that while a dramatic event has occured, it is not the dominating mechanism in our measurement. We now fix misorientation and examine the properties of the interfaces and their evolution with anneal. We begin with examination of boundary area's contribution to the peak's changing profile. To begin this determination, we produce a $90 \times 90$ equal area histogram in the space parameterized by $(\cos\theta, \phi)$, like we did in our mesh resolution studies. This binning of boundaries within $4.28°$ of the $\Sigma3$ misorientation is demonstrated in Figure 6.34 and uses the same $1,034$ boundaries and their component patches. Like in Figure 6.27, the distribution of the coherent twin peak clearly sharpens with anneal, specifically from the initial to first anneal state.

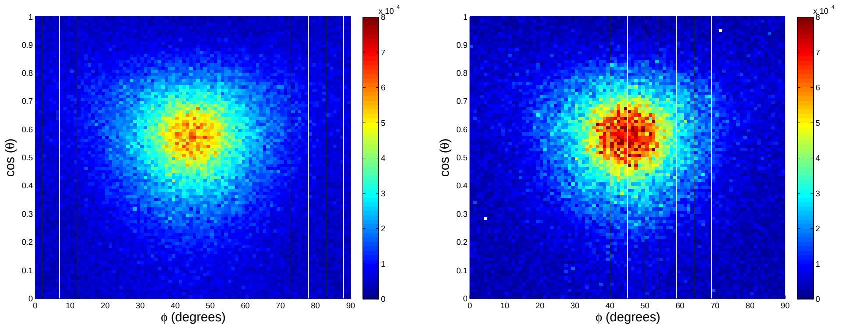

**Initial** **Anneal1**

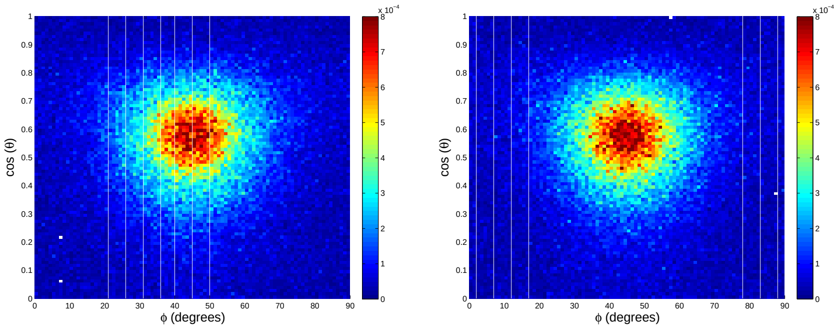

**Anneal2** **Anneal3**

*Figure 6.34: Patch area weighted histograms in $(\cos\theta, \phi)$ space of boundary normals for patches with misorientation angle within $4.28°$ of $\Sigma3$, encompassing $1,034$ boundaries. The distribution is normalized over area, with the same color scale illustrated for each histogram.*

These next two sections decompose the origins of this sharpening in the context of boundary area and boundary normal. Since the *GBCD* is an area weighted histogram of boundary normals, this decomposition is appropriate. To begin our discussion of boundary area, we must first discuss the areal distribution of the entire tracked boundary

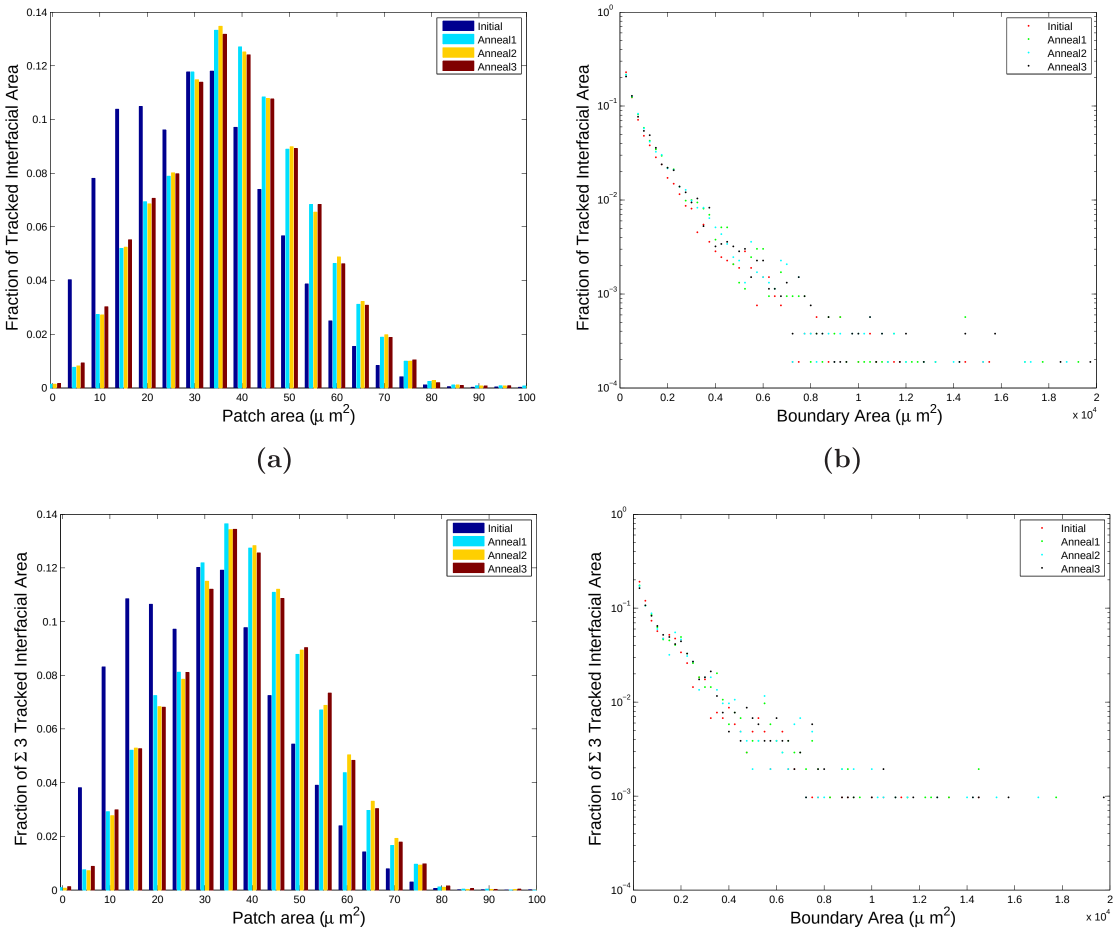

**(a)** **(b)**

**(c)** **(d)**

*Figure 6.35: Distribution of tracked interfacial area through the four sample states. (a) and (c) histogram the individual triangular elements (or patches) that compose the boundary, while (b) and (d) histogram by boundary area. Hence, (a) and (c) show the size distribution of the building blocks of our mesh, while (b) and (d) illustrate how those building blocks are collected into boundaries. (a) illustrates the distribution of patches that compose the boundaries seen in (b). A few outlier patches of large area exist in (a), but have been supressed. (b) is displayed on a logarithmic scale in fraction, to illustrate that a few exceptionally large boundaries are present. The second row shows the distribution of the Σ3 boundaries in terms of interfacial area, analogous to (a) and (b). The difference is that the area fractions are with respect to the collection of Σ3 patches and boundaries. Binning is accompished with $5\mu m^2$ and $250\mu m^2$ increments for the patch and boundary distributions, respectively.*

network. This is illustrated in Figure 6.35, where both the entire collection of boundaries ((a) and (b)) and only our selected Σ3 boundaries ((c) and (d)) are presented. The distributions are strikingly similar, but since Σ3s account for 30.3±0.3% of the interfacial area over the four states, the similarity is expected.

The area distribution is further partitioned as boundaries ((b) and (d)) and their constitutive patches ((a) and (c)). We display this distinction because the analysis we will perform is based on evolution at a scale we can confidently correlate. As stated earlier, despite the patches in the microstructure being tracked in a one-to-one manner and therefore providing the fullest representation of boundary evolution, the explicit mapping is prone to errors. Alternatively, we know the tracking of *boundaries* is well defined since we are simply looking for grain pairs that persist in the microstructure. Thus, if we look at the entire group of patches that compose a boundary through multiple states, we are confident that the grouping is representing the same portion of microstructure, but on a constitutive level, the tracking might not be exact. Henceforth, we will look at boundaries unless otherwise explicitly stated.

The discussion of area for boundaries instead of patches is straightforward: the area of a boundary is the sum of its component patch areas. Conversely, direction is not as simply defined. Since each patch has a local direction in the crystal frame, we must devise a way to represent boundaries with an approximated direction. Further, we have two grains composing a boundary and therefore two local boundary normal directions, one in each grain's crystal frame. These are related due to the known misorientation between the grains, but do not always result in the exact same boundary plane habit.

Since the coherent twin is the object of interest and its boundary normal is defined as the $\{111\}$ direction, we can determine a boundary normal's deviation from this direction by performing an area weighted projection on this $\{111\}$ axis

$$\overline{\cos\alpha} = \sum \frac{A_i}{A} \cos\alpha_i \tag{6.11}$$

where the subscript $i$ runs over all patches composing a given boundary, with $\alpha_i$ as the projection angle of the crystal frame normal onto the $\{111\}$ axis. $A_i$ is the patch area. Therefore, $\overline{\cos\alpha}$ gives a measure of the how aligned a boundary is with the coherent twin direction and ranges from 0 (no alignment) to unity ( flat boundary composed of the $\{111\}$ plane). For each boundary, two of these values are presented: one for each crystal frame. We histogram these $\overline{\cos\alpha}$ for each boundary associated with the Σ3 in Figure 6.36. Evidently, boundary normals are evolving towards the coherent twin as we anneal, with an increasing population of large $\cos\alpha$ with each incremental anneal. This will be investigated further as the probable cause of the growth of the coherent annealing twins population, but for now we focus on area changes instead of directional changes.

Using our $\cos\alpha$ distribution as a reference, we define a boundary as a 'coherent twin' when its normal falls within the FWHM of the initial state distribution. This leads to a cut-off angle of 15.8°, which corresponds to $\overline{\cos\alpha} = 0.962$. The areal distribution of incremental boundary area changes is then classified as coherent twins ($\overline{\cos\alpha} \geq 0.962$) and remaining boundaries. The incremental area change histograms are shown in Figure 6.37. The integrated histogram has six times the number of boundaries as were measured

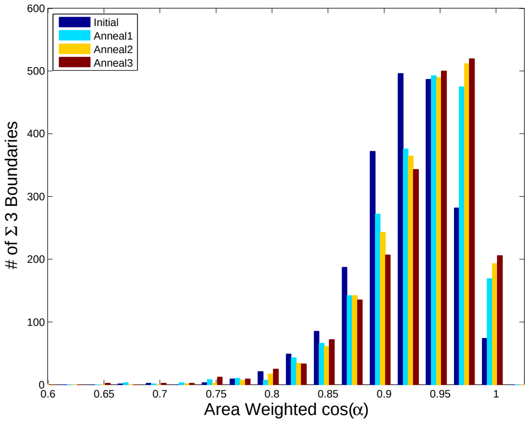

*Figure 6.36: Histogram of the $\overline{(}\cos\alpha)$ quantity for tracked $\Sigma 3$ boundaries. A $\overline{(}\cos\alpha) \sim 1$, indicates that the boundary normal is aligned with the $\{111\}$ direction.*

in the distribution, because each boundary has two normals (one from each crystal frame) and was tracked over three anneals. Hence, we are simply incrementing the area change of a boundary by its coherence classification $(\overline{(}\cos\alpha))$. The distribution in (a) uses the initial state as the reference area for a given boundary and therefore only looks at boundaries that had some coherent patches to begin the experiment. The plot in (b) relaxes this restriction and looks at single step anneals. Therefore, a boundary is classified as coherent if it was within the $\overline{\cos\alpha}$ threshold in the previous state, not only the initial state. Area changes here are over one anneal step, while (a) is cummulative.

Evidently, the change in area of coherent twin boundaries does not exhibit an exceptional behavior with respect to the remaining population of boundary normals. We conclude that areal change of coherent twins is not the dominant cause of the distribution sharpening. This is further illustrated by taking advantage of the correlated patches through anneals. If area changes were actually the dominating process, we would see the sharpening of Figures 6.27 and 6.34, if we replaced each patch with the normal in the initial state. We perform this test and produce the $(\cos\theta, \phi)$ distribution in Figure 6.38. Keeping the normal distribution static and only permitting areas to fluctuate between states results in a broader distribution with anneal and therefore we can not argue that the boundary area is the principle cause of coherent twin distribution strengthening. This leads to the final assumption to explain the evolution in the tracked microstructure: changes in boundary normal.

### 6.5.5 Coherent Twins and Boundary Normal Evolution

In the context of the coherent twin distribution, we have already established that the strengthening is not strongly influenced by changes in grain orientations, with only two

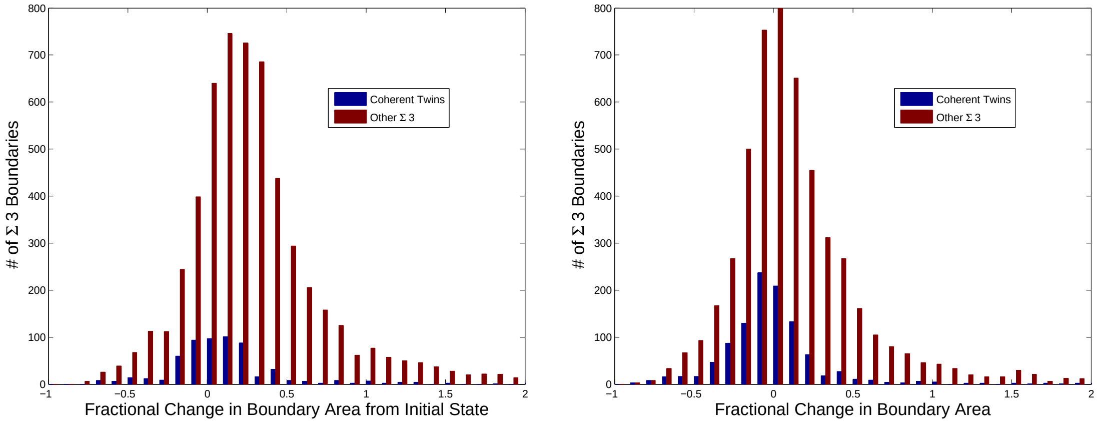

**(a)** **(b)**

*Figure 6.37: Histograms illustrating the area distribution as classified by grain boundary normal coherence. Boundaries that are coherent fall within the FWHM of the GBCD peak in the initial state, which means boundary normals are within* 15.8° *of the* {111} *direction. The binning is done with respect to fractional change in boundary area, where the plot in (a) uses the initial state boundary area as the reference, while (b) interprets incremental changes in area and uses the previous state as the reference. Distinction is not made for anneal state in (b). All incremental changes are binned.*

extreme events displaying all the conditions that would result in a stronger coherent twin distribution: a misorientation becoming more aligned with Σ3, an increase in interfacial area, and reorientation of boundaries towards the {111} boundary plane. We have also explored area changes as a possible evolutionary cause, and while boundaries grow, there is no evidence to suggest that the coherent twin boundaries are growing faster than the remaining Σ3s. That leaves changes in boundary normal orientation as the last possibility for coherent twin sharpening that is seen in the tracked boundary *GBCD*.

We have already established $\overline{\cos\alpha}$ as a metric for characterizing how aligned a boundary is with the {111} direction, essentially describing the 'coherent twin character' of the boundary. Figure 6.37 has already illustrated that the alignment of boundaries with the coherent twin direction is not static, and is in fact migrating towards the {111} direction. We can further explore this distribution by producing scatter plots of the $\cos\alpha$ distribution across anneal states. We begin with at how the two normals from the same boundary evolve, with anneals (Figure 6.39).

The most dramatic feature is the trend for the coherent twin character ($\cos\alpha$) to become equivalent in each reference frame, as well as denser near $\overline{\cos\alpha} \sim 1$. This would point towards boundaries becoming more coherent twin like with anneal, i.e. the boundary is reorienting itself so that the boundary plane is {111}. In the limit of having an exact {111} boundary plane, with an exact {111}|60° misorientation, the other boundary plane is constrained to also be a {111}. Thus, the fact that we have

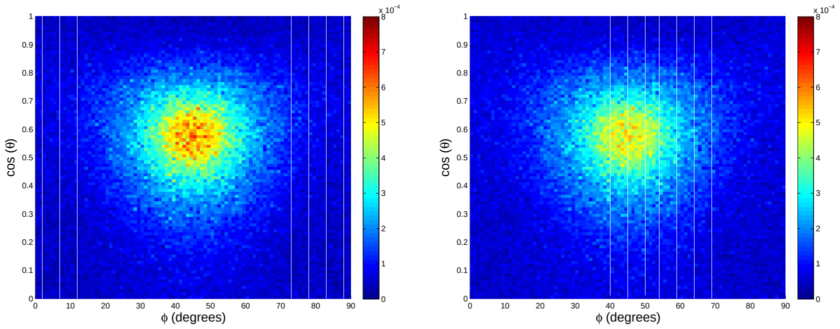

**Initial** **Anneal1**

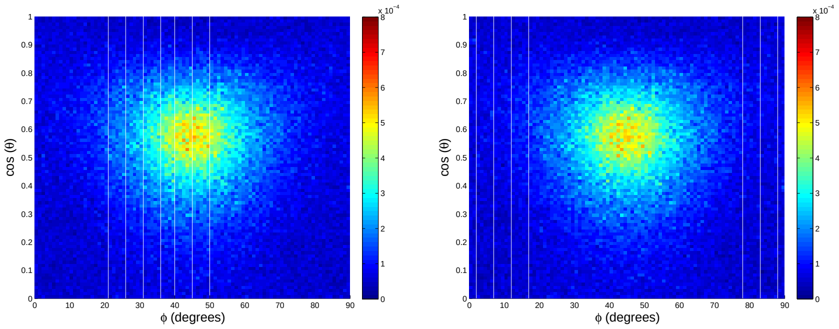

**Anneal2** **Anneal3**

*Figure 6.38: Patch area weighted histograms in* $(\cos\theta, \phi)$ *space of boundary normals for patches with misorientation angle within* $4.28^\circ$ *of* $\Sigma 3$, *encompassing* $1,034$ *boundaries. The boundary plane normal distribution has been held static, using the patch normals from the initial anneal state. Corresponding areas of the tracked patches for each anneal state were assigned to this boundary normal distribution. Normalization is performed over area, with the same color scale illustrated for each histogram, which is the same scale Figure* 6.34.

a strong $\overline{\cos\alpha_A} \simeq \overline{\cos\alpha_B}$ with increasing anneals would indicate the character of the boundary is becoming more $\{111\}$ like. In fact, the discrepancy from $\overline{\cos\alpha}$ is likely due to small patches (probably near the boundary edges) contributing a non-$\overline{\cos\alpha} \sim 1$ value, which moves the weighted average away from unity. Put differently, the nearer an interface is to the $\cos\alpha_A = \cos\alpha_B$ line, in Figure 6.39 (a) and (b), the greater the proportion of coherent twin like patches in the given grain boundary.

The distribution in Figure 6.39 clearly illustrates a movement towards $\overline{\cos\alpha_A} \sim \overline{\cos\alpha_B}$, but no correlation is made between boundaries through each state. We simply observe a distribution that suggests a movement towards a higher coherent twin character. This is observed by histograming the differences in $\overline{\cos\alpha}$ between the two frames and looking at the distribution with respect to the initial microstructure state (c) and in terms of incremental anneal steps (d). To interpret the quantities in the context of individual boundary evolution, we monitor changes in a given boundary's $\overline{\cos\alpha}$ quantity with respect to the initial coherent twin character and through incremental anneals

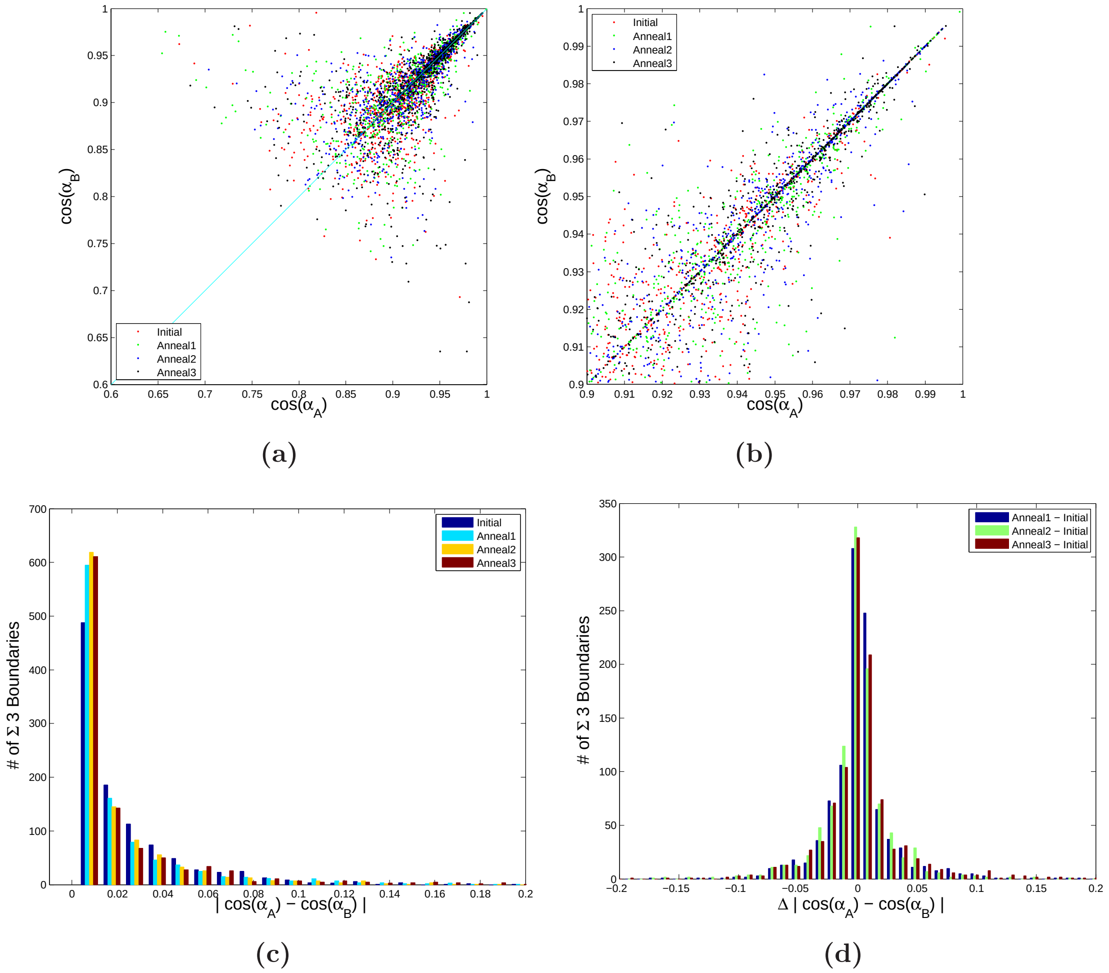

**(a)** **(b)**

**(c)** **(d)**

*Figure 6.39: Plots illustrating the coherent twin character of the boundary normal distribution as defined by $\overline{\cos\alpha}$, the area weighted boundary normal projection onto the coherent twin ({111}) axis. Each boundary is composed of two atomic planes, one for each composing grain, and here we compare their relative magnitudes. (a) illustrates the distribution with the different crystal frames on the two axes. The scatter plot shows a clustering towards both unity and $\cos\alpha_A = \cos\alpha_B$ as we anneal, suggestive of a higher coherent twin population. See text for details. (b) shows the top right corner of (a), to illustrate the movement towards $\cos\alpha_A = \cos\alpha_B$, with increasing anneal state. Specifically, the third anneal state shows a large number of boundaries with $\cos\alpha_A = \cos\alpha_B$, suggesting many coherent twin patches composing the boundary. (c) and (d) are histograms showing the difference in coherent twin character in the two crystal frames. (c) shows the population as a function of anneal state, while (d) shows incremental differences after each anneal.*

(Figure 6.40). Both reference frames for the grain boundary are binned in these plots. The distribution in (a) shows a symmetric peak about ($\overline{\cos\alpha_i} - \overline{\cos\alpha_0} > 0$), indicating a migration towards coherent twin type boundaries. (b) shows a shorter time scale, by looking at changes in the coherent twin character as a function of incremental anneals. This is symmetric, but at a value closer to zero, indicating the subtly of the changes that are occuring.

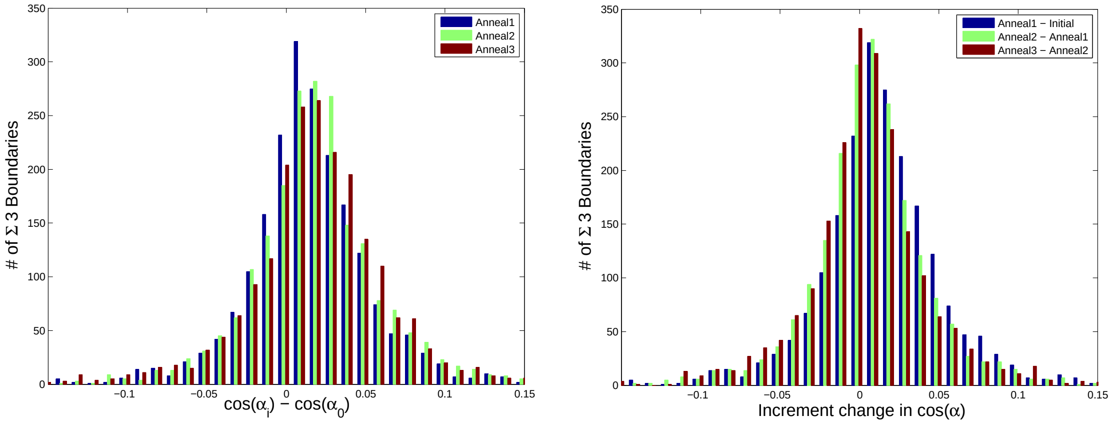

**(a)** **(b)**

*Figure 6.40: Changes in $\overline{\cos\alpha}$ for a given boundary as a function of anneal state. (a) uses the initial state as a reference, while (b) shows the incremental changes. The distribution in (a) is peaked at positive $\overline{\cos\alpha} - \overline{\cos\alpha_0}$, indicating that boundaries become more coherent as we anneal. (b) displays incremental changes after each anneal and the distribution is centered around zero.*

We can introduce how area is changing with these changes in grain boundary normal direction, by integrating the distribution as a function of coherent twin character ($\overline{\cos\alpha}$), as in Figure 6.41. We see for each anneal state, the distribution's area is associated with larger $\overline{\cos\alpha}$ values than the previous state.

Lastly, we repeat the process we introduced for the area evaluation of the coherent twin, by assigning the boundary normals of the initial state to all subsequent anneal states. This illustrated how changes in area were influencing the *GBCD*. Here, we perform the complement. We fix the areas of the tracked patches to their initial state area. The boundary normals evolve, as were measured in each anneal state. These are shown in Figure 6.42. In contrast to Figure 6.38, which did not exhibit peak sharpening and actually had the profile become broader with anneal, using fixed areas and allowing the normals to evolve captures the sharpening of the coherent twin that we saw in our first picture of the tracked $\Sigma 3$ distribution (Figure 6.27).

## 6.5.6 Comments on the Coherent Twin Sharpening

In Figures 6.38 and 6.42 we attempted to illustrate the area weighted distribution of boundary normals by isolating the contribution of areal changes and normal changes.

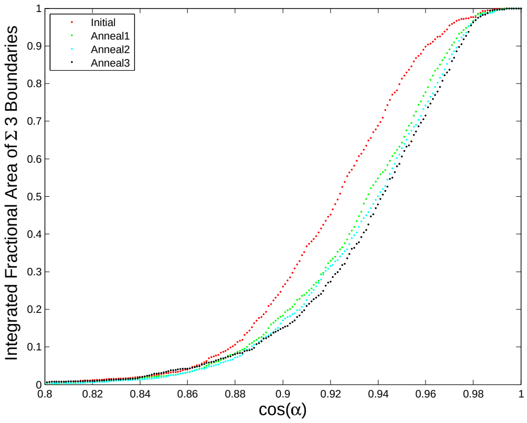

*Figure 6.41: Fractional integrated area of the* $\Sigma3$ *boundaries as described by their coherent twin character (*$\overline{\cos\alpha}$*). For a given* $\overline{\cos\alpha}$ *on the horizontal, its integrated area is the fractional area of all boundaries, in that given state, that have* $\overline{\cos\alpha_i} \leq \overline{\cos\alpha}$*. The shift in curves from left to right indicates that more of the boundary area is aligned with the* $\{111\}$ *direction than the previous anneals.*

This was done in an effort to clarify the origins of the evolution observed in Figure 6.34, the boundary tracked coherent twin peak. In both histograms, we isolated one aspect of the evolving microstructure and fixed all other components to the initial state distribution. While a bit simplistic in application, it does show what appears to be the cause of the coherent twin evolution: a reorientation of existing $\Sigma3$ boundaries towards the $\{111\}$ normal.

Previously, we established that integrating across each of the boundary normal dimensions and fitting the resulting distribution with a Lorentzian form provided the best quantitative way to characterize the $\Sigma3$ peak, producing accurate estimates of both peak amplitude and width. We conduct this same analysis on the histograms where we have isolated the cause of coherent twin strengthening. These are displayed in Figure 6.43, where the peak amplitude, width, and $\theta_{cone}$ are displayed for the original distribution and the distributions with area and boundary normals fixed to the initial state. The plot shows clear evidence that the changes in the tracked evolution of the coherent twin peak is more directly attributed to changes in boundary normal, instead of growth of pre-existing coherent twins.

### 6.5.7 Comments on the $\Sigma3$ Distribution

If we now reflect back on the list of possible origins of the sharpening coherent twin distribution, we have shown that all three mechanisms can contribute to the sharpening, though each to a variable degree. We found two boundaries that performed in an

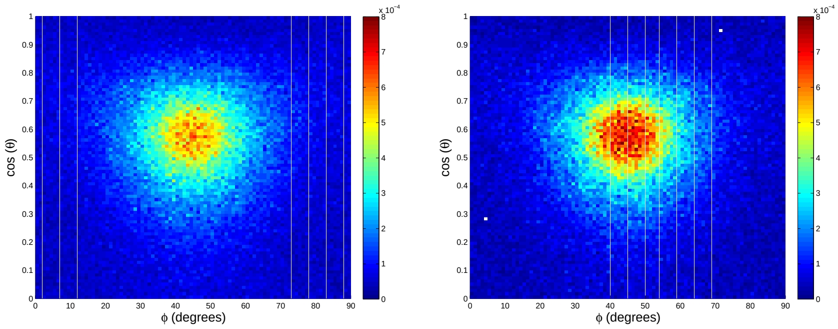

**Initial** **Anneal1**

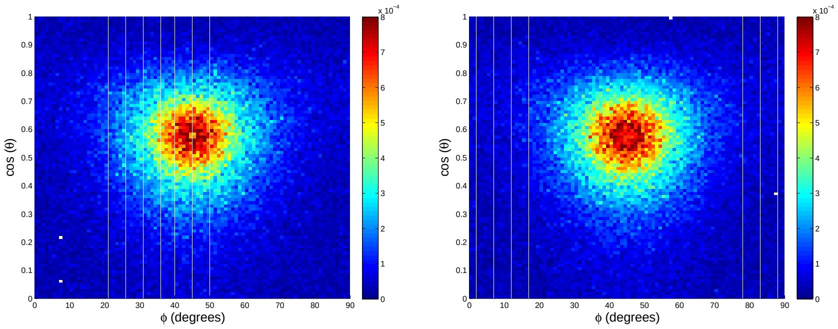

**Anneal2** **Anneal3**

*Figure 6.42: Plots illustrating the* $(\cos\theta, \phi)$ *distribution of the coherent twin. The interfacial area of the distribution has been held fixed with each tracked patch being assigned its initial state area. The boundary normals are maintained to their observed values in the given anneal state. This is the complement to Figure* 6.38*. The black points are the actual* $\Sigma 3$ *anneal signal, while green is attributed to changes in area and red to changes in normal direction.*

exceptional manner, by agreeing with the first three of the tracked hypotheses. The boundaries became more $\Sigma 3$ like in misorientation, through reorientation of one of the grains composing the boundary. This boundary was then found to both grow in area and re-orient towards the $\{111\}$ plane. While this is a dramatic instance of coherent twin sharpening, it is an outlier observation in the collection of tracked boundaries. Instead, it was found that the change in interfacial area of the boundaries of a coherent nature, replicated the growth of the other $\Sigma 3$ boundaries, with non-$\{111\}$ boundary planes. Therefore, while growth of all these $\Sigma 3$ boundaries are present, there is not a bimodal growth distribution, with coherent twins exhibiting different growth dynamics compared to ‘incoherent’ twins.

Analysis of the boundary normal distribution is where the most dramatic change was present with anneal. By associating each boundary with its area weighted projection along the $\{111\}$, it was found that with each anneal step, boundaries tended to become more aligned with the $\{111\}$. We quantified this through the introduction of the coherent twin character parameter, $\overline{\cos\alpha}$, which is a singular value for each boundary. This

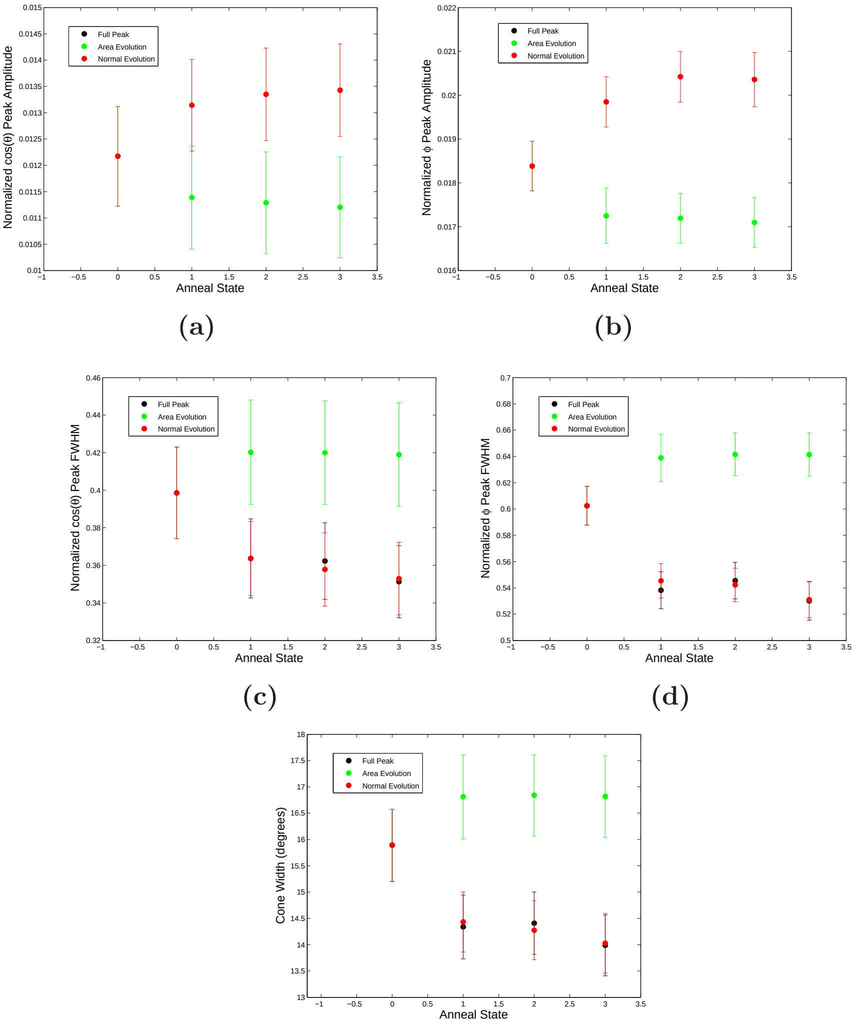

**(a)** **(b)**

**(c)** **(d)**

**(e)**

*Figure 6.43: Summary of fits with a Lorentzian function to the decomposed* $\Sigma 3$ *peak, where each anneal state was assigned either the boundary plane normal distribution or area distribution of the initial state. (a) and (b) show the peak amplitude with respect to* $\cos\theta$ *and* $\phi$*. (c) and (d) illustrate changes in the peak width, while (e) describes the cone angle that provides a width of the distribution on a sphere.*

metric was used as a simple alternative to boundary curvature. Correlations between boundary curvature and $\overline{\cos\alpha}$ should be performed. One would expect boundaries with $\overline{\cos\alpha} \sim 1$ to have low curvature, since $\overline{\cos\alpha} \sim 1$ suggests a boundary composed of many coherent twin patches. Spatially, this should form a flat boundary. Therefore, the expectation is for an increase in $\overline{\cos\alpha}$ for $\Sigma 3$ boundaries to be associated with a decrease in boundary curvature. Lastly, we decomposed the $\Sigma 3$ peak in the tracked microstructure into changes in boundary normal and interfacial area. This plot, shown in Figure 6.43, firmly illustrates that the observations in this sample were driven more by boundary normal contributions than changes in the boundary area.

Earlier, we suggested that the nucleation of twin boundaries could also produce an increase in the coherent twin population, assuming that boundaries that are forming are of the coherent twin configuration. At this stage of analysis of this nickel data set, we can not conclusively determine if such occurances were present or not. Confirming such critical events is a difficult process. Unlike the aluminum data set presented in Chapters 3 and 4, this nickel microstructure does not easily lend itself to identification of nucleations due to the sheer number of grains present and the number of states that are tracked.

At the time of the presented analysis, software to mine such data sets is in its infancy and determining new ways to look at the microstructure is still an evolving process. For instance, indentifying boundary nucleation conceptually seems like an easy process. One simply searches for boundaries which are not tracked in previous states. But the lack of tracking does not mean that they were not present in an earlier state, only that the software did not identify it as tracked. In fact, the processing of *.mic* files into the rectilinear grid *.dx* files and then the list of meshed triangular patches composing boundaries offers many points where a boundary can be lost. Adding to this problem is that we are searching for small features, which will inherently be the first objects to be removed through smoothing in the meshing process (see Chapter 5.6.2). Therefore, stating that a boundary or grain has nucleated in the mesh, does not necessarily indicate that it is not present in the original reconstruction. It just means that it was not of an appreciable size or amenable geometry to be inserted into the mesh.

It is issues like critical event identification that present challenges for the next generation of nfHEDM analysis. As with all emerging scientific disciplines, there will be periods where analysis leads experiment and vice versa. Here, we have seen the creation of an x-ray microscope that can monitor the evolution of a bulk microstructure as external stimuli change the properties of the system. Now, we have created a new collection of data that is unique in its field. Volumetric microstructures have been measured in the past, but restricted to destructive measurement techniques. Therefore, one-to-one correlation between components of the granular ensemble was never developed because it was never necessary. Alternatively, simulations of microstructures have been present over the past decades with the advent of greater computational resources. But these simulated systems also do not suffer from the tracking problems inherent in our data sets, because the evolution can be fully tracked: the changes realized by the grain ensemble are deterministic in that any point in the system can be tracked from the initial to final, and all intermediate states. It is in these contexts that the orientation maps produced through nfHEDM must operate and to reach a maturation level, where significant science can be readily accesible, computational tools must be developed to bridge these unique registration difficulties.

# Chapter 7

# Conclusions and Future Work

## 7.1 Summary

In this thesis, we have presented the capabilities of near-field High Energy X-ray Diffraction Microscopy as a microstructure characterization tool for monitoring evolution in response to annealing. Data collected with the dedicated near-field setup, at the 1-ID beamline at the Advanced Photon Source, was interpreted with the forward modeling method of microstructure reconstruction. The analysis produces microstructure maps with micron spatial resolution and orientations resolved to within $0.1^\circ$. Achieved through the assignment of crystallographic orientations to a triangular grid in sample space, the reconstruction is sensitive to intra-granular orientation variations and unique grain boundary shapes, which are difficult to capture using other spatially resolved x-ray imaging techniques. Experiments were performed on two microstructures with contrasting initial measurement states and subsequently followed very different evolutionary paths. It was with a deformed aluminum wire and fully recrystallized nickel cylinder that the three stages of annealing: recovery, recrystallization and grain growth, were explored.

Forward modeling's ability to measure localized orientations affords sensitivity to the recovery process. In coarse grained aluminum, a deformed microstructure served as the initial measurement state for an annealing experiment. Here, a movement towards uniform orientations were observed as a dominating and global signal to the application of heat. Orientation spreads were quantified by using the kernel averaged misorientation $KAM$ and intra-granular misorientation $IGM$ metrics, both of which characterize variations in the spatial distribution of orientations. It was observed that in each successive anneal state these recovery linked quantities decreased.

In addition to the volume reduction of deformed microstructure through recovery, the process of recrystallization was also suggested in the reconstructed orientation maps. A series of critical events were observed that resulted in the appearance or extinction of grains. The majority of these grain initiation events were confined to the surface of the sample, but were also identified within the bulk, where one grain was found to grow out of a heavily deformed region of microstructure (as characterized by both map reconstruction confidence and high *KAM*). Conversely, the tail end of a grain disappearance event was identified in the bulk region. A spatially disconnected grain was found to possess high orientation variation (deformed microstructure) and eventually be eroded via the encroachment of neighboring high angle grain boundaries of undeformed grains. A general observation that critical events were confined to the surface of the cylindrical sample suggests that measurements using surface techniques may not be measuring the same dynamics as present in the bulk.

An extensive data set of fully recrystallized polycrystalline nickel was used to study grain coarsening in a high purity microstructure. In direct contrast to the aluminum experiment, this nickel specimen afforded reconstructions of macroscopic volumes of material that were measured with very fine 2D samplings ($4\mu m vs. 20\mu m$). The wealth of science available from this experiment is overwhelming and we chose to focus on just one aspect of grain growth: the evolution of the coherent twin distribution. Here, an exceptionally low energy grain boundary configuration was studied on a per boundary basis. Such a dynamics study is unachievable using destructive microscopy techniques. These special boundary typse were found to account for $\sim 30\%$ of the interfacial area of the polycrystal and therefore their investigation is noteworthy. The specific analysis explored the evolution of the coherent twin boundary, described as a boundary possessing a $\{111\}, 60^\circ$ misorientation with its neighbor, as well as having a boundary interface that is also the $\{111\}$ plane. By limiting the analysis to only tracked boundaries that could be identified through four sample states, it was found that the distribution of these coherent twins increased, when interpreted with the grain boundary character distribution.

The mechanism for sharpening of this coherent twin peak was explored with tracked twin (both incoherent and coherent) boundaries. The grain boundary character distribution is a means of describing the mesoscale grain boundary space, by characterizing boundary normal and misorientation. The *GBCD* is an area weighted histogram in this five dimensional space, so identifying the origin(s) of sharpening in the context of boundary misorientation, normal, and area contributions was explored. The dominant signal for evolution in the microstructure was a re-orienting of boundaries of the twin misorientation into the coherent twin boundary plane ($\{111\}$). Within this grouping of boundaries that exhibited a more $\{111\}$ character, it was found that a grain re-oriented itself with respect to its neighbors (misorientation) to produce a more coherent twin like boundary. The twin boundary for this grain dominated its interfacial area distribution. This grain was an exceptional instance of moving towards the coherent twin in all five parameters of *GBCD* space. Lastly, area changes were explored, but were found to be negligibly responsible for the coherent twin evolution.

## 7.2 Suggestions for Future Work

While the annealing results in both high purity nickel and aluminum have been detailed in this thesis, the presentation has suffered from being a bit topical in nature. Currently, the field of nfHEDM is in a transition period. It can confidently be stated that measurements can now be readily produced using the available resources at the 1-ID beamline and reconstructions can be accomplished with presently static reconstruction software. While this is of great benefit to the community, it now places pressure on the development of computational tools to extract content of scientific merit from the reconstructed maps. Such tools are currently in their infancy and are constantly evolving and providing new ways to look at datasets, not restricted to the two presented. To conclude this work, we will provide some suggestions for future work on measurements of annealing phenomena using this variant of High Energy X-ray Diffraction Microscopy.

### 7.2.1 Nickel

The aluminum and nickel experiments laid the foundation for future measurements involving thermal treatments of polycrystalline microstructures. The nickel data set has provided a satisfactory collection of differential anneal states for polycrystalline material (aside from anomolous bowing of the sample in the final two states). Still, if exploration of isotropic grain growth is desired, then the appreciable density of a specific boundary type (the coherent twin) must be eliminated in future studies.

The nickel measurement does provide sufficient statistics for characterization of grain growth in anisotropic material. By classifying our microstructure through interface misorientation, we found a significant population of boundaries with misorientations of the form of $\Sigma 3^n$. Further exploration of this subset of boundaries could provide some interesting analysis as to how the microstructure evolved. Specifically, the $\Sigma 9$ boundary displayed a change in population away from $\{111\}$ boundary planes and towards $\{110\}$ tilts. This is curious from the prospective of the energy landscape in *GBCD* space. The $\{111\}$ is a local energy minima for this boundary misorientation, but it does not follow the inverse energy-population relationship that has been repeatedly observed [11]. The assumption is that the *global* energy minima associated with the $\Sigma 3$ is responsible for boundary normal evolution of the $\Sigma 9$s. Determining the environment of $\Sigma 9$ boundaries could provide evidence that clarifies this observation. Do the $\Sigma 9$s predominantly occur at triple lines with the other boundaries of the $\Sigma 3$ type? Do isolated (non-$\Sigma 3$) $\Sigma 9$ boundaries exist and does their distribution follow the expected inverse energy relation? Triple line analysis with this perspective has been produced with other measurement techniques [91] as well as initiated with nfHEDM measurements of copper [96].

Since boundaries in the nickel data set have been correlated across states, investigation of the components of boundary migration (curvature, mobility, energy) can begin to be isolated and studied. While non-trivial and relying upon computational geometry algorithms, the curvature of each boundary in the mesh can be quantified in each anneal state. Additionally, boundary mobility can be quantified, which is difficult to accomplish with other (destructive) mapping techniques because mobility inherently assumes dynamics. Since the sample states have been both aligned and correlated, the distance a boundary has been displaced, between anneals, should provide a description of this mobility variable. And similar to boundary energy, mobility can be framed in the context of grain boundary character space [42]. Lastly, a determination of energy through use of triple line equilibrium should produce estimates of interfacial energy for different points in grain boundary character space. These quantities can be compared with other measurements, gathered form simulation [2] and experiment [31]. Experimentally determining all three of these variables should produce some insight into the relevant variables for grain growth, albeit in a highly anisotropic material.

In the last paragraph, we mentioned energy comparisons to existing models. This process should definitely be explored with the grain which became more coherent twin like in all mesoscopic grain boundary character parameters. Did the grain's 'rotation' result in a cumulatively lower surface energy arrangement than in the earlier state? By associating our grain boundaries with energies from existing calculations in *GBCD* space [2], we should be able to draw a quick conclusion as to this question.

Lastly, with several thousand grains tracked, the statistics of the measurement suggest the observation of some critical events, such as grain initiation or extinction. While the data set should have captured such events, the analysis software for identification is still maturing. Earlier we outlined how the aluminum data set was perfect for grain-by-grain tracking because it was a coarse microstructure and was correlated by hand. This is not true of the nickel data and manual identification of critical events will be laborious. Therefore, development of software to determine such critical events is necessary and once produced should be able to give a picture of how the microstructure evolves. Does the production of a critical event have a global influence on the microstructure, or does the local microstructure simply adjust to accomendate the change? Such questions should be the first ones answered once critical event identification gains solid footing.

### 7.2.2 Aluminum

The most obvious deficiency of the aluminum data set is the spatial inadequacy of the measurement. With an experimental setup that has drastically improved over the one used to perform the aluminum measurement, repeating the experiment performed in this thesis shoud take (at most) half a day, given current capabilities. Increased spatial resolution in the mapped 2D plane should provide even better characterization of local orientation gradients, while rapid collection times would permit smaller vertical translations than the $20\mu m$ steps used here. Performing the exact same experiment would obviously be redundant, but with improved experimental capabilities a measurement encompassing all three annealing phenomena could be achieved. Beginning with a deformed microstructure, the sample could be annealed through recovery and recrystallization and conclude with coarsening during grain growth. This would be the ultimate annealing experiment.

As for the current aluminum data set, there are still several analysis paths which can be taken. The two dominating signals in this data set were recovery and recrystallization, both of which were associated with replacing a deformed microstructure with one that is undeformed. While not presented, there were very subtle boundary motions within the microstructure. Therefore, grain growth might have also been present (on a small scale) in this measurement. Correlating grains that exhibit exceptional changes in size with an estimate of their dislocation density [97] could provide more evidence of deformed microstructure being replaced by undeformed. Such an event was already suggested in the presentation of a grain which disappeared within the bulk and the comparision between its $KAM$ and that of its successor.

A final suggestion for continued analysis of this data set is to fully characterize the new grains which formed on the surface of the microstructure, which special attention given to initiation site properties. We have simply looked at the misorientation between the new grain and its parent and concluded that no high symmetry ($CSL$) boundaries were formed. Still, exploration of the relationship between the new and parent grain should be performed. Can anything be conclusively stated about the boundary plane of the parent grain where these events occured and do they differ from the other boundary planes of surface grains? The obvious anisotropy in the location of initiation sites is still a mystery, though discussion of boundary plane might provide some correlation. Such a calculation will be crude at best, due to the lack of spatial resolution along the wire axis. Estimation of the boundary normal would likely be achieved with some form of grain boundary stereology [98].

# Bibliography

[1] W. T. Read and W. Shockley. Dislocation models of crystal grain boundaries. *Phys. Rev.*, 78:275–289, May 1950.

[2] David L. Olmsted, Stephen M. Foiles, and Elizabeth A. Holm. Survey of computed grain boundary properties in face-centered cubic metals: I. grain boundary energy. *Acta Materialia*, 57(13):3694 – 3703, 2009.

[3] Christopher M. Hefferan, Jonathan Lind, Shiu Fai Li, Ulrich Lienert, Anthony D. Rollett, and Robert M. Suter. Observation of recovery and recrystallization in high-purity aluminum measured with forward modeling analysis of high-energy diffraction microscopy. *Acta Materialia*, 60(10):4311 – 4318, 2012.

[4] J. McKean and J. Roering. Objective landslide detection and surface morphology mapping using high-resolution airborne laser altimetry. *Geomorphology*, 57(34):331 – 351, 2004.

[5] N.H. Woodcock. Specification of fabric shapes using an eigenvalue method. *Geological Society of America Bulletin*, 88(9), 1977.

[6] D. Kar. *Correlating grain boundary properties to distributions during anisotropic grain growth - an interface field study in two and three dimensions.* PhD thesis, Carnegie Mellon University, 2012.

[7] Liesbeth Venema. Silicon electronics and beyond. *Nature*, 479(7373):309, November 2011.

[8] V. Levitin. *High Temperature Strain of Metals and Alloys.* Wiley, 2006.

[9] Masami Mayuzumi and Takeo Onchi. Creep deformation of an unirradiated zircaloy nuclear fuel cladding tube under dry storage conditions. *Journal of Nuclear Materials*, 171(23):381 – 388, 1990.

[10] Chang-Soo Kim, Anthony D. Rollett, and Gregory S. Rohrer. Grain boundary planes: New dimensions in the grain boundary character distribution. *Scripta Materialia*, 54(6):1005 – 1009, 2006. Viewpoint set no. 40: Grain boundary engineering.

[11] Brent L. Adams, Bassem S. El-Dasher, Gregory S. Rohrer, Anthony D. Rollett, David M. Saylor, and Paul Wynblatt. The distribution of internal interfaces in polycrystals. *Zeitschrift fur Metallkunde*, 2003.

[12] David M. Saylor, Bassem El Dasher, Ying Pang, Herbert M. Miller, Paul Wynblatt, Anthony D. Rollett, and Gregory S. Rohrer. Habits of grains in dense polycrystalline solids. *Journal of the American Ceramic Society*, 87(4):724726, 2004.

[13] F.J. Humphreys and M. Hatherly. *Recrystallization and Related Annealing Phenomena (Second Edition)*. Elsevier, Oxford, second edition, 2004.

[14] R.E. Reed-Hill. *Physical metallurgy principles*. University series in basic engineering. Van Nostrand, 1973.

[15] J.W. Martin, R.D. Doherty, and B. Cantor. *Stability of Microstructure in Metallic Systems*. Cambridge Solid State Science Series. Cambridge University Press, 1997.

[16] R.D. Doherty, D.A. Hughes, F.J. Humphreys, J.J. Jonas, D.J. Jensen, M.E. Kassner, W.E. King, T.R. McNelley, H.J. McQueen, and A.D. Rollett. Current issues in recrystallization: a review. *Materials Science and Engineering: A*, 238(2):219–274, 1997.

[17] R. D. Doherty. The deformed state and nucleation of recrystallization. *Metal Science*, 8(1):132–142, 1974-01-01T00:00:00.

[18] R.W. Cahn. A new theory of recrystallization nuclei. *Proceedings of the Physical Society. Section A*, 63(4):323, 1950.

[19] W. W. Mullins. Two-dimensional motion of idealized grain boundaries. *Journal of Applied Physics*, 27(8):900–904, 1956.

[20] J. Von Neumann. In *Metal Interfaces*, page 108. American Society for Metals, Cleveland, OH, 1952.

[21] C.S. Smith. In *Metal Interfaces*, page 65. American Society for Metals, Cleveland, OH, 1952.

[22] R.D. MacPherson and D.J. Srolovitz. The von neumann relation generalized to coarsening of three-dimensional microstructures. *Nature*, 446:1053–1055, 2007.

[23] M. E. Glicksman. Analysis of 3-d network structures. *Philosophical Magazine*, 85(1):3–31, 2005.

[24] S.J. Dillon, S. Lee, A.D. Rollett, and G.S. Rohrer. Measuring the five parameter grain boundary character distribution from three-dimensional orientation maps. *Microscopy and Microanalysis*, 14(Supplement S2):978–979, 2008.

[25] A. Khorashadizadeh, D. Raabe, S. Zaefferer, G. S. Rohrer, A. D. Rollett, and M. Winning. Five-parameter grain boundary analysis by 3d ebsd of an ultra fine grained cuzr alloy processed by equal channel angular pressing. *Advanced Engineering Materials*, 13(4):237–244, 2011.

[26] David Saylor, Bassem El-Dasher, Brent Adams, and Gregory Rohrer. Measuring the five-parameter grain-boundary distribution from observations of planar sections. *Metallurgical and Materials Transactions A*, 35:1981–1989, 2004. 10.1007/s11661-004-0147-z.

[27] Gregory S. Rohrer and Valerie Randle. Measurement of the five-parameter grain boundary distribution from planar sections. In Adam J. Schwartz, Mukul Kumar, Brent L. Adams, and David P. Field, editors, *Electron Backscatter Diffraction in Materials Science*, pages 215–229. Springer US, 2009.

[28] V. Randle. *The Measurement of Grain Boundary Geometry.* Electron Microscopy in Materials Science Series. Taylor & Francis, 1993.

[29] Saylor D.M., Morawiec A., and Rohrer G.S. The relative free energies of grain boundaries in magnesia as a function of five macroscopic parameters. *Acta Materialia*, 51(13):3675–3686, 2003.

[30] David M Saylor, Bassem S El Dasher, Anthony D Rollett, and Gregory S Rohrer. Distribution of grain boundaries in aluminum as a function of five macroscopic parameters. *Acta Materialia*, 52(12):3649 – 3655, 2004.

[31] Jia Li, Shen J. Dillon, and Gregory S. Rohrer. Relative grain boundary area and energy distributions in nickel. *Acta Materialia*, 57(14):4304 – 4311, 2009.

[32] V. Randle. *The role of the coincidence site lattice in grain boundary engineering.* Matsci Series. Institute of Materials, 1996.

[33] Valerie Randle. The coincidence site lattice and the sigma enigma. *Materials Characterization*, 47(5):411 – 416, 2001.

[34] R. L. Fullman. Interfacial free energy of coherent twin boundaries in copper. *Journal of Applied Physics*, 22(4):448–455, 1951.

[35] S. Ranganathan. On the geometry of coincidence-site lattices. *Acta Crystallographica*, 21(2):197–199, Aug 1966.

[36] H. Grimmer. The generating function for coincidence site lattices in the cubic system. *Acta Crystallographica Section A*, 40(2):108–112, Mar 1984.

[37] M.L. Kronberg and F.H. Wilson. Secondary recrystallization in copper. *American Institute of Mining and Metallurgical Engineers - Journal of Metals*, 1:501, 1949. cited By (since 1996) 6.

[38] D.A. Porter and K.E. Easterling. *Phase transformations in metals and alloys.* Chapman & Hall, 1992.

[39] M.G. Ardakani and F.J. Humphreys. The annealing behaviour of deformed particle-containing aluminium single crystals. *Acta Metallurgica et Materialia*, 42(3):763 – 780, 1994.

[40] A.P. Brahme, J.P. Fridy, and A.D. Rollett. Modeling recrystallization in aluminum using input from experimental observations. *Materials Science Forum*, 558-559:1057–1061, 2007.

[41] D.G Brandon. The structure of high-angle grain boundaries. *Acta Metallurgica*, 14(11):1479 – 1484, 1966.

[42] David L. Olmsted, Elizabeth A. Holm, and Stephen M. Foiles. Survey of computed grain boundary properties in face-centered cubic metalsii: Grain boundary mobility. *Acta Materialia*, 57(13):3704 – 3713, 2009.

[43] A.R. Eivani, H. Ahmed, J. Zhou, and J. Duszczyk. Correlation between electrical resistivity, particle dissolution, precipitation of dispersoids, and recrystallization behavior of aa7020 aluminum alloy. *Metallurgical and Materials Transactions A*, 40:2435–2446, 2009.

[44] A.J. Schwartz, M. Kumar, B.L. Adams, and D.P. Field. *Electron Backscatter Diffraction in Materials Science*. Springer, 2009.

[45] D. J. Dingley and V. Randle. Microtexture determination by electron back-scatter diffraction. *Journal of Materials Science*, 27:4545–4566, 1992. 10.1007/BF01165988.

[46] V. Randle. Application of electron backscatter diffraction to grain boundary characterisation. *International Materials Reviews*, 49(1):1–11, 2004-02-01T00:00:00.

[47] Brent Adams, Stuart Wright, and Karsten Kunze. Orientation imaging: The emergence of a new microscopy. *Metallurgical and Materials Transactions A*, 24:819–831, 1993. 10.1007/BF02656503.

[48] D. Rowenhorst and P. Voorhees. Measurements of the grain boundary energy and anisotropy in tin. *Metallurgical and Materials Transactions A*, 36:2127–2135, 2005. 10.1007/s11661-005-0333-7.

[49] Michael D. Uchic, Michael A. Groeber, Dennis M. Dimiduk, and J.P. Simmons. 3d microstructural characterization of nickel superalloys via serial-sectioning using a dual beam fib-sem. *Scripta Materialia*, 55(1):23 – 28, 2006. Viewpoint set no. 41 3D Characterization and Analysis of Materials Organized by G. Spanos.

[50] Shen J. Dillon and Gregory S. Rohrer. Characterization of the grain-boundary character and energy distributions of yttria using automated serial sectioning and ebsd in the fib. *Journal of the American Ceramic Society*, 92(7):1580–1585, 2009.

[51] B.C. Larson, W. Yang, G.E. Ice, J.D. Budai, and J.Z. Tischler. Three-dimensional x-ray structural microscopy with submicrometre resolution. *Nature*, 415:887–890, 2002.

[52] J.D. Budai, W. Yang, N. Tamura, J-S. Chung, J. Tischler, B.C. Larson, G.E. Ice, C. Park, and D.P. Norton. X-ray microdiffraction study of growth modes and crystallographic tilts in oxide films on metal substrates. *Nature Materials*, 2(7):487–492, 2003.

[53] W. Ludwig, S. Schmidt, E.M. Lauridsen, and H.F. Poulsen. X-ray diffraction contrast tomography: a novel technique for three-dimensional grain mapping of polycrystals. i. direct beam case. *Journal of Applied Crystallography*, 41(2):302–309, 2008.

[54] W. Ludwig, A. King, P. Reischig, M. Herbig, E.M. Lauridsen, S. Schmidt, H. Proudhon, S. Forest, P. Cloetens, S. Rolland du Roscoat, J.Y. Buffire, T.J. Marrow, and H.F. Poulsen. New opportunities for 3d materials science of polycrystalline materials at the micrometre lengthscale by combined use of x-ray diffraction and x-ray imaging. *Materials Science and Engineering: A*, 524(12):69 – 76, 2009.

[55] A. King, G. Johnson, D. Engelberg, W. Ludwig, and J. Marrow. Observations of intergranular stress corrosion cracking in a grain-mapped polycrystal. *Science*, 321(5887):382–385, 2008.

[56] A. King, P. Reischig, Simon Martin, Joao F. B. D. Fonseca, M. Preuss, and Wolfgang Ludwig. Grain Mapping by Diffraction Contrast Tomography: Extending the Technique to Sub-grain Information. In *Risø International Symposium on Materials Science: Challenges in materials science and possibilities in 3D and 4D characterization techniques*, Denmark, September 2010.

[57] H.F. Poulsen. *Three-Dimensional X-Ray Diffraction Microscopy: Mapping Polycrystals and their Dynamics*. Number no. 205 in Springer Tracts in Modern Physics. Springer, 2004.

[58] H.F. Poulsen, W. Ludwig, E.M. Lauridsen, S. Schmidt, W. Pantleon, U.L. Olsen, J. Oddershede, P. Reischig, A. Lyckegaard, J. Wright, and G. Vaughan. 4D Characterization of Metals by 3DXRD. In *Risø International Symposium on Materials Science: Challenges in materials science and possibilities in 3D and 4D characterization techniques*, 2010.

[59] U. Lienert, M.C. Brandes, J. V. Bernier, M.J. Mills, H.M. Miller, C. Hefferan, S.F. Li, J. Lind, and R. Suter. 3dxrd at the advanced photon source: Orientation mapping and deformation studies. In *Risø International Symposium on Materials Science: Challenges in materials science and possibilities in 3D and 4D characterization techniques*, 2010.

[60] U. Lienert, S.F. Li, C.M. Hefferan, J. Lind, R.M. Suter, J.V. Bernier, N.R. Barton, M.C. Brandes, M.J. Mills, M.P. Miller, B. Jakobsen, and W. Pantleon. Advanced materials analysis, part ii: High-energy diffraction microscopy at the advanced photon source. *JOM Journal of the Minerals*, 63:70–77, 2011.

[61] R. M. Suter, D. Hennessy, C. Xiao, and U. Lienert. Forward modeling method for microstructure reconstruction using x-ray diffraction microscopy: Single-crystal verification. *Review of Scientific Instruments*, 77(12), 2006.

[62] S.F. Li and R.M. Suter. Adaptive reconstruction method for three-dimensional orientation imaging. In preparation, 2012.

[63] R. M. Suter, C. M. Hefferan, S. F. Li, D. Hennessy, C. Xiao, U. Lienert, and B. Tieman. Probing microstructure dynamics with x-ray diffraction microscopy. *Journal of Engineering Materials and Technology*, 130(2), 2008.

[64] C. M. Hefferan, S. F. Li, J. Lind, and R. M. Suter. Tests of microstructure reconstruction by forward modeling of high energy x-ray diffraction microscopy data. *Powder Diffraction*, 25(2):132–137, 2010.

[65] C. M. Hefferan, S. F. Li, J. F. Lind, U. Lienert, A. D. Rollett, P. Wynblatt, and R. M. Suter. Statistics of high purity nickel microstructure from high energy x-ray diffraction microscopy. *Computers, Materials, & Continua*, 14:209–219, 2009.

[66] S.F. Li. *Imaging of Orientation and Geometry in Microstructures: Development and Applications of High Energy X-ray Diffraction Microscopy.* PhD thesis, Carnegie Mellon University, 2011.

[67] D. Hennessy. *Three Dimensional X-Ray Diffraction Microscope Studies of Bulk Materials Microstructure.* PhD thesis, Carnegie Mellon University, 2006.

[68] U. Lienert, M.C. Brandes, J.V. Bernier, J. Weiss, S.D. Shastri, M.J. Mills, and M.P. Miller. In situ single-grain peak profile measurements on ti-7al during tensile deformation. *Materials Science and Engineering: A*, 524(1-2):46 – 54, 2009. Special Topic Section: Probing strains and Dislocation Gradients with diffraction.

[69] H. F. Poulsen, L. Margulies, S. Schmidt, and G. Winther. Lattice rotations of individual bulk grains: Part i: 3d x-ray characterization. *Acta Materialia*, 51(13):3821 – 3830, 2003.

[70] H. F. Poulsen, S. F. Nielsen, E. M. Lauridsen, S. Schmidt, R. M. Suter, U. Lienert, L. Margulies, T. Lorentzen, and D. Juul Jensen. Three-dimensional maps of grain boundaries and the stress state of individual grains in polycrystals and powders. *Journal of Applied Crystallography*, 34(6):751–756, 2001.

[71] Henning Friis Poulsen and Soeren Schmidt. Reconstruction of grain boundaries in polycrystals by filtered back-projection of diffraction spots. *Journal of Applied Crystallography*, 36(2):319–325, 2003.

[72] S. Schmidt, S. F. Nielsen, C. Gundlach, L. Margulies, X. Huang, and D. Juul Jensen. Watching the growth of bulk grains during recrystallization of deformed metals. *Science*, 305(5681):229–232, 2004.

[73] S.F. Li, J. Lind, C.M. Hefferan, R. Pokharel, U. Lienert, A.D. Rollett, and R.M. Suter. Three dimensional plastic response in polycrystalline copper via near-field high energy x-ray diffraction microscopy. *Journal of Applied Crystallography*, 2012.

[74] R. Pokharel, S.F. Li, J. Lind, C.M. Hefferan, U. Lienert, R.A. Lebensohn, R.M. Suter, and A.D. Rollett. Quantifying damage accumulation using state-of-the-art fft method. *Materials Science Forum*, 702-703:515–518, 2012.

[75] Bo Jakobsen, Henning F. Poulsen, Ulrich Lienert, Jonathan Almer, Sarvjit D. Shastri, Henning O. Sørensen, Carsten Gundlach, and Wolfgang Pantleon. Formation and subdivision of deformation structures during plastic deformation. *Science*, 312(5775):889–892, 2006.

[76] F. Frank. Orientation mapping. *Metallurgical and Materials Transactions A*, 19:403–408, 1988. 10.1007/BF02649253.

[77] J. K. MacKenzie. Second paper on statistics associated with the random disorientation of cubes. *Biometrika*, 45(1-2):229–240, 1958.

[78] Valerie Randle. Representation of grain misorientations (mesotexture) in rodrigues-frank space. *Proceedings: Mathematical and Physical Sciences*, 431(1881):61–69, 1990.

[79] N.W. Ashcroft and N.D. Mermin. *Solid State Physics*. Saunders College, Philadelphia, 1976.

[80] Charles Kittel. *Introduction to Solid State Physics*. John Wiley & Sons, Inc., New York, 6th edition, 1986.

[81] P. Kenesei, U. Lienert, A.M Khounsary, S.F. Li, J. Lind, C.M. Hefferan, and R.M. Suter. Registration of concurrent hedm and tomographic measurements. Demonstrated at 1-ID March 2010. Unpublished, 1997.

[82] S.T. Thornton and J.B. Marion. *Classical Dynamics of Particles and Systems*. SPCK Publishing, 5th edition, 1995.

[83] J. Lind, 2011. Private communication.

[84] D. Marr and E. Hildreth. Theory of edge detection. *Proceedings of the Royal Society of London. Series B. Biological Sciences*, 207(1167):187–217, 1980.

[85] S. Weissmann. Characterization of lattice defects and concomitant strain distribution. In *Advances in X-Ray Analysis (Volume 35A)*, pages 221–237. Plenum Press, New York, NY, 1992.

[86] John F. Bingert, Veronica Livescu, and Ellen K. Cerreta. Characterization of shear localization and shock damage with ebsd. In Adam J. Schwartz, Mukul Kumar, Brent L. Adams, and David P. Field, editors, *Electron Backscatter Diffraction in Materials Science*, pages 301–315. Springer US, 2009.

[87] R. M. Suter. Lorentz factor calculation.

[88] A.W. Larsen, H.F. Poulsen, L. Margulies, C. Gundlach, Q.F. Xing, X.X. Huang, and D. Juul Jensen. Nucleation of recrystallization observed in situ in the bulk of a deformed metal. *Scripta Mater.*, 53:553–557, 2005.

[89] CGAL, Computational Geometry Algorithms Library. http://www.cgal.org.

[90] Hsun Hu. Texture of metals. *Texture*, 1(4):233–258, 1974.

[91] Bryan W. Reed, Roger W. Minich, Robert E. Rudd, and Mukul Kumar. The structure of the cubic coincident site lattice rotation group. *Acta Crystallographica Section A*, 60(3):263–277, May 2004.

[92] N.I. Fisher, T. Lewis, and B.J.J. Embleton. *Statistical Analysis of Spherical Data*. Cambridge University Press, 1993.

[93] N.H. Woodcock and M.A. Naylor. Randomness testing in three-dimensional orientation data. *Journal of Structural Geology*, 5(5):539 – 548, 1983.

[94] E. Cohen. Fitting non-cosine 3-d directional tuning profiles to motor cortial spike counts. Technical report, Carnegie Mellon University, 2008.

[95] D. Moldovan, D. Wolf, S.R. Phillpot, and A.J. Haslam. Grain roation as a mechniasm of grain growth in nanocrystalline materials. 2004.

[96] S.F. Li. Annealing study of grain boundary engineered copper using high energy x-ray diffraction microscopy. TMS Presentation, March 2012.

[97] B.S El-Dasher, B.L Adams, and A.D Rollett. Viewpoint: experimental recovery of geometrically necessary dislocation density in polycrystals. *Scripta Materialia*, 48(2):141 – 145, 2003.

[98] David Saylor, Bassem El-Dasher, Brent Adams, and Gregory Rohrer. Measuring the five-parameter grain-boundary distribution from observations of planar sections. *Metallurgical and Materials Transactions A*, 35:1981–1989, 2004. 10.1007/s11661-004-0147-z.